Endosomal ionic balance and its role in bunyavirus entry

Samantha Elizabeth Hover

Submitted in accordance with the requirements for the degree of
Doctor of Philosophy

The University of Leeds
Faculty of Biological Sciences
School of Molecular and Cellular Biology

September 2019

The candidate confirms that the work submitted is her own, except where work which has formed part of jointly authored publications has been included. The contribution of the candidate and the other authors to this work has been explicitly indicated below. The candidate confirms that appropriate credit has been given within the thesis where reference has been made to the work of others. Chapter three forms work published in PLOS Pathogens: Hover S, Foster B, Fontana J, Kohl A, Goldstein SAN, Barr JN and Mankouri J "Bunyavirus requirement for endosomal K^+ reveals new roles of cellular ion channels during infection" 2018. All work was completed by the candidate, except part of Figure 4 performed by Miss Becky Foster, which forms Chapter 3 Figure 3.16 and 3.18.

Acknowledgements

A massive thank you goes to my primary supervisor Dr Jamel Mankouri, right back from my undergraduate dissertation project when I was just a lowly undergraduate student with no clue about research. Through encouragement and quirky diagrams you have been teaching me ever since then, improving my scientific understanding and giving me every opportunity to improve myself and realise my aspirations. Without your guidance and the opportunities you have given me I would not have become the scientist I am today, so thank you!

I also thank my co-supervisor Dr John Barr for his help and bunyavirus advice across the years, especially for the many months when you were ‘in charge’. Thank you for listening to all my grievances.

To my surrogate supervisor Dr Juan Fontana, thank you (and the Astbury Biostructure Facility staff) for helping me with my BUNV EM, including all the times that it didn’t work. Also, for all the time that you put in to teach me how it all works and how to do the data analysis. You have a million things to do a week, with so many different side projects, so I really appreciate you taking the time to help me. Thanks for answering all my questions and thank you for employing me (I guess I’m doing something right)!

To the present Team Mankouri members Hayley Pearson, Frankie Charlton and Ibrahim Al-Masoud, I bequeath you all my protocols, an organised lab space, Trevor & Doris, and my label maker. Hayley and Frankie, thank you for all the troubleshooting chats, help with lab work and keeping every day interesting. I wish you all the best of luck during your PhDs and although you won’t need me, I will be around to help if you need a chat (P.S. Hayley is in charge now). Becky Foster, thank you in particular for your help on the AG4 work during your MBiol and your help during manuscript preparations; even though you did abandon me for the Whitehouse lab. A special thanks to Ellie Todd, for joining me in airing grievances, for providing constant companionship during the year that you were part of Team Mankouri, and being there for me even after leaving me. May you never drift too far! To the rest of Barr group, thank you for your support, especially to Francis Hopkins for helping me figure out a BUNV purification protocol and how to not blow up the ultracentrifuges. To the other past Mankouri group members, thank you for letting me teach you at some stage or another and helping me improve: Jamie Royle, Theo Georgious, Aseel

Alyahyawi, Samah Zurqi, Luke Moore, Dan Mega, James Murphy, Molly Patterson, Henry Blest, Brad Hall, Toby Richardson and Beth Rebecca.

To the rest of Virology and Garstang 8.54, thank you for providing advice and keeping yourselves available for Friday night frivolity. Thank you Nat Kingston for being there for me through all the drama and continually providing emotional support in the form of chocolate and wine. Thank you Joe Ward (and TimTom) for putting up with my obsessive cleaning for 2 years and my ranting! Kinder eggs are not the same without you. In Garstang 8.54, thank you to Sarah Good, Eleni Anna-Loundras, Becky Holdich, Dan O'Brien, Georgia Pangratiou, Lee Sherry, Keith Grehan and Jay Miles for your entertainment and keeping me sane for the past 4 years.

An important thank you goes to my parents for giving every opportunity in life and to realise my career aspirations, and for the financial and emotional support to do so. Thank you for always being there for me, even when you ran away abroad for a year. Also, thanks Oscar for all the cuddles they were much needed, sorry/not sorry that you hated them.

Finally, thank you to Sam Dobson for providing continued emotional support, particularly during all the drama, and giving me advice both in science and in life. Thanks for putting up with me and for being an amazing cook; it helped, a lot.

Abstract

The *Bunyavirales* are the largest group of negative-sense RNA viruses with new members emerging due to changes in virus/host relationships and segment reassortment. The *Bunyavirales* are of interest as they require host-cell potassium (K^+) channels during the early stages of their infectious lifecycle. The mechanism(s) governing this dependence had not been previously defined.

In Chapter 1, using the prototype member of the family, Bunyamwera virus (BUNV), the role of K^+ channels during virus entry was investigated. It was shown that BUNV encounters high-K^+ containing endosomes during virus entry which is controlled by endosome-resident K^+ channels. The inhibition of these channels disrupted endosomal K^+ uptake and prevented viruses escaping the endosomal system. Mimicking the ionic environment of late endosomes *in vitro* (pH 6.3/K^+) expedited BUNV entry and reduced its susceptibility to K^+ channel inhibition. This highlighted endosomal K^+ as a biochemical cue for BUNV, explaining its requirement for host-cell K^+ channels.

In Chapter 2, the effects of pH/K^+ priming on virion architecture were investigated using cryo-electron tomography and sub-tomogram averaging (STA). BUNV glycoprotein (GP) spike averages identified key definitions in the GP trimer that became disordered in response to pH/K^+ priming. STA indicated uncoupling of the GP trimers in response to K^+, likely facilitating a pre-fusion intermediate that exposes the fusion loop. This begins to explain the changes triggered by endocytic pH/K^+ to expedite infection.

In Chapter 3, through K^+ channel silencing it was identified that the two-pore K^+ channel TWIK2 was necessary for BUNV infection. TWIK2 localized to endo/lysosomal compartments through which BUNV traversed during infection. This inferred a role for TWIK2 during BUNV entry and revealed this channel as a new anti-BUNV target.

The culmination of these findings reveal for the first time, the basis for why inhibiting K^+ channels impedes BUNV.

Table of Contents

Chapter 1 | Introduction 1

1.1 The *Bunyavirales* order 2

1.1.1 Classification 2

1.1.2 Zoonosis, emergence and disease 3

1.1.3 Prevention and treatments 8

1.2 BUNV structure and genome 11

1.2.1 Genome organisation 12

1.2.1.1 The L segment 13

1.2.1.2 The M segment 13

1.2.1.3 The S segment 15

1.3 Mammalian replication cycle 15

1.3.1 Attachment, entry and virion uncoating 16

1.3.2 Viral factory formation 18

1.3.3 Protein production and replication 19

1.3.4 Virion assembly, maturation and release 21

1.3.5 Perturbing the host-cell immune response 21

1.3.6 Late stages of the BUNV lifecycle 22

1.3.7 Arthropod replication cycle 22

1.4 Host-cell ion channels 23

1.4.1 Potassium channels 24

1.4.1.1 K_V channels 25

1.4.1.2 K_{Ca} channels 25

1.4.1.3 K_{IR} channels 26

1.4.1.4 K_{2P} channels 26

1.4.2 Calcium channels 27

1.4.3 Sodium channels 28

1.4.4 Anionic chloride channels 28

1.5 Ion channels and disease 29

1.6 Viral manipulation of host-cell ion channels 30

  1.6.1 Ion channel modulation by viral proteins 31

  1.6.2 Virus requirement for cellular ion channels 32

    1.6.2.1 Ion channel requirements during virus entry 33

1.7 Thesis aims 36

Chapter 2 | Materials and methods 38

2.1 Chemicals 39

2.2 Mammalian cell culture and virus 39

  2.2.1 Cell culture and maintenance 39

  2.2.2 WT BUNV stock propagation 39

  2.2.3 Virus titre determination by plaque assay 39

2.3 SYTO82/DiD-BUNV production and purification 40

  2.3.1 Propagation and nucleic acid labelling 40

  2.3.2 Clarification and lipid labelling 40

  2.3.3 Purification 41

2.4 BUNV purification for electron microscopy 41

  2.4.1 BUNV propagation optimisation 41

  2.4.2 BUNV purification 42

2.5 Virus infection assays 42

  2.5.1 SYTO82/DiD-BUNV infection assays 42

  2.5.2 BUNV-N protein production timecourse 43

  2.5.3 BUNV virion release timecourse 43

  2.5.4 Pre-infection drug treatments 43

  2.5.5 Ammonium chloride addition timecourse 43

2.6 Virus priming assays 44

  2.6.1 Virus pH/ion priming protocol 44

    2.6.1.1 Priming buffers 44

2.6.2 [K^+] range priming 44

2.6.3 Priming reversibility assay 44

2.6.4 Virus priming and ion channel modulators 44

2.6.5 pH/K^+ BUNV-N expression timecourse 45

2.6.6 BUNV antibody neutralisation assay 45

2.7 Fluorescent labelling of endosomal compartments 45

2.7.1 Fluorescent tracking of SYTO82/DiD-BUNV localisation 45

2.7.1.1 Rab7 and Rab11 Transfections 46

2.7.2 Endosomal K^+ AG4 labelling 46

2.7.2.1 SYTO82-DiD-BUNV localisation with AG4 46

2.7.2.2 Assessment of AG4 localisation to endosomal compartments 46

2.8 K_{2P} channel knockdowns and overexpression 48

2.8.1 K_{2P} channel siRNA knockdown 48

2.8.2 TWIK2-GFP mammalian cell transfections 48

2.8.2.1 TWIK2-GFP transfection and SYTO82/DiD-BUNV infection 48

2.8.2.2 Determining TWIK2-GFP endosomal localisation 48

2.9 Biochemical methods 49

2.9.1 Harvesting mammalian cells for lysis 49

2.9.2 SDS-PAGE 49

2.9.3 Western blotting 50

2.9.3.1 Antibodies 50

2.9.4 Silver staining 50

2.9.5 Immunofluorescence 51

2.9.6 IncuCyte Zoom imaging and analysis 51

2.9.7 Fixed cell confocal microscopy 52

2.9.8 Live cell confocal microscopy 52

2.9.9 Determination of K_{2P} channel expression 52

2.9.9.1 RNA extraction and cDNA synthesis 52

2.9.9.2 K_{2P} channel RT-PCR 53

2.9.9.3 K_{2P} channel siRNA knockdown RT-PCR 54

2.9.10 TWIK2 site-directed mutagenesis 54

2.9.10.1 PCR mutagenesis and amplification 54

2.9.10.2 KLD reaction and bacterial cell transformation 55

2.9.10.3 DNA amplification, purification and sequence confirmation 55

2.9.10.4 Generating multiple mutations 55

2.10 Electron microscopy 56

2.10.1 Negative stain EM 56

2.10.2 Virion priming, grid loading and vitrification 56

2.10.3 Cryo-EM grid screening and cryo-electron tomography 57

2.10.4 Reconstructing 3D tomograms 57

2.10.5 Sub-tomogram averaging 58

2.10.5.1 Template generation 58

2.10.5.2 Automated particle selection and refinement 59

Chapter 3 | BUNV requires endosomal K^+ for entry into cells 61

3.1 Introduction 62

3.2 Assessing the timeline of BUNV infection 64

3.3 K^+ ions influence BUNV infectivity 66

3.3.1 pH 6.3 and K^+ mimic an endosomal cue for virion uncoating66

3.3.2 BUNV priming occurs at physiological [K^+] and causes irreversible changes 70

3.3.3 K^+ priming permits more efficient endosomal escape 70

3.3.4 K^+ primed virions are more resistant to host cell K^+ channel inhibition 72

3.4 Production of infectious dual-fluorescently labelled BUNV to track virus entry 73

3.4.1 BUNV entry can be visualised in live cells 76

3.5 Defining the route of virion trafficking 80

3.5.1 BUNV enters late endosomes during entry 80

3.5.2 BUNV does not traffic via recycling endosomes 81

3.6 BUNV traffics through high [K^+]-containing endosomes 85

3.7 K^+ channel modulators influence the K^+ distribution across the endosomal network 87

3.8 BUNV endocytic processes are disrupted by K^+ channel inhibition 91

3.9 Discussion 95

3.9.1 BUNV is trafficked through EEs and accumulates in LEs during entry 96

3.9.2 Ionic balance in endosomes dictates BUNV infectivity 97

3.9.3 K^+ channel modulation alters endosomal K^+ accumulation 99

Chapter 4 | Using cryo-electron tomography to elucidate K^+-induced structural changes in the BUNV glycoproteins 103

4.1 Introduction 104

4.2 BUNV release is optimal at 48 hpi in BHK-21 cells infected at an MOI of 0.1 106

4.3 Producing BUNV for cryo-ET 108

4.4 pH 6.3 and K^+ cause changes in the BUNV architecture 111

4.5 Cryo-ET confirms that pH 6.3 and K^+ alter virion morphology and GP arrangements 115

4.6 STA of pH 7.3 GPs at 14 Å reveals newly identified structures within the trimer 120

4.7 STA confirms that pH 6.3 + K^+ priming leads to uncoupling of the GP trimers 125

4.8 Discussion 130

Chapter 5 | BUNV is dependent upon TWIK2 channels for infection of mammalian cells 137

5.1 Introduction 138

5.2 BUNV infection-competent cell lines reveal four candidate K_{2P} channels required for infection 139

5.3 siRNA silencing identified a specific K_{2P} channel required for BUNV infection 142

5.4 Defining the role of TWIK2 in BUNV infection 144

5.4.1 BUNV traffics through TWIK2-containing endosomes 144

5.4.2 SDM to abolish endosomal trafficking motifs leads to TWIK2 re-localisation 147

5.5 Discussion 151

Chapter 6 | Final Discussion 154

6.1 What is the cellular role for endosomal [K^+] regulation? 155

6.2 K^+-priming for improving therapeutic delivery 157

6.3 Ion channel drug repurposing for anti-viral therapeutics 159

6.4 Conclusions 161

List of Tables

Table 1.1 Summary of human and animal-infecting bunyaviruses 7

Table 2.1 Fluorescent markers used to label cellular and viral components 47

Table 2.2 SDS-PAGE gel recipe per gel.. 49

Table 2.3 Silver staining recipes 51

Table 2.4 K_{2P} channel and GAPDH PCR primers 53

Table 2.5 TWIK2-GFP SDM primers 54

Table 2.6 TWIK2 mutants generated using SDM.. 55

Table 2.7 EM priming buffer contents 57

List of Figures

Figure 1.1 Bunyaviruses undergo reassortment, generating new virus species 5

Figure 1.2 BUNV virions 12

Figure 1.3 BUNV possesses a tri-segmented genome 14

Figure 1.4 Schematic of the BUNV lifecycle in mammalian cells 16

Figure 1.5 Predicted mechanism of virus-endosome membrane fusion 18

Figure 1.6 BUNV M Segment Translation and Protein Topology 20

Figure 1.7 Ion channel gating 24

Figure 1.8 K^+ channel classification 25

Figure 1.9 Predicted model of EBOV entry 34

Figure 1.10 K^+ channels are required for early BUNV lifecycle stages 35

Figure 3.1 A K^+ gradient exists within endosomes, where $[K^+]$ increases with decreasing pH 63

Figure 3.2 Investigating the timeline of BUNV infection 65

Figure 3.3 An acidic environment alone cannot prime BUNV for entry 67

Figure 3.4 K^+ priming at pH 6.3 expedites BUNV infection 68

Figure 3.5 K^+ priming is independent of the cell type 69

Figure 3.6 K^+ priming occurs at physiologically relevant K^+ and increases the rate of BUNV infection 71

Figure 3.7 K^+ priming reduces the BUNV sensitivity to K^+ channel inhibition 73

Figure 3.8 Propagation of dual-fluorescent labelled BUNV 77

Figure 3.9 Labelled-BUNV is infectious and penetrates cells 78

Figure 3.10 Internalised BUNV can be visualised in live cells and colocalises with internalised EGF 79

Figure 3.11 BUNV can be visualised in endosomes up to 8 hpi 82

Figure 3.12 BUNV localises to late endosomes 83

Figure 3.13 BUNV does not enter recycling endosomes 84

Figure 3.14 Endosomal $[K^+]$ can be assessed using a K^+-sensitive dye AG4 and is high within late endosomes 86

Figure 3.15 BUNV traffics through sites of high endosomal $[K^+]$ 87

Figure 3.16 K^+ channel inhibition disrupts the distribution of endosomal $[K^+]$ 89

Figure 3.17 Disruption of endosomal $[K^+]$ by K^+ channel blockade confirmed using an alternative pH-sensitive dye 90

Figure 3.18 K^+ channel inhibition does not prevent BUNV internalisation into endosomes 92

Figure 3.19 K^+ channel inhibition leads to the endosomal accumulation of virions 93

Figure 3.20 K^+ channel inhibition causes BUNV to accumulate in lysosomes 95

Figure 3.21 Schematic of BUNV entry facilitated by K^+ channels 102

Figure 4.1 BUNV propagation is optimal in BHK-21 cells at an MOI of 0.1107

Figure 4.2 BUNV purification produces high titre virus sufficiently pure for cryo-ET 109

Figure 4.3 Negative stain of purified BUNV confirms sample purity for cryo-ET 110

Figure 4.4 Cryo-EM reveals changes in the BUNV structure upon K^+ treatment 113

Figure 4.5 Cryo-EM of pH 6.3 treated virions reveal that K^+ prevents virion aggregation at lower pH 114

Figure 4.6 Schematic of cryo-ET workflow 116

Figure 4.7 Cryo-ET of pH 7.3 (ctl) virions shows an arrangement of GP spikes present across the entire virion surface 117

Figure 4.8 Cryo-ET of pH 6.3 + K^+ (primed) virions identifies clear changes in virion morphology and GP arrangements 118

Figure 4.9 Comparison of Control and pH 6.3 + K^+ virions 119

Figure 4.10 STA confirms the tripodal arrangement of BUNV GPs 122

Figure 4.11 Determining the ‘handedness’ of the virtual GP particles 124

Figure 4.12 The crystal structure of *Orthobunyavirus* head and stalk domains fit within the electron density STA reconstruction 125

Figure 4.13 STA of pH 6.3 + K^+ primed BUNV GPs identifies an altered spike arrangement 127

Figure 4.14 Comparison of control versus primed BUNV GP reconstructions 128

Figure 4.15 Neutralisation of BUNV by BUNV-Gc antibodies indicates that the core monomeric GP structure has not been completely disrupted by priming 130

Figure 4.16 Comparison of BUNV GP structures with the protein organisation reveals mechanistic insight into Gc function 132

Figure 4.17 Predicted mechanism of pH 6.3/K^+ induced changes in BUNV GP spikes 136

Figure 5.1 K_{2P} channel structure 138

Figure 5.2 BUNV infects cell lines that express 4 of the 15 K_{2P} channels .. 141

Figure 5.3 TWIK2 knockdown is detrimental to BUNV infection 143

Figure 5.4 TWIK2 silencing leads to a concentration dependent decrease in BUNV infection.. 144

Figure 5.5 TWIK2 localises to lysosomes 146

Figure 5.6 BUNV localises to TWIK2-containing endosomes........................ 147

Figure 5.7 Generating TWIK2 localisation mutants 149

Figure 5.8 Mutations in TWIK2 endosomal localisation signals reduce TWIK2 endosomal sorting 150

Abbreviations

aa	Amino acids
AG4	Asante potassium green-4
ANDV	Andes virus
APS	Ammonium persulfate
BATV	Batai virus
BK_{Ca}	Large-conductance calcium-activated potassium channel
BMP	Bis(monoacylglycerol)-phosphate
bp	Base pairs
BSA	Bovine serum albumin
BSL	Biosafety level
BUNV	Bunyamwera virus
C3	Three-fold (symmetry)
Ca^{2+}	Calcium
CCHFV	Crimean-Congo haemorrhagic fever virus
CF	Cystic fibrosis
CFTR	Cystic fibrosis transmembrane conductance regulator
CHIKV	Chikungunya virus
Cl^{-}	Chloride
CLIC	Chloride intracellular channels
CNS	Central nervous system
Cryo-EM	Cryo-electron microscopy
Cryo-ET	Cryo-electron tomography
Ctl	Control
CytoP	CytoPainter
DC-SIGN	Dendritic cell-specific ICAM-grabbing nonintegrin
dH_2O	Deionised water

DiDvbt	DiD-vybrant
DMEM	Dulbecco's modified eagle's medium
dsRNA	Double-stranded RNA
EBOV	Ebola virus
EE	Early endosome
EGF	Epidermal growth factor
EGFR	Epidermal growth factor receptor
EM	Electron microscopy
ENaC	Amiloride-sensitive epithelial Na^+ channels
ER	Endoplasmic reticulum
FBS	Foetal bovine serum
FL	Fusion loop
FSC	Fourier shell correlation
GAPDH	Glyceraldehyde 3-phosphate dehydrogenase
GP	Glycoprotein
H^+	Hydrogen
HA	Haemagglutinin
HAZV	Hazara virus
HCV	Hepatitis C virus
HIV-1	Human immunodeficiency virus 1
hpi	Hours post-infection
hr	Hour
HRP	Horseradish peroxidase
hRSV	Human respiratory syncytial virus
HSV-1	Herpes simplex virus 1
IAV	Influenza A virus
IFN	Interferon
IFNAR-/-	Interferon type 1 receptor A knockout

IMEM	Iscove’s modified Dulbecco’s medium
IRF-3	Interferon regulatory factor-3
ISG	Interferon-stimulated gene
K^+	Potassium
$[K^+]$	Potassium concentration
K_{2P}	Two-pore potassium (channels)
K_2SO_4	Potassium sulphate
K_{ATP}	ATP-sensitive potassium (channels)
kb	Kilobases
K_{Ca}	Calcium-activated potassium (channels)
KCl	Potassium chloride
kDa	Kilodaltons
K_{IR}	Inwardly-rectifying potassium (channels)
K_v	Voltage-gated potassium (channels)
L	Large (segment)
LACV	La Crosse virus
LDL	Low-density lipoprotein
LDLR	Low-density lipoprotein receptor
LE	Late endosome
LLB	Leeds lysis buffer
M	Medium (segment)
M1	Matrix protein 1
MC	Methyl cellulose
MDA	MDA-MB-231
min	minute
$MitoK_{ATP}$	Mitochondrial ATP-sensitive potassium (channels)
MOI	Multiplicity of infection
MR	Magic Red Cathepsin-B dye

mRNA	Messenger RNA
MVA	Modified vaccinia virus ankara
MVBs	Multivesicular bodies
N protein	Nucleoprotein
Na^+	Sodium
NaCl	Sodium chloride
NH_4Cl	Ammonium chloride
NHE	Na^+-H^+ exchanger
NHP	Non-human primate
NPC1	Neimann-pick factor 1
NRIV	Ngari virus
NSm	Non-structural M protein
NSs	Non-structural S protein
nt	Nucleotides
ORF	Open reading frame
PBS	Phosphate buffered saline
PEET	Particle Estimation for Electron Tomography
Pen/strep	Penicillin (100 U/ml) and streptomycin (100 µg/ml)
PFA	Paraformaldehyde
PFU/ml	Plaque forming units per millilitre
pHRodo	pH rhodamine red dextran
px	Pixels
Qd	Quinidine
RABV	Rabies virus
Rbv	Ribavirin
RE	Recycling endosome
RNA	Ribonucleic acid
RNAPII	RNA-polymerase II

RVFV	Rift Valley fever virus
S	Small (segment)
SBV	Schmallenberg virus
Scr	Scrambled
SD	Standard deviation
SDM	Site-directed mutagenesis
SDS-PAGE	Sodium dodecyl sulphate-polyacrylamide gel electrophoresis
SFTSV	Severe fever with thrombocytopenia syndrome virus
ssRNA	Single-stranded RNA
STA	Sub-tomogram averaging
Ta	Annealing temperature
TASK	TWIK-related acid sensitive
TEA	Tetraethylammonium
TEMED	Tetramethylethylenediamine
Tf	Transferrin
TMD	Transmembrane domain
TPC	Two-pore channel
TREK	TWIK-related
TULV	Tula virus
TWIK	Tandem-pore domain in weak inwardly rectifying K^+ channel
UBE3A	E3 ubiquitin ligase
Unt	Untreated
UTRs	Untranslated regions
UUKV	Uukuniemi virus
VACV	Vaccinia virus
vRdRp	Viral RNA-dependent RNA-polymerase
vRNA	Viral ribonucleic acid
vRNP	Viral ribo-nucleoprotein

VSV	Vesicular stomatitis virus
WHO	World Health Organisation
WT	Wild-type

α	Alpha
β	Beta
δ	Delta
ɣ	Gamma

Chapter 1 | Introduction

1.1 The *Bunyavirales* order

1.1.1 Classification

The *Bunyavirales* are a recently re-classified order of single-stranded RNA (ssRNA) viruses, with over 500 named isolates (~300 species), and one of the largest taxonomic groups of viruses. In recent years, there have been multiple changes in the bunyavirus taxonomy, the first of which in 2017 established the *Bunyavirales* as a new order to allow the incorporation of related or newly discovered bunya-like viruses, previously classified into different orders or unassigned (1). Currently the order is separated into twelve families on the basis of nucleotide sequence homology and serological characteristics; these are termed: *Arenaviridae, Cruliviridae, Fimoviridae, Hantaviridae, Leishbuviridae, Mypoviridae, Nairoviridae, Peribunyaviridae, Phasmaviridae, Phenuiviridae, Tospoviridae* and *Wupedeviridae* (2,3). Large-scale meta-transcriptomic sequencing projects led to a dramatic increase in the number of bunya-like viruses which have prompted further re-classifications, and with projects ongoing it is likely that further changes will be made (4–6).

Bunyaviruses exhibit negative sense polarity, however some species employ an ambisense coding strategy. All bunyaviruses have a segmented genome typically with two to three segments, but can have up to eight segments. The original five bunyavirus genus' contained three viral RNA (vRNA) segments and are present in the same distinct groups however were re-classified as families within the order: *Hantaviridae, Nairoviridae, Peribunyaviridae* (previously *Orthobunyavirus* genus)*, Phenuiviridae* (previously *Phlebovirus* genus) *and Tospoviridae* (7). The *Arenaviridae* contain only two RNA segments with ambisense polarity (8) and two new genus within the *Phenuiviridae* and *Fimoviridae* families contain members with up to six and eight segments, respectively (9,10). All bunyaviruses protect their vRNA by encapsidation within multiple copies of the nucleoprotein (N protein), forming viral ribo-nucleoprotein (vRNP) segments which make up the genome (7).

The first isolated bunyavirus was found in the Semliki forest in Uganda in 1943, obtained from *Aedes* mosquitoes, and termed Bunyamwera virus (BUNV) which gives the order its name. BUNV remains the prototypic bunyavirus and is the most widely used in studies of bunyavirus infection (11). BUNV is a biosafety level 2 (BSL2) virus that causes mild febrile illness and Bunyamwera fever, with symptoms including rash, headache and central nervous system (CNS) effects. BUNV is not associated with severe disease and as such is a useful research model (12). BUNV is the model species of the order and belongs to the *Peribunyaviridae* family, however other BSL2 models have been utilised from other families permitting cross-analysis; including hazara virus (HAZV), *Nairoviridae* family, and Uukuniemi virus (UUKV), *Phenuiviridae* family (13,14).

1.1.2 Zoonosis, emergence and disease

Bunyaviruses have a considerably wide host range with different members capable of infecting mammals, birds, reptiles, invertebrates or plants (3,7). Vertebrate hosts are infected by members of the *Arenaviridae, Hantaviridae, Nairoviridae, Peribunyaviridae* and *Phenuiviridae* families and transmission occurs via arthropods or rodents (Table 1.1). Viruses belonging to the *Hantaviridae* and *Arenaviridae* families are transmitted by rodent vectors (8,15). Natural maintenance of these viruses occurs due to transmission between small animal species upon host contact with aerosolised excreta or through bites, which although rare, can cause lethal infections in humans (15). A large majority of bunyavirus are transmitted by arthropods including mosquitoes, ticks and thrips, and are hence termed arboviruses. This includes the *Peribunyaviridae, Nairoviridae* and *Phenuiviridae* families, multiple members of which are major human or animal pathogens and result in severe disease or death.

Arboviruses are continually cycled between arthropod vectors and their hosts, allowing their persistence in nature. Arthropods become infected after blood-feeding on an infected host. Within the vector, the viruses replicate to relatively low titres allowing persistent infections that are not detected or cleared by anti-viral responses. The viruses migrate to the salivary glands and are transmitted upon blood-feeding to a naïve host, where the viruses replicate in the host to considerably higher titres and are often asymptomatic (16). With high viremia in the blood, the viruses are transmitted through biting from a new uninfected arthropod, allowing viral maintenance in nature and establishment of a zoonotic cycle. In many cases the virus is cleared by host immune responses, however infection is often transmitted horizontally to uninfected species and outbreaks occur when the virus is continually passed to further uninfected hosts. Human-to-human horizontal transmission is rare, with humans classed as dead-end hosts, the infection of which is propagated through vector contact. Some cases of human-human transmission have however been described (17,18).

New bunyaviruses can emerge and cause outbreaks for multiple reasons, most commonly through error-prone replication by the viral RNA-dependent RNA-polymerase (vRdRp), segment reassortment and change in vector distribution.

During negative sense RNA virus replication, the virally-encoded vRdRp is responsible for generating the complementary positive sense strand and new negative sense copies during viral genome replication. The vRdRp however has poor proof-reading capability and is therefore error prone, leading to common mutations during replication (19). This is termed antigenic drift and can result in pro-viral mutations that enhance virus infectivity. All bunyaviruses possess segmented genomes the majority of which are tri-segmented into the Small (S), Medium (M) and Large (L) segments, where replication occurs within infected cells and a copy of each is incorporated into new virions. During co-infection by two closely related bunyaviruses, nascent virions can exchange S, M and L segments from different input viruses, termed reassortment (Figure 1.1). This combination leads to the production of new bunyavirus species which possess properties from either parent with devastating consequences in host species (20). Ngari virus (NRIV), for example, is a Peribunyavirus that has arisen through segment reassortment of BUNV and batai virus (BATV), obtaining the BUNV L and S segments and the BATV M segment. Both parent viruses cause mild febrile illness in host species, however NRIV causes severe haemorrhagic fevers and occasional death in human hosts; demonstrating the threat posed by segment reassortment (21). Indeed nearly 300 viruses are reassortants of different bunyaviruses and it is postulated that most have arisen through reassortment of existing or now extinct bunyaviruses (20).

As many bunyaviruses are arthropod-borne, infections are also becoming more widespread through geographic spread of the vectors. *Aedes* mosquitoes, such as *Aedes aegypti* known to harbour several bunyaviruses, are currently limited to locations close to the equator as they require a warm climate (22). With the ever increasing movement of humans around the globe, this increases the possibility of vector movement across physical barriers such as seas, to establish infections in other global regions. In addition, the increase in global warming is establishing warmer climates in regions further from the equator, where arthropods can thrive (22,23). Both factors have increased the geographic spread of viral vectors which can contact a wider array of naïve hosts, increasing outbreaks. This is thought to be partly responsible for the increasing number of human and animal infections by Rift Valley fever virus (RVFV), which is transmitted by an array of tick species (24).

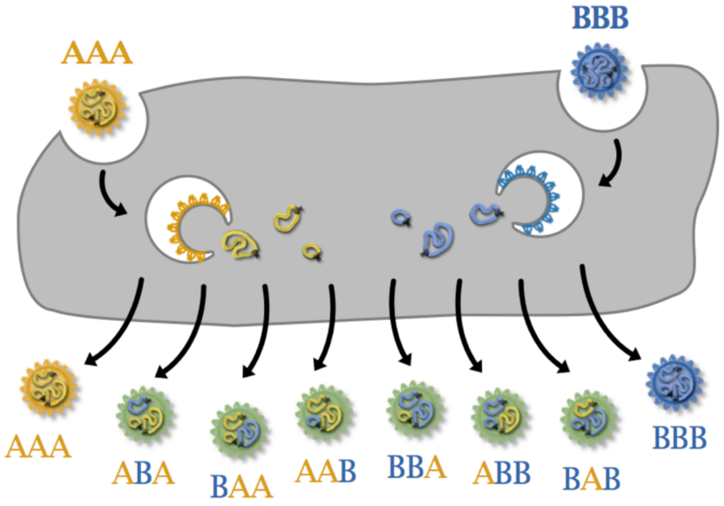

Figure 1.1 Bunyaviruses undergo reassortment, generating new virus species When two bunyaviruses infect the same cell (yellow A and blue B), virions can incorporate genomic strands from each virus, owing to the segmented nature of the viral genome. This can generate new bunyavirus species with altered tropism or physiological characteristics (adapted from *Briese et al* (2013) (20)).

Infection by a range of bunyaviruses across multiple families can lead to devastating consequences to human, animal or plant hosts. Over 20 bunyaviruses are capable of causing disease in humans, some of which are major human pathogens, previously leading to fatal pandemics (25). Of the *Nairoviridae* family, Crimean-Congo haemorrhagic fever virus (CCHFV) is an important human pathogen predominantly spread by ticks with human infections leading to severe haemorrhagic fevers and death, hence it is classified as BSL4. The first large outbreak of CCHFV occurred in the Crimean peninsula in the 1940s, where 200 cases of severe haemorrhagic fever were reported. The virus has since become endemic in over 30 countries with fatality rates as high as 30 % (26,27). Outbreaks are also continually emerging in new areas owing to the expansion of its host-range (Hyalomma ticks), leading the World Health Organisation (WHO) to classify it as a priority pathogen (28,29). Viruses from multiple other families also cause haemorrhagic fever and death in humans, key examples include RVFV (*Phenuiviridae* family), NRIV (*Peribunyaviridae* family), Lassa virus (*Arenaviridae* family) and Hantaan virus (*Hantaviridae* family) (8,21,30). Other bunyaviruses cause severe fevers and/or encephalitis which can lead to death. Severe fever with thrombocytopenia syndrome virus (SFTSV) (*Phenuiviridae* family) for example is endemic in east Asia and is highly pathogenic (31) (Table 1.1).

It is not only humans that suffer from bunyavirus infections, with significant economic losses incurred by animal infections. RVFV for example is endemic in parts of Africa, where infection is associated with high mortality in cattle (90 % in new-borns), particularly sheep, with the largest outbreak in 1977 resulting in >18,000 animal and 200,000 human cases (25,32). The number of outbreaks has risen dramatically since its isolation in the 1930s owing to an increased geographical range of its tick vector (24). With continuing viral spread, the worse-case-scenario would be expected to cost the US economy over 50 billion dollars if it becomes endemic (US Department of Agriculture) (33). Similarly to CCHFV, it is now classified as one of eight priority infectious diseases by the WHO (29). Nairobi sheep disease virus (*Nairoviridae* family) also causes fatal disease in cattle and is endemic within parts of Africa and India (34). It is likely that these viruses are currently limited to warmer climates due to vector intolerance to colder temperatures. Schmallenberg virus (SBV) (*Peribunyaviridae* family) for example was identified in 2011 and is transmitted to cattle by culicoides midges causing loss of appetite, hypothermia, and teratogenic effects in new-borns. In 2011-2013 an outbreak caused over 6,000 cases and originated in The Netherlands but rapidly spread across Europe, including France, Germany, Belgium, Estonia, Poland, Finland, Italy and the UK (35,36). The causes of SBV emergence in Europe are unknown, however it is predicted to be a reassortant virus of other Simbu serogroup Peribunyaviruses which are found in the Far East, Africa, Australia and southern Mediterranean regions (35,37). It is thought that SBV emerged from these viruses many years ago with limited or unreported clinical manifestations, remaining in these warmer climates until 2011 when it emerged in northern Europe. The reasons for this are unknown but could be due to a switch in the vector or an enhanced ability of the vector to survive winter months, allowing infections to persist across winter seasons (35,38). This highlights the need for effective treatments.

Economic losses are also significant from plant-infecting bunyaviruses. Tomato spotted wilt virus (*Tospoviridae*) is a significant pathogen, causing crop failure in a surprising large (>900 species) range of hosts; including tomato, peanut, celery, potato and tobacco plants. It has been widespread across western Europe and the USA since the 1940s, when efforts to control viral spread through vector control were hampered by a switch in viral vector and it is now found globally (39,40). Importantly this costs the US economy over a billion dollars per year in crop losses and, similarly to the devastating disease caused by some animal bunyaviruses, highlights the requirement for effective anti-viral agents (41).

Table 1.1 Summary of human and animal-infecting bunyaviruses

Summary of the five *Bunyavirales* families that infect humans/animals, denoting the number of species as identified by the ICTV (2019) (3). Example species cause severe disease or are model family members (*) which cause mild/no infection in humans. † a modified Pichinde virus can cause death in guinea pigs and mimics haemorrhagic Arenaviruses. HFRS = haemorrhagic fever with renal syndrome, severe cases characterised by increased vascular permeability (haemorrhage), thrombocytopenia and renal failure.

Family	No. of species	Vector	Key family members	Abbreviation	Host	Associated disease
Arenaviridae	43	Rodents	Junín virus	JUNV	Human	Haemorrhagic fever, death
			Lassa virus	LASV	Human	Haemorrhagic fever, death
			Pichinde virus *	PICV	Guinea pigs	Fever (†*death*)
Hantaviridae	47	Rodents	Hantaan virus	HTNV	Human	Severe HFRS, death
			Puumala virus *	PUUV	Human	Mild HFRS disease
			Seoul virus	SEOV	Human	Moderate HFRS
Nairoviridae	17	Ticks & midges	Crimean-Congo haemorrhagic fever virus	CCHFV	Human	Haemorrhagic fever, death
			Nairobi sheep disease virus	NSDV	Cattle	Fever, diarrhoea, death
			Hazara virus *	HAZV	Human	Mild febrile illness
Peribunyaviridae	95	Mosquitoes, ticks & midges	Batai virus	BATV	Human, animal	Mild febrile illness
			Bunyamwera virus *	BUNV	Human, animal	Mild febrile illness
			La Crosse virus	LACV	Human	Fever, encephalitis
			Ngari virus	NRIV	Human, animal	Haemorrhagic fever, death
			Schmallenberg virus	SBV	Cattle	Hypothermia, teratogenic
Phenuiviridae	38	Mosquitoes & ticks	Rift Valley fever virus	RVFV	Human, cattle	Haemorrhagic fever, death
			Sever fever with thrombocytopenia syndrome virus	SFTSV	Human	Thrombocytopenia, haemorrhagic fever
			Uukuniemi virus *	UUKV	Seabirds	Mild febrile illness

1.1.3 Prevention and treatments

There are no FDA approved vaccines or therapies for any bunyaviral disease in humans and a limited number in animals, which is particularly surprising considering the time period for which these viruses have been a health problem. For animal viruses, vaccines are available for some of the more widespread viruses, the most successful of which is the live-attenuated MP-12 vaccine against RVFV which provided significant protection in cattle, however is only licensed for animal use (42). Research is ongoing to investigate the efficacy of MP-12 use in humans, where it appears to retain strong immunogenicity (43). Two candidate vaccines, generated by SBV inactivation, to protect against SBV infections in cattle have shown some efficacy (44). Similarly vaccines against other teratogenic viruses are being generated, such as a tri-valent vaccine for prevention of Aino, Akabane and Chuzan virus infections (*Peribunyaviridae* family) which have shown promising results in cattle (45).

For human bunyaviruses, vaccines and therapies tend to focus on CCHFV, as a BSL4 virus which can cause fatalities in humans. As a preventative measure, attempts have been made (and are continuing) to control the spread of the mosquito and tick vectors to limit arbovirus infections, however current methods are expensive and inefficient (46,47). Multiple efforts have been made towards a CCHFV vaccine and the development of anti-viral drugs since the 1960s, but progress has been slow and the results are limited. This was predominantly due to the lack of animal models until 2010, as rodents including rats and mice and many non-human primates (NHPs) classically used as models for CCHFV fail to recapitulate the clinical symptoms (13). In 2010, the first breakthrough in this area was made through the generation of an interferon (IFN) Type I receptor A knockout (IFNAR-/-) mouse model, infection of which with CCHFV was lethal and produced symptoms reminiscent of those in humans (48). This provided the first platform for initial animal testing in adult mice for the development of CCHFV vaccines. Other mouse models have since been generated targeting IFN Type I and II pathways, however the original IFNAR-/- model remains most efficacious as the knockout model is easily reproducible and shows consistent CCHFV infectivity (13). Success has also been shown using IFN Type I-targeting antibodies to block IFN signalling, which allowed CCHFV infection (49). This is particularly useful as it does not require selective cross-breeding to generate knockout mice, which can simply be inoculated with these antibodies prior to infection. Investigation into NHP models showed that baboons and African green monkeys are not susceptible to CCHFV, however it was importantly shown in 2018 that cynomolgus macaques harbour CCHFV and produce symptoms similar to those of humans (50). Infection was shown for two strains of CCHFV (Kosova Hotis and Afg09-2990) and other strains now require evaluation. This does however represent an important advancement. The production of immune-competent animal models is anticipated to bridge the gap between immune-compromised mouse models and humans.

The development of IFNAR-/- mouse models has allowed significant improvements in vaccine testing, however no vaccines are to date licensed for human use. The efficacy of vaccines derived from multiple vectors have been tested in mouse models, including a (non-viral) DNA vaccine, modified Vaccinia virus Ankara (MVA)-vectored, poxvirus-vectored, vesicular stomatitis virus (VSV)-vectored and Bovine Herpesvirus-vectored, all of which express the CCHFV N protein or GPs (13,51). In particular, a VSV-vector with CCHFV GPs showed protection upon CCHFV challenge in mice (52), as was observed for Bovine Herpesvirus vectors expressing the N protein (53). Neither have been tested for efficacy in NHPs or humans however, with the only human vaccine to date being an inactivated CCHFV whole virus vaccine derived from mouse brains and inactivated using chloroform and heat. At-risk individuals in Bulgaria have been vaccinated although efficacy is difficult to establish (54,55). Given the recent improvements in animal models, it is hoped that more effective CCHFV vaccines will be developed.

Prophylactic drug treatments for infected individuals are limited, with their development complicated by the segmented nature of the bunyavirus genome, which is prone to mutation and drug resistance. To-date, the only drug tested in animal models is Ribavirin (Rbv), which has been used for the prophylactic treatment of CCHFV for over 30 years (46). Rbv is a guanosine nucleoside analogue which interferes with viral replication through incorporation into newly forming vRNAs, increasing the frequency of mutagenesis and leading to error catastrophe (56). It is approved for use against multiple RNA and DNA viruses including human respiratory syncytial virus (hRSV), Influenza A (IAV) and B viruses, and a bunyavirus Lassa fever virus (*Arenaviridae* family) (57,58). The efficacy of Rbv against CCHFV has not been definitively determined, with evidence suggesting that it improves the survival of CCHFV infected IFNAR-/- mouse models with minimal effects in human studies (13,59,60). Similarly, Rbv is used as a prophylaxis against RVFV in humans with its efficacy controversial (61). An alternative, favipiravir, has been suggested as a treatment for multiple bunyavirus infections. Favipiravir is a nucleotide analogue similar to Rbv and acts by inhibiting the catalytic domain of vRdRps, with broad-spectrum activity against multiple RNA viruses (62). Although no efficacy has been shown in humans, activity has been shown against multiple bunyaviruses from different families *in vitro*, including RVFV (*Phenuiviridae* family), La Crosse virus (LACV) (*Peribunyaviridae* family), Maporal virus (*Hantaviridae* family) and Pichinde virus (*Arenaviridae* family) (63,64). Interestingly for Pichinde virus and RVFV, favipiravir was shown to improve the outcome of infection in hamster models, even when administered once the virus had become established (61,65). Although further experiments are required, favipiravir could prove to be an efficacious alternative to Rbv with greater activity against bunyavirus infections (64).

The other experimental post-exposure treatment currently used against CCHFV is the injection of high anti-CCHFV immunoglobulin-containing human serum from either vaccinated individuals or CCHFV survivors. Intramuscular injections have been used since 1967, but with varying degrees of success (46). When administered to patients in Bulgaria through intravenous injection, higher patient survival was observed, although these studies were limited by a lack of controls (66). Similarly to Rbv, the efficacy of this treatment in humans leads to variable outcomes, with both minimal effects or improvements in disease outcome reported (13,66).

Given the limited options available for those infected with bunyaviruses, there is a clear need for drug development and new treatment options. Recent developments in automated drug development have permitted the generation of multiple high-throughput compound libraries to target viral or host factors (61). One screen was developed which utilised antibodies that specifically target N protein oligomers. This identified multiple compounds that affected oligomerisation and vRNP formation of RVFV and Lassa fever virus, however these compounds have not been taken forward *in vitro* or *in vivo* (67). Other screens have targeted a variety of cellular components to prevent virus infection, using recombinant RVFV encoding a luciferase reporter. The strongest hit for one particular screen, Sorafenib, elicited a 93 % reduction in virus infection in cell culture, however only marginally improved survival rates *in vivo* (68). Using non-targeted screens of this nature, generating drugs suitable for approval in humans is challenging, as a considerable body of work is required to translate the findings to human trials (61).

Also under development for CCHFV treatment is the use of anti-CCHFV monoclonal antibodies, typically targeting the GPs, Gn and Gc, and the non-structural GP38 protein (61). Screening of neutralising and non-neutralising monoclonal antibodies has identified some that provide protection in neonatal mouse models, however in adult mice only mAb-13G8, a non-neutralising anti-GP38 antibody provided protection (69). Interestingly, antibodies are being tested against another bunyavirus, SFTSV which is endemic in Asia. An anti-Gn antibody was shown to protect against multiple strains of SFTSV in cell culture and conferred 80 % protection in mouse models when administered up to 5 days after infection (70).

It is clear that the development of mouse and NHP models has significantly advanced the development of treatments and vaccines against a number of bunyaviruses, predominantly CCHFV. There is however a clear need for the development of effective anti-virals and, with the continual mutation of bunyaviruses, the identification of host-cell factors that can be modulated to prevent virus infection represents an attractive alternative.

1.2 BUNV structure and genome

Model viruses are often used to study bunyavirus infections. As such, work in this thesis uses the prototypic virus BUNV. As a BSL2 virus, BUNV provides a relatively safe alternative compared to other more pathogenic bunyaviruses, including the BSL3E/4 pathogens RVFV and CCFHV.

BUNV virions are pleomorphic and approximately 108 nm in diameter, primarily consisting of a host-derived lipid membrane, external viral GPs and the genomic vRNPs (71) (Figure 1.2). The three vRNP segments encompass the S, M and L negative sense ssRNA, each contained within N protein monomers that oligomerise to encapsidate the entire strand. Each vRNP is associated with the vRdRp and the 3’ and 5’ terminal residues of each strand base pair to form ring-like ‘pan-handle’ structures (72). The three vRNP segments are tightly packed within a host-derived lipid enveloped, formed upon viral budding into the Golgi during nascent virion assembly (73). The two BUNV GPs Gn and Gc are type I integral membrane proteins which hetero-oligomerise to form trimers (3-fold symmetry), which protrude out in 18 nm spike-like projections from the virion surface (74). The Gn GPs additionally extend within the virion interior and interact with the vRNPs, which may be required for virion stability (75). Trimers interact with one another and form a locally ordered lattice-like arrangement covering the virion exterior (74). This local arrangement of GPs is also found in other bunyaviruses, including the Nairovirus HAZV and the Hantavirus Tula virus (TULV), which alternatively form GP tetramers (4-fold symmetry) (76,77). Members of the *Phenuiviridae* family however, form T=12 icosahedral symmetry of GP pentamers and hexamers, as shown for UUKV and RVFV (78,79).

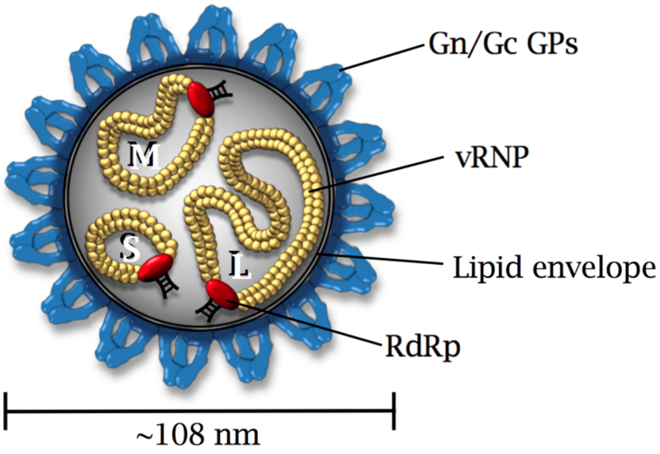

Figure 1.2 BUNV virions

BUNV virions are near-spherical and approximately 108 nm in diameter. The three vRNP segments (S, M and L) are encapsidated within a host-derived lipid envelope which is covered in trimeric spike of Gn/Gc GPs. Adapted from *Walter and Barr* (2011) (7).

1.2.1 Genome organisation

Three individual vRNA segments S, M and L designated according to the relative size, encode an open-reading frame (ORF) which is flanked by 3' and 5' untranslated regions (UTRs) (Figure 1.3). RNA segments within the family share high nucleotide homology and segments are of a similar size, but differ between families (36). Both genomic and anti-genomic vRNA strands are co-transcriptionally encapsidated within the N protein to form vRNPs to continuously protect the ssRNA strands (72).

The UTRs are relatively conserved between virus species within the family and are predicted to govern the activation and termination of transcription, the switch to genome replication, and vRNP packaging into virions (80–82). Complementary sequences in the final 11 nucleotides (nt) in the 3' and 5' UTRs are predicted to associate with one another and with vRdRp, to generate the 'pan-handle' structures that circularise the vRNA strands, as shown in electron microscopy of purified vRNPs from multiple bunyaviruses (7,83,84).

1.2.1.1 The L segment

The BUNV L segment of ~6.9 kilobases (kb) encodes the vRdRp, or L-protein (~259 kilodaltons (kDa)), which is required for the production of the complementary positive sense (antigenome) vRNA strands during genome replication and transcription (85). The L protein contains three characteristic structural subdomains, termed the fingers, palm and thumb (shared between vRdRps), which create a catalytic cavity essential for protein function (86). There are two highly conserved domains between bunyaviruses (Figure 1.3). The first is the polymerase domain that recognises promoter and transcription termination sequences in the BUNV UTRs and facilitates replication (87). The second is the endonuclease domain that is less well conserved between families, but contains highly similar motifs essential for 'cap-snatching' from host messenger RNAs (mRNAs) to cleave primers for viral transcription (85) (Figure 1.3). Although essential for viral replication, the vRdRp of all bunyaviruses is error prone and often mis-incorporates bases, causing point mutations in the viral genome which can produce viruses with altered characteristics (19).

1.2.1.2 The M segment

The BUNV M segment is ~4.5 kb and encodes a polyprotein of Gn-NSm-Gc from a single ORF (1,433 amino acids (aa)), which is co-translationally cleaved by host-cell signal-peptide peptidases to form the three distinct proteins (88) (Figure 1.3). Post-translational N-linked glycosylation occurs at two sites on Gc and one on Gn, which are required for correct protein folding and function (89). The structural Gn (~32 kDa) and Gc (~110 kDa) GPs cover the virion surface and facilitate host-cell attachment and entry. Gn/Gc bind to receptors on the cell surface to initiate BUNV internalisation into endosomes. The larger Gc is formed of two domains, an N-terminal variable domain and a C-terminal core domain (Figure 1.3); named due to sequence complementarity between Peribunyaviruses (90). Although not essential for some steps in bunyavirus infection, the N-terminal variable region facilitates the formation of nascent virions in the Golgi (91). The C-terminal core region contains a class II fusion domain, also termed the fusion loop, which must be activated at a specific stage of virus entry to facilitate virus-host membrane fusion in endosomes and genome release into the cytoplasm (92). Investigation of the specific roles of the considerably smaller

Gn indicate that it binds Gc and acts as a chaperone, promoting Gc folding and Golgi targeting and retention (89,92).

The non-structural M protein (NSm, ~18 kDa) is additionally encoded by the M segment of some but not all bunyaviruses, the function of which is not fully understood and differs between viruses. NSm contains two membrane-spanning regions (Figure 1.3) and similar to Gn/Gc resides on Golgi membranes (93). During BUNV infection, NSm localises to viral factories in the Golgi and is thought to promote virus replication, virion assembly and virus maturation (73,94).

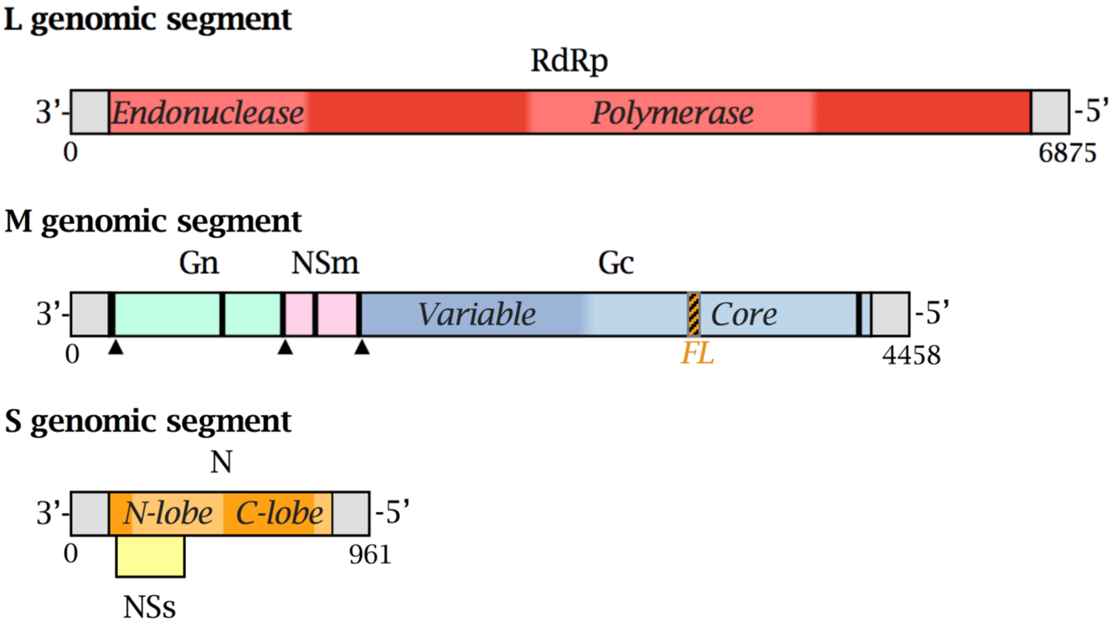

Figure 1.3 BUNV possesses a tri-segmented genome

BUNV genomes are comprised of three segments of negative sense polarity; L, M and S. Each segment ORF is flanked by UTRs (grey) which regulate genomic transcription, replication and segment packaging. The L segment (~6.9 kb) encodes the vRdRp (red) which contains an endonuclease and polymerase domain. The M segment (~4.5 kb) encodes a single polyprotein of Gn-NSm-Gc viral mRNA. The Gc protein (blue) contains a variable and core domains, and a fusion loop (FL, orange/black striped). Gn (turquoise), NSm (pink) and Gc all contain transmembrane regions (black bars) and are cleaved co-translation by host-cell proteases (▲). The S segment (~1 kb) encodes the N protein (orange), which consists of the N- and C-terminal 'lobes' making up the core region. The S segment also encodes the NSs protein (yellow) via an overlapping ORF, from an alternative start codon to N. Adapted from *Walter and Barr* (2011) (7).

1.2.1.3 The S segment

The structural N protein (~26 kDa) is encoded from the BUNV S segment (~1 kb) and encapsidates vRNA, protecting the vRNA strands from degradation and detection by host-cell immune responses (95). N monomers oligomerise and bind both the negative sense genomic and positive sense antigenomic strands (produced during genome replication) within a positively charged crevice (72). Rather than forming helical symmetry, like those adopted by other RNA viruses (for example members of the *Mononegavirales* order) (96), bunyavirus N proteins largely form 'beads-on-a-string'-like structures 10 nm in diameter. Small regions within these vRNPs possess helical symmetry and their combination with a less-ordered arrangement generates a highly flexible structure (97–99). N proteins of BUNV have been shown to oligomerise, where N- and C-terminal arms protrude from the N core and form head-to-tail interactions (72). Ring-shaped tetramers are thought to form (99) and at the N-N protein interface is the hydrophobic cleft that accommodates vRNA binding (72).

Similarly to NSm, the non-structural S protein (NSs, ~11 kDa) is not encoded by all bunyaviruses and although non-essential for viral replication, is a key virulence factor that alters host immune responses and apoptosis mechanisms (100–102). In the BUNV genome, NSs is translated by 'leaky' ribosome scanning from overlapping ORFs, where the NSs ORF is +1 shifted to that of N and translation begins from different AUG initiation codons (95) (Figure 1.3). NSs is predicted to inhibit host transcription from RNA-polymerase II (RNAPII) and is a key IFN-β antagonist inhibiting immune responses (101,103). Interference with RNAPII function leads to protein degradation and suppression of IFN regulatory factor-3 (IRF-3), and IFN-associated anti-viral responses (104).

1.3 Mammalian replication cycle

Key stages in the mammalian lifecycle are generally shared between the *Bunyavirales* order, including endocytosis following receptor binding, virus-host membrane fusion and the release of vRNPs into the cytoplasm, formation of viral factories at the Golgi as the sites of viral genome transcription and replication, nascent virion formation by membrane budding into the Golgi and release from the plasma membrane.

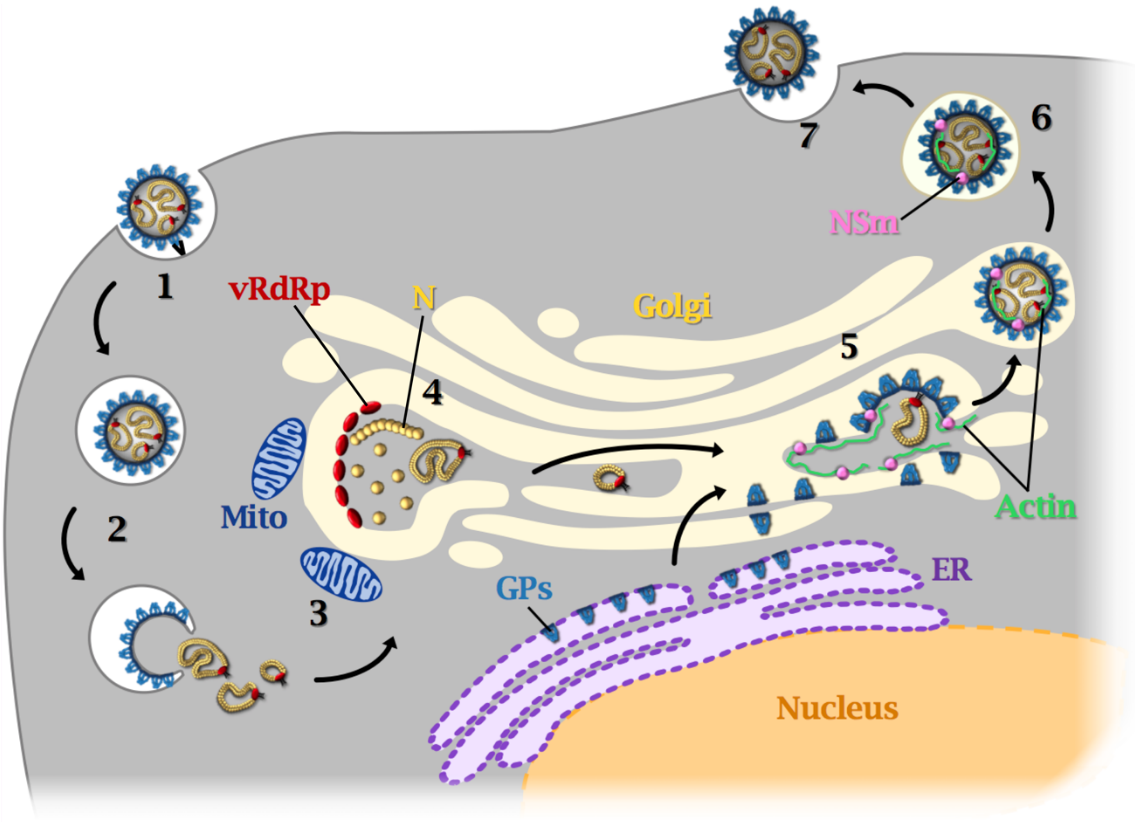

Figure 1.4 Schematic of the BUNV lifecycle in mammalian cells

(1) BUNV virions bind to host-cell receptors and are internalised into EEs. Virions are trafficked through endosomal compartments, **(2)** where an acidic environment and other unknown factors initiate fusion of the viral and endosomal membranes. vRNPs are released into the cytoplasm and traffic to **(3)** viral factories formed in the Golgi; in association with mitochondria (Mito) and the endoplasmic reticulum (ER). **(4)** Viral proteins are transcribed by vRNP-attached vRdRp and newly formed vRdRp and N accumulate on the Golgi. GPs are translated on the ER membrane and traffic to the Golgi. Replication follows translation, to form new vRNPs, **(5)** which migrate to packaging sites on the trans-Golgi. New virions form by budding into the Golgi, aided by actin (green filaments) and NSm (pink spheres) which are thought to be encapsidated. **(6)** Virions mature with passage through the trans-Golgi and exocytosis to the cell membrane. **(7)** Mature virions are released from the cell, lacking both actin and NSm within the mature virion. Adapted from *Ter Horst et al* (2019) and *Fontana et al* (2008) (73,105).

1.3.1 Attachment, entry and virion uncoating

Bunyaviruses bind a variety of receptors, but the identity of those required for virus entry are largely unknown, including those for BUNV (106). Studies into pathogenic Hantavirus attachment and entry identified $\beta 3$ integrins as required for endothelial cell entry (107). Similarly RVFV, UUKV and SFTSV (*Phenuiviridae* family) utilise DC-SIGN (Dendritic Cell-Specific ICAM-Grabbing Non-integrin) or L-SIGN lectins as dendritic or endothelial cell receptors, and DC-SIGN is predicted to be a CCHFV receptor (108–110). For most Peribunyaviruses, no receptor has been identified, although DC-SIGN has been implicated in LACV entry (106) and recently the attachment of SBV and Akabane virus to hamster epithelial cells was shown to require heparan sulphate proteoglycan (111). Heparan sulphate is a transmembrane protein present on cell membranes of many cell types and is involved in cell entry of multiple viruses; including Ebola virus (EBOV) and hRSV, and is also implicated in RVFV attachment (112–114). It therefore presents a likely BUNV receptor as BUNV similarly has a wide host-cell range. During Peribunyavirus infection, receptor binding is facilitated by the viral Gc GP for infection of both mammalian and insect cells (91,115,116). For other bunyaviruses however, such as RVFV, intact Gn and Gc are both required for infection, although the Gn requirement may be to permit correct Gc folding and structural rearrangements required for virus entry (117).

To gain access to the host cell, receptor binding initiates internalisation of receptor bound virions into early endosomes (EEs) (Figure 1.4 (1)). In many cases, such as LACV, this occurs by clathrin-mediated endocytosis, however other bunyaviruses utilise calveolin-mediated and clathrin-independent mechanisms of entry, dependent on the cell type (106,118). BUNV is trafficked through endosomal compartments that is accompanied by an increasingly acidic environment during endosomal maturation. The pathways through which virions are trafficked differ between bunyaviruses and virus-host membrane fusion occurs within different compartments (118,119). Peribunyaviruses traffic through EEs into late endosomes (LEs), however CCHFV traffics from EEs into multivesicular bodies (MVBs) where fusion is predicted to occur (119–121).

It is generally considered that the acidity of endosomes causes conformational changes in the Gn and/or Gc GPs which exposes a hydrophobic region in Gc that is inserted into host membranes to initiate membrane fusion events (122) (Figure 1.4 (2)). Indeed multiple bunyaviruses including BUNV depend upon endosomal acidification to trigger fusion, as the inhibition of endosomal acidification using ammonium chloride prevents virus entry (123–125). Gc contains a class II fusion domain, also termed a fusion loop, which is critical for BUNV entry (91) and is characteristic of GPs from some positive sense RNA viruses (126). Mutations in the C-terminus of BUNV Gn also abrogate virus fusion, indicating its role in viral fusion events (123). Viral GPs are first activated by cellular components, such as pH, ‘priming’ virions for fusion events. During this stage, virions are presumed capable of interacting with host endosomal membranes (the ‘extended intermediate’, Figure 1.5 (2)), facilitated by Gc (123). A series of undefined triggers and events then take place, in which the viral and host membranes are pulled into close proximity (the ‘pre-fusion hairpin’, Figure 1.5 (3)). Subsequent structural changes initiate membrane fusion, forming a pore through which the three vRNPs can be released into the cell cytoplasm (Figure 1.5 (4)) (106). Specific details of the stages and fusion triggers for BUNV, and most other bunyaviruses, are uncharacterised. It has however been shown that some bunyaviruses require the function of specific lipids such as LE-resident bis(monoacylglycerol)-phosphate (BMP, required by UUKV) and cholesterol (required by BUNV, HAZV and Andes hantavirus (ANDV)) (78,127,128).

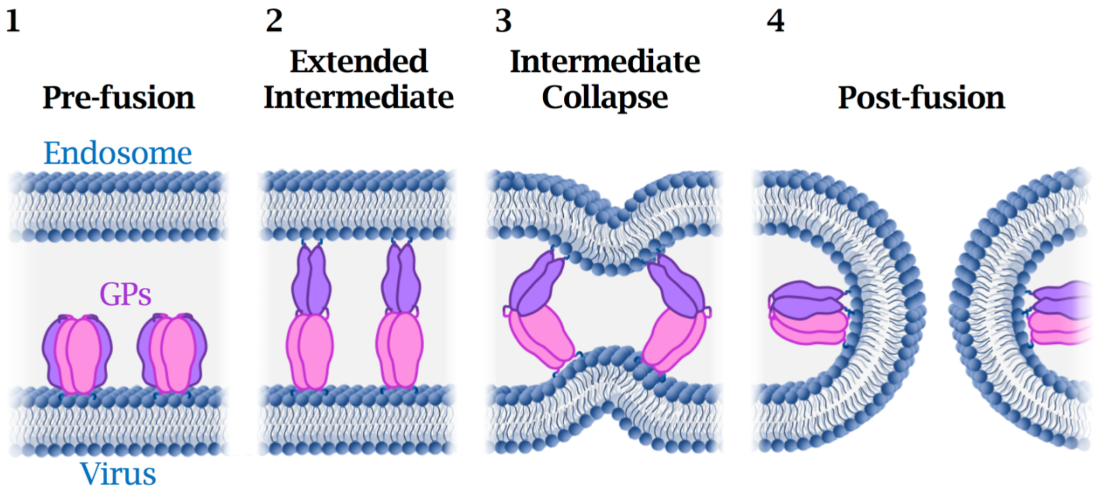

Figure 1.5 Predicted mechanism of virus-endosome membrane fusion

(1) Viral GPs are in an inactive state. **(2)** GPs are ‘primed’ for fusion by different endosomal stimuli, causing conformational changes which expose the fusion loop and allow interaction with the host endosomal membrane. **(3)** Further structural changes in the GPs pull the viral and endosomal membranes into close contact (termed the ‘pre-fusion hairpin’ arrangement). **(4)** GPs subdomains come together to form the ‘hairpin’ fusion state and virus-endosome membrane fusion creates a pore through which vRNPs are released (adapted from *Halldorsson et al* (2018) (129)).

1.3.2 Viral factory formation

After release of the vRNPs from endosomes, the segments are trafficked to the Golgi where viral protein production and replication take place (73). Many viruses alter components of the host cell to form a stable environment for viral genome replication and the transcription of new viral proteins (130). Bunyaviruses create distinct ‘viral factories’ formed by rearrangements of the Golgi structure, which are the sites of viral replication (73,94). Golgi cisternae become condensed, forming cylindrical and globular domains which are open to the cell cytoplasm (73) (Figure 1.4 (3)). Viral factories form in association with other cellular organelles, including close association with mitochondria and the ER, and the Golgi globular domains are enriched with vRdRp (94). It is likely that these interactions permit the concentration of cellular components, such as ribosomes, and produce the energy required for replication processes (73). It is unclear how bunyaviruses elicit these cellular changes, however for BUNV, considerable actin rearrangements are predicted to be involved in the formation of viral factories (94).

1.3.3 Protein production and replication

Upon the formation of viral replication factories, the RNP-associated vRdRp begins transcription of the viral mRNAs (+ sense) from each negative sense (-) strand, directed by signals in each of segment UTRs (80,131) (Figure 1.4 (4)). The vRdRp is also responsible for 'cap-snatching' of ~12-18 nt 5' strands from cytoplasmic host mRNAs (including their 5' caps) to generate viral transcription primers (132). During Hantavirus infection, the N protein aids transcription initiation by facilitating the dissociation of the pan-handle at the UTRs, freeing the 3' end and allowing the vRdRp to begin transcription (133). A similar mechanism occurs during BUNV infection, as mutations in different regions of the N protein abrogate viral transcription or replication, indicating roles for these regions (134). Transcription is terminated by a pentanucleotide termination signal at the 3' end of L and S segments, however no sequences were identified in the M segment and termination is predicted to occur via 'run-off' of the vRdRp (82). Nascent viral proteins are co-transcriptionally translated using the host-cell translational machinery including ER-bound and free ribosomes, simultaneously preventing dsRNA formation (7,135). The vRdRp and N proteins accumulate within the Golgi viral factory globular domains, the sites of new vRNP formation (73). The M segment proteins however are translated on the ER membrane and the transmembrane proteins produced are co-translationally cleaved to form the two GPs and NSm (Figure 1.6). Gn and Gc contain predicted transmembrane domains, which form membrane-bound GPs extending predominantly within the ER lumen to allow presentation on the exterior of nascent virions (Figure 1.6 B). The Gc GP also undergoes N-linked glycosylation and dimerises with Gn to allow targeting to the trans-Golgi for virion assembly (89,92). The NSm protein contains two predicted transmembrane domains, however localisation within membranes has not been proven, and the topology of the protein on the ER membrane is also predicted (Figure 1.6 B) (90).

Viral protein translation and genome replication do not occur simultaneously and an unknown switch causes protein translation to end and replication to begin, likely due to the production of sufficient nascent N protein to bind newly synthesised viral antigenomes (+) and genomes (-) (136,137). The production of new negative sense ssRNA firstly requires the vRdRp to produce a complementary template antigenome strand (+ sense), identical in size to the original strand. From this antigenomic template, multiple copies of the nascent negative ssRNA can be generated (82). As both template and new genomic vRNA are single-stranded, the newly synthesised N protein binds the vRNA strands as they are produced, preventing the formation of double-stranded RNA (dsRNA) which can be detected by the host immune system (84).

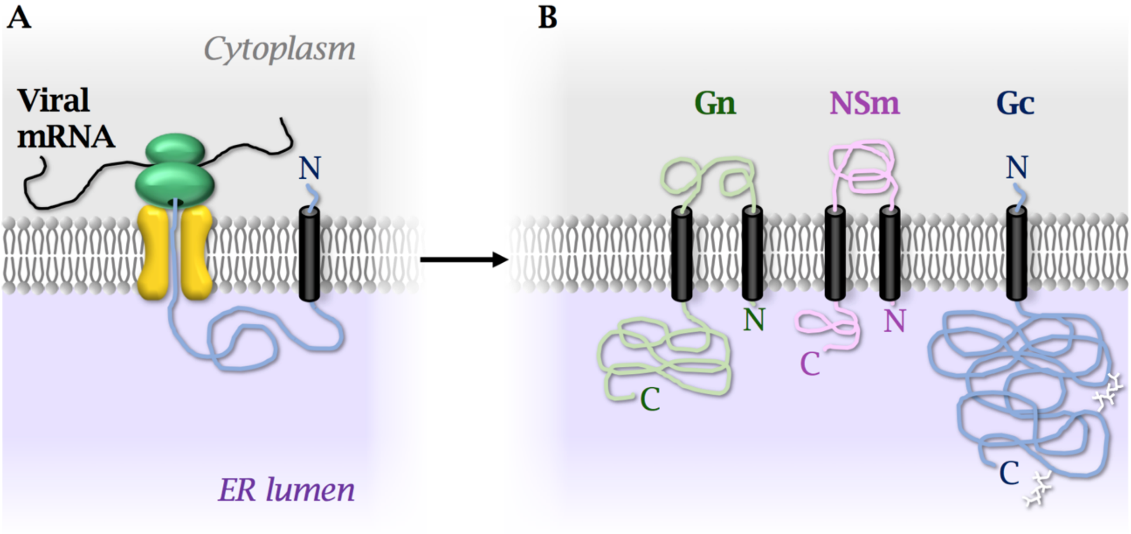

Figure 1.6 BUNV M Segment Translation and Protein Topology
(A) The BUNV M segment vRNA is transcribed in the cytoplasm into viral mRNA by the vRdRp. Cellular ribosomes (green) begin translation with the Gc protein. Unidentified signal sequences in Gc are predicted to direct translation onto the ER membrane, where nascent proteins are translated through the translocon (yellow pore) on the ER membrane. Gc, NSm and Gn can then be translated onto the ER membrane, and are co-translationally cleaved by ER-resident peptidases into the three proteins. **(B)** Gn (green) contains two predicted TMDs (black). The N- and C-terminal ends are located within the ER lumen and therefore on the exterior of viral particles, which form by budding into the Golgi lumen. Little is known about NSm (pink), however it is predicted to contain two TMDs and N- and C-terminal ends within the ER lumen. The Gc protein (blue) contains one TMD, with the majority of the protein translated into the ER lumen, to allow presentation on the exterior of the virion. Gc undergoes post-translational N-linked glycosylation (white) at two sites, which facilitates correct protein folding. Adapted from *Hellert et al* (2019) and *Shi et al* (2004) (90,92).

1.3.4 Virion assembly, maturation and release

Newly formed vRNPs traffic to sites of accumulated Gn and Gc GPs on the Golgi membrane (Figure 1.4 (5)). Gn contains a Golgi targeting and retention signal, and binding to Gc permits the viral GPs to be retained within assembly sites in the Golgi (92). The mechanism by which the vRNPs move to the assembly sites is unknown, although for Hantaviruses, interaction of the N protein with host proteins is thought to aid trafficking (138). At the assembly sites on the Golgi cisternae, interaction of the vRNPs with the GP cytoplasmic tails is directed by the UTRs on each segment (81). This interaction, alongside the involvement of host-cell actin filaments, initiates curvature of the Golgi membrane towards the lumen (71,73,81,123). Immature virions form upon budding into the Golgi, where the host-derived lipid envelope encapsidates the three vRNP segments and attached vRdRps (Figure 1.4 (5)). In addition, actin filaments and viral NSm protein can be identified within immature virions (see Figure 1.4 (5)) (73).

Immature virions are passed through trans-Golgi cisternae and undergo the first stage of maturation (Figure 1.4 (6)), identifiable by formation of a more dense virion interior with changes in viral GP structure, where the attached oligosaccharides become resistant to endoglycosidase-H digestion (139). These changes are essential for virion exocytosis and virions that only partially mature are retained in the trans-Golgi (94). Similarly, incomplete virions lacking an S, M or L vRNP are unable to escape the trans-Golgi (94). Vesicles exocytose the partially matured virions towards the plasma membrane for release (Figure 1.4 (7)). Further unidentified changes occur during the second stage of virion maturation either with passage to or release by vesicle fusion at the plasma membrane (94). Mature virions have clearly identifiable spike GPs on the virion surface and can infect new cells (73). The NSm and actin filaments encapsidated within the immature virions are not present in mature virions, indicating a role in virion maturation and/or release (see Figure 1.4 (7)) (73).

1.3.5 Perturbing the host-cell immune response

During viral infections, Type I IFN innate immune pathways are activated through the recognition of pathogen associated molecular patterns by cellular receptors such as RIG-I, which is strongly activated by binding to dsRNA (140,141). A signalling cascade leads to phosphorylation of IFN transcription factors, production (by RNAPII) and secretion of IFN-alpha (α) and/or beta (β) from infected cells ('anti-viral state' is established), which activates expression of IFN-stimulated genes (ISGs) that directly inhibit virus replication (140). The

ISG MxA inhibits bunyaviruses, and has been shown to bind to and redistribute N proteins from multiple bunyaviruses including BUNV, preventing their role during viral replication (142–144).

NSs is a key IFN antagonist, that effectively switches off IFN signalling during BUNV infection. However, NSs knockout BUNV (BUNV-ΔNSs) induces IFN expression and display significantly abrogated levels of virus infection (100,145). Similarly, in IFN knockout mice, the presence or absence of NSs does not affect virus infection (145,146). NSs interacts with the MED8 protein of the Mediator complex, which regulates the transcription of IFN by RNAPII. This interaction prevents the phosphorylation of RNAPII and elongation of host mRNA strands (104). Expression of IFN-*α*/β by RNAPII is therefore inhibited, which is thought to prevent the induction of the IFN response and associated inhibition of the virus (146).

1.3.6 Late stages of the BUNV lifecycle

Host-cell shut-off and eventual cell lysis occurs during the late stages of BUNV infection (147). This block in host protein synthesis is thought to be facilitated by the inhibition of RNAPII by NSs. Indeed, BUNV-ΔNSs viruses show impaired host-cell shut-off compared to WT BUNV (147). In cell culture, BUNV infection of BSC-1 cells (African green monkey kidney cells) leads to near-complete host protein synthesis shut-off as early as 7 hours (hrs) (148). The mechanisms of this process are not fully understood and the MED8-NSs interaction alone is insufficient to induce protein synthesis shut-off (147).

1.3.7 Arthropod replication cycle

Studies on the BUNV lifecycle in arthropod cells, including *Aedes* mosquitoes, are limited, but in general the stages are comparable to those of mammalian cells (149). The key difference is that the infection of insect cells does not cause cell lysis but generates a stable infection, likely to allow virus persistence in the vector (149). Concomitantly, infected arthropod cells do not display a reduction in host-protein synthesis, and no cellular functions are abrogated (150). The reasons for this are unknown, however it is thought that reduced activity of the vRdRp or reduced levels of viral proteins minimises cell damage (151,152). In addition, RNAPII in mosquito cells do not possess the same C-terminal region as mammalian cells, which contains the residues phosphorylated by the Mediator complex in mammalian cells. NSs may therefore fail to prevent vector protein synthesis (101).

1.4 Host-cell ion channels

Ion channels are pore-forming proteins which act as catalysts for the movement of charged ions across lipid membranes and are found in all organisms. Unlike ion transporters that require cellular energy, the transfer of ions across a membrane via ion channels is rapid (up to ~1-100 million ions/second) (153,154). Channels are made up of a number of subunits comprising transmembrane and pore domains. The subunits multimerise to form a central pore which permits ion passage through the membrane (Figure 1.7). The selectivity filter controls selective ion passage and channels are classed according to the ions they pass (155). Potassium (K^+) channels for example are 10,000-fold more selective for K^+ ions than sodium (Na^+) ions due to the TXGXG signature sequencing within the selectivity filter (153). In contrast chloride (Cl^-) channels are less specific and permit the passage of a range of anions (156). Key ion channel 'superfamilies' include Na^+, K^+, calcium (Ca^{2+}) and Cl^- channels.

Pore opening and ion channel activation (gating) is controlled by many cellular factors (Figure 1.7 B), in particular voltage that represents a key gating mechanism for Na^+, K^+, Ca^{2+} and Cl^- channels. Other gating mechanisms including membrane stretch, ion-sensing, and ligand-binding exist (153) (Figure 1.7 B). It was not until the discovery of the first ion channel structure that the gating mechanisms of ion channels began to be appreciated. *Doyle et al* (1998) determined the crystal structure of KcsA, a K_V channel in bacteria (*Streptomyces lividans*) similar in amino acid sequence to mammalian K_V channels, which revealed key mechanisms of K^+ channel selectivity (157). This led the way for following research into gating mechanisms, for example *Perozo et al* (1999) identified a counter clockwise rotation in the extracellular side of the KcsA transmembrane helices, which facilitates pore opening following activation (158).

Ion channels are known for their function within excitable cells where they regulate action potential firing and neuronal excitability (153). Their functions in non-excitable cells are however of equal importance where they regulate membrane potential, cell signalling, cell growth and apoptosis (159). Over 300 ion channel subunits are expressed per cell within the plasma membrane and in the membranes of subcellular organelles (160).

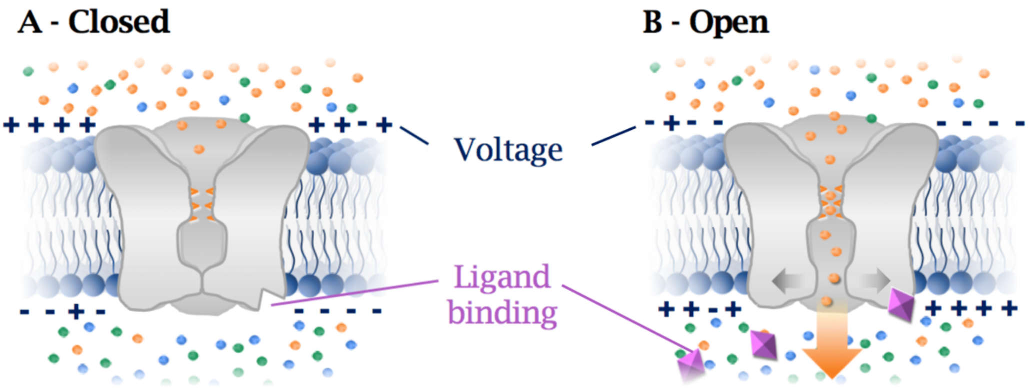

Figure 1.7 Ion channel gating
Ion channels are comprised of transmembrane subunits which oligomerise to form the channel pore, which contains a selectivity filter that only allows specific ion passage (orange triangles). **(A)** In an inactive state, the pore is closed and no ions (spheres) can pass. **(B)** Upon channel activation, for example by ligand binding (pink diamond) or a change in voltage across the membrane, the channel gate opens (grey arrows) and allows selective ion passage down its electrochemical gradient (orange arrow); from a high to low concentration. Adapted from *Catterall* (2000) and *Doyle et al* (1998) (157,161).

1.4.1 Potassium channels

There are over 70 different K^+ channel isoforms (154), that all contain the TXGXG selectivity sequence in the pore domain, regulating high specificity and rapid ion diffusion through the pore (155,157). *Doyle et al* (1998) revealed that the selectivity filter forms a narrow aperture and is lined with carbonyl oxygen atoms, which form a 'cage' around each dehydrated K^+ ion, similar to H_2O coordination around hydrated K^+. The spacing of the atoms allows the coordination of two K^+ ions in single file, although will not conduct Na^+ ions which are too small. Within this close proximity, the repulsion between the two K^+ ions leads to the rapid, selective conduction of ions through the pore (157).

K^+ channels consist of subunits containing two, four or six transmembrane domains (TMD), which form tetramers of subunits containing one pore domain or dimers of two pore domain subunits (154). K^+ channels primarily control the plasma membrane potential, the electrical potential across a membrane that acts as a driving force regulating the transport of charged ions and downstream cellular processes (162). There are four subfamilies of K^+ channels, classified on the basis of the number of TMDs, alongside their gating properties (Figure 1.8).

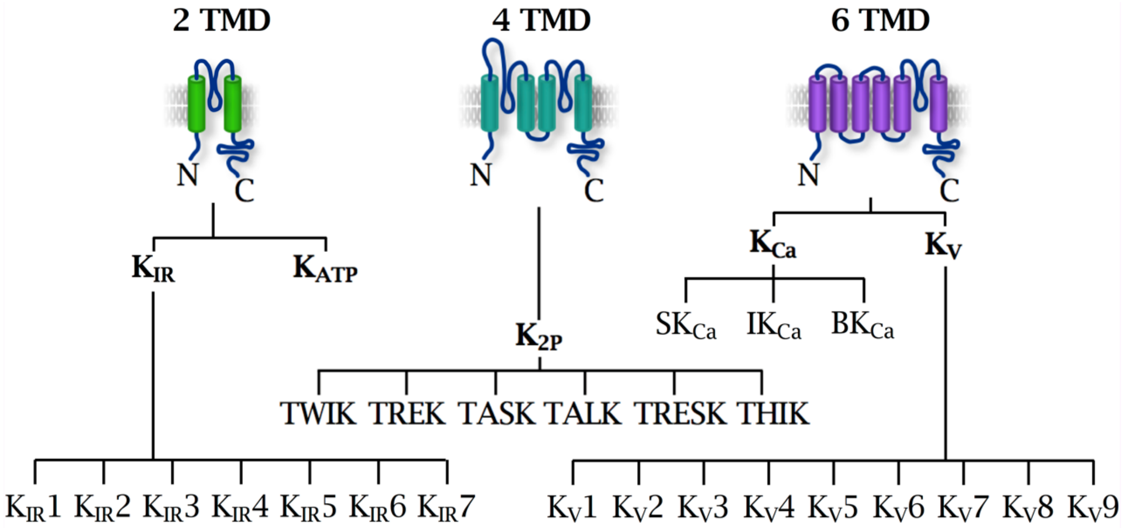

Figure 1.8 K^+ channel classification

K^+ channels are made up of subunits containing 2, 4 or 6 TMDs and are classified into different channel families; K_V, K_{Ca}, K_{IR}, K_{ATP} and K_{2P} (adapted from *Zhong et al* (2013) (163)).

1.4.1.1 K_V channels

Voltage-gated K^+ (K_V) channels contain 6 TMDs and are activated by membrane depolarisation, mediated by voltage sensors that initiate pore opening and K^+ efflux out of cells in order to re-polarise the membrane (154). In excitable cells, K_V channels work in conjunction to voltage-gated Na^+ channels (Na_V) channels, to regulate action potentials and K_V channels initiate post-firing repolarisation (153). In non-excitable cells however, these channels regulate cell volume, hormone secretion and apoptosis (154).

1.4.1.2 K_{Ca} channels

Ca^{2+}-activated K^+ (K_{Ca}) channels (6 TMD) are regulated by the intracellular Ca^{2+} concentration and regulate Ca^{2+} homeostasis by controlling the membrane potential, and the activity of voltage-gated Ca^{2+} channels (164). Additional roles have been proposed in cell volume regulation, proliferation and secretion (165). Three channels have been identified thus far and termed small-, intermediate- and large-conductance (BK_{Ca}), based upon their biophysical (rate of K^+-conduction) and pharmacological properties (166). Each subunit possesses a calmodulin-binding domain which is responsible for pore opening upon signalling by Ca^{2+}-bound calmodulin (167).

1.4.1.3 K_{IR} channels

Inwardly-rectifying K^+ (K_{IR}) channels differ to other K^+ channels as they typically pass K^+ ions into cells, opposite to the normal diffusion of K^+ down its electrochemical gradient which is generally in an outward direction (168). This is achieved by intracellular magnesium ions that block the channel pore to limit K^+ movement out of the cell (169). K_{IR} channels tend to be voltage-gated but can be regulated by a multitude of intracellular ligands, including G-proteins, ATP, protein kinases or other ions. K_{IR} channels are involved in action potential regulation, vasodilation and muscle contraction (168,170).

ATP-sensitive channels (K_{ATP}) are a subfamily of inward rectifiers inhibited by intracellular ATP, and are expressed on the plasma membrane and membranes of subcellular organelles. Channel gating is in response to the metabolic status of the cell and channel inhibition leads to cell depolarisation, linking cell metabolism to membrane potential. In pancreatic Beta cells, K_{ATP} channels are key regulators of insulin and glucose secretion. K_{ATP} channel closure and membrane depolarisation lead to a rapid increase in intracellular Ca^{2+} concentrations, which stimulates hormone secretion (171). On mitochondrial membranes for example, MitoK_{ATP} channels are responsible for maintaining mitochondrial volume in the intermembrane space, which is important for electron transport, and also required for signalling increased reactive oxygen species production (172).

1.4.1.4 K_{2P} channels

In contrast to the other K^+ channels, each 4 TMD subunit of two-pore K^+ (K_{2P}) channels (also termed tandem/twin-pore or leak K^+ channels) by definition contains two pore domains, and subunits therefore dimerise to form a functional channel. K^+ concentration ($[K^+]$) is high within the cell cytosol (~150 mM) and K^+ diffusion primarily occurs down its electrochemical gradient, out of cells (173). K^+ efflux through these constitutively active channels play a pivotal role in the regulation of the resting membrane potential. Furthermore K_{2P} channels have roles in cytoskeletal organisation, nociception, proliferation and hormone secretion, however the roles of specific channels are not well characterised (174). The 'Tandem-pore domain in Weak Inwardly rectifying K^+ channel 1' (TWIK-1) was first identified in 1996 and since a further 14 K_{2P} channels have been identified (175). The 15 K_{2P} channels are divided amongst TWIK, TREK (TWIK-RElated), TASK (TWIK-related Acid Sensitive), TALK (TWIK-related ALkaline-activated), TRESK (TWIK-RElated Spinal cord) and THIK

(TWIK-related Halothane-Inhibited) subfamilies, which differ in their sensitivity to activation by different signals, including pH, stretch, temperature and local anaesthetics (176).

Some K_{2P} channel subunits are able to heterodimerise with one another, such as TASK-1 with TASK-3, which produces channels with altered properties and sensitivity to pharmacological inhibitors (177). This makes it increasingly difficult to study the cellular roles of K_{2P} channels, especially as the number of specific pharmacological inhibitors are already limited. The limited research available has identified some cellular functions attributed to specific K_{2P} channel subfamilies, for example TREK channels were shown to be sensitive to heat and acidification, and are involved in regulating nociception, immune-cell trafficking into the CNS, cytoskeletal organisation during neuron development and hormone secretion (174,178). Research in the field is increasing however, which will improve the understanding of expression profiles and functions of specific K_{2P} channels.

1.4.2 Calcium channels

Most Ca^{2+} channels are voltage gated and are primarily formed from one of ten isoforms of α (and delta (δ)) subunits which make up the pore-forming domain and contain key residues that control voltage sensing. The channels are thought to co-assemble with ancillary β and/or gamma (γ) subunits to regulate channel gating (179). Ca^{2+} channels are divided into subfamilies based on their association with different ancillary subunits regulating currents and channel function (179). This includes the high-voltage activated long-lasting (L-type) and the low-voltage activated transient (T-type) channels, which are widely distributed across cell types. Other voltage gated channels are primarily found in the brain and CNS, such as purkinje (P/Q-type), neural (N-type) and residual (R-type) channels (180). Ligand-gated Ca^{2+} channels are activated upon binding of different ligands such as two-pore channels (TPCs), activated by NAADP binding, and ryanodine-receptor Ca^{2+} channels (181).

Ca^{2+} channels are activated in response to membrane depolarisation and initiate Ca^{2+} influx into cells, which regulates a multitude of cellular processes including cell cycle progression, apoptosis, neurotransmitter release and gene transcription due to the role of Ca^{2+} as a key second messenger in cell signalling pathways (182,183).

1.4.3 Sodium channels

The nine identified isoforms of Na^+ channels form a complex of α and β subunits, although distinguishing the functions of different Na^+ channel isoforms is challenging owing to similar activity and amino acid conservation (161,184). They are most commonly associated with control of action potential generation in excitable cells such as muscle and nerve cells. Multiple roles of Na^+ channels in non-excitable cells have been implicated, such as proliferation, endosomal acidification and migration, although these processes are not well-understood (185).

Many Na^+ channels are voltage-gated (Na_V) and are activated by a small membrane depolarisation, which open the channel pore and leads to a rapid influx of Na^+ ions. This influx causes further depolarisation sensed by the channel leading to rapid inactivation, within milliseconds, by pore blockage with the ‘inactivation gate’, permitting action potential propagation in excitable cells (184). Due to their roles in action potential propagation in excitable cells, Na^+ channels are key drug targets blocked by licensed local anaesthetics, antiepileptic and antiarrhythmic drugs (186).

1.4.4 Anionic chloride channels

Cl^- channels conduct negatively charged anions, predominantly Cl^- ions, which have cellular roles in cell excitability, trans-epithelial transport, cell motility, ion homeostasis, endosomal acidification and cell volume (156). Similarly to other ion channel families there are subfamilies of Cl^- channels, principally Cl^- intracellular channels (CLIC), Cl^-/H^+ exchangers, cystic fibrosis transmembrane conductance regulator (CFTR) and Cl^- channels which are gated by cAMP, Ca^{2+}, voltage, stretch or ligand binding (156,187). Research into anionic channels is limited compared to cationic channels, and therefore the specific functions and mechanisms are poorly defined. Cellular functions have often been linked to Cl^- channels owing to the identification of channel dysfunction causing symptoms in different diseases. The function of the CFTR channel for example, was identified owing to impaired trans-epithelial Cl^- transport in cystic fibrosis (CF) patients (156).

1.5 Ion channels and disease

Ion channels are vital for cellular function and their dysfunction correlates with a wide variety of diseases termed ‘channelopathies’ (188). The most studied of which is the dysfunction of the CFTR Cl^- channel in CF patient epithelial airway cells. Mutation of this channel, most commonly a deletion in phenylalanine at position 508, leads to aberrant protein folding which is then degraded (189). This prevents Cl^- secretion, affecting Na^+ and Cl^- flux across epithelial membranes and leads to thick mucus build up in the airway, increasing the likelihood of infections and severe pulmonary dysfunction (190). In Dent’s disease, low molecular weight proteins are abundant in the urine, indicating impaired degradation in kidney cells. Mutations in ClC5 were found to be responsible for altered endosome acidification, required for endo/lysosomal function and protein degradation down the endosomal system (191).

As ion channels are key regulators of electrical excitability in cells, it is unsurprising that channel dysfunction in neurons, cardiac and skeletal muscle is associated with a number of diseases. Gain-of-function mutations in a number of Na^+ channels and loss-of-function mutations in K^+ or Cl^- channels have been shown to cause hyperexcitability, particularly in skeletal muscle cells (192–194). In cardiac heart muscle, mutations which prolong the action potential often lead to cardiac arrhythmias, termed long-QT syndrome. This is primarily caused by mutations in the KCNH2 K^+ channel (HERG channels), which lead to a slow repolarisation following action potential propagation. The associated ventricular arrhythmias significantly increase the risk of syncopal attacks and sudden death (195). Similarly, mutations in SCN5A (Na_V) channel prevent inactivation and also prolong the action potential in cardiac muscle (192). Ion channel mutations in the CNS are also associated with some forms of epilepsy. Gain-of-function mutations in SCN1A and SCN1B (Na^+) channels for example, prevent channel inactivation and increases Na^+ influx into neurons which is thought to be a causal factor in generalised epilepsy with febrile seizures (196).

Interestingly, the dysfunction of ion channels is increasingly being identified in different forms of cancer. In prostate cancer, mutations in several different voltage-gated Na_V channels have been identified, which increase invasiveness and metastasis of cancer cells (185). Abnormal K^+ channel function has also been associated with cancers. In some cases this occurs through increased channel expression, such as an increase in KCNK5 (TASK2) stimulated by activation of oestrogen receptor-α in some breast cancers, which is associated with increased cancer cell proliferation. In most cases however the mechanisms of K^+ channel overexpression in tumours are not well understood (197,198).

Acquired channelopathies can also arise through acquired disorders, drug use or toxins. In a number of autoimmune diseases, autoantibodies are generated which alter channel function (188). In autoimmune autonomic ganglionopathy, autoantibodies bind a neuronal acetylcholine receptor Na^+ channel impairing fast synaptic transmission, leading to autonomic failure (199). Similarly, in Isaac syndrome (neuromyotonia), autoantibodies prevent an outward K^+ current (K_V) causing repetitive action potential firing, which leads to muscle hyperexcitability, cramps and CNS effects (such as insomnia and hallucinations) (200). In drug-induced acquired channelopathies, drug overuse can alter channel function. Use of a number of anti-arrhythmic drugs can lead to long QT syndrome, characterised by a prolonged repolarisation interval between action potential firing, leading to abnormal heart arrhythmias (201).

With such a wide array of cellular processes and ‘channelopathies’ arising from dysfunction, ion channels are the second largest target for existing drugs (202). They therefore also represent an interesting host target for the development of novel anti-viral drugs.

1.6 Viral manipulation of host-cell ion channels

Viruses alter the host-cell environment in order to survive and replicate. Many viruses have evolved to encode their own ion channels, known as viroporins, which disrupt cellular ion homeostasis to produce a favourable cellular environment (203,204). Viroporins are transmembrane proteins which mimic the functions of host-cell ion channels, facilitating the passage of ions across lipid membranes. In viral infections, viroporins have been shown to manipulate cellular pathways such as those that control apoptosis and trafficking, and viral mechanisms including virion assembly and release (203). The best studied of which is the IAV M2 viroporin present within the virion membrane which coordinates H^+ ions into the virus, essential for virus entry and fusion events (205,206). Other viruses with their own viroporins include hepatitis C virus (HCV) which encodes p7 (H^+) to aid virion assembly, and human immunodeficiency virus 1 (HIV-1) which encodes Vpu (K^+) that facilitates virus release (207–209).

Whilst this highlights the importance of ion homeostasis in viral infections, many viruses encode no known viroporin and have adapted other mechanisms to manipulate the host-cell environment, including for mechanisms of virion entry and persistence in host-cells (210).

1.6.1 Ion channel modulation by viral proteins

Viruses require the viability of host cells in order to survive and replicate, and many alter the function of cellular ion channels to achieve this. HCV not only encodes its own viroporin, but alters the function of cellular K^+ and Cl^- channels to allow sustained virus persistence in hepatocytes. Activation of a K_V channel (K_V2.1) in liver cells signals apoptosis by initiating K^+ efflux from cells (211), however in HCV infection K_V2.1 function is inhibited. The block was found to be mediated by NS5A, which supresses p38 MAPK signalling and associated apoptotic activation of K_V2.1, allowing virus persistence (212,213). HCV also increases intracellular Cl^- flux via ClC1, 5 and 7 channels, pharmacological inhibition of which perturbs HCV replication through an unknown mechanism (187). This further demonstrates the vital roles of ion flux and host-cell ion channels in the HCV lifecycle.

Another virus which establishes prolonged infection of host cells is HIV-1 in CD4+ T cells. Multiple ion channels are manipulated during HIV-1 infection, including the increased expression of K_V1.3 (K_{IR} channel, by HIV-1 Tat) and the inhibition of BK_{Ca} channels (by HIV-1 Nef), although the reasons for this are unknown (214,215). HIV-1 manipulation of the K^+ channel K_V11.1 by the binding of viral gp120 perturbs channel function, which is required for particle release. Similarly HIV-1 Vpu prevents TASK1 K_{2P} channel function, which causes membrane depolarisation and promotes virion release (209,216,217). In late stages of infection the HIV-1 Tat protein induces cellular apoptosis. This is facilitated by increasing MitoK_{ATP} currents, identified through pharmacological inhibition of MitoK_{ATP} channels using tolbutamide, which reduced Tat-mediated apoptosis (218).

In excitable cells, a number of viruses associated with abnormal neuronal firing alter ion channel function. Varicella-zoster virus for example, causes post-herpetic neuralgia and during infection alters the function of Na_V1.6 and Na_V1.7 increasing Na^+ currents associated with neuropathic pain (219). Similarly, rabies virus (RABV), reduces Na_V and K_{IR} channel currents and increases Ca^{2+} entry into cells. Ca^{2+} influx in the CNS in monkeys is associated with aggressiveness, which could account for some of the characteristic RABV symptoms; including aggressiveness and convulsions (220,221). The reasons for this in the context of promoting RABV infection are not understood.

Viruses associated with respiratory diseases also manipulate ion channel function. IAV is well-known for its effects on the respiratory system and during infection IAV-haemagglutinin (HA) inhibits phospholipase C, which prevents Na^+ entry into lung epithelial cells via amiloride-sensitive epithelial Na^+ (ENaC) channels (222,223). Similarly M2 downregulates expression of ENaC and CFTR channels, which alters Na^+ and Cl^- flux across epithelial membranes and dysregulates fluid clearance in the lungs (224,225). Similarly, ENaCs are also inhibited during infection by severe acute respiratory syndrome coronavirus, Sendai virus and hRSV, although the reasons for this dysregulation in promoting virus infection are unknown (222,226,227). *Lingemann et al* (2019) recently showed that attachment of the hRSV G protein stimulates activation of the ATP1A1 subunit of the Na^+/K^+-ATPase, which activates Src and EGF receptor (EGFR) activation. Inhibition of the Na^+/K^+-ATPase prevented efficient uptake of hRSV by macropinocytosis (228). In epithelial cells, the Na^+/K^+-ATPase maintains electrolyte balance and fluid clearance (229), the dysregulation of which could play a role in hRSV respiratory disease.

Other viruses have been shown to modulate ion channel function, although the viral mechanisms and reasons for this are unknown. Examples include monkeypox virus which downregulates a number of K^+, Na^+, Cl^- and Ca^{2+} channels, Epstein-Barr virus which promotes *Orai1* expression and increased Ca^{2+} influx into the ER, and human T -cell leukaemia virus which triggers K^+ influx into infected cells (230–232).

1.6.2 Virus requirement for cellular ion channels

The plethora of pharmacological ion channel modulators available has led to the identification of a number of viruses which require channel function during infection. The inhibition of Cl^- channels for example, using tamoxifen and 5-nitro-2-(3-phenylpropylamino)-benzoate significantly inhibits herpes simplex virus (HSV-1) infection. Cl^- channels are required for multiple stages of HSV-1 infection including virion binding, virus-host membrane fusion, nuclear translocation, protein expression and nascent virion production. For most viral functions the mechanisms of the Cl^- channel requirement are unknown, however in HSV-1 entry channel inhibition prevents viral protein binding to lipid rafts and alters Ca^{2+} homeostasis (233).

Cl^- channels are also required for chikungunya virus (CHIKV) replication in mammalian and insect (vector) cells (234). Using a panel of pharmacological inhibitors and siRNA silencing of specific CLIC (Cl^-), CLIC1 and CLIC4 were identified as essential for efficient CHIKV replication. Although the mechanisms of this requirement are unknown, the interaction of CLIC1 with the non-structural CHIKV protein nsP3 indicates CLIC channels may play a role in the formation of viral replication complexes (234).

1.6.2.1 Ion channel requirements during virus entry

Filoviruses, including EBOV and marburg virus, are thought to enter the cell through micropinocytosis and pass through the endocytic network where fusion of the viral and cellular membranes occurs to release the viral genomes into the cytosol (235). *Gehring et al* (2014) identified that inhibition of L-type Ca^{2+} channels prevented filovirus entry (235). The Ca^{2+} TPC1 and TPC2 channels, which regulate endosomal trafficking, were subsequently identified as the specific channels required for early stages in the EBOV entry processes (236). It is predicted that TPC activation by NAADP permits EBOV trafficking away from neimann-pick factor 1 (NPC1)-containing LEs, required for fusion events. TPC channel inhibition therefore prevented EBOV trafficking and host membrane fusion, which impeded capsid release into the cytosol (Figure 1.9). Inhibition of TPC function was similarly debilitating to marburg virus entry and may therefore be a common regulatory mechanism in filovirus entry (236).

Membrane potentials control an array of cellular processes, including actin depolymerisation, matrix remodelling in mitochondria-induced apoptosis, regulating intracellular Ca^{2+} signalling and Ras GTPase signalling networks (159,237–240). The role of membrane potential and pH have been investigated for human rhinovirus type 2 infection, which enters host cells by receptor mediated endocytosis and undergoes conformational changes and membrane fusion in LEs. It was identified that virus infection does not depend on the endocytic pH gradient, however disruption of the plasma membrane potential using the K^+ ionophore valinomycin caused membrane hyperpolarisation which enhanced infection; compared to depolarised membrane potentials (241). Similarly, altering extracellular K^+ was used to identify that Semliki forest virus is dependent upon membrane hyperpolarisation for fusion processes, however vesicular stomatitis virus required depolarised membranes for fusion (242,243).

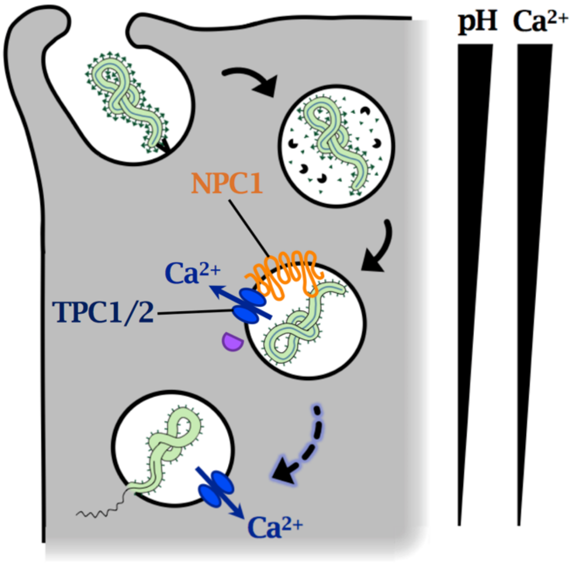

Figure 1.9 Predicted model of EBOV entry
EBOV is internalised into EEs by macropinocytosis and is trafficked into a LE, during which GPs are cleaved by cathepsins. In LEs EBOV associates with NPC1 and NAADP activates TPC1 and TPC2 channels on LE membranes, which mediates endosomal release of Ca^{2+} (concomitant with decreasing pH). TPC function is required for EBOV trafficking to an NPC1-negative compartment, where fusion is predicted to occur (adapted from *Hover et al* (2017) (210)).

Hover et al (2016) identified that host-cell K^+ channels are required for bunyavirus infection. Utilising the prototypic bunyavirus order member, BUNV, pharmacological inhibition of K^+ channels was shown to be detrimental to BUNV infection of mammalian and insect cells (244). This was determined using a panel of broad-spectrum inhibitors against different ion channel families, where inhibitors of K^+ channels were detrimental to infection, however those targeting Na^+, Cl^- or Ca^{2+} channels had no effect. This was thought to be bunyavirus specific as K^+ channel inhibitors also abrogated infection by the other *Bunyavirales* order members SBV and HAZV, however did not affect hRSV (paramyxovirus) infection; indicating a potential pan-bunyaviral requirement. The range of K^+ channel inhibitors used was then extended to utilise inhibitors of more specific K^+ channel subfamilies; including K_{Ca}, K_V, K_{IR}, K_{ATP} and K_{2P} channels. Inhibitors targeting the K_{2P} sub-family of channels were able to inhibit BUNV infection, however not those targeting other channel sub-families. There are 15 K_{2P} channels currently identified within mammalian cells, however the identity of those expressed in the A549 cell line used are unknown. In addition, the lack of inhibitors against specific channel species has limited further characterisation during BUNV infection.

Hover et al (2016) also began to investigate the BUNV lifecycle stage(s) requiring K^+ channel function. Predominantly utilising the broad-spectrum K^+ channel inhibitor tetraethylammonium (TEA), time-of addition assays were performed by application of TEA at increasing post-infection time points. TEA was shown to inhibit infection when applied during the first 6 hours post-infection (hpi) and thereafter ineffective, identifying a requirement during events early in the BUNV lifecycle (see Figure 1.10). Further time-of-addition assays showed that TEA did not prevent virus attachment and entry into cells, which occurred during the first 1 hr of infection. Subsequently, a BUNV mini-replicon system (245) was utilised to assess the effects of TEA on viral genomic replication, where no effects were observed; indicating a lifecycle stage shortly after virus entry but prior to viral RNA synthesis requires K^+ channel function. This early time frame is thought to include post-entry endosomal trafficking, viral-host membrane fusion for vRNP release and the formation of viral factories at the Golgi (244).

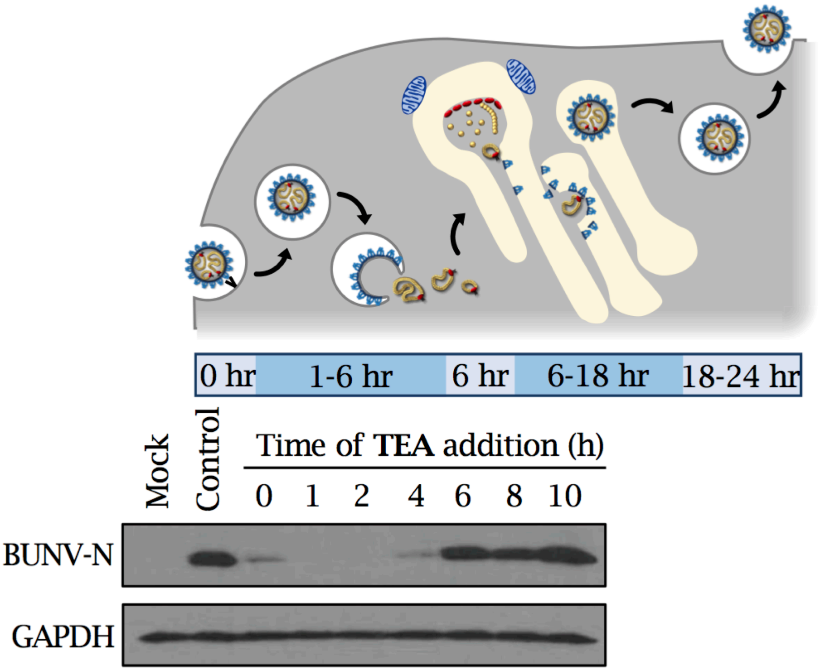

Figure 1.10 K^+ channels are required for early BUNV lifecycle stages

Schematic representing the various stages of the BUNV lifecycle at the corresponding time points. At 0-1 hpi, BUNV is internalised into EEs. From 1-6 hpi virions are trafficked through endosomal compartments, where fusion and vRNP release into the cytoplasm occurs. vRNPs are trafficked to the replication factories in the Golgi through an undefined mechanism. Translation of viral proteins and genome replication occur at 6-12 hpi, after which nascent virions begin to be released at 18 hpi. Western blot from *Hover et al* (2016) showing time of addition assays whereby TEA inhibits BUNV during the first <6 hpi (244).

The role of ion channels in virus infection is an emerging field, where many viruses require the function of different ion channels, the inhibition of which can prevent virus infection (210). For example, using high-throughput screens compounds were identified which inhibit IAV infection, such as an increase in Na^+ channel currents by SDZ-201106 which significantly inhibited IAV infection (223). Similarly, *Dubey et al* (2019) recently identified that pharmacological inhibition of $K_{IR}1.1$ prevents an unknown post-entry stage in HIV-1 infection (246). For many viruses, the mechanisms by which ion channels promote infection are not understood and by understanding these mechanisms novel anti-viral targets could be identified.

1.7 Thesis aims

Following from the identification that cellular K^+ channels are required during early stages in BUNV infection (244), Chapter 3 will investigate the mechanisms of this K^+ channel requirement during the early stages of BUNV infection; focusing on a potential role in virion endocytic transit. Dual-fluorescently labelled BUNV virions will be generated to track virion entry in live cells, which can then be used alongside fluorescent endocytic markers to define the post-internalisation route of virion trafficking; which for BUNV is currently unknown. The role of K^+ channel inhibition on BUNV endocytic trafficking and release can then be assessed. Using fluorescent endocytic markers, the endosomal K^+ ion concentration ($[K^+]$) will be assessed in different compartments, to confirm the predicted rise in $[K^+]$ within endo/lysosomes. Finally a role of K^+ ions will be assessed, using *in vitro* assays to mimic endosomal ionic conditions to determine the role of specific ions in virus entry, in particular H^+ and K^+.

Chapter 4 will utilise techniques in electron microscopy to investigate the structural changes in virions that may be induced by the reducing pH and rising $[K^+]$ within endocytic compartments. Using cryo-electron tomography and sub-tomogram averaging the structural changes in the viral GPs will also be examined, as viral GPs classically undergo structural changes to facilitate cellular attachment and virus-endosome fusion processes.

Chapter 5 will then seek to identify the specific K^+ channels required for BUNV infection. Previous work determined that inhibitors of the K_{2P} channels were detrimental to infection and therefore contain members mediating the BUNV K^+

channel dependence (244). In this chapter an array of BUNV-permissive cell lines and siRNA silencing of individual K_{2P} channels will be used to determine candidate K_{2P} channels which may be facilitating the BUNV K^+ channel requirement.

In summary, this work aims to further characterise the dependence of BUNV on cellular K^+ channel function, investigating the mechanistic basis for this requirement in the viral lifecycle and the identity of the K_{2P} channel species involved. The identification of a specific K_{2P} channel may provide an anti-viral target for new or existing pharmacological drugs. Importantly, the requirement for K^+ channel function was previously shown to be shared with other bunyaviruses, including SBV and HAZV, and therefore implicates a potential pan-bunyaviral virus-host interaction (244).

Chapter 2 | Materials and methods

2.1 Chemicals

All communal chemicals and solvents were obtained from Fisher Scientific, Sigma-Aldrich (Sigma) or New England Biolabs (NEB). Deionised water (dH_2O) was obtained using an ELGA PURELAB ultra machine (ELGA). Sterile solutions were filtered (0.22 µm) or autoclaved prior to use.

2.2 Mammalian cell culture and virus

2.2.1 Cell culture and maintenance

A549 (human alveolar carcinoma epithelial), SW13 (human adrenal carcinoma), MDA-MB-231 (human breast cancer epithelial) and BHK-21 (baby hamster kidney) cells were maintained in a humidified incubator at 37 °C, with 5 % CO_2. Cells were obtained from the European Collection of Cell Cultures (ECACC) and MDA-MB-231 cells were kindly provided by Dr Will Brackenbury (University of York). Cells were cultured in Dulbecco's modified eagle's medium (DMEM, Sigma) supplemented with 10 % foetal bovine serum (FBS), 100 U/ml penicillin and 100 µg/ml streptomycin (1 % pen/strep). HAP-1 (human haploid cells; Horizon) were maintained in Iscove's modified Dulbecco's medium (IMEM; Sigma) supplemented with 20 % FBS and 1 % pen/strep. All cell lines were split every 2-3 days with trypsin. A549 cells were used for all experiments, unless otherwise stated.

2.2.2 WT BUNV stock propagation

Wild-type (WT) BUNV supernatants (~$5.6\text{x}10^8$ plaque forming units per ml (PFU/ml)) [provided by Dr John Barr] were used to infect 3 x T175 cm^2 flasks of 60-70 % confluent A549 cells (seeded at ~$2.5\text{x}10^6$ cells/flask), at a multiplicity of infection of 0.2 (MOI = 0.2) in Optimem (Sigma) for 3 hours (hrs). Optimem was removed and replaced with low-serum DMEM containing 2 % FBS. WT BUNV supernatants were harvested after 36 hrs and clarified by centrifugation at 375 x *g* for 10 minutes (min). BUNV titres were estimated by plaque assay (see 2.2.3), yielding ~$2.1\text{x}10^6$ PFU/ml. Clarified supernatants were subsequently used to infect cells.

2.2.3 Virus titre determination by plaque assay

SW13 cells (~$3\text{x}10^5$ cells/well) were seeded into 6-well plates and BUNV infections were performed in duplicate once cells reached 80-90 % confluency.

BUNV supernatants were diluted 1:10 in serum free media (10 µl in 990 µl), generating a 10^{-1} dilution which was serially diluted from 10^{-2} to 10^{-6} (10^{-3} to 10^{-8} for purified BUNV, see 2.4.2). Dilutions were infected onto SW13 cells for 1 hr at 37 ˚C, after which media was removed and replaced with a methyl cellulose (MC, Sigma) overlay - 1.6 % (w/v) high viscosity MC diluted 1:1 in complete media. Cells were incubated for 6 days and fixed with 4 % paraformaldehyde (PFA) by addition directly into the MC/media overlay, for 1 hr at 4 ˚C. Cells were then washed with dH_2O and stained using 0.1 % crystal violet solution (Sigma) for 15 min. Cells were finally washed with dH_2O and the number of plaques counted to estimate viral titre using the following equation:

$$\frac{\text{number of plaques}}{(\text{dilution factor x volume})} = \text{virus titre (PFU/ml)}$$

2.3 SYTO82/DiD-BUNV production and purification

2.3.1 Propagation and nucleic acid labelling

A549 cells (~5x10^6 cells/flask) were seeded into 2 x T175 cm^2 flasks and incubated at 37 ˚C for 24 hrs to adhere. Cells were infected with BUNV (MOI = 0.5) in optimem for 3 hrs at 37 ˚C, with gentle rocking. Optimem was then removed and replaced with low-serum DMEM media (2 % FBS). At 18 hours post-infection (hpi), the nucleic acid dye SYTO82 (Thermo Fisher Molecular Probes) was added directly into the media at a final concentration of 2.5 µM. Infected cells were incubated for a further 6 hrs (24 hpi) and supernatants containing released SYTO82-BUNV virions were collected. Supernatants were spun at 375 x *g* for 10 min to pellet the cellular debris and virus-containing media collected.

2.3.2 Clarification and lipid labelling

Clarified supernatants from both flasks were combined in a 250 ml sterile glass bottle with a sterile stirrer bar. 50 % (w/v) poly (ethylene glycol) (PEG) 6,000 (in 1 x TNE buffer; 10 mM Tris-HCl, 0.1 M NaCl, 1 mM EDTA, pH 7.4) was added to the supernatant at a final concentration of 10 % (w/v) PEG. The virus-PEG solution was placed on a low stir at 4 ˚C overnight and then spun at 3,000 x *g* for 40 min at 4 ˚C to pellet virus-PEG. Media supernatant was removed and virus-PEG precipitate was re-suspended in 1 x TNE. Preps were concentrated on a double iodixanol (optiprep density gradient medium; Sigma) cushion column, containing a 10 % iodixanol fraction over a 60 % iodixanol fraction. The cushion was loaded into SW40 Ti rotor buckets (Beckman Coulter) and spun in an ultra-centrifuge at 160,000 x g for 90 min at 4 ˚C (maximum acceleration and deceleration). Virus was collected from the 10-60 % iodixanol interface.

Collected viruses were labelled with fluorescent DiD-vybrant cell-labelling solution (DiDvbt; Thermo Fisher Molecular Probes), which labels the viral lipid membranes by incubation in 5 µM DiDvbt for 2 hrs at 4 ˚C with gentle rocking.

2.3.3 Purification

SYTO82/DiD-BUNV was loaded onto an iodixanol gradient column, formed with fractions of 30 %, 25 %, 20 %, 15 % and 10 % iodixanol (made up in 1 x TNE). Virus was purified by ultra-centrifugation at 250,000 x *g* for 90 min at 4 ˚C (maximum acceleration and deceleration). Fractions (1 ml) were collected (stored at -80 ˚C), frozen in dry-ice prior to assessments (247). A549 cells were infected with each fraction (20 µl) for 18 hrs, to confirm the presence of infectious virus by western blot and immunofluorescent staining (IncuCyte). Virus titres were determined by plaque assay (see 2.2.3).

2.4 BUNV purification for electron microscopy

2.4.1 BUNV propagation optimisation

A549, SW13 and BHK-21 cells were seeded (~5x10^6 cells/flask) into 1 x T175 flask each and allowed 24 hrs to adhere. Cells were infected with BUNV (MOI = 0.5) for 3 hrs at 37 ºC and non-internalised viruses were removed and replaced with 15 ml fresh low-serum (2 % FBS) DMEM. At the indicated time points post-infection (24, 48 72, 96 and 120 hpi) a 1 ml aliquot of virus-containing supernatant was collected until cell death. Supernatants were clarified by centrifugation at 375 x *g* for 10 min, frozen in dry-ice and stored at -80 ºC. Viral titres were determined by plaque assay as in 2.2.3.

In subsequent experiments a BUNV MOI range was performed in BHK-21 cells, where cells were seeded and infected as above with MOIs of 1, 0.5, 0.1, 0.05, 0.01, 0.005, 0.001, 0.0005, 0.0001. Virus-containing supernatants were collected at 48 hpi, clarified and viral titres were determined.

2.4.2 BUNV purification

BHK-21 cells were seeded (~5x10^6 cells/flask) into 7 x T175 flasks. After 24 hrs, cells were infected for 3 hrs (as in 2.4.1) with an MOI of 0.1. Media was replaced with low-serum media (2 % FBS) DMEM and incubated until 48 hpi at 32 ºC, with gentle rocking at 24 hpi. Virus-containing supernatants were collected and clarified by centrifugation at 3700 x *g* for 20 mins at 4 ºC. Virus supernatants were passed through a 0.22 µm filter to remove impurities and re-spun at 3700 x *g* for 20 mins (4 ºC). Viral supernatants (38 ml) were added to an SW32 Ti tube and under-layered with 30 % sucrose (made in 1 x TNE buffer, see 2.3.2). Virus was purified by ultracentrifugation through sucrose at 150,000 x *g* for 3 hrs at 4 ºC (maximum acceleration and deceleration). Supernatants and sucrose were removed and the pelleted virus allowed to air dry for 5 mins in a sterile tissue culture hood. Virus was resuspended in 15 µl of 0.1 x phosphate buffered saline (PBS (Gibco); to dilute the salts in PBS by gentle rocking at 4 ºC overnight. Samples were collected and split into 6 µl aliquots and frozen on dry-ice (stored at -80 ºC). BUNV titres were determined by plaque assay (2.2.3), purity was determined by SDS-PAGE and silver staining (2.9.4), and negative stain electron microscopy (2.10.1).

2.5 Virus infection assays

A549 (used unless otherwise stated), BHK-21 or SW13 cells were seeded into 6 well plates (unless specified) (~3x10^5 cells/well) and allowed 24 hrs to adhere. Cells were infected with BUNV (MOI = 0.1) in complete media and infection was allowed to proceed for 18 hrs (unless otherwise stated) prior to cell lysis or fixing for western blot and immunofluorescence analysis, respectively.

2.5.1 SYTO82/DiD-BUNV infection assays

A549 cells were seeded onto 9 cm^2 glass-bottom dishes (~3x10^5 cells/well) or 1 cm^2 glass-bottom µ-slide (Ibidi) (~4x10^4 cells/well) onto polylysine-coated glass coverslips, 24 hours prior to treatment. SYTO82/DiD-BUNV was added to cells (MOI = 2) for the indicated time points at 37 ˚C. Prior to fixing (30 mins), epidermal growth factor (EGF)-488 (2 µg/ml; Biotinylated EGF complexed to Alexa-Fluor 488; ex. 490 nm, em. 525 nm; Thermo Fisher Molecular Probes) was added to cells for the final 15 mins to allow identification of cell peripheries; unless otherwise specified. Cells were fixed in 4 % PFA, washed with PBS (as in 2.9.5), mounted onto glass slides and imaged by confocal microscopy as in 2.9.7.

In experiments where K^+ channels are inhibited, the broad spectrum K^+ channel inhibitors tetraethylammonium (TEA, 10 mM, Sigma) or quinidine (Qd, 200 µM, Sigma) were added to cells (or absent in controls) for 30 mins prior to infection and drug was maintained throughout (247). The number of virions per cell were determined by manual counting of the virions and cells, which were averaged and normalised to untreated controls.

2.5.2 BUNV-N protein production timecourse

Cells were infected with BUNV (MOI = 0.1) for 1 hr to allow virus entry. Media and non-internalised virions were removed (1 hpi) and replaced with fresh media. At 3 hr intervals from 1 hpi to 24 hpi, cells were lysed and the presence of BUNV-N protein was determined by western blot analysis (see 2.9.2 and 2.9.3) (247).

2.5.3 BUNV virion release timecourse

A549 cells were infected with BUNV (MOI = 0.1) as described in 2.5.2 and media replaced 1 hr post-virus entry (1 hpi). Supernatants were collected at 3 hr intervals from 3 hpi to 24 hpi and stored at $^{-}80$ °C. Supernatants (undiluted) were used to directly infect new A549 cells and infection was allowed to proceed for 18 hrs before fixing in 4 % PFA, immunofluorescent staining and IncuCyte analysis (247).

2.5.4 Pre-infection drug treatments

BHK-21 or SW13 cells were treated with TEA (10 mM) or Qd (200 µM) for 45 mins. Cells were then infected with BUNV (MOI = 0.1) for 24 hrs, with drug maintained throughout (as previously described (244)).

2.5.5 Ammonium chloride addition timecourse

Cells were infected with BUNV (MOI = 0.1) for 1 hr, to allow virus entry, non-internalised virions were removed and replaced with fresh DMEM. Ammonium chloride (NH_4Cl, 10 mM) was added at increasing post-infection time points; 0 (pre-BUNV infection), 1, 2, 4, 6, 8 and 10 hpi; and then infection was allowed to proceed until 24 hpi at which point cells were lysed and infection assessed by western blot (247).

2.6 Virus priming assays

2.6.1 Virus pH/ion priming protocol

BUNV (2 µl; MOI = 0.1) was incubated at 37 ˚C for 2 hrs in the presence of a high-salt buffer (20 µl) at pH 7.3, 6.3 or 5.3 (see 2.6.1.1). Control experiments were performed through incubation in PBS or buffers at pH 7.3, 6.3 or 5.3, without high-salt addition. High-salt and low pH buffers were subsequently diluted in 1 ml DMEM and immediately added to cells. Infection was allowed to proceed for 18 hrs prior to cell lysis and western blot (2.9.1-2.9.3) (247).

2.6.1.1 Priming buffers

Buffers were prepared containing 20 mM tris for pH 7.3, 30 mM bis-tris for pH 6.3 and 50 mM sodium-citrate for pH 5.3. The desired high-salt concentrations were achieved by addition of 140 mM potassium chloride (KCl), 120 mM sodium chloride (NaCl) or 140 mM potassium sulphate (K_2SO_4); plus 12 mM NaCl (mimicking intracellular concentrations; or 5 mM KCl for the high-NaCl buffer). Buffers were heated to 37 ºC and fine adjusted to the desired pH using hydrochloric acid for tris and bis-tris buffers, and citric acid for sodium-citrate buffers. pH was re-checked after the 2 hrs priming to confirm buffer had not drifted beyond pH -/+0.2 of starting value.

2.6.2 [K^+] range priming

BUNV was primed as above (2.6.1) using a range of KCl concentrations in the prepared buffers from 0-140 mM (0, 5, 20, 50 and 140 mM). Buffers were diluted and cells were infected for 18 hrs as in 2.6.1 (247).

2.6.3 Priming reversibility assay

BUNV priming at pH 6.3 or pH 6.3 + K^+ was performed as in 2.6.1. Priming buffers were diluted and virions were incubated at 37 ºC for 0, 1, 2 or 4 hrs prior to cell infection for 18 hrs and lysis (247).

2.6.4 Virus priming and ion channel modulators

In experiments where cellular K^+ channels were inhibited. BUNV priming was performed as described (2.6.1) using pH 6.3 and pH 6.3 + K^+ buffers. During the final 30 mins, cells were treated with TEA (10 mM) for 30 min prior to addition of the primed BUNV. The drug remained present throughout infection.

Where BUNV was treated with TEA, virions were primed in pH 6.3 or pH 6.3 + K^+ buffers, with the addition of 10 mM TEA (or equivalent dH_2O control) into the priming mixture. Buffer and drug were diluted in media and used to infect the cells (247).

2.6.5 pH/K^+ BUNV-N expression timecourse

BUNV was primed in pH 6.3 (-K^+) or pH 6.3 + K^+ buffers for 2 hrs as in 2.6.1, and added to cells for 1 hr. Non-internalised viruses were removed and replaced with fresh DMEM. Cells were lysed at increasing post-infection time points (as in 2.5.2) (247).

2.6.6 BUNV antibody neutralisation assay

To determine the neutralisation ability of anti-BUNV-Gc (M742 Mab, kindly provided by Dr Cheryl Walter (248)), BUNV (MOI = 0.1) was treated with 1:10,000 antibody in 1 ml DMEM for 1 hr with gentle rocking. Samples were diluted into 3 ml and added to A549 cells. At 24 hpi, cells were fixed and BUNV-N expression was assessed by immunofluorescent staining using anti-BUNV-N antibodies (2.9.5). The IncuCyte system was used to quantify BUNV-N fluorescence.

To assess neutralisation of primed BUNV, virions (MOI = 0.1) were primed in pH 7.3, pH 6.3 and pH 6.3 + K^+ buffers for 2 hrs at 37 ºC. Buffer was then diluted (to 1 ml) and virions were treated with an anti-BUNV-Gc antibody (1:10,000) or an equal volume of dH_2O for 1 hr at room temp with gentle rocking. hRSV (MOI = 0.1) control treatments with antibody or dH_2O were performed alongside to confirm anti-BUNV-Gc specificity. Samples were further diluted (to 3 ml) and added to A549 cells, where infection was allowed to proceed for 18 hrs. hRSV was propagated and kindly provided by Miss Hayley Pearson, at a titre of $1x10^8$ PFU/ml.

2.7 Fluorescent labelling of endosomal compartments

See Table 2.1 for the cellular markers used to fluorescently label different endo/lysosomal compartments.

2.7.1 Fluorescent tracking of SYTO82/DiD-BUNV localisation

A549 cells were seeded into 9 cm^2 glass-bottom dishes (~$3x10^5$ cells/well) or 1 cm^2 glass-bottom µ-slide (Ibidi) (~$4x10^4$ cells/well) 24 hrs prior to infection, to allow live fluorescent imaging. Cells were infected with SYTO82/DiD-BUNV (MOI

= ~8 as in 2.5.1) at 4 °C for 1 hr and simultaneously loaded with EGF-488 or transferrin (Tf)-488 (4 µg/ml; Biotinylated Tf complexed to Alexa-Fluor 488; ex. 495 nm, em. 519 nm; Thermo Fisher Molecular Probes) to synchronise dye and virus uptake. Cells were heated to 37 °C and live imaged (2.9.8) at the indicated time points 2-8 hpi.

For the determination of BUNV lysosomal localisation, cells were seeded as above, however TEA (10 mM) was added 30 mins prior to infection (or an untreated control) and maintained through experimentation. CytoPainter (CytoP, lysosomal staining reagent; ex. 450 nm, em. 505 nm Life Technologies) was added to cells alongside SYTO82/DiD-BUNV for 1hr at 4 °C, prior to heating to 37 °C and live imaging (2.9.8) at the indicated time points (247).

2.7.1.1 Rab7 and Rab11 Transfections

A549 cells were transfected with Rab7-GFP (late endosomes) (249,250) or Rab11-GFP (recycling endosomes) (251,252). Cells were washed with PBS and replaced with serum-free DMEM 30 mins prior to transfection. Transfections were performed using FuGENE HD Transfection Reagent (3:1 ratio FuGENE (µl):DNA (µg); Promega) and 0.5 µg DNA (or reagent-only control), mixed and incubated at room temperature for 15 mins. Mixtures were added dropwise to each well and cells were incubated for 24 hrs at 37 °C to allow expression. Cells were infected for 1 hr at 4 °C with SYTO82/DiD-BUNV as in 2.7.1, warmed to 37 °C and live imaged at the indicated time points, 2 and 8 hpi (247).

2.7.2 Endosomal K^+ AG4 labelling

2.7.2.1 SYTO82-DiD-BUNV localisation with AG4

Cells were seeded onto glass-bottom dishes as in 2.7.1 and allowed 24 hrs to adhere. The membrane-impermeable K^+-sensitive dye Asante potassium green-4 (AG4; 10 µM, ex. 490 nm, em. 540 nm; TEF Labs) was added to cells simultaneously with SYTO82/DiD-BUNV (MOI = ~0.1) at 4 °C for 1 hr, then cells were warmed to 37 °C (0 hpi). Non-internalised dye was removed at 1 hpi and cells were live imaged at 2 and 8 hpi (247).

2.7.2.2 Assessment of AG4 localisation to endosomal compartments

Cells were seeded as above and AG4 (see 2.7.2.1) was added to cells at 4 °C (1 hr) with Texas-red labelled EGF (2 µg/ml, biotinylated EGF complexed to Texas red streptavidin, ex. 595 nm, em. 615 nm; Thermo Fisher Molecular Probes), Magic Red cathepsin-B dye (Magic Red or MR; 3.8 µg/ml, ex. 590 nm, em. 620 nm; ImmunoChemistry Technologies) or pH rhodamine red-dextran (pHRodo; 10 µg/ml, ex. 560 nm, em. 585 nm; Thermo Fisher Molecular Probes). Cells were warmed to 37 °C for 40 mins and live imaged.

In experiments where the effects of K^+ channel inhibition were assessed, 10 mM TEA (or untreated control) was added 30 mins prior to addition of dyes and was maintained throughout. Where total AG4 or MR fluorescence was assessed, cells were seeded into 6-well plates and treated with dye as above +/- TEA (10 mM) and mean fluorescence intensity was quantified (GCU, green calibration units) after 40 mins using live IncuCyte Zoom imaging (2.9.6) (247).

Table 2.1 Fluorescent markers used to label cellular and viral components
Fluorescent dyes and constructs used as described to label different endo/lysosomal compartments and used in dual-fluorescently labelled BUNV production. Excitation and emission wavelengths (nm) are indicated.

Marker	Abbreviation	Target	Ex. max	Em. max
Asante potassium green-4 dye	AG4	K^+-rich endosomes	490	540
CytoPainter dye	CytoP	Acidic endo/lysosomes	450	505
DiD-Vybrant dye	DiDvbt	Lipids	645	665
EGF-488	EGF-488	EE and LEs	495	519
EGF-Texas red	EGF-TR	EE and LEs	595	615
Magic Red cathepsin B dye	Magic Red/ MR	Lysosomes	590	620
pH rhodamine red-dextran dye	pHRodo	Acidic endo/lysosomes	560	585
Rab7-GFP construct	Rab7-GFP	LEs	488	510
Rab11-GFP construct	Rab11-GFP	REs	488	510
SYTO82 dye	SYTO82	Nucleic acids	540	560
Transferrin-488	Tf	EEs and REs	495	519

2.8 K_{2P} channel knockdowns and overexpression

2.8.1 K_{2P} channel siRNA knockdown

A549 cells were seeded (~0.8×10^5 cells/well) into 12-well plates. After 24 hrs, cells were transfected with siRNA targeting the K_{2P} channels TWIK1 (KCNK1), TREK1 (KCNK2), TASK2 (KCNK5) or TWIK2 (KCNK6) (Santa Cruz). Transfection mixes were made up in siRNA transfection medium (Santa Cruz), containing 6 µl siRNA transfection reagent (Santa Cruz) and 60 nM of siRNA. Scrambled siRNA (Control siRNA-A, Santa Cruz) was used as a control siRNA transfection. For the TWIK2 siRNA concentration range, 10, 20, 40 or 80 nM siRNA was used. Transfection mixes were incubated at room temperature for 30 mins and added to cells pre-washed in PBS. After 24 hrs at 37 °C, transfection mixes were removed from cells, the cells were washed in PBS, and fresh DMEM was added and incubated for a further 24 hrs to allow cell recovery. Cells were infected with BUNV (MOI = 0.1) as in 2.5 for 24 hrs, at which point cells were lysed and infection assessed by western blot (see 2.9.1-2.9.3).

2.8.2 TWIK2-GFP mammalian cell transfections

2.8.2.1 TWIK2-GFP transfection and SYTO82/DiD-BUNV infection

A549 cells were seeded into 1 cm^2 glass-bottom µ-slides (Ibidi) (~4×10^4 cells/well) and incubated for 24 hrs. Cells were transfected with TWIK2-GFP (KCNK6 with a C-terminal GFP tag, in a pCMV vector; OriGene) using FuGENE HD transfection reagent (3:1) and 0.2 µg DNA. Mixtures were made up and transfected as in 2.7.1.1 and incubated for 24 hrs at 37 °C. Cells were infected with SYTO82/DiD-BUNV as in 2.5.1 and live imaged (2.9.8) at 1 and 6 hpi.

2.8.2.2 Determining TWIK2-GFP endosomal localisation

A549 cells were seeded into 24-well plates (~6×10^4 cells/well) with glass coverslips. Cells were transfected as above (2.8.2.1) with TWIK2-GFP or TWIK2-GFP mutants (0.4 µg DNA) (2.9.10) for 24 hrs. Magic Red (3.8 µg/ml) or Texas-red EGF (2 µg/ml) was then added to transfected cells for 40 mins at 37 °C and live imaged.

2.9 Biochemical methods

2.9.1 Harvesting mammalian cells for lysis

At the indicated time points, cells were washed with PBS and lysed using a triton-based lysis buffer (termed LLB; 25 mM glycerol phosphate, 20 mM tris, 150 mM NaCl, 1 mM EDTA, 1 % triton, 10 % glycerol, 50 mM NaF, 5 mM $Na_4O_7P_2$, pH 7.4) supplemented with a protease inhibitor cocktail (Thermo Scientific), with gentle rocking for 15 min at 4 °C. Cell lysates were harvested using a cell scraper and clarified by centrifugation at 17 x *g* for 10 mins. Protein-containing supernatants were collected and protein concentrations were determined using BCA assay kits (bicinchoninic assay, Thermo).

2.9.2 SDS-PAGE

Laemmli sample buffer (4 x, Bio-Rad, supplemented with β-mercaptoethanol) was added to samples (final sample buffer concentration: 1 x) and normalised protein concentrations were loaded onto 15 % acrylamide SDS (sodium dodecyl sulphate) gels and resolved by SDS-PAGE (SDS-polyacrylamide gel electrophoresis) (see Table 2.2 for gel recipes). For the analysis of BUNV purification (2.4.2) by silver staining (2.9.4), 12 % resolving gels were used. SDS-PAGE gels were run for 1 hr at 180 V. SDS-PAGE running buffer consisted of 25 mM tris, 250 mM glycine, 1 % (w/v) SDS.

Table 2.2 SDS-PAGE gel recipe per gel

APS = ammonium persulfate, SDS = sodium dodecyl sulphate, TEMED = tetramethylethylenediamine.

15 % resolving gel	12 % resolving gel	Stacking gel
2.5 ml tris-HCl (1.5 M, pH 8.8)	2.5 ml tris-HCl (1.5 M, pH 8.8)	0.13 ml tris-HCl (1 M, pH 6.8)
2.3 ml dH_2O	3.3 ml dH_2O	1.50 ml dH_2O
5 ml 30 % acrylamide	4 ml 30 % acrylamide	0.33 ml 30 % acrylamide
0.1 ml 10 % SDS	0.1 ml 10 % SDS	0.02 ml 10 % SDS
0.1 ml 10 % APS	0.1 ml 10 % APS	0.02 ml 10 % APS
0.016 ml TEMED	0.016 ml TEMED	0.01 ml TEMED

2.9.3 Western blotting

Samples were resolved by SDS-PAGE and transferred onto polyvinylidene difluoride (PVDF; Millipore) membranes using a Bio-Rad Trans-blot Turbo in a tris-based transfer buffer (25 mM tris, 88.5 mM glycine, 20 % (v/v) methanol), at 25 V for 30 mins. Non-specific binding of antibodies was prevented by blocking in 10 % milk in TBS-tween (25 mM tris, 137 mM NaCl, 0.1 % (v/v) tween-20, pH 7.5) for 1 hr. Proteins were labelled with primary antibodies (in 5 % milk) overnight at 4 ˚C and unbound antibodies were removed by three washes in TBS-tween. Blots were then incubated with corresponding HRP-tagged (horseradish peroxidase) secondary antibodies (in 5 % milk) for 1 hr at room temperature and membranes were washed four times in TBS-tween. Labelling was detected using the enhanced chemiluminescence (ECL) system and films were developed in an Xograph processor. Results were scanned and cropped to antibody bandwidths; where film was over-exposed and non-specific bands can be seen in full-length gels. Densitometry was performed using ImageJ (NIH) to determine band intensities and normalised to each GAPDH loading control.

2.9.3.1 Antibodies

As a marker for infection (244), sheep anti-BUNV-N primary antibodies generated in the laboratory of Dr John Barr were used and membranes were labelled with HRP-conjugated anti-sheep (Sigma) secondary antibodies. GAPDH (Glyceraldehyde 3-phosphate dehydrogenase) was labelled with rabbit anti-GAPDH primary antibodies (Santa Cruz) and anti-rabbit (Sigma) secondary antibodies as a loading control, identifying equal protein concentrations loaded onto SDS gels.

2.9.4 Silver staining

To determine the purity of BUNV propagated for EM (2.4.2), 10 µl of each sample was collected during the purification process alongside 0.5 µl purified BUNV, were resolved by SDS-PAGE (2.9.2). Due to the sensitivity of the assay, protein ladders were diluted 50-fold prior to gel loading.

Samples were resolved on SDS-PAGE gels and fixed by incubation in solution A (see Table 2.3 for solution recipes) for 30 min. For this stage and all subsequent stages, gels were gently agitated during room temperature incubations. Gels were incubated in solution B for 15 mins, followed by 3 x 5 min washes in dH_2O. Solution D was then added for 1-2 min to bind proteins and enhance staining. Gels were then washed x3 for 30 sec with dH_2O and incubated in solution E for

20 mins to embed the gel with silver ions. Gels were washed (3 x 30 sec) and incubated in solution F until bands were visible through the reduction of protein-bound silver ions to metallic silver. Solution G was then added to stop further development of the stain and to prevent background staining. Gels were then washed in dH_2O and imaged.

Table 2.3 Silver staining recipes

Solution	**Components** (total volume 100 ml)
A	50 % (v/v) ethanol, 10 % (v/v) acetic acid
B	5 % (v/v) ethanol, 1 % (v/v) acetic acid
C	0.2 g sodium thiosulphate
D	10 ml solution C
E	0.2 g silver nitrate, 75 µl formaldehyde
F	6 g sodium carbonate, 50 µl formaldehyde, 0.2 ml solution C
G	5 % (v/v) acetic acid

2.9.5 Immunofluorescence

A549 cells infected with BUNV were fixed in 4 % PFA for 10 min at 4 °C. Cells were permeabilised with 0.1 % triton-X100 in PBS for 10 min and blocked in 1 % (w/v) bovine serum albumin (BSA; Sigma) in PBS for 30 min. Cells were labelled with primary anti-BUNV-N antibodies in blocking buffer for 1.5 hrs, washed in PBS (x4), and stained with the corresponding fluorescent Alexa-Fluor 488 nm or 594 nm conjugated anti-sheep (Invitrogen-Molecular Probes) secondary antibodies for a further 1 hr, washed and imaged.

2.9.6 IncuCyte Zoom imaging and analysis

Widefield images of 2.15 mm^2 were taken using the IncuCyte Zoom imaging system to identify fluorescently-labelled cells. The number of fluorescent cells or mean fluorescence intensity (green calibration units, GCU) was quantified and normalised to controls (i.e. non-drug treated (untreated) controls) (247).

2.9.7 Fixed cell confocal microscopy

Cells were fixed on glass coverslips and mounted onto glass slides using ProLong Gold reagent containing DAPI (Invitrogen). An inverted LSM-700 laser-scanning confocal microscope (Zeiss) was used with an oil-immersion 40x or 60x objective lens to image fluorescently labelled cells. Widefield images were taken and represent single optical sections of 50 µm thickness. The excitation$_{max}$ (ex.$_{max}$) and emission$_{max}$ (em.$_{max}$) spectra of the fluorophores were as follows: SYTO82 ex.$_{max}$ 540 nm and em.$_{max}$ 560 nm and DiDvbt ex.$_{max}$ 645 nm and em.$_{max}$ 665 nm. Bleed-through between channels was not observed. Colocalisation of the fluorophores was analysed by line scan and fluorescence quantified at various z-stacks through the cell (Zeiss Zen 2011 software). Three-dimensional images were obtained from the Z-stacks using ICY software.

2.9.8 Live cell confocal microscopy

Cells were plated onto glass-bottom dishes (Ibidi) for live-cell imaging of SYTO82/DiD-BUNV infection and/or endosomal fluorescence markers. Cells were warmed to 37 ˚C and imaged on an inverted 510-META laser-scanning confocal microscope (as with 2.9.7), in a humidified 37 ºC environment [microscope training and live images were taken with the help of Dr Jamel Mankouri]. Time series images were acquired at 20 sec intervals to visualise virion entry and post-entry trafficking. Co-localisation was quantified by physically counting the number of co-localising puncta per cell for each condition (247).

2.9.9 Determination of K_{2P} channel expression

2.9.9.1 RNA extraction and cDNA synthesis

To determine K_{2P} channel expression in A549 and MDA-MB-231 cells or confirm siRNA knockdown in A549 cells, whole cell lysates were extracted using TRIzol (Life Tech) and total cellular RNAs were purified using the Direct-zol RNA MiniPrep kit (Zymo). First-strand synthesis of cDNA from 0.75 µg of cellular mRNA was performed using NEB's first-stand synthesis kit and an oligo $d(T)_{12\text{-}18}$ primer (Invitrogen). Samples were heated to 65 ºC for 5 mins, 42 ºC for 1 hr and then 65 ºC for 20 mins. cDNA was stored at -20 ºC until RT-PCR amplification.

2.9.9.2 K_{2P} channel RT-PCR

RT-PCR amplification was performed using 2 µl of cDNA (generated in 2.9.9.1) and OneTaq hot start DNA polymerase (NEB). PCR mixtures (50 µl total) were produced according to the manufacturer's instructions, with the addition of 5 % glycerol to aid primer binding. Fifteen reactions were performed using primers to amplify each KCNK channel, alongside a no-primer control. Primer sequences can be found in Table 2.4 and annealing temperatures (Ta) for each pair were initially optimised using a Ta range. The reaction mixture was put through an initial 3 min denaturing stage (95 ºC), followed by x35 cycles of denaturing (95 ºC, 45 sec), annealing (varied ºC, 30 sec) and elongation (72 ºC, 60 sec), and then a final elongation step (72 ºC) for 10 mins. Amplicons were run alongside a 100 bp DNA ladder (NEB) on a 2 % agarose gel, using SyberSafe (Invitrogen) and a UV gel dock imager to visualise bands.

Table 2.4 K_{2P} channel and GAPDH PCR primers

Primers designed by Dr J Mankouri and ordered from Sigma.

KCNK	**Forward Primer** (5'-3')	**Reverse Primer** (5'-3')	**Ta (ºC)**
1	CACCGTGCTCTCCACCACAGG	TTGCAGGGCCATCCACGCAG	58
2	ATCGGAGCCACCGTGTTCAAAGC	CGCAGGCAGAGCCACAAAGAG	70
3	ACCAGAGAGCAAAAGGCAAA	TCAAACAATCCTCCCACCTC	52
4	ATCTGGGGGAGAAGGACACT	CTGCCGATCCCTAACTGGTA	54
5	GGTGGCCAGGGCGCTGCAAG	GGTGCAGGGCAGGAGGGCAG	58
6	CTGGACGCCTTCGTGGAGCG	GTCGGACACGTGGCGGAAGG	58
7	CAGCCTCCTTAGCTCTCGTG	GAGCGAGCTGAAGCAGAAGT	62
9	CAGCATGGTCATTCACATCC	GGTGGTCGGTAAAGCTGTGT	58
10	GCTCTGCCAAAAGGAATCAG	GCACATGCCAAAATGTCAAC	50
12	AGAGCGAGTCCACGTAGTCC	GGGACCATCCTGTTCTTCAA	50
13	GGGAACAAAAATTGCGAAGA	CCCTACACCACCATCTTGCT	46
15	GGCAAGGTCTTCTGCATGTT	GGTGAGGGATGATGAAGCAGT	48
16	CAAGTCACACCCCAGGACTT	TCCCACACCTCTGTCCTTTC	54
17	TAGAGGCTGGGTGCAGCTAT	CAAACATTGCCGCTACTTCA	50
GAPDH	TCACCACCATGGAGAAGGCT	GCCATCCACAGTCTTCTGGG	62

2.9.9.3 K_{2P} channel siRNA knockdown RT-PCR

From siRNA knockdowns of select K_{2P} channels performed in 2.8.1, parallel samples to those infected with BUNV were transfected with siRNA. Forty-eight hours post-transfection, all samples were lysed, RNA extracted and subjected to cDNA synthesis (using an oligo d(T)) primer performed as in 2.9.9.1). RT-PCRs were performed as described in 2.9.9.2 using the indicated primers (Table 2.4); comparing expression between Scr and siRNA knockdown cells. GAPDH primers were used for each sample in parallel to confirm successful RNA extraction, cDNA synthesis and PCR amplification.

2.9.10 TWIK2 site-directed mutagenesis

2.9.10.1 PCR mutagenesis and amplification

Primers were designed using NEBaseChanger (NEB) to mutate key functional and localisation residues in TWIK-GFP; outlined in Table 2.5 (motifs identified by *Bobak et al* (2017) (253)). Quick change mutagenesis was performed using the Q5 site-directed mutagenesis (SDM) kit (NEB), following manufacturer's instructions. Amplicons were resolved on 2 % agarose gels (see 2.9.9.2) alongside a 1 kb DNA ladder (NEB) to confirm successful amplification.

Table 2.5 TWIK2-GFP SDM primers

Red indicates mutated residues.

Mutation	**Forward/Reverse Primers** (5'-3')	**Ta (ºC)**
Y109A	TGGGTACACAACGCCACTGACTG GCGCCCACGGTGGTGGTGATCAGC	62
LL270/271AA	GGCGCCCCCTCCGTGCCCTGCC GCGATGAGCTCCGTGAGGCCGTGG	70
IL289/290AA	CGCCGCGGGCCCCCAGCCGGAGT TCCACCCGATCGTCCTCATCCGCATTGAA	67
Y308A	TTCCATCCCCAGGACGCGTACGC GCGGCGTCGGTGTGGGAGCTGGC	70

2.9.10.2 KLD reaction and bacterial cell transformation

PCR products were treated with a KLD (kinase, ligase and DpnI) enzyme mix to re-ligate plasmids and degrade input DNA strands (that will not contain mutations). Products were transformed into DH5-*α* bacterial cells (NEB), following the manufacturer's instructions. Cells were subsequently plated onto ampicillin-containing (100 µg/ml) sterile LB agar plates and incubated at 37 °C overnight to allow colony growth.

2.9.10.3 DNA amplification, purification and sequence confirmation

Sterile LB (5 ml) containing ampicillin (100 µg/ml) was inoculated with a colony; two tubes per mutant and one colony in each tube. Cultures were agitated (160-200 rpm) at 37 °C overnight to allow bacterial cell multiplication. Cells were lysed and DNA extracted using a MiniPrep DNA Extraction kit (Qiagen). A sample of each was then sent for sequencing (Genewiz) using CMV-Forward and GFP-reverse primers provided by Genewiz, to sequence the KCNK6 region.

2.9.10.4 Generating multiple mutations

TWIK2 localisation mutants required a number of rounds of SDM, which are outlined in Table 2.6. Following the outlined procedure, the first mutation was generated for Y109A and IL289/290AA. After confirmation of mutagenesis by sequencing, the IL289/290AA construct was used to add a further Y308A mutation, and the double mutant (X2M) was used to add LL270/271AA; generating the X3M construct.

Once complete all constructs were amplified using bacterial cell transformation and a MaxiPrep DNA extraction kits (Qiagen), generating yields >750 ng/µl.

Table 2.6 TWIK2 mutants generated using SDM

Name	Mutations required
Y109A	Y109A
X2M	IL289/290AA, Y308A
X3M	LL270/271AA, IL289/290AA, Y308A

2.10 Electron microscopy

2.10.1 Negative stain EM

WT BUNV purification (in 2.4.2) was confirmed by negative stain electron microscopy (EM). Carbon-coated EM grids were made hydrophilic by glow discharge (PELCO easyGlow glow discharge system) and 5 µl of sample was applied to the grid for 30 sec. Excess sample was removed using blotting paper and the grid was washed x3 with dH_2O, blotting between each wash. Final, samples were embedded with 1 % (v/v) uranyl acetate for ~10 sec and excess liquid was remove. The grid was allowed to air dry for ~5 mins before imaging. Negatively stained grids were loaded into a single tilt holder and inserted into the FEI Tecnai T12 electron microscope for imaging, at a defocus of -1 µm to -5 µm.

2.10.2 Virion priming, grid loading and vitrification

Purified BUNV was primed as in 2.6.1, using buffers at pH 7.3 and pH 6.3 -/+ 140 mM KCl. Buffers were produced as described in 2.6.1.1, however concentrations of the components were increased to produce the same final concentration at a 1:1 dilution BUNV:buffer (previously 1:11); this limited virus dilution (Table 2.7). Purified BUNV (2 µl) was combined with 2 µl buffer (x4, one for each) and pre-heated to 37 °C prior to pH adjustments. Priming mixtures were incubated at 37 °C for 2 hrs and then taken for immediate grid loading.

To act as fiducial markers during tomogram alignment, 2 µl of a Gold particle solution (Conventional ImmunoGold Reagent, Orion) was added to each priming mixture (all procedures were performed with the help of Dr Juan Fontana) and grid loading was performed using a Leica EM GP automated grid plunge freezer. Lacey-carbon EM grids (kindly provided by Dr Juan Fontana) were glow discharged and mounted into the chamber; at a pre-set temperature under high humidity. Priming mixture (3 µl) was added to a grid, and excess sample was removed through blotting (3 sec blotting time) and rapidly plunged into liquid ethane (2 grids were made for each condition, 8 in total). Frozen grids were stored in pre-cooled grid boxes and maintained in liquid nitrogen.

Table 2.7 EM priming buffer contents

	pH	Buffer	KCl (mM)	NaCl (mM)
7.3	7.3	Tris (36 mM)	0	20
7.3+K$^+$	7.3	Tris (36 mM)	280	20
6.3	6.3	Bis-tris (55 mM)	0	20
6.3+K$^+$	6.3	Bis-tris (55 mM)	280	20

2.10.3 Cryo-EM grid screening and cryo-electron tomography

The vitrified EM grids were clipped and loaded into an FEI Titan Krios I by University of Leeds facility managers Dr Rebecca Thompson, Dr Emma Hesketh and Dr Daniel Maskell. Each grid was screened to confirm successful grid loading of a significant quantity and the spread of viral particles. A significant volume of gold particles, low levels of background contaminants, and a thin layer of ice covering the virions was confirmed. Images were collected with the help of Dr Juan Fontana (pixel size = 4.7 Å).

For cryo-electron tomography (cryo-ET), tilt series data were collected for pH 7.3 and pH 6.3 + K$^+$ treated BUNV grids, using the FEI Titan Krios II with the help of the Astbury Biostructure Laboratory staff to set up automated data collection using Tomography 4 software (FEI). A pixel size of 2.72 Å was used, with an electron dose of 1.8 e-/image, at 53,000x magnification, a defocus of -1 µm and using a Volta phase plate. Microscope alignments were performed by Dr Rebecca Thompson and Dr Emma Hesketh. Suitable grid locations were selected manually and then Tomography 4 was utilised to perform the autofocus and data collection. 20-21 single axis tilt series were collected for each condition (2 days of imaging) at grid angles from -60 to +60 °C, at 2 °C increments.

2.10.4 Reconstructing 3D tomograms

Following data collection, tilt series were pre-processed by CTF (contrast transfer function) correction and motion correction, which was applied (Relion) to limit large distortions introduced by sample movement during imaging. Tilt series were then imported into IMOD software for batch tomogram reconstruction. Batch tomography allows tomograms to be generated in a high-throughput manner. Initially pre-processing was performed to remove outlying pixels (px) and/or artefacts, and an initial alignment was made between each 2D projection in the series. Gold particles were used to fine align the tilt series, with some manually selected to generate a model automatically assessing particle movement between the images. The gold particle alignment was then utilised by IMOD to reconstruct 3D volumes (254). A binning factor of 2 was applied, generating a final pixel size of 5.44 Å. ImageJ was used to collect images, which were filtered using Gaussian Blur 3D. Reconstructions were generated by S Hover, with help from Dr Juan Fontana.

2.10.5 Sub-tomogram averaging

To determine GP structure, sub-tomogram averaging (STA) was performed using Particle Estimation for Electron Tomography (PEET) software (IMOD), which allows the alignment, averaging and iterative refinement of 3D particles (following a methodology similar to *Punch et al* (2018) (77,254,255)). For both pH 7.3 (control) and pH 6.3 + K^+ (primed) STA, a template or reference was generated which was used for automatic particle selection. Several stages were then performed to refine selected particle alignment. All STA was performed by S Hover, with help from Dr Juan Fontana.

2.10.5.1 Template generation

A template or reference particle was first generated to guide the software for spike selection during automatic particle picking and in determining the correct alignment of particles. Firstly, using 3dmod (IMOD) a model was generated for each of 3 tomograms, defining the centre of the virus particles and the position of the viral membrane in the 3D volume; assuming viruses are near-spherical. The centre of ~200 spikes across the 3 tomograms were manually defined and spikeInit (PEET programme, IMOD) was then used to generate an initial orientation list (motive list), which assumes that each spike sits perpendicular to the viral membrane. PEET was then used to extract these sub-tomograms using the information provided by the models and motive lists. Particles were averaged and an initial alignment was generated, which was partly refined by allowing PEET to alter the lateral location of the spikes on the membrane and the twist-orientation of the particles (around the y-axis, phi), to identify the optimal alignment. The roughly aligned averages were used as templates for automatic particle alignment.

2.10.5.2 Automated particle selection and refinement

A model was generated (3dmod, as above) for all tomograms, defining the centre of all virions that was used to generate a model with estimated spike (pseudo-spike) locations, termed 'seed' spikes (PEET, IMOD), which are spaced ~8.2 nm apart. An initial orientation list was generated for all pseudo-spikes and an initial average generated, using the template as a guide. Note that a greater number of pseudo-spikes was chosen than actual spikes, to ensure all spikes present were selected. A number of iterative refinement steps were performed in PEET to refine the selected spikes. For all subsequent stages the template was used as a reference to guide alignment and PEET was used to improve the template using the new particle alignment. Parameters were also set to limit duplicate particles owing to the wide initial search parameters, where any spike closer than a set number of px from another (ctl = ~8.2 nm, primed = ~5.4 nm) was considered a duplicate and discounted from the generated average. Missing-wedge compensation was also enabled to account for the missing angles from the tilt-series where no data was collected; i.e. greater than +60 °C and lower than -60 °C tilt.

Given that the selected spikes were generated from predicted spike spacing and locations, PEET was initially allowed to refine each spike location over a broad search range (e.g. 10 px in every direction). A relatively large sub-tomogram volume was also set (54 px (~294 nm) square), using a large spherical mask, until an initial average could be found to define the estimated spike size.

In the second stage, a smaller sub-tomogram volume was defined (~185 nm x 228 nm x 185 nm) and using a smaller spherical mask, to limit background interference during averaging. Particles were then iteratively refined, predominantly refining the orientations of the spike; twisting (around the y-axis, phi) and tilting ('forward/back' and 'left/right', theta and psi). This began with a large search range (e.g. +/- 180 °C) at large increments (e.g. 60 °C), then decreasing at each iterative stage to improve the alignment. This is the stage reached during refinement of the primed BUNV spike, where no three-fold (C3) symmetry was evident.

In the final stage, the ctl spike exhibited a tripod-like arrangement (74), indicating C3 symmetry. The average was refined by further iterative alterations to the spike orientations and location in small increments. Additionally, more stringent high and low frequency cut-offs were applied to focus on the high resolution information and improve the final resolution.

Using calcFSC (PEET) the final resolution was estimated, using Fourier shell correlation (FSC) and a threshold of 0.5. UCSF Chimera (RBVI) was used to render 3D reconstructions of the averaged density maps (256) and for rigid-body-fitting of crystal structures (from *Hellert et al* (2019) (90)) into the electron density. Crystal structures can be obtained from the Protein Data Bank (PDB) under accession numbers: 6H3V for BUNV Gc head domain (residues 478-721), 6H3S for SBV Gc head and stalk domains (residues 465-874) (90).

Chapter 3 | BUNV requires endosomal K^+ for entry into cells

3.1 Introduction

Host-cell K^+ channel function is essential for bunyavirus infection, as the pharmacological inhibition of K^+ channels prevents virus infection (*Hover et al* (2016) (244)). Previous work using the broad spectrum K^+ channel inhibitor TEA identified that early stages in the virus lifecycle require K^+ channels, as TEA is ineffective from 6 hpi (see Figure 1.10). This time frame implicated K^+ channel involvement in BUNV trafficking through the endosomal network, virus-host membrane fusion for vRNP release, vRNP cytoplasmic trafficking or the formation of replication factories in the Golgi. The data outlined in this chapter investigated the role of K^+ channels in BUNV endocytic trafficking.

Many enveloped virions must traverse the endocytic network, fuse with host endosomal membranes and release their genome into the cytoplasm. The trafficking route through the endosomal network differs between bunyaviruses and for most, has not been fully defined. CCHFV (*Nairoviridae* family) for example traffics through EEs and fusion occurs within MVBs (119). UUKV (*Phenuiviridae* family) however traffics through EEs into LEs, not MVBs (a type of LE), predicted as the site of virus fusion (257). For BUNV, the route of entry has not been determined, however as a Peribunyavirus it is predicted to require endosomal acidification for entry; as described for the *Nairoviridae* and *Hantaviridae* families (120). The increasingly acidic environment through the endosomal network is predicted to elicit structural changes in the Gn-Gc GPs which promote interaction with endosomal membranes and subsequent fusion and genome release (120). Beyond endosomal acidification, there are no studies regarding the specific cellular triggers required for BUNV fusion.

The role of ion channels in virus entry is an emerging area of research. An investigation of EBOV entry showed a direct requirement for Ca^{2+} TPCs during EBOV endosomal trafficking and genome release (236). The disruption of which prevented EBOV virion trafficking to LEs/lysosomes and hence endocytic release (see Chapter 1, Figure 1.9) (236). This study represented not only the first link to a role of cellular ion channels during virus-endosomal trafficking events but also a role of endosomal ions other than H^+ influencing virus entry. In line with this *Stauffer et al* (2014) linked endosomal $[K^+]$, alongside $[H^+]$, to IAV, specifically during virion fusion (258). The decreasing pH (increasing H^+) during endosomal maturation from EEs to lysosomes is well understood, however the change in other ionic concentrations is largely undefined (173). For K^+, a concentration gradient exists across the cell membrane with a low extracellular concentration

(~5 mM) and a high intracellular cytoplasmic concentration (~150 mM); see Figure 3.1. As endosome formation takes up the extracellular environment it therefore follows that EEs contain a low K^+ concentration ($[K^+]$), which increases with maturation into LEs. It is also thought that this increase continues through to lysosomes, but this has not been exclusively determined (173). *Stauffer et al* (2014) investigated the role of ions during IAV fusion by treating virions with high $[H^+]$ and $[K^+]$ buffers mimicking the LE/lysosome environment. It was shown that a stepwise process facilitates IAV uncoating, whereby H^+ ions are required for preliminary structural changes in IAV GPs, followed by further H^+ and K^+ increases which facilitate secondary changes in the virion 'priming' the virus for fusion. K^+ was essential in destabilising the viral capsid for efficient viral genome release (258). This was not linked to a requirement for K^+ channels, however it demonstrates that ions other than H^+ are important for viral fusion events.

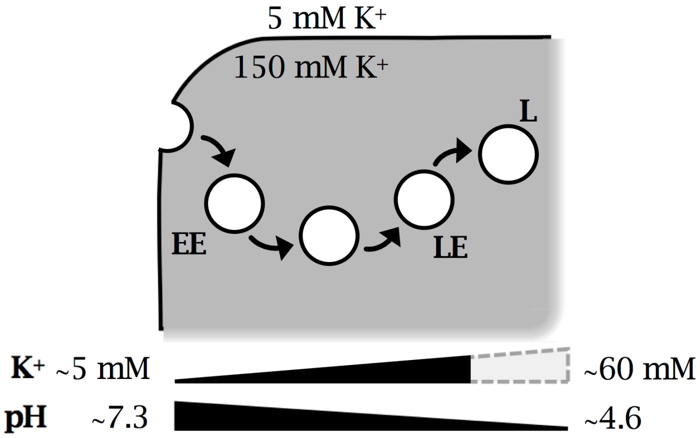

Figure 3.1 A K^+ gradient exists within endosomes, where $[K^+]$ increases with decreasing pH

Schematic demonstrating the extracellular (5 mM) and cytoplasmic (150 mM) $[K^+]$, alongside the change in endosomal $[K^+]$ and pH with passage through EEs, LEs and to lysosomes (L). Whilst pH decreases, K^+ is thought to increase during endosomal maturation. Adapted from *Scott et al* (2011) (173).

The discovery of the role of endosomal ions in entry of EBOV and IAV, indicates that the requirement for K^+ channels in bunyavirus infection previously identified could be through the manipulation of endosomal K^+. It was therefore logical to investigate the role of endosomal ions and ion channels during BUNV endocytic processes. The data presented in this chapter investigated the role of endosomal K^+ during BUNV infection, through the development of a dual-fluorescently labelled BUNV that allowed the tracking of individual virions through the endocytic network. This revealed that BUNV traffics through EEs to LEs, where K^+ and H^+ act as biochemical cues for BUNV endosomal escape. In addition a novel cellular role of K^+ channels was identified whereby endosome-resident K^+ channels control the endosomal K^+ balance, providing the first evidence of how cells accumulate endosomal K^+.

3.2 Assessing the timeline of BUNV infection

Limited information is available regarding the specific time points for the different BUNV lifecycle stages in A549 cells. Initially a one-step growth curve was generated, whereby A549 cells were infected with BUNV (MOI = 0.5) and the quantity of virus released at increasing time points was determined by plaque assay (Figure 3.2 A). A canonical growth-curve was observed, whereby viral titre increased with time during an exponential phase until 48 hpi, at which point the curve plateaued and viral titre remained similar (~$1x10^7$ PFU/ml) until 120 hpi. To further characterise the kinetics of BUNV infection, the expression of BUNV-N known to correlate with virus production, was assessed from 1-24 hpi. BUNV protein expression was assessed by western blot analysis of BUNV-N which could be detected ≥15 hpi and continued to increase up to 24 hpi (Figure 3.2 B). This indicated that viral protein expression is initiated shortly before 15 hpi.

BUNV release was also assessed through the identification of infectious BUNV progeny produced from the cells at each time point. BUNV supernatants from each time point (3-24 hpi) were re-infected onto A549 cells to identify the time points at which infectious BUNV virions are released. Cells were fixed, stained for BUNV-N and virus infection assessed by IncuCyte Zoom live imaging (Figure 3.2 C). Quantification of the number of infected (fluorescent) cells indicated low levels of virus release at 15 hpi (Figure 3.2 D). Re-infection was however higher at later time points from 18 to 24 hpi, indicating that the cells began to release BUNV shortly after protein expression was initiated, but was highest from 21-24 hpi in the time points assessed. Taken together, these data reveal the kinetics of BUNV-N expression and virion release in A549 cells. This timeline additionally indicated that early pre-translation stages of the viral lifecycle are that which require K^+ channel, as TEA is not effective >6 hpi (see Figure 1.10).

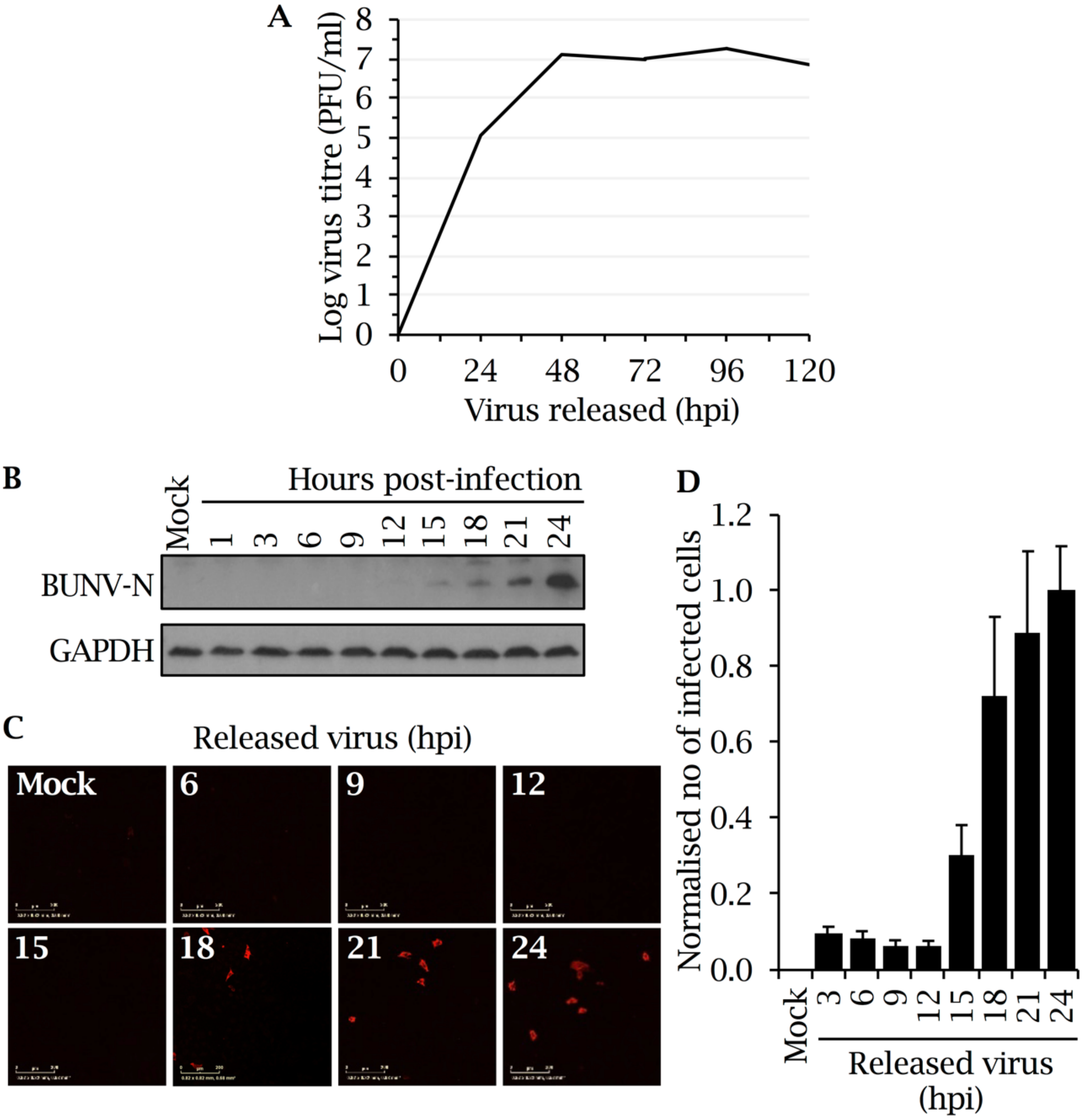

Figure 3.2 Investigating the timeline of BUNV infection

(A) A549 cells were infected with BUNV (MOI = 0.5) for 3 hrs, at which point remaining input virus was removed and fresh 2 % FBS DMEM was added. Virus-containing supernatant was collected at 24, 48, 72, 96 and 120 hpi. Virus titre was determined by plaque assay, where SW13 cells were re-infected with each sample at dilutions of 10^{-2} to 10^{-7} and plaques allowed to develop over 6 days, at which point cells were fixed and stained using crystal violet. Plaque numbers were quantified, titres were determined (PFU/ml) and plotted as a log scale of viral titre. **(B)** Time course of A549 cells infected with BUNV (MOI = 0.1) and lysed at increasing time points post-infection. Western blot analysis of BUNV-N and GAPDH (loading control) (n = 3). **(C)** Time course as in *(A)*, however cell supernatants were collected at each time point (hpi) and used to infect naïve A549 cells for 24 hrs. BUNV-N protein in re-infected cells was labelled using anti-BUNV-N antibodies alongside Alexa-Fluor 594 nm secondary antibodies. Widefield images taken on the IncuCyte Zoom, scale bar = 200 μm (n = 3). **(D)** Quantification of the number of fluorescent infected cells in *(B)* using IncuCyte software, normalised to the 24 hpi time point (mean of n = 3 ± standard deviation (SD)).

3.3 K^+ ions influence BUNV infectivity

3.3.1 pH 6.3 and K^+ mimic an endosomal cue for virion uncoating

The specific role of endosomal pH and [K^+] during BUNV entry has not been defined. To first address this, virions were incubated for 2 hrs at 37 ºC in a range of buffers that mimic the pH that BUNV virions would likely be exposed to during endosome transit (pH 7.3 to 5.3). Following treatment, buffers were diluted out with media and A549 cells were infected with the treated virions (MOI = 0.1) for 18 hrs; meaning any effects on BUNV virions would be elicited by direct effects on the virions during pre-treatment and not through changes to the cellular environment (Figure 3.3 A). For each experiment outlined, 'mock' indicates uninfected controls and 'control' indicates PBS treatment. Cells were lysed at 18 hours post-infection (hpi) and proteins were resolved by SDS-PAGE. Western blot analysis was performed and BUNV infection was assessed using antibodies targeting the BUNV-N protein (BUNV-N); an established method for quantifying BUNV multiplication (244,259). The standard 'housekeeping' protein GAPDH was additionally probed for to confirm equal gel loading.

Pre-treatment of BUNV virions at pH 7.3 or pH 6.3 caused no significant changes in BUNV-N expression (and thus BUNV infection) compared to control (PBS-treated) viruses, suggesting it did not influence the ability of BUNV to infect cells (Figure 3.3 B). Incubation at pH 5.3 however inhibited BUNV infection as no BUNV-N was detected. This suggested that structural changes in BUNV elicited by the low pH conditions prevented virions from infecting cells entirely (Figure 3.3 B). It is unclear however whether this treatment prevents virion binding to its receptor and subsequent internalisation, or if it prevents fusion processes occurring within endosomal compartments. Interestingly, pH 5.3 is that of LE/lysosomal compartments late in the endocytic network and may indicate that within cells BUNV is released prior to this stage, before reaching a highly acidic environment that inactivates the virus.

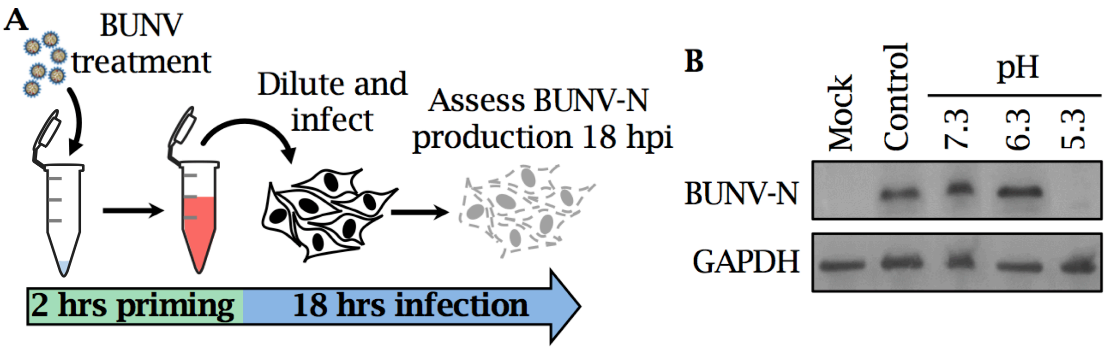

Figure 3.3 An acidic environment alone cannot prime BUNV for entry

(A) Schematic of BUNV priming, where virions are incubated pre-infection at 37 ˚C with buffers at varying pH for 2 hrs. Buffers were subsequently diluted out with media and A549 cells are infected with treated BUNV (MOI = 0.1) for 18 hrs prior to cell lysis. Western blot analysis was carried out with cell lysates using anti-BUNV-N protein and anti-GAPDH (loading control) antibodies. **(B)** Cells were uninfected (mock) or infected with BUNV treated with buffers at pH 7.3, 6.3, 5.3 or PBS controls (control). Cell lysates were analysed by western blot for BUNV-N, as described in *(A)* (n = 3).

Following this, the role of the increasing endosomal K^+ at each pH was investigated. BUNV virions were primed as above at each pH for 2 hrs in buffers with (+) or without (-) 140 mM KCl, and cells infected with the primed BUNV (MOI = 0.1) for 18 hrs (see previous schematic in Figure 3.3 A above). The salt KCl was used to supplement the [K^+] required. At pH 7.3, the addition of KCl led to a modest inhibition of BUNV production (Figure 3.4 A). Reducing the pH to 6.3 alone caused a decrease in BUNV infection without KCl, however a significant upregulation was observed when BUNV was pre-treated with 140 mM KCl (+). This data strongly suggests that BUNV virions at pH 6.3 require a high [K^+] to evoke virus priming. As with Figure 3.3 B, BUNV was completely inhibited at pH 5.3 irrespective of the addition of KCl.

To confirm that the effects of KCl are due to the K^+ and not the Cl^- ions, an identical experiment to that in Figure 3.4 A was performed but using NaCl instead of KCl. Interestingly however, the addition of NaCl caused identical effects on BUNV infectivity as those observed for KCl; little to no-change at pH 7.3 (with or without NaCl), reduced infectivity at pH 6.3 which was significantly upregulated by the addition of NaCl, and complete BUNV-N inhibition at pH 5.3 (Figure 3.4 B). The equivalent pattern of BUNV inhibition at pH 5.3 and at pH 6.3 without salt, alongside the BUNV upregulation at pH 6.3 plus KCl or NaCl treatment, suggests the mechanism causing BUNV upregulation is shared between either Na$^+$, K$^+$ or Cl$^-$ ions. In addition, quantification of the fold increase in BUNV-N comparing control to pH 6.3 '+' salt confirmed KCl enhanced BUNV infection 4.3-fold, greater than the 2.8-fold by NaCl (Figure 3.4 C).

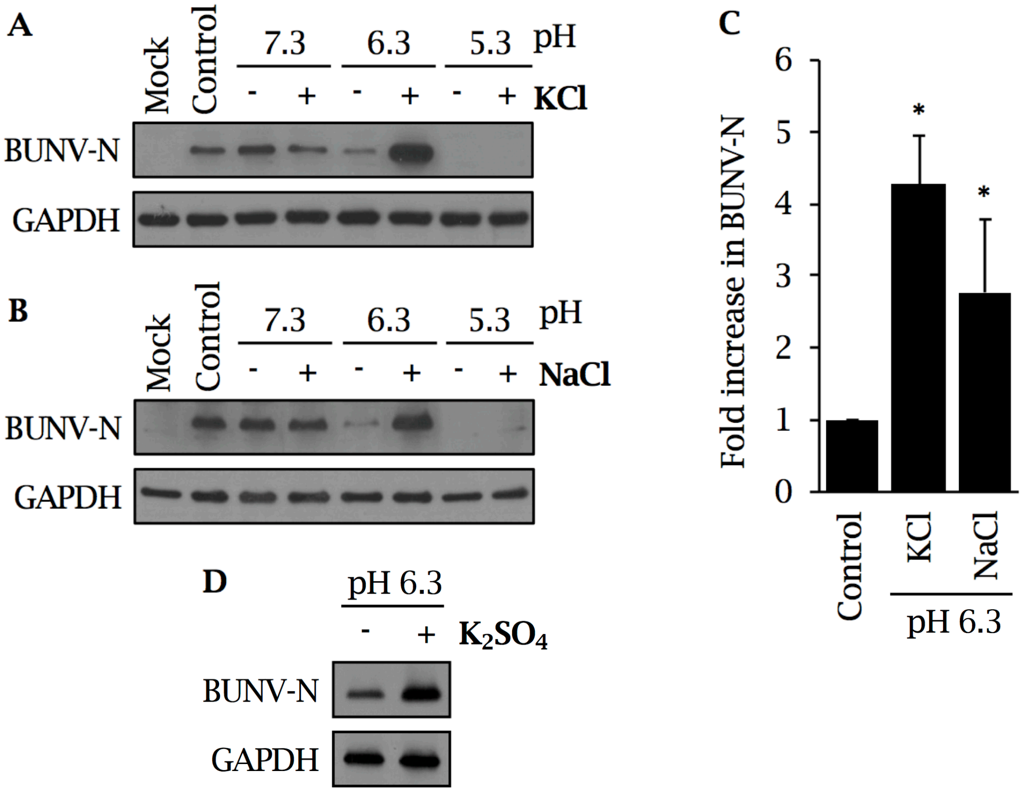

Figure 3.4 K$^+$ priming at pH 6.3 expedites BUNV infection

(A) BUNV was treated pre-infection using buffers with and without 140 mM KCl at pH 7.3, 6.3 and 5.3 and cells were infected with primed BUNV. Lysates were analysed by western blot as described in *Figure 3.3 (A)* (n=3). **(B)** As in *(A)*, however buffers were treated with or without physiological concentrations (120 mM) of NaCl, instead of KCl (n=3). **(C)** Quantification of n=3 western blots in *(A)* and *(B)*, normalised to each virus control (error bars represent the mean of n = 3 ± SD, * = $p<0.05$). **(D)** As in *(A)*, however virions were treated at pH 6.3 only with or without 140 mM K_2SO_4, instead of KCl (n=3).

As both salts used thus far contain Cl$^-$, a role for Cl$^-$ ions could not be conclusively ruled out at this stage, therefore it was essential to utilise an alternative K$^+$ salt to address the role of Cl$^-$. BUNV virions were treated as previous with buffers at pH 6.3 with (+) or without (-) 140 mM K_2SO_4; a non-Cl$^-$ K$^+$ salt. K_2SO_4 was able to successfully prime BUNV at pH 6.3 (Figure 3.4 D), confirming that Cl$^-$ ions are not facilitating the BUNV priming. This importantly ruled out Cl$^-$ ions as both KCl and K_2SO_4 prime BUNV, and thus established that

K^+ ions are facilitating the priming effect. It is likely that Na^+ also prime virions in this experiment as Na^+ and K^+ possess similar ionic radii (116 picometers (pm) vs 152 pm) and charge (both monovalent, 1+) (260). A virion however would never encounter an endosomal environment of low pH (6.3) and high Na^+, as Na^+ is rapidly removed from maturing endosomes; the opposite of K^+. As the NaCl induced priming was not physiological, further experiments to investigate the priming effects were performed with KCl.

To determine if the priming of BUNV with pH 6.3 + K^+ was specific to A549 cells, two other cell lines previously shown as permissive to BUNV infection were investigated. BHK-21 (BHK; baby hamster kidney) cells and SW13 (human adrenal carcinoma) cells were infected with pH 6.3 -/+ K^+ treated virions for 18 hrs (Figure 3.5 A & B). An increase in BUNV-N upon pH 6.3 + K^+ treatment was observed in both BHK and SW13 cells, confirming the effect is not specific to A549 cells. BUNV similarly requires K^+ channel function for infection of BHK and SW13 cells as the K^+ channel inhibitors TEA and quinidine (Qd) inhibited infection (Figure 3.5 C & D).

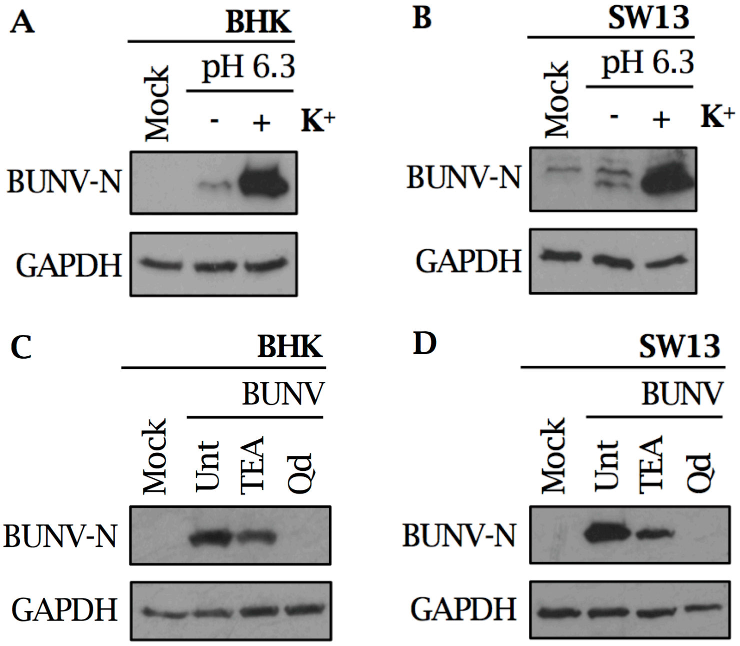

Figure 3.5 K^+ priming is independent of the cell type
(A) BUNV virions were treated with pH 6.3 -/+ 140 mM KCl and BHK-21 cells were infected for 18 hrs before lysis and western blot analysis (n=3). **(B)** As in *(A)*, for SW13 cells (n=3). **(C)** BHK-21 cells were pre-infection treated for 45 mins with TEA (10 mM) or Qd (200 µM). Cells were then infected with BUNV (MOI = 0.1) in presence of drug for 24 hrs. Cells were lysed and BUNV infection assessed by western blot (n=3). Non-toxic concentrations of TEA and Qd were used, as previously determined (244). **(D)** As in *(C)* using SW13 cells (n=3).

3.3.2 BUNV priming occurs at physiological [K$^+$] and causes irreversible changes

The intracellular [K$^+$] reaches approximately 150 mM in the cytoplasm, however [K$^+$] within endosomes is less well characterised and is difficult to assess, but is thought to increase from 5 mM to ~60 mM. As experiments were performed at 140 mM KCl, the effects of more physiological LE-like [K$^+$] were assessed and BUNV was primed at a range of KCl concentrations (5 to 140 mM). Figure 3.6 A shows clear virus priming at 140 mM conditions (pH 6.3, previously termed +). It was also evident that priming also occurs at 50 mM and 20 mM KCl to a similar extent as 140 mM KCl treated virus. This indicates that LE-like [K$^+$]s are able to prime BUNV. At 5 mM however, KCl reminiscent of EEs was not able to prime virions, further indicating LE conditions are required for virion uncoating. The fact that BUNV priming occurs to the same extent at 20, 50 and 140 mM KCl validates the use of 140 mM KCl in previous experiments.

The reversibility of this priming effect was next assessed by priming virions in pH 6.3 buffers – or + K$^+$ (140 mM KCl), diluting out buffer with media and incubating for 0-4 hrs prior to infection (18 hrs) (Figure 3.6 B). This allowed us to determine whether the changes induced in the virus would revert in the absence of priming buffer, within the timeframe of regular endosomal transit (<6 hpi). When BUNV-N was assessed at 18 hpi, priming was induced irrespective of post-priming incubations 0 to 4 hrs. This indicates that once priming changes have occurred at pH 6.3 + K$^+$, viruses do not revert back to their native state.

3.3.3 K$^+$ priming permits more efficient endosomal escape

At this stage, it was not known whether the K$^+$ priming increases virus infectivity and associated BUNV-N expression, or whether the 18 hpi timepoint of cell lysis for pH 6.3 + K$^+$ primed virus represents more efficient N production. The temporal expression of BUNV-N was therefore assessed to determine the time point N expression began for (pH 6.3) -K$^+$ versus +K$^+$ treated virions in the experiments that followed. BUNV was primed pH 6.3 – or + K$^+$ and A549 cells were infected for a range of time points from 12 to 24 hpi; as depicted in Figure 3.6 C. At 12 hpi BUNV-N was detectable in +K$^+$ treated samples but absent in -K$^+$ viruses (compare lanes 2-3, Figure 3.6 D). In the absence of K$^+$ priming BUNV-N protein was undetectable until 15 hpi (lane 4). BUNV-N was continually expressed to greater levels in +K$^+$ primed virus than those primed without K$^+$ (lanes 2-7), an effect which continued until 21 hpi at which point the expression of BUNV-N was comparable between primed and unprimed viruses (compare lanes 8-9). This was an important finding as it indicated that the primed virus does not produce higher levels of N protein, however possessed an expedited lifecycle, expressing BUNV-N at an earlier stage. Therefore, previously assessing the K⁺ priming effect at 18 hpi shows a snapshot of BUNV-N (the time of cell lysis), implicating pH 6.3 + K⁺ as a biochemical cue that increases the rate of BUNV infection.

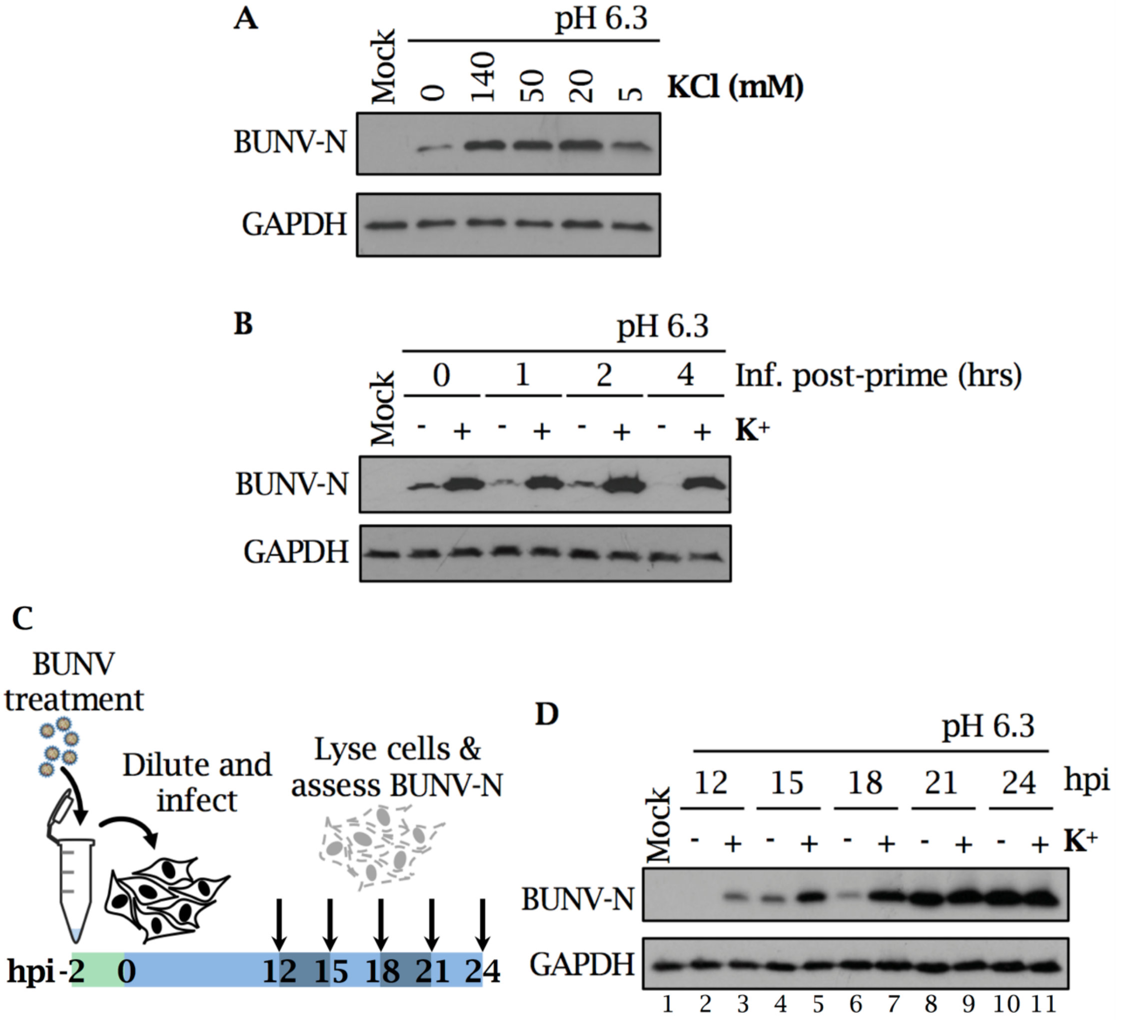

Figure 3.6 K⁺ priming occurs at physiologically relevant K⁺ and increases the rate of BUNV infection

(A) BUNV virions were primed as in *Figure 3.3 (A)* at pH 6.3 with a KCl concentration range from 0-140 mM. Buffers were diluted out and cells infected with virus for 18 hrs and lysed. Western blot for BUNV-N (n=3). **(B)** BUNV virions were primed as previous with pH 6.3 -/+ 140 mM KCl for 2 hrs. Post-priming, buffers were diluted out and virions maintained at 37 ºC for 0, 1, 2 or 4 hrs before infecting cells for 18 hrs. Western blot for BUNV-N (n=2). **(C)** Schematic of the BUNV priming time course, where BUNV virions are primed at pH 6.3 +/- KCl, A549 cells are infected with primed virus and lysed at increasing post-infection time points to assess BUNV-N production at each time point. **(D)** Virions primed and cells infected as in *(C)*. Western blot for BUNV-N (n=3).

3.3.4 K^+ primed virions are more resistant to host-cell K^+ channel inhibition

The data presented in this chapter thus far have shown a role of endosomal pH and K^+ ions during BUNV entry, which was pursued as the requirement for K^+ channels was predicted to be during endosomal transit. The increased efficiency of viral infection by pH 6.3 + K^+ treatment indicates a biochemical cue that could circumvent the requirement for K^+ channels during BUNV infection. This was tested experimentally by comparing BUNV inhibition using the broad spectrum K^+ channel inhibitor TEA; previously shown to inhibit BUNV infection (244). BUNV was primed at pH 6.3 -/+K^+ as previous for 2 hrs and during the final 45 mins A549 cells were treated with TEA (10 mM) prior to virus infection. Cells were then infected with primed virions and infection was allowed to proceed for 18 hrs prior to lysis, as depicted in Figure 3.7 A. Comparing pH 6.3 - K^+ (without K^+, lanes 2 and 4) without (-) to with (+) TEA drug treatment, a clear inhibition of BUNV infection was observed upon K^+ channel block consistent with previous data (Figure 3.7 B). It was interesting however that when comparing pH 6.3 + K^+ primed virions without (-) versus with (+) TEA (compare lanes 3 to 5), the inhibition of BUNV infection by TEA was less pronounced, indicating that the +K^+ primed virus is more resistant to K^+ channel inhibition. The levels of BUNV-N were not equivalent however, suggesting that K^+ channels were still required to some extent.

Another possibility was that BUNV virions can conduct K^+ across the envelope where K^+ facilitates priming inside the virion, as shown for the IAV M2 viroporin which conducts ions into the virion for capsid destabilisation (258). To confirm that TEA treatment was not inhibiting K^+ channels within the viral envelope or virus priming, BUNV was primed at pH 6.3 – or + K^+ however with the addition of 10 mM TEA (+) or H_2O as a control (- TEA) into the priming mix (schematic depicted in Figure 3.7 C). Buffer and drug were then diluted prior to infection of A549 cells for 18 hrs. In Figure 3.7 D the priming effect without drug in -/+ K^+ treated samples was clearly evident and the addition of TEA to the priming buffer did not prevent the effects of K^+. This confirmed that K^+ channel inhibitors prevent BUNV infection by acting on a host-cell factor and not a viral-factor, such as a virion associated viroporin. In addition TEA did not interfere with virion priming by K^+, therefore the partial inhibition of infection by the K^+ primed virus shown in Figure 3.7 B was also due to effects of TEA on host-cell K^+ channels.

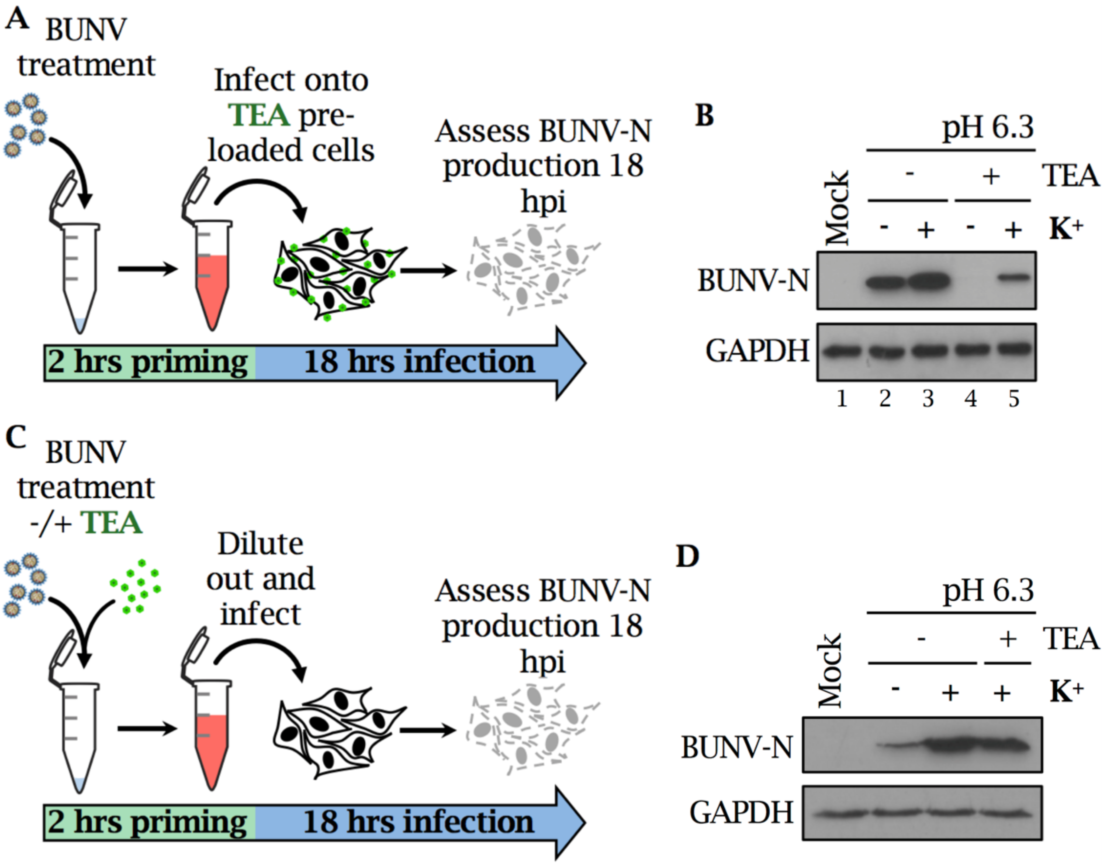

Figure 3.7 K⁺ priming reduces the BUNV sensitivity to K⁺ channel inhibition
(A) Schematic representation of the priming protocol as with *Figure 3.3 (B)*, however A549 cells were infected with pH 6.3 -/+ KCl primed-BUNV (MOI = 0.1). Cells were additionally pre-infection treated with (+) or without (-) 10 mM TEA (45 mins) which was maintained throughout infection (18 hrs). Cells were lysed at 18 hpi and analysed by western blot. **(B)** A549 cells were TEA treated, infected with BUNV for 18 hrs and lysed as in *(A)* (n=3). **(C)** Schematic of the priming protocol, where BUNV virions were primed pH 6.3 -/+ KCl and -/+ TEA (10 mM) pre-infection. Buffer and drug were diluted out prior to infection, which proceeded for 18 hrs before lysis and western blot as in *(A)*. **(D)** Virions were treated and cells were infected as in *(C)* (n=3).

3.4 Production of infectious dual-fluorescently labelled BUNV to track virus entry

After identifying that K⁺ channels are required for the early events of the BUNV lifecycle, and that K⁺ can influence virion infectivity, the next stage in this investigation was to visualise BUNV entry events. A dual-fluorescently labelled BUNV was produced to track virion movement through endosomal compartments and a dual-labelling system would be used to ensure intact virions were tracked, by colocalisation of the two spectrally distinct fluorophores. Two fluorescent dyes were selected, firstly a nucleic acid dye SYTO82 (em.$_{max}$ 560 nm) to label the three vRNPs, which has previously been used to visualise poliovirus entry (261). For successful labelling as vRNA is encapsulated within the N protein, labelling would need to occur during vRNA replication. Additionally, a lipid label DiD-vybrant (DiDvbt; em.$_{max}$ 665 nm) was selected to label the host-derived lipid envelope; previously used to label IAV virions (262). For DiDvbt labelling, released BUNV virions would require labelling and purification away from unincorporated dye.

The schematic in Figure 3.8 A demonstrates the procedure for the generation of fluorescent BUNV, where A549 cells were infected (MOI = 0.5) for 18 hrs, at which point the nucleic acid dye SYTO82 was added to cells. Addition at this time point allowed the labelling of nascent BUNV vRNA during the stage when BUNV-N expression was detectable (and thus BUNV replication would be expected to be occurring; see Figure 3.2 B). SYTO82 treatment continued up to 24 hpi, the point at which the release of infectious BUNV was high (see Figure 3.2 C & D). Released virions were collected in the supernatants and BUNV was concentrated using a double-iodixanol cushion. As BUNV is an enveloped virus, the lipid-specific DiDvbt stain was added to the concentrated virus fraction to label the host-derived lipid envelope. Ultracentrifugation on a 5-30 % iodixanol gradient purified the SYTO82/DiD-BUNV from unincorporated dye and impurities. All fractions were collected and analysed for the presence of infectious BUNV (Figure 3.8 A).

Infection of A549 cells with each fraction, alongside unlabelled BUNV was performed and BUNV-N expression (and thus successful BUNV infection) was assessed by western blot analysis. BUNV-N was highest in cells infected with Fraction 24 and 25, suggesting that these fractions contain the highest levels of infectious BUNV (Figure 3.8 B). Small quantities of BUNV-N were detected in fractions 22 and 23, which was unsurprising owing to their proximity to the highest BUNV-containing fractions. In addition a small quantity of BUNV-N was detectable in fractions 5 and 6, which also mark the top of the iodixanol gradient and are likely virions that have been unable to properly enter the iodixanol column. As fraction 28 represents the very bottom of the column, the presence of infectious virus was not assessed as these samples were expected to be impure. As BUNV-N expression was not detectable in cells infected with all fractions, the concentration of infectious BUNV was successful (Figure 3.8 B). For additional confirmation of these data, fractions 16-25 were assessed for BUNV infection using IncuCyte analysis of A549 cells infected with each fraction (Figure 3.8 C & D). Cells were infected for 18 hrs, fixed and stained for BUNV-N. Widefield images were taken identifying BUNV staining in cells infected with fraction 24, concomitant with the western blot results. A number of infected cells were also detected in fractions 23 and 25. Quantification of the number of fluorescent cells from Figure 3.8 C using IncuCyte software similarly identified infectious BUNV in fraction 24, with a significant number of infected cells, suggesting the labelling procedure did not impact virus infectivity (Figure 3.8 D).

To determine the titre of this virus, plaque assays were performed on SW13 cells using fraction 24 serial diluted from 10^{-2} to 10^{-4}, alongside a WT BUNV control and uninfected mock. All dilutions showed plaques where BUNV has lysed the cells and were of a similar size to individual plaques in the control (Figure 3.9 A). Control BUNV at 10^{-2} dilution however clearly contained more virus compared to the labelled-BUNV, as identified by a greater number of plaques in the control which overlapped. To determine the titre, the number of plaques in the 10^{-3} dilution were quantified as separate plaques had formed which are easily identified; yielding a titre of ~1x10^5 PFU/ml.

A549 cells were subsequently infected with purified BUNV to confirm dual-fluorescent labelling. Infection was allowed to proceed for 2 hrs and EGF conjugated to Alexa Fluor-488 (herein termed EGF-488) was added during the final 15 mins to allow identification of cells and the optimal plane for live imaging (channel removed in images) (Figure 3.9 B). Cells were live imaged 2 hpi and both DiDvbt and SYTO82 fluorescence signals could be identified that colocalised (white arrowheads). Line scan analysis was performed to assess fluorescence intensity across a given distance, where colocalisation of the two signals was confirmed by the overlapping peaks of fluorescence intensity in the same location (Figure 3.9 C). Zeiss software allowed the intensity to be mapped onto line scans, which confirmed the fluorescence intensity peaks came from the predicted virions. The diameter of the fluorescence signal can also be estimated at ~1-1.5 µm, which at this resolution is as close as is likely to be obtained for BUNV virions, which are ~0.1 µm (Figure 3.9 C, black arrowhead).

These data suggested that BUNV purification and labelling was successful. Analysis by western blot, immunofluorescence and plaque assay confirmed that the labelled propagated virus was infectious. Confocal microscopy subsequently indicated successful dual-labelling of virions in fraction 24, termed

SYTO82/DiD-BUNV, taken forward for subsequent experiments. Note that when this fraction was depleted, labelling and propagation was repeated alongside all confirmations outlined above.

3.4.1 BUNV entry can be visualised in live cells

The ability of SYTO82/DiD-BUNV to be tracked through endocytic compartments was first determined, by infection in the presence of EGF-488. Cells were incubated at 37 ºC for 20 mins to allow endosomal uptake and live cell images were taken at t = 20 mins (Figure 3.10). EGF can be clearly identified throughout the cell localised in small punctate vesicles with this time point most likely representing EGF internalisation into EEs (Figure 3.10 A). A SYTO82/DiD-BUNV virion could also be identified intracellularly within 20 mins where colocalisation was observed not only between SYTO82 and DiDvbt, but also with the EGF-488 (white arrowhead). This indicates BUNV enters EGF-positive EEs during endosomal transit into the cell. To additionally confirm virion movements in live cells, images were taken post-internalisation of a single virion every 20 secs (Figure 3.10 B). SYTO82/DiD-BUNV was initially localised to an EGF-positive compartment (white arrowhead), however the two appeared to diverge within 60 secs indicating the virion, compared to EGF uptake, could have taken a different route during endosomal transit. The virion was also clearly active within the cell as it moved very rapidly from its starting location (white arrowhead indicates initial virion position) and after 100 secs the virion had completely vanished. Although this disappearance was visualised multiple times it is unclear whether this was simply the virion moving out of the plane or represented fusion events previously described (262). The DiDvbt lipid dye is predicted to diffuse from the virion envelope onto the endosomal membrane upon a fusion event; leading to unquenching and a flash of fluorescence, prior to dilution across the endosomal membrane (262). This was however not observed in any of the assays outlined here. It is clear that the SYTO82/DiD-BUNV could be used to visualise virus entry, however the specific route of endosomal transit and fusion were yet to be determined.

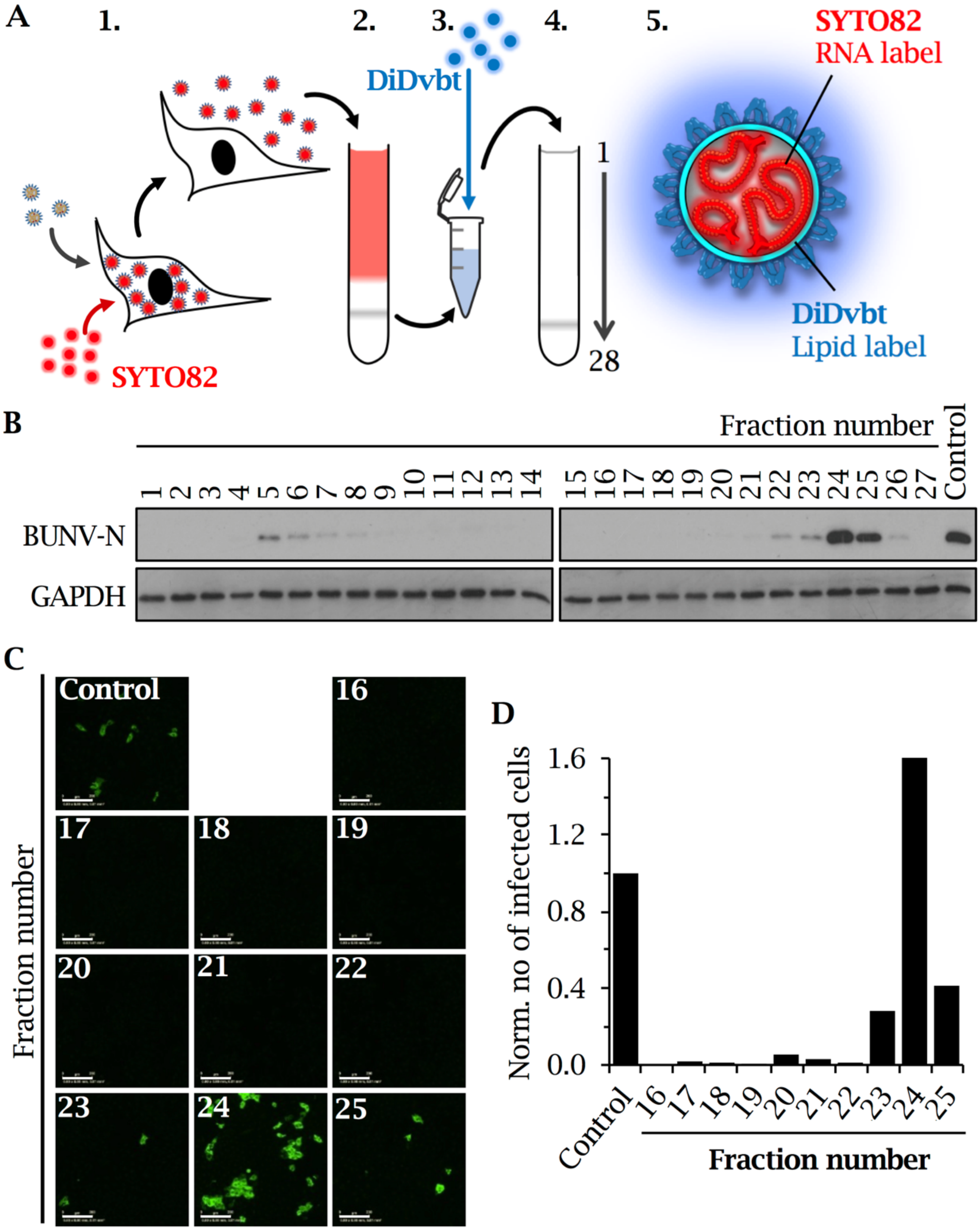

Figure 3.8 Propagation of dual-fluorescent labelled BUNV

(A) Schematic representation of BUNV labelling and purification. **1.** A549 cells were infected with BUNV (MOI = 0.5) and SYTO82 dye was added (18 hpi) to label the vRNA. Viral supernatants were collected at 24 hpi. **2.** BUNV was concentrated on a double-iodixanol cushion, **3.** viral lipid envelopes were labelled with DiDvbt and **4.** SYTO82/DiD-BUNV was purified on a 5-30 % iodixanol gradient. Fractions (x28) were collected. **5.** Virion structure indicating the location of each dye (n = 6). **(B)** A549 cells were infected with fractions from *(A)*, alongside a WT BUNV control (MOI = 0.1). Western blot analysis was carried out using anti-BUNV-N protein and anti-GAPDH (loading control) antibodies (n = 1, per purification). **(C)** Cells were infected with later fractions 16-25 as with *(B)*, BUNV-N protein was labelled using anti-BUNV-N and Alexa Fluor-488 antibodies. Widefield images were taken on the IncuCyte Zoom (scale bar = 300 µm). **(D)** Quantification of the number of fluorescent infected cells from *(C)*, normalised to the WT BUNV 'control' (n = 1, per purification).

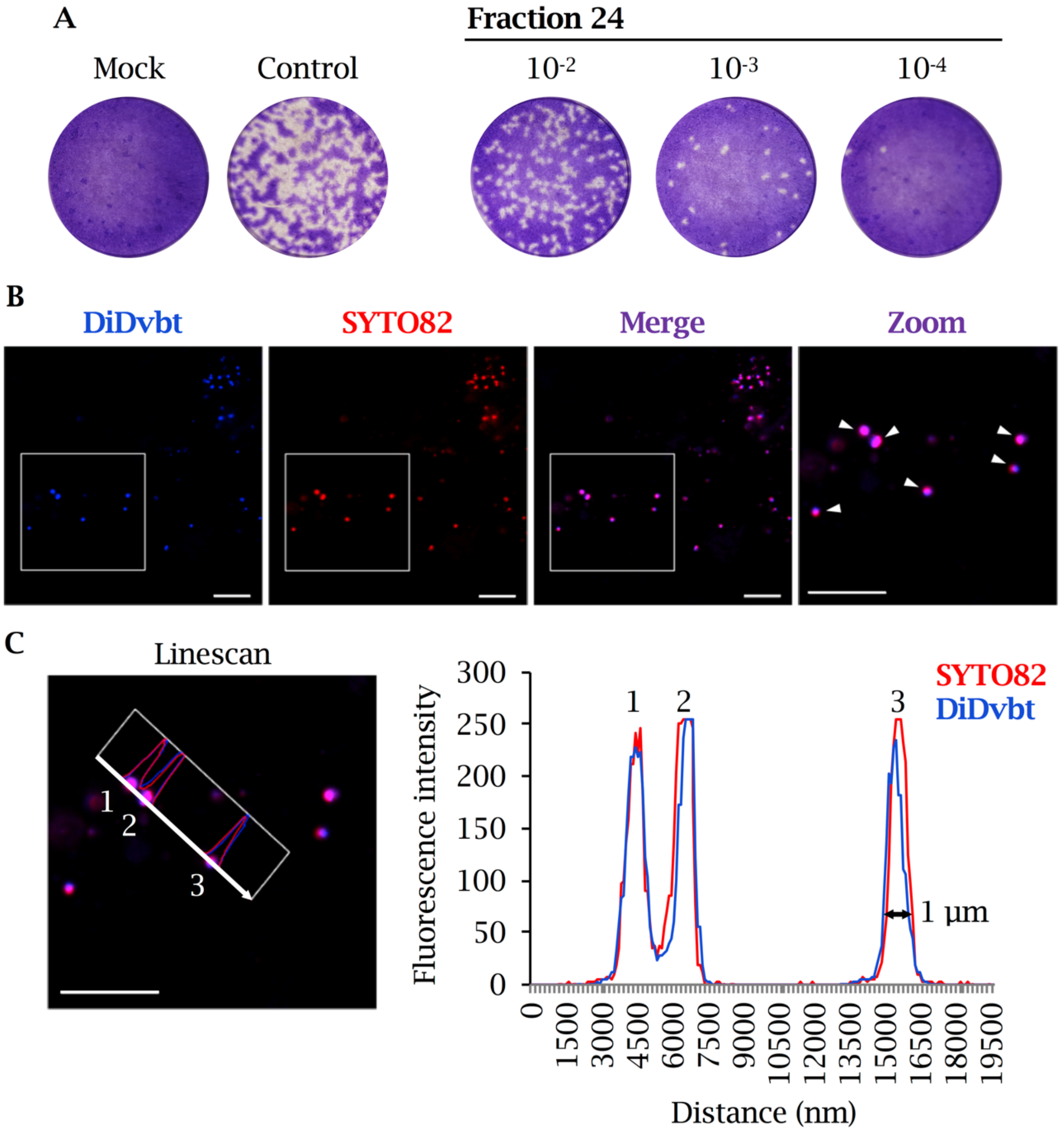

Figure 3.9 Labelled-BUNV is infectious and penetrates cells

(A) SW13 cells were infected with 10^{-2} to 10^{-4} serial dilutions of BUNV-containing fraction 24 for 1 hr; alongside an uninfected (mock) or WT BUNV (10^{-2}, control). Virus was removed and infected cells were incubated for 6 days covered with a methyl cellulose/DMEM overlay. Cells were fixed in 4 % PFA and stained with crystal violet. Plaques were counted and virus titre determined as ~$1x10^{5}$ PFU/ml (n = 2). **(B)** A549 cells were infected with labelled BUNV (MOI = 2) for 2 hrs, Alexa Fluor-488 conjugated EGF (EGF-488) was added during the final 30 mins to identify cells (fluorescence channel not shown). Cells were live imaged on an LSM700 confocal microscope, SYTO82 (em.$_{max}$ 560 nm) and DiDvbt (em.$_{max}$ 665 nm). Widefield and zoom images were taken and white arrowheads indicate colocalisation of SYTO82 and DiDvbt signals (scale bar = 10 µm). **(C)** Line scan analysis was performed on images from *(B)* using Zeiss Zen 2011 image analysis software, assessing the relative fluorescence intensity of each dye (SYTO82 & DiDvbt) at each location along a line; drawn on image. The 3 peaks (1, 2 and 3) can be mapped back onto the confocal image.

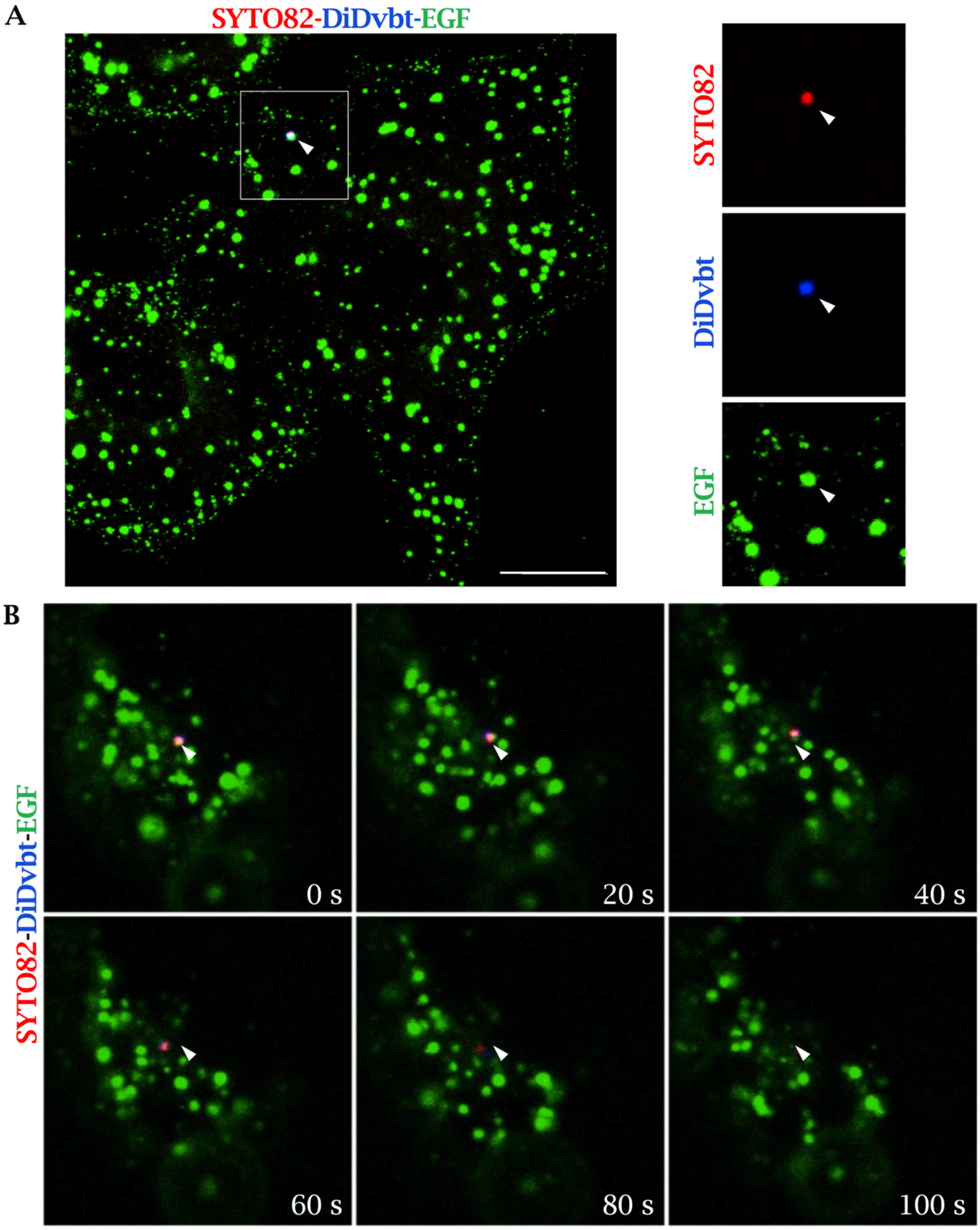

Figure 3.10 Internalised BUNV can be visualised in live cells and colocalises with internalised EGF

(A) A549 cells were infected with SYTO82/DiD-BUNV in the presence of EGF-488 (2 μg/ml; additionally acting as a cellular marker) at 4 ˚C to prevent internalisation. Cells were heated to 37 ºC and live imaged at t = 20 min (scale bar = 10 μm). White arrowheads indicate EGF-SYTO82-DiDvbt colocalisation. **(B)** Live tracking of an internalised virion, following *(A)*, imaging at t = 20 mins. Images were taken every 20 secs and white arrowheads indicate the starting position of a virion.

3.5 Defining the route of virion trafficking

It has been shown that BUNV is internalised into endosomes within 1 hr (244) and BUNV-N is detectable at 15 hpi (Figure 3.2 B). As virion fusion with endosomal membranes was difficult to assess in these assays, the number of virions within cells at increasing time points post-internalisation were assessed as a surrogate marker of endosomal escape. Virions were bound to the cell at 4 °C for 1 hr and then heated to 37 °C to synchronise entry. Images were collected at 2, 4 and 8 hpi where internalised virions were clearly identifiable at all time points (Figure 3.11 A). The number of virions also increased with time and at 8 hrs, a considerable number of virions were resident in endosomes. This indicated that virions are endocytosed and accumulate within endocytic compartments prior to their fusion and escape.

To confirm the timeline of endosomal transit, ammonium chloride (NH_4Cl) was used to inhibit endosomal acidification and hence prevent BUNV fusion events, as described for BUNV and LACV (123,125). Following NH_4Cl addition at defined time points post-BUNV infection complete inhibition of virus infection was observed at 0 hpi addition (Figure 3.11 B), low levels of BUNV-N were detectable at 1-4 hpi indicating BUNV had not traversed the endosomal system. At 6-10 hpi however BUNV began to recover, with BUNV-N expression recovering to control levels, suggesting resistance to NH_4Cl treatment at these time points. This indicated BUNV began to escape endosomes from 6 hpi, which is consistent with the timeline of K^+ channel requirement during the initial 1-4 hpi of virus infection (Figure 1.10). This further implicated the BUNV K^+ channel requirement during endosomal transit and fusion events.

3.5.1 BUNV enters late endosomes during entry

The endosomal compartments through which BUNV traffics were next investigated. EGF is endocytosed into EEs and trafficked to LEs, and represents an LE marker ≥45 mins post-addition (258,263). A549 cells were simultaneously loaded with EGF-488 and SYTO82/DiD-BUNV at 4 °C, then heated to 37 °C to synchronise entry. Live images were taken at 2 and 8 hpi, where SYTO82/DiD-BUNV localised to EGF-positive compartments (Figure 3.12 A, white arrows) indicating BUNV accumulates in LEs. This was confirmed with line scan analysis, where all three signals (EGF, SYTO82 and DiDvbt) colocalised at the same cellular location (Figure 3.12 B). To confirm LE accumulation, cells were transfected with GFP-tagged Rab7 LE marker (264), and infected with

SYTO82/DiD-BUNV (Figure 3.12 C). Live imaging at 2 and 8 hpi identified BUNV localisation within Rab7-GFP coated vesicles (white arrows), confirming trafficking to LEs.

3.5.2 BUNV does not traffic via recycling endosomes

The co-localisation with a recycling endosome (RE) marker was next assessed, using Alexa Fluor-488 conjugated transferrin ligand (Tf-488) which passes through EEs and into REs (265). Live imaging was performed on BUNV infected cells at 2 and 8 hpi, and minimal colocalisation between BUNV and Tf was observed at both time points (Figure 3.13 A, white arrow); suggesting that BUNV does not enter REs (violet arrows). Tf and BUNV (and EGF) did colocalise to low levels in earlier timepoints, likely reflecting the co-transit through EEs, however divergence into REs and LEs respectively; hence the limited colocalisation at these later time points (Figure 3.13 B). To confirm these finding, cells were transfected with Rab11-GFP to identify REs and infected with labelled BUNV (266). No colocalisation of BUNV in Rab11-containing vesicles at 2 or 8 hpi were observed. This further confirmed BUNV did not transit through REs and is likely to be trafficked with EGF into LEs, where it would encounter a reduced pH (6.3) which likely facilitates fusion.

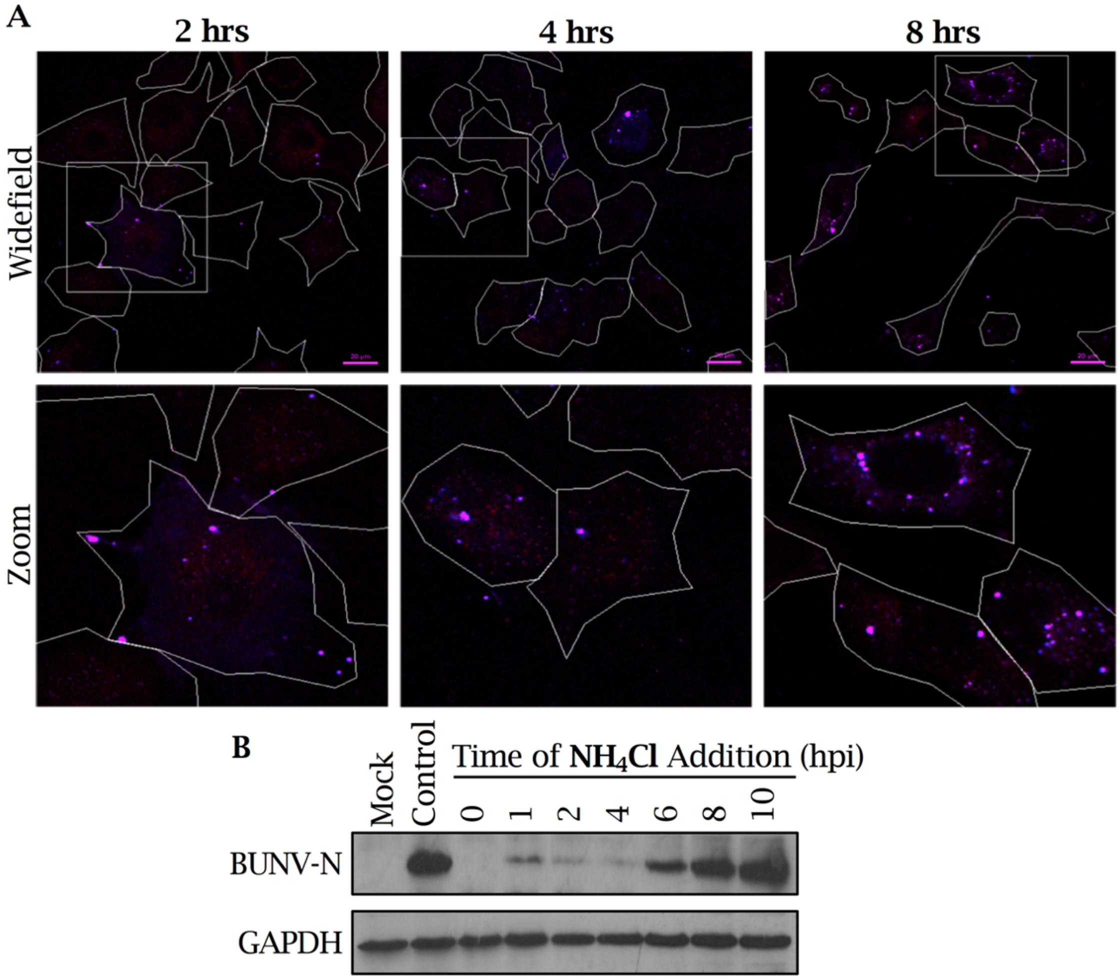

Figure 3.11 BUNV can be visualised in endosomes up to 8 hpi

(A) Cells were infected with SYTO82/DiD-BUNV at 4 ºC for 1 hr to permit surface binding, which were then heated to 37 ºC and EGF-488 was added for the final 15 mins to identify cells. Cells were fixed at the indicated time points (2, 4 and 8 hpi), confocal images were taken from ≥80 cells for each time point and the above are representative images with EGF-488 channel removed. White line indicates cell periphery (scale bar = 20 µm). **(B)** Time of addition assay using NH_4Cl (10 µM) added to cells at increasing times post-BUNV infection (MOI = 0.1) time points from 0 to 8 hpi. Cells were lysed at 24 hpi and BUNV-N expression was assessed by western blot (n = 3).

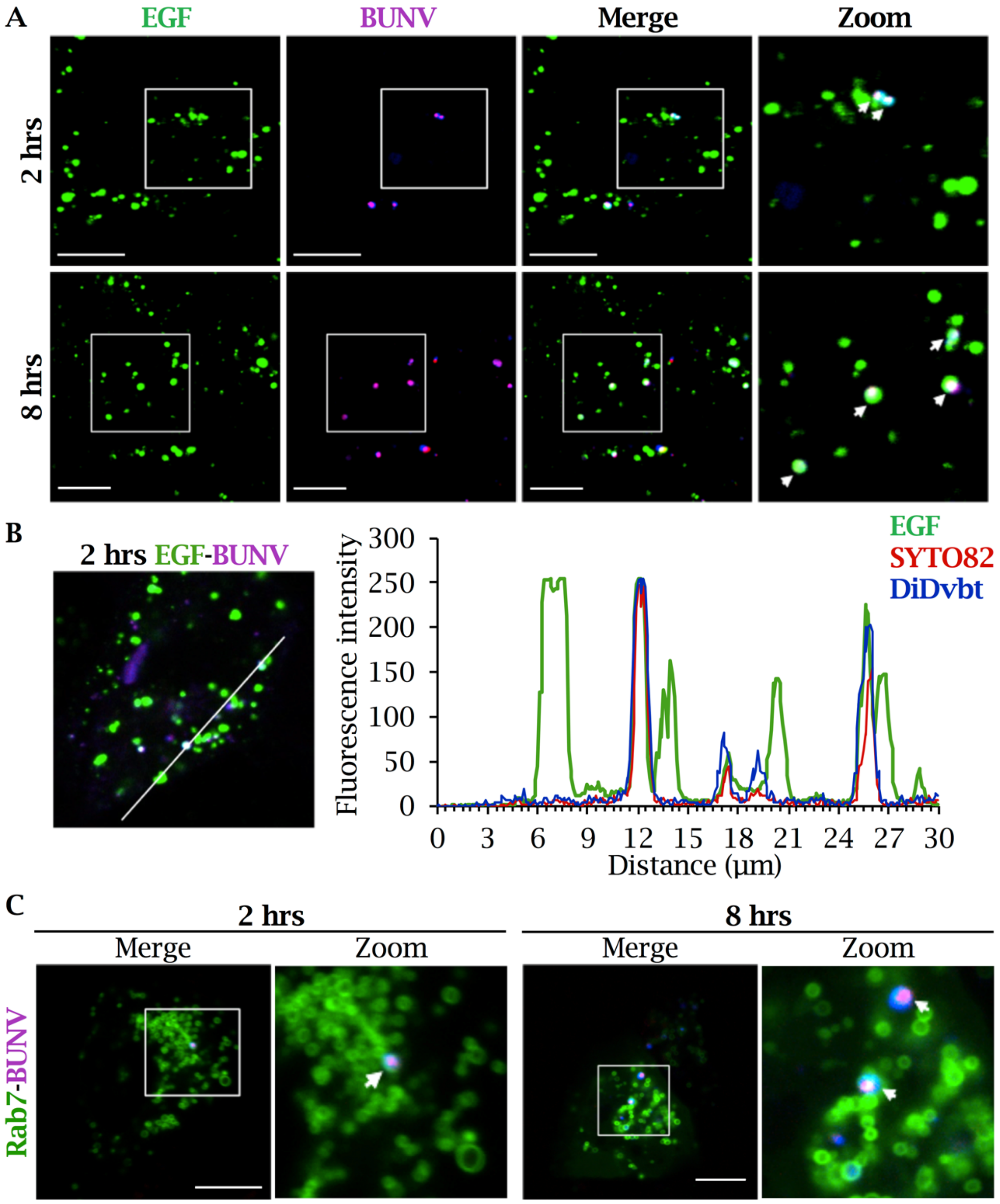

Figure 3.12 BUNV localises to late endosomes

(A) Cells were infected with SYTO82/DiD-BUNV for 1 hr at 4 ºC and simultaneously loaded with EGF-488 (2 µg/ml). Infection was initiated by warming to 37 ºC and live cell images were taken at the indicated time points post-infection. Representative images are shown from >60 cells, white arrows indicate EGF-BUNV colocalisation (scale bar = 10 µm). **(B)** Line scan analysis of an EGF-488 containing, SYTO82/DiD-BUNV infected cell from *(A)*, using Zeiss Zen 2011 image analysis software. Lines represent fluorescence intensity for each fluorophore; EGF-488 (green line), SYTO82 (red) and DiDvbt (blue). **(C)** Cells were transfected with Rab7-GFP 24 hrs prior to infection with SYTO82/DiD-BUNV as in *(A)*. Images were taken of >40 cells and representative images are shown (scale bar = 10 µm).

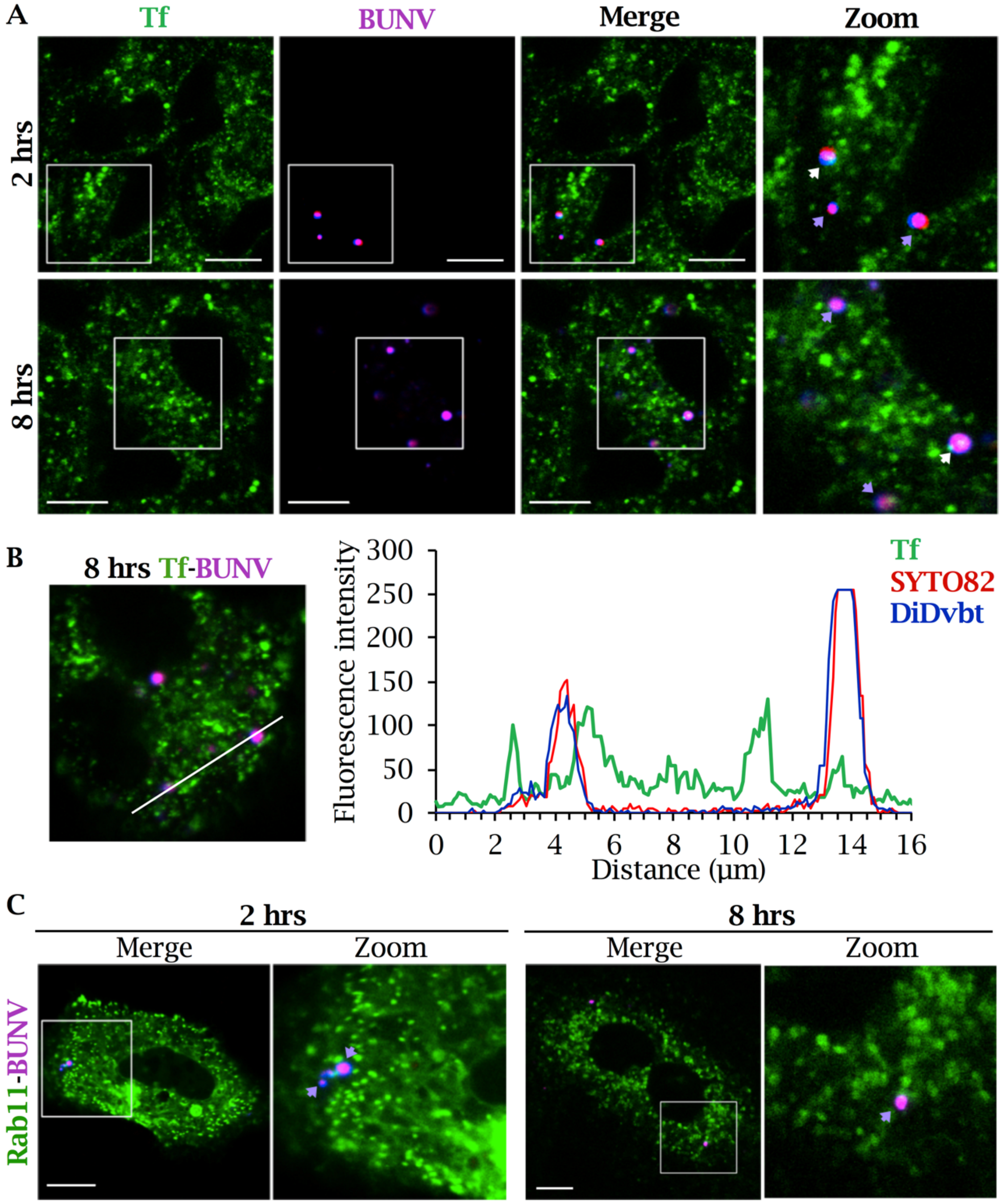

Figure 3.13 BUNV does not enter recycling endosomes

(A) Cells were loaded with biotinylated Tf-488 (25 µg/ml) and simultaneously infected with SYTO82/DiD-BUNV as in *Figure 3.12 (A)*. White arrows indicate Tf-BUNV colocalisation, violet arrows indicate BUNV virions (scale bar = 10 µm). **(B)** Line scan analysis of an infected, Tf-labelled cell from *(A)*. Analysis performed as in *Figure 3.12 (B)*. **(C)** Cells were transfected for 24 hrs with Rab11-GFP as in *Figure 3.12 (C)* and infected with SYTO82/DiD-BUNV as in *Figure 3.12 (A)*. Violet arrows indicate non-colocalised Tf and BUNV virions (scale bar = 10 µm).

3.6 BUNV traffics through high [K^+]-containing endosomes

[K^+] is known to increase with passage along the endocytic pathway and high [K^+] are present in LEs (258) (Figure 3.1). Owing to the requirement for K^+ channel function during the early stages of the BUNV lifecycle and the BUNV accumulation identified within LEs, the [K^+] within the endocytic system was further characterised. The membrane-impermeable K^+-specific fluorescent probe Asante potassium green-4 (AG4) was used to assess the [K^+] in endosomal compartments as previously described (258). When added to cells AG4 is taken up into endosomes and fluoresces when bound to K^+, increasing at higher [K^+]. Figure 3.14 A (panel 1) shows fluorescent puncta within cells which correspond to high-[K^+] containing endosomes. AG4 uptake was only identified when added at 37 ºC (panel 2) however not at low temperatures (4 ºC, panel 3) which prevent endosomal uptake, confirming the endosomal nature of these fluorescent puncta.

The specific location of high-[K^+] endosomes was next determined using markers for specific endosomal compartments. The schematic in Figure 3.14 B demonstrates the endosomal uptake of AG4 alongside the Texas-red-conjugated EGF used to label LEs and Magic Red Cathepsin B (MR) used to label lysosomes. Magic Red fluorescence is unquenched when cleaved by cathepsin B, which is predominantly active within lysosomes (Ex/Em = 550/610 nm) (267,268). The dotted grey bar indicates the predicted rise in [K^+] through endocytic compartments and is expected to be highest within lysosomes. AG4 was added with each marker for 40 mins, at which point non-internalised markers were removed by washing and cells were live imaged (Figure 3.14 C). The most intense AG4 puncta, representing areas of high K^+ colocalise with EGF-containing vesicles (row 1, white arrows) indicating that [K^+] is high within LEs, as previously described (178). Interestingly, AG4 did not localise to the same level with Magic Red suggesting that lysosomes do not contain high [K^+] (Figure 3.14 C, row 2). When quantified (Figure 3.14 D) this revealed ~46 % AG4 localised to LEs (EGF) compared to ~10 % AG4 within lysosomes (MR). This suggested that the [K^+] increases with passage along the endocytic pathway, peaking in LEs, and decreasing in lysosomes; as depicted in Figure 3.14 B.

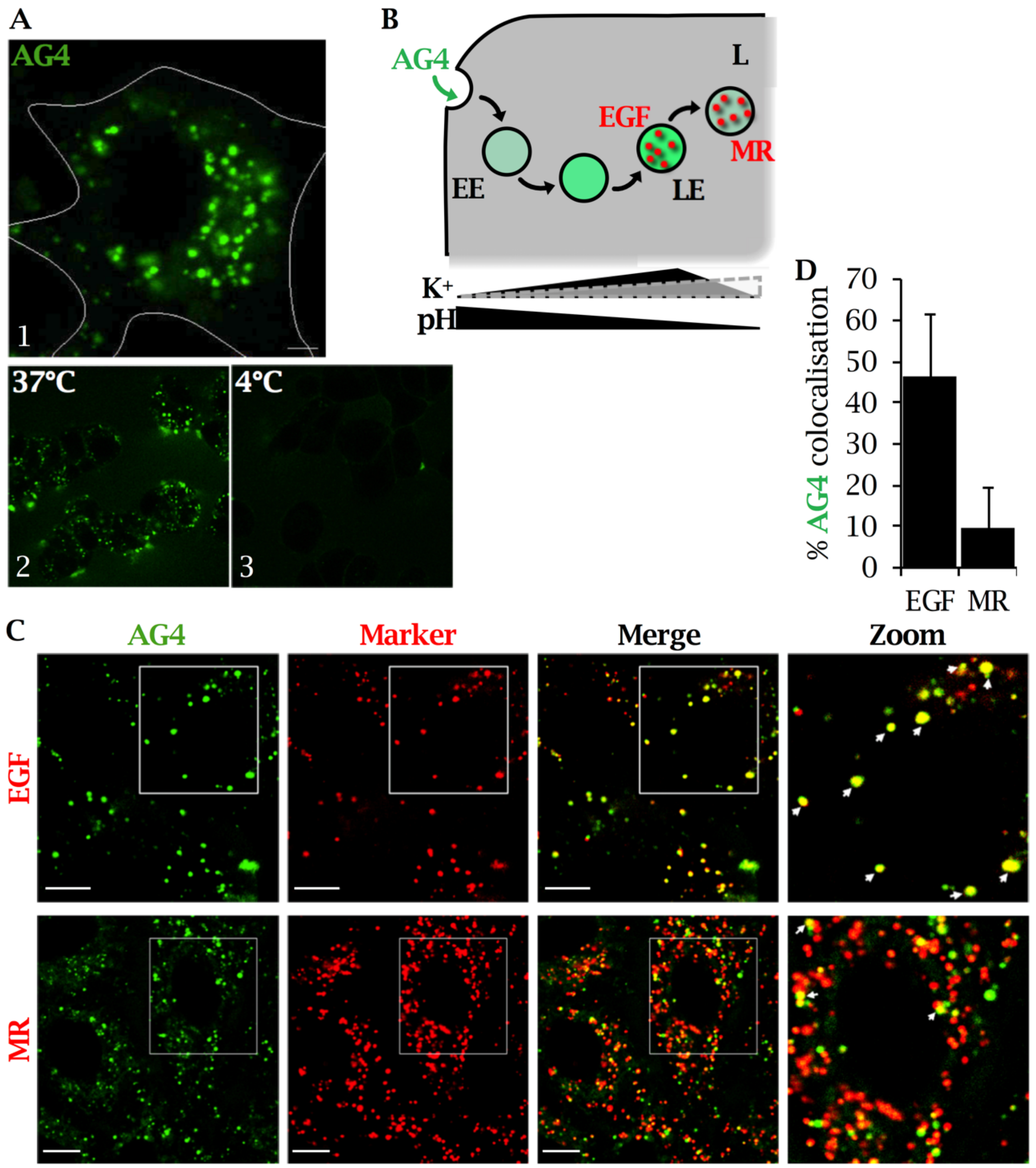

Figure 3.14 Endosomal [K$^+$] can be assessed using a K$^+$-sensitive dye AG4 and is high within late endosomes

(A) 1. AG4 was added to cells (10 µM) for 40 mins and live imaged (scale bar = 5 µm). White line indicates the cell periphery. **2.** AG4 was added at 37 °C for 40 mins to internalise into cells. **3.** AG4 puncta were not observed when AG4 was added at 4 °C, confirming endosomal uptake (247). **(B)** Schematic identifying AG4 fluorescence in K$^+$-rich compartments, where [K$^+$] increases with passage through EEs into LEs and lower is within lysosomes (L); black K$^+$ bar. Texas-red labelled EGF was used to label LEs and Magic Red (MR) to label lysosomes. The grey K$^+$ bar indicates previously predicted [K$^+$] across the endosomal system (178). **(C)** AG4 was added to cells with markers of LEs (Texas-red conjugated EGF) and lysosomes (Magic Red, MR) for 40 mins to allow endosomal uptake. Non-internalised dyes were removed and cells live imaged, >100 cells. White arrows indicate AG4-cell marker colocalisation (scale bar = 10 µm). **(D)** Number of AG4 puncta co-localising with EGF or MR were counted per cell from *(C)* and expressed as a percentage of the total number of AG4 puncta per cell (>100 cells ± SD).

As [K$^+$] expedites BUNV infection, the association of virions with high-[K$^+$] containing endosomes was investigated. Cells were infected with SYTO82/DiD-BUNV and simultaneously loaded with AG4. Live imaging at 2 and 8 hpi revealed significant colocalisation of BUNV-AG4 (Figure 3.15), indicating BUNV transits through endosomal compartments of high [K$^+$]. These compartments are likely the [K$^+$]-rich LEs identified in Figure 3.14. These data confirm that BUNV encounters high [K$^+$] during its endosomal trafficking.

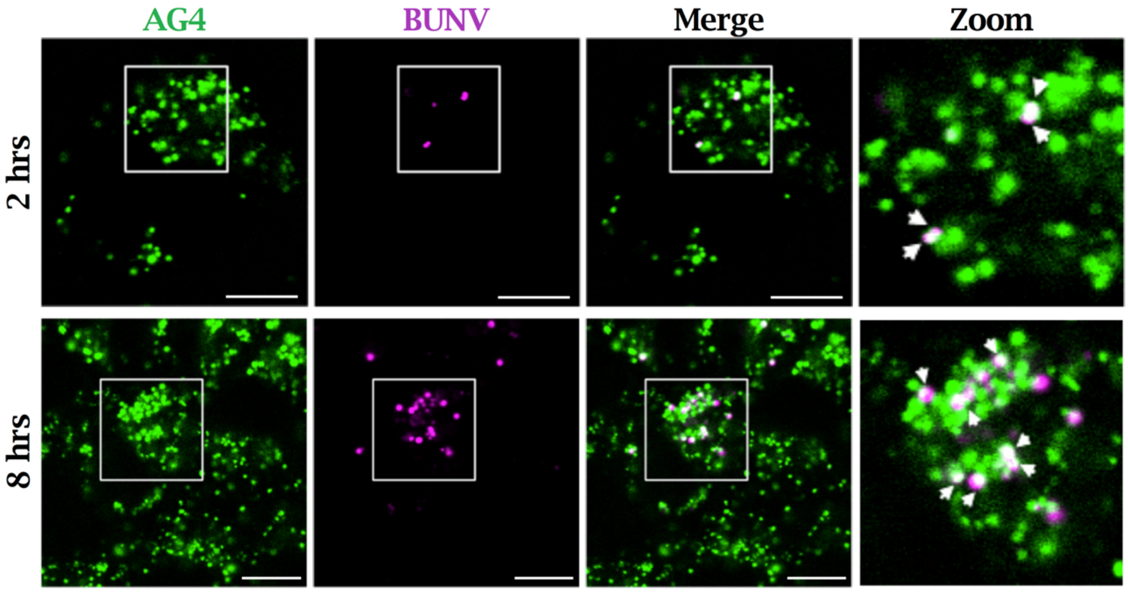

Figure 3.15 BUNV traffics through sites of high endosomal [K$^+$]

Cells were simultaneously loaded with AG4 (10 µM) and SYTO82/DiD-BUNV for 1 hr at 4 °C and warmed to 37 °C and imaged at the indicated time points in live cells; 2 or 8 hpi. Representative images are shown from >30 cells. White arrows indicate AG4-BUNV colocalisation (scale bar = 10 µm).

3.7 K$^+$ channel modulators influence the K$^+$ distribution across the endosomal network

K$^+$ channels control the selective passage of K$^+$ ions across cell membranes, but their role in the endosomal accumulation of K$^+$ has not been defined. To investigate whether K$^+$ channel activity contributes to these processes, the total fluorescence of AG4 and Magic Red was assessed in cells treated with the K$^+$ channel inhibitor TEA. No differences were observed in AG4 fluorescence when K$^+$ channels were inhibited (TEA), confirmed by quantification of total AG4 fluorescence intensity using IncuCyte Zoom software (Figure 3.16 A). This indicated K^+ channel inhibition did not interfere with total levels of endosomal K^+. Similarly K^+ channel inhibition did not interfere with lysosome formation, as similar intensities of Magic Red were identified upon TEA treatment (Figure 3.16 B). This also confirmed that TEA caused no drastic alterations to the endosomal system.

As TEA did not prevent $[K^+]$-rich endosome formation, it was reasoned that K^+ channel inhibition may delay the accumulation of endosomal K^+. To investigate this, cells were similarly untreated (Unt) or treated with TEA (10 mM), then simultaneously loaded with AG4 and Magic Red for 40 mins in the presence of drug and live imaged. As previously shown, when K^+ channels are active (Unt) AG4 puncta show minimal colocalisation with Magic Red positive lysosomes (Figure 3.16 C, panel 1 'Unt'). Upon addition of TEA, AG4 staining was still evident in puncta throughout the cytoplasm, however regions of high AG4 fluorescence were observed to colocalise with Magic Red positive lysosomes (Figure 3.16 C, panel 2 'TEA', white arrows). This indicated that the high endosomal $[K^+]$ had shifted from LEs, into lysosomes, in the face of K^+ channel inhibition. Quantification confirmed this finding, where TEA treatment increased AG4-lysosome colocalisation from ~10 % to ~36 % (Figure 3.16 D).

To confirm these findings, K^+ re-localisation was assessed using a pH-sensitive dye pH-rhodamine red dextran (pHRodo) the fluorescence of which increases with increasing H^+, or decreasing pH, concomitant with endosomal maturation (173,269). In untreated cells, pHRodo was visible as distinct puncta, identifying vesicles of low pH. As expected there was colocalisation with AG4 (Figure 3.17 A, panel 1 'Unt'), as the pH of LEs is ~6.3. When K^+ channels were inhibited, there was increased localisation with more acidic compartments further suggestive of K^+ accumulation within lysosomes (Figure 3.17 A, panel 2 'TEA'). This was confirmed in quantifications of >60 cells and increased from ~38 % to ~60 % (Figure 3.17 B). This confirmed the prediction that K^+ channels maintain the endosomal K^+ distribution and that channel inhibition slows the accumulation of K^+, where the high-$[K^+]$ is shifted into lysosomes (Figure 3.17 C).

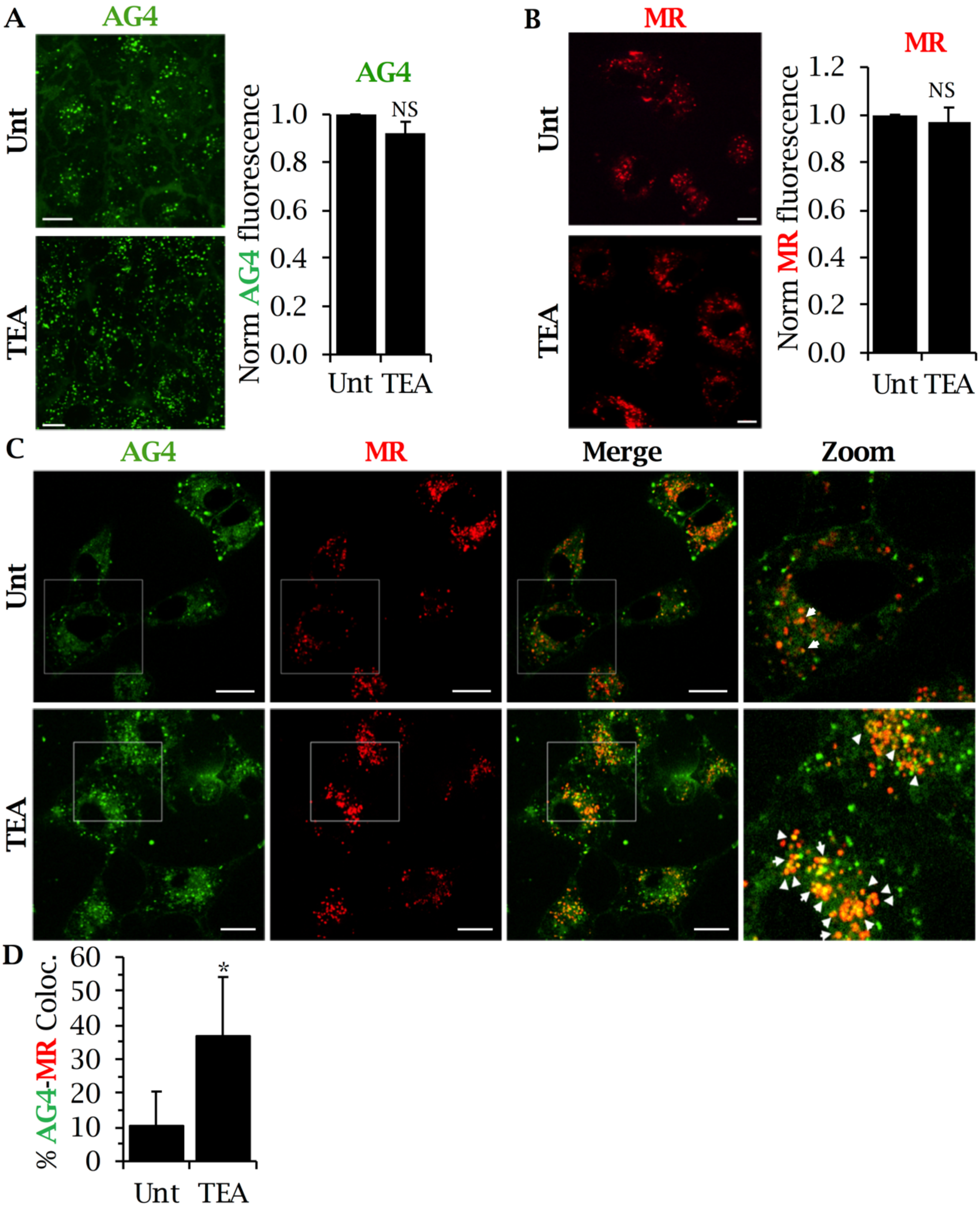

Figure 3.16 K^+ channel inhibition disrupts the distribution of endosomal [K^+]

(A) Cells were treated with TEA (10 mM) or left untreated (Unt) for 30 mins, prior to addition of AG4 (10 µM) with drug still present for 40 mins. Non-internalised dye was removed and live images were taken on a confocal microscope (scale bar = µm). AG4 fluorescence intensity was subsequently quantified and fluorescence was normalised to the Unt control. Averages were obtained from three independent repeats (mean ± SD), NS = non-significant difference in intensity ($p<0.05$). **(B)** As in *(A)*, however loaded with MR lysosomal dye +/- TEA. Images were taken on a confocal microscope and quantification performed as in *(A)*. **(C)** Cells were treated as with *(A)*, in the presence (TEA) and absence (Unt) of 10 mM TEA maintained throughout imaging. AG4 and MR were loaded simultaneously onto cells and incubated for 40 mins prior to live imaging (>60 cells, scale bar = 10 µm). **(D)** Total number of AG4-MR colocalised puncta in *(C)* were quantified and normalised to the total number of AG4 puncta per cell (* = $p\geq0.05$) [performed by S Hover and B Foster].

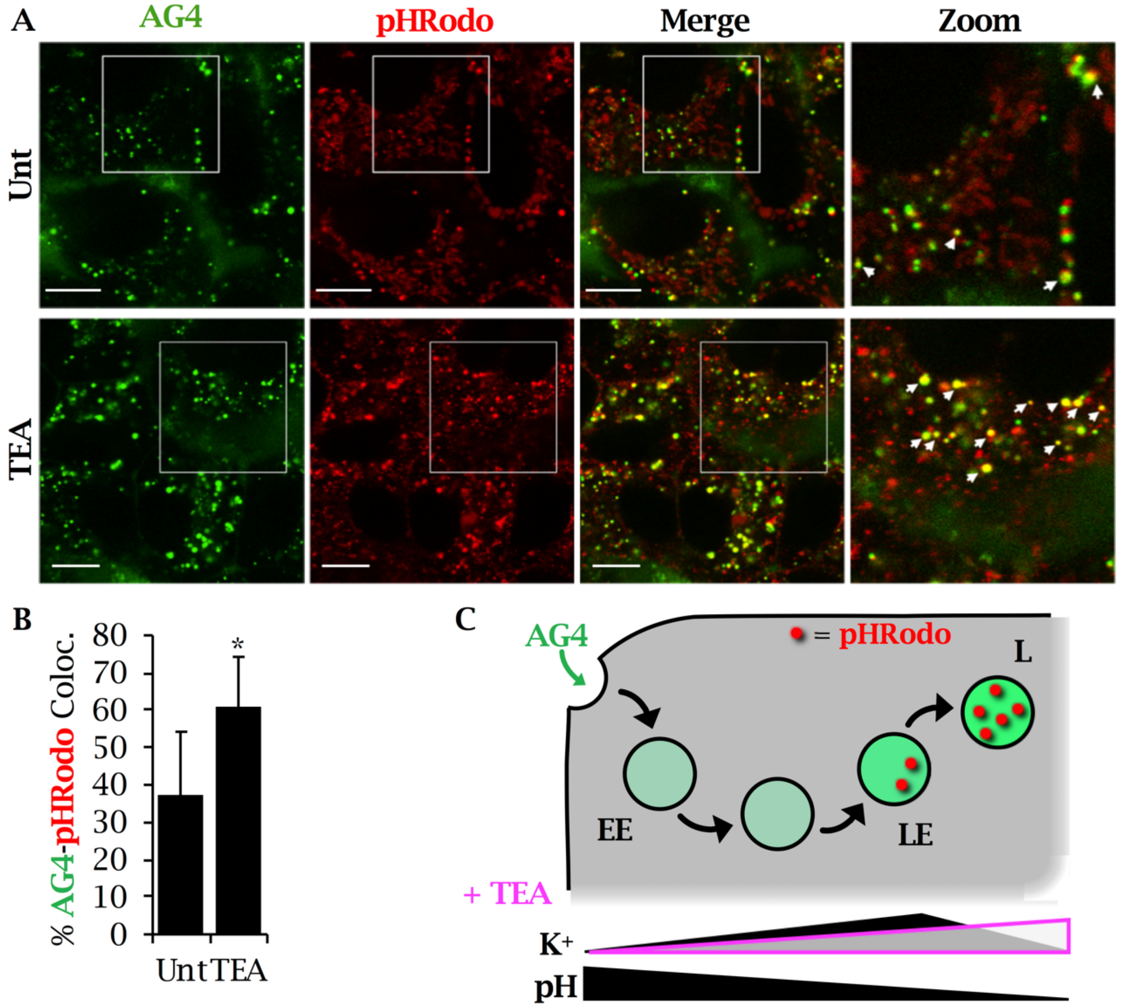

Figure 3.17 Disruption of endosomal [K$^+$] by K$^+$ channel blockade confirmed using an alternative pH-sensitive dye

(A) Cells were pre-treated with TEA (10 mM) or Unt control, then loaded with AG4 and pHRodo (10 µg/ml) as in *Figure 3.16 (C)*. Cells were live imaged at 40 mins and images are representative of >60 cells (scale bar = 10 µm). **(B)** Quantification of % AG4-pHRodo colocalised puncta from *(A)*, as was performed in *Figure 3.16 (D)* (mean of n = 3 ± SD, * = $p \leq 0.05$). **(C)** Schematic representation of the [K$^+$] shift upon TEA treatment, where pHRodo is predominantly localised to lysosomes (L) and significantly more AG4 [K$^+$]-rich puncta localise to lysosomes when cells are TEA treated [experiments performed by S Hover and B Foster].

3.8 BUNV endocytic processes are disrupted by K^+ channel inhibition

As K^+ channel modulation alters the endosomal K^+ distribution, it was reasoned that channel modulation would also affect BUNV endocytic processes. To confirm that BUNV was still able to penetrate cells upon K^+ channel inhibition, and hence confirm a post-penetration stage requiring K^+ channel function, cells were TEA treated or untreated (Unt) for 30 mins prior to infection with labelled-BUNV; EGF-488 was added in the final 15 mins to identify cells. Cells imaged at 4 hrs post-infection identified the presence of internalised SYTO82/DiD-BUNV within cells (Figure 3.18 A, white arrows). This confirmed previous data that established BUNV is still able to internalise into endosomes in the face of K^+ channel modulation (244). Z-stacks of EGF-488 and SYTO82/DiD-BUNV containing cells were also obtained and 3D image reconstructions additionally confirmed virion penetration (Figure 3.18 B). This data confirmed that K^+ channel modulation was not required for initial BUNV internalisation, but may play a role during BUNV trafficking and release.

To investigate this, cells were treated with TEA and infected with SYTO82/DiD-BUNV to examine virion endocytosis at increasing time points post-infection. As previously demonstrated (Figure 3.11 A) the number of virions within endosomes increased between 2 and 8 hpi, which similarly occurred upon TEA treatment (Figure 3.19 A). Upon comparison to the Unt, it was clear that the number of virions was significantly higher upon K^+ channel inhibition. As DiDvbt fluorescence signals are predicted to disappear upon fusion and genome release (262), this suggested virions were trapped within endocytic compartments, particularly at 8 hrs. To confirm this finding, a second broad spectrum K^+ channel inhibitor Qd was assessed as in Figure 3.19. Comparable accumulation of endocytic virions was observed at 8 hpi upon Qd treatment (Figure 3.19 B). Quantification of the number of virions at 8 hpi in TEA and Qd treated cells additionally confirmed these observations, where TEA elicited a ~2.7-fold increase in the number of virions and Qd a ~3.1-fold increase (Figure 3.19 C). These data suggest that endocytic escape was inhibited by K^+ channel inhibition, however the fate of ‘trapped virions’ required confirmation.

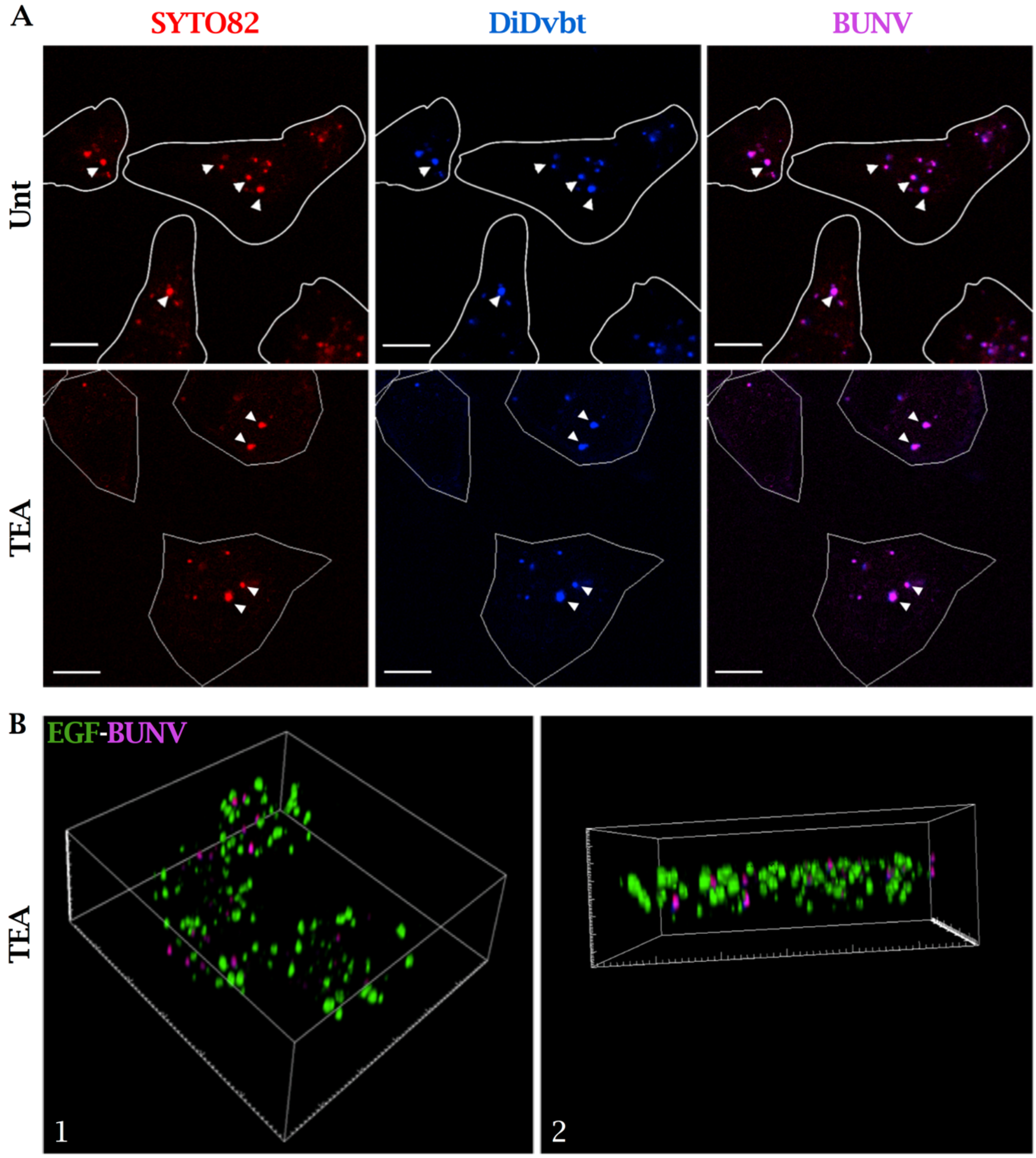

Figure 3.18 K^{+} channel inhibition does not prevent BUNV internalisation into endosomes

(A) Cells were treated with TEA (10 mM) of left untreated (Unt) for 30 mins, prior to infection with SYTO82/DiD-BUNV for 4 hrs. EGF-488 (2 µg/ml) was added 15 mins and cells were fixed at 4 hpi, followed by confocal imaging. EGF-488 was used to identify cells and was removed from representative images (>40 cells). White line indicates cell periphery and arrows indicate virions within cells (scale bar = 10 µm). **(B)** TEA treatment and SYTO82/DiD-BUNV infection was performed as in *(A)*, EGF-488 was added 1 hr prior to fixation at 8 hpi. Z-stacks were obtained and 3D reconstructions were generated using ICY software; panels 1 and 2 show two rotations of the same Z-stack.

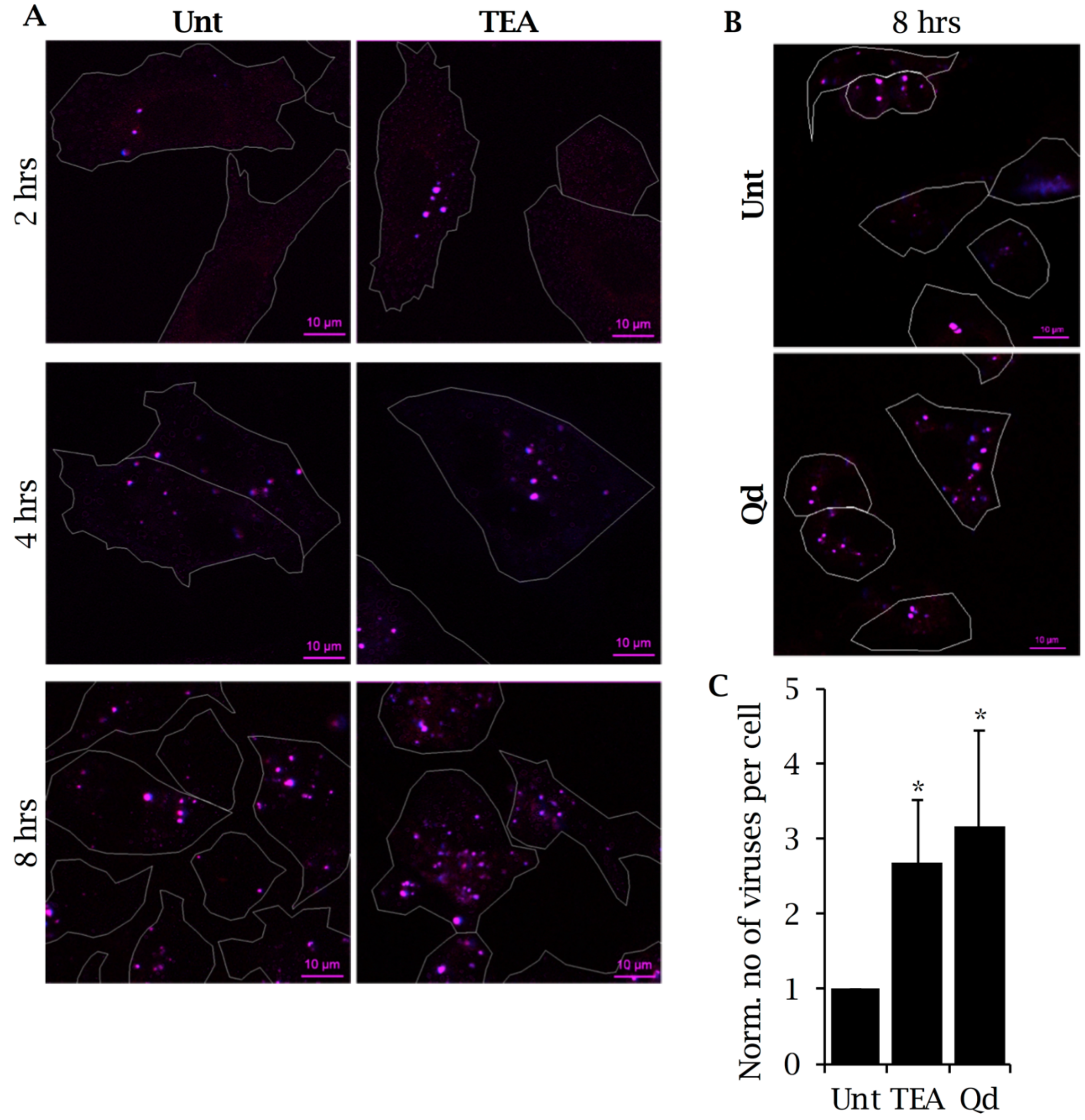

Figure 3.19 K$^+$ channel inhibition leads to the endosomal accumulation of virions

(A) A549 cells were TEA treated (10 mM) or untreated (Unt) as in *Figure 3.18 (A)* and infected with SYTO82/DiD-BUNV. EGF-488 (2 µg/ml) was added (to identify cells) 15 mins prior to fixation at 2, 4 or 8 hpi. Representative images from >65 cells are shown, with EGF-488 removed. White line indicates cell periphery (scale bar = 10 µm). **(B)** As in *(A)*, however cells are pre-infection treated with Qd (200 µM), instead of TEA. Images were taken from cells (>65 cells) fixed at 8 hpi. **(C)** Quantification of number of virions per cell at 8 hpi from TEA treated *(A)* and Qd treated *(B)* cells, normalised the Unt control (mean ± SD, * = p≤0.05).

As [K^+] distribution shifts into lysosomal compartments upon K^+ channel inhibition, the localisation of SYTO82/DiD-BUNV to lysosomes was assessed; BUNV was previously identified within LEs at 6 hpi (Figure 3.12). A lysotropic, membrane-impermeable dye, CytoPainter (CytoP), was use to label lysosomes as its fluorescence (Ex/Em = 490/525 nm) was spectrally distinct to SYTO82 and DiDvbt. Upon cell contact CytoP is taken up into endosomes and follows the pH gradient accumulating within lysosomes, at which point fluorescence significantly increases (Figure 3.20 A) (270). Cells were left untreated (Unt) or TEA treated, and then CytoP was added to cells simultaneously with SYTO2/DiD-BUNV. In untreated cells, imaging at 8 hpi revealed green fluorescent CytoP puncta identifying lysosomal compartments (Figure 3.20 B, 'Unt'). In addition, minimal colocalisation of SYTO82/DiD-BUNV virions within CytoP-labelled lysosomes was identified (colocalisation was identified as white puncta of the three overlapping signals, CytoP-SYTO82-DiDvbt). This indicated that BUNV traffics through EEs and into LEs, however is unlikely to enter the highly acidic lysosomes. In contrast, when K^+ channels were inhibited, SYTO82/DiD-BUNV accumulates to higher levels within CytoP-containing lysosomes where significantly more colocalisation was observed (Figure 3.20 B). This was confirmed by quantifying the number of SYTO82/DiD-BUNV virions colocalised with CytoP puncta, revealing an increase from ~13.5 % to ~45.1 % upon TEA treatment (Figure 3.20 C).

The build-up of virions within lysosomes indicates that K^+ channel inhibition prevents endosomal escape, likely due to the altered [K^+] distribution, where virions are instead trafficked to lysosomes for degradation. This provides a potential mechanism for how K^+ channel modulation prevents BUNV infection, as BUNV is inactivated by the acidic environment of lysosomes (pH ~5.5).

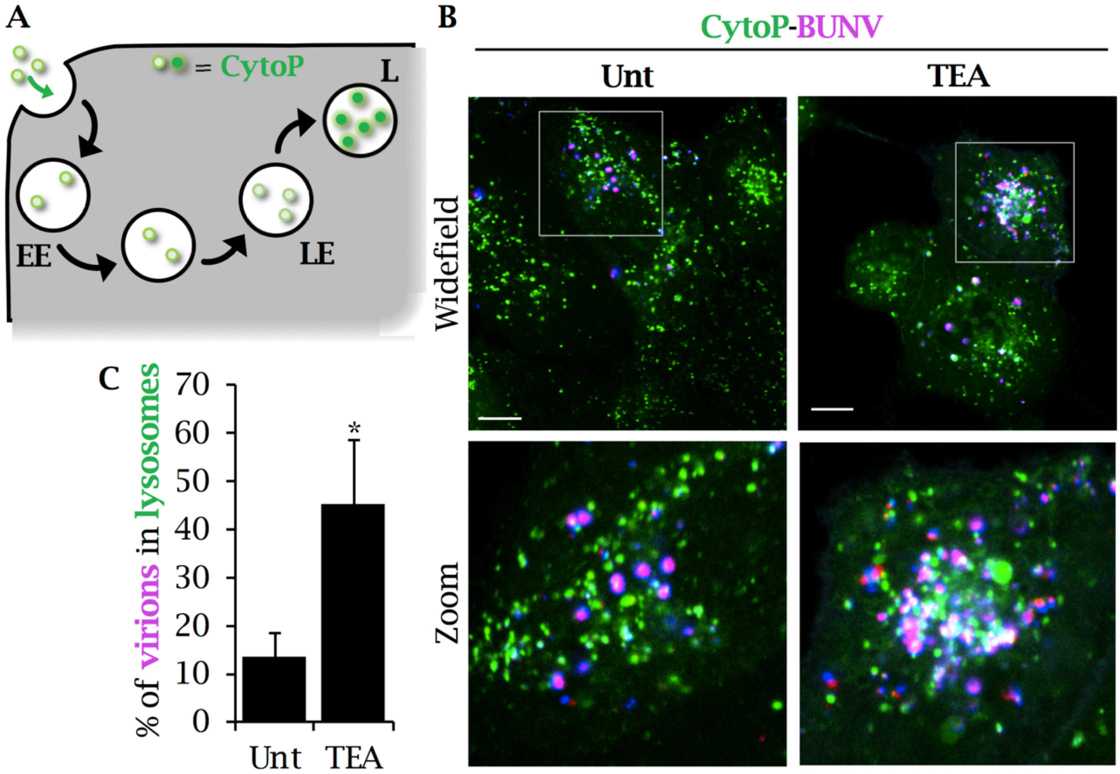

Figure 3.20 K^+ channel inhibition causes BUNV to accumulate in lysosomes
(A) Schematic showing CytoPainter (CytoP, Abcam) uptake into endosomes. This hydrophobic, lysotropic dye (271) localises to lysosomes (L) where fluorescence increases significantly upon reaching lysosomes. **(B)** Cells were pre-infection treated with TEA (10 mM) or untreated (Unt) for 30 mins, then simultaneously loaded with CytoP and SYTO82/DiD-BUNV for 1 hr at 4 ºC. Cells were warmed to 37 ºC and live imaged at 8 hpi. Images were taken (>80 cells each) and representative images are shown (scale bar = 10 µm). **(C)** Quantification of BUNV-CytoP colocalised puncta for each condition in *(B)*, as a percentage of total number of virions per cell (mean ± SD, * = $p \leq 0.05$).

3.9 Discussion

The requirement of host-cell K^+ channels, which are ubiquitously expressed in all cells, for BUNV infection was previously identified and this dependence is shared across other bunyaviruses; namely SBV (*Peribunyaviridae* family) and HAZV (*Nairoviridae* family). Using time-of-addition assays with TEA (Figure 1.10), an early requirement for K^+ channel function during BUNV infection was identified (244). This implicated a role for K^+ channels in BUNV endocytic trafficking, virion-endosome membrane fusion for vRNP release, vRNP transport to replication sites in the Golgi, or viral factory formation. A role for K^+ channels during replication was previously discounted in replicon assays, consistent with these findings. As endo/lysosomal roles for ion channels are emerging, the aim of this chapter was to investigate the role of K^+ channels in virion endosomal trafficking, membrane fusion and vRNP release from endosomal compartments. The data presented reveals a requirement for not only K^+ channels, but also endosomal $[K^+]$ in BUNV endosomal escape.

3.9.1 BUNV is trafficked through EEs and accumulates in LEs during entry

Limited studies have been performed to identify the route of BUNV (Peribunyavirus) trafficking upon entry. The entry of CCHFV (Nairovirus) was characterised by *Shtanko et al* (2014), who identified that CCHFV virions traffic through Rab5-positive EEs and MVBs. CCHFV vRNPs were further shown to be released from MVBs, requiring components of the endosomal-sorting complex required for transport (119). Studies on the Phlebovirus UUKV showed that virions traffic to lysosomes through their association with VAMP3, an essential pre-requisite for vRNP release (257).

In this study, the production of dual-labelled BUNV allowed the route of BUNV to be monitored. The dual-labelled virus was produced by labelling the genomic vRNA segments with SYTO82 during virus production, and following virus purification of released SYTO82-labelled BUNV, the viral envelope was labelled with a spectrally distinct fluorophore DiDvbt. It was verified that labelling did not interfere with normal BUNV processes since the dual-labelled BUNV was indistinguishable from WT virus in terms of its infection kinetics, as measured by the accumulation of BUNV-N protein and plaque assay (Figure 3.8 & Figure 3.9). Confocal microscopy of cells infected with SYTO82/DiD-BUNV allowed the visualisation of internalised BUNV virions which could be tracked in live cells (Figure 3.10). SYTO82/DiD-BUNV was tracked into EGF-positive vesicles at 20 min post-internalisation and, at this timepoint, *Kornilova et al* (1996) demonstrated that EGF bound to EGFR is primarily localised to EEs, but not LEs or lysosomes (272). Thus the early colocalisation of SYTO82/DiD-BUNV and EGF may represent transit through EEs, which is corroborated by the limited colocalisation with Tf, which also transits through EEs during entry. Although the low levels of colocalisation with Tf and Rab11 indicates that virions do not follow Tf/Rab11 into REs (Figure 3.13). Instead virions follow the route of EGF, where significant colocalisation is identified at 2 and 8 hpi indicating virions are rapidly endocytosed, trafficked to and accumulate within LEs for up to 6 hrs prior to release (Figure 3.12), unlike CCHFV. This was also indicated by the observed build-up of virions over time and limited colocalisation with lysosomes, indicating that fusion occurs prior to progression into these highly acidic compartments (Figure 3.11 and Figure 3.20), unlike UUKV. Despite efforts to visualise fusion and uncoating, the disappearance of fluorescence signals was too ambiguous for its definitive definition as a fusion event. The different trafficking routes co-opted by BUNV compared to CCHFV and UUKV may indicate different biochemical cues for uncoating. However, it would be interesting to investigate the role of endosomal [K^+] especially considering the Nairovirus HAZV similarly requires K^+ channels for infection (244).

3.9.2 Ionic balance in endosomes dictates BUNV infectivity

Viruses employ different triggers to initiate membrane fusion events, typically involving low pH or host interactions, such as receptor binding, at neutral pH (273). For many enveloped viruses, including bunyaviruses, a low pH elicits structural changes required for virion fusion and subsequent interaction of the virion structural proteins with host membranes, initiating viral-host membrane fusion and vRNP release. Bunyavirus fusion is facilitated by the Gn/Gc GPs and research into LACV identified that a low pH environment mediates oligomerisation and major conformational changes in Gc, exposing hydrophobic ectodomains (106,122,274). This allows the hydrophobic domains in Gc to insert into target membranes exposing Gn to protease cleavage (122,126). For Type I integral membrane proteins, subsequent conformational changes pull the two membranes into close proximity, initiating fusion (274). For bunyaviruses this has not been mechanistically defined.

In this study, treatment of BUNV virions at pH ~6.3, reminiscent of EE-LEs, and a high KCl (140 mM) concentration dramatically increased the rate of virus infection (primed virion BUNV-N protein production began at 12 hpi, as opposed to 15 hpi (WT), Figure 3.6). As these conditions were only present for the 2 hr pre-infection treatment and not during infection, the resultant upregulation is predicted to be due to direct changes in the virions that enhance their infectivity. Whilst it is unclear how K^+ facilitates these changes, these data reveal that acidification may not be the only trigger for BUNV release. As shown for Gn/Gc cathepsin protease cleavage in LACV entry and the presence of cholesterol in target membranes for Hantavirus fusion (106). In agreement with these findings, priming of IAV by *Stauffer et al* (2014) identified a second priming stage in entry after virion acidification, requiring pH <6.0 and high [K^+]s. Conditions which altered the interactions between IAV vRNPs and the M1 protein were required for efficient core destabilisation and virion uncoating (258). Unlike IAV and other negative RNA viruses, bunyaviruses lack a viral matrix protein (such as the IAV M1 protein) that stabilises the virus core by interacting with vRNPs; however the Gn cytoplasmic tails of BUNV interact directly with vRNPs within the virion membrane (75). It is therefore speculated that K^+ may facilitate the uncoating of BUNV and release the vRNPs from Gn binding, reminiscent of core destabilisation in IAV infection. This may explain the presence of BUNV virions in cellular vesicles rich in K^+ identified in Figure 3.15.

Of note, an increase in BUNV infectivity was also generated by pre-treatment with high NaCl (Figure 3.4). Na^+ and K^+ possess similar atomic radii and BUNV may not easily distinguish these ions (260). This is contrast to IAV, where 120 mM Na^+ had no effect on virus priming; the ionic requirements of BUNV may therefore differ to IAV. In this regard, it is interesting to note that the K^+ influx into IAV virions is mediated by the M2 viroporin, which like cellular ion channels can select for K^+ over Na^+ owing to the selectivity of the channel pore (275). BUNV has no known viroporin but given the requirement of reduced pH concomitant with the effect of these ions, a pH-mediated alteration of the BUNV virion surface, such as those previously shown to occur for the Gn/Gc GPs, may facilitate K^+ entry into BUNV virions promoting virion destabilisation and enhancing BUNV infection (106). Alternatively low pH may not facilitate K^+ entry into virions and instead K^+ acts upon the external Gn/Gc GPs to aid structural changes required for membrane insertion and fusion (see Chapter 4). Importantly, priming by Na^+ can be excluded as Na^+ is rapidly removed from maturing endosomes, therefore it is not physiologically relevant as BUNV would not encounter an endosomal environment of low pH and high $[Na^+]$.

In this regard, some viruses have been shown to require acid-priming for infection and undergo two priming stages for efficient entry. IAV infection requires initial priming at pH <6.5, followed by the second stage at a pH <6.0 with a high $[K^+]$, both of which are essential prior to virus-host membrane fusion at pH <5.5 (258). Additionally, two-step acid-activation is predicted for successful vaccinia virus (VACV) fusion in endosomes (276). Similarly to our BUNV-priming experiments, *Townsley and Moss* (2007) acid-treated VACV virions at pH 6.0, which increased infectivity 10-fold. It was subsequently identified that infection was still inhibited by blocking endosomal acidification (NH_4Cl) despite virion activation (276). Interestingly, when VACV virions were adsorbed onto target cells and then acid-activated (rather than prior to host-cell contact), infection was unaffected by inhibition of endosomal acidification. It is predicted that an initial rate-limiting acid-activation step is required, and a subsequent second low-pH step is required following membrane binding, which mediates membrane fusion (276). Acid-treatment prior to host membrane binding may cause conformational changes too early in the VACV lifecycle, preventing binding to host-cell factors required to initiate fusion events. In the experiments outlined above, infection by pH/K^+ primed-BUNV was importantly more resistant to K^+ channel inhibition (however, still somewhat sensitive), indicating K^+ priming of BUNV within endosomes is mediated by K^+ channels. Virions pre-treated with K^+ therefore do not require channel function to the same extent as they have already encountered this [K^+] (Figure 3.7). K^+ channels are still required to some extent, indicating that BUNV may (similarly to VACV and IAV) carry out two-step priming during entry into host cells requiring a high [K^+] at both stages, where the second stage could take place after interaction with an unknown host-cell factor. Future work would seek to investigate this using a two-step priming protocol varying pH and [K^+] timings, similar to *Townsley and Moss* (2007) and *Stauffer et al* (2014) (258,276). Acid-bypass experiments could be performed whereby primed virions are adsorbed onto the cell surface and the ability to fuse at the plasma membrane can be assessed, identifying if an additional cellular/endosomal factor is required.

3.9.3 K⁺ channel modulation alters endosomal K⁺ accumulation

It has long been established that the progressive acidification of endosomes is essential for normal function, with the neutralisation of the luminal pH (for example by treatment of cells with NH_4Cl) preventing cargo transport and the formation of intraluminal vesicles required for efficient cargo sorting (173,277). More recently, it has been identified that luminal ion concentrations are regulated across the endocytic network (173). Whilst this ion movement is difficult to assess (due to the internal localisation and small size of endocytic compartments) by classical techniques such as patch clamp analysis, it is known that multiple ion transporters, channels and exchangers function within endo/lysosomes to control the luminal ionic milieu; the dysfunction of which can lead to defects in endo/lysosome pH and lysosomal storage-disorders (173). Multiple Cl^- channels have been identified within endo/lysosomes (e.g. ClC3 and ClC7), that function to increase luminal Cl^- concentrations through the exchange of two Cl^- ions for one H^+ ion. Other ion transporters and channels abundant in endo/lysosomes include the transient receptor potential Ca^{2+} channels (mucolipins), Na^+/H^+-exchangers and the TPC (Ca^{2+}) channels; previously shown to be required for EBOV entry (173,236).

Despite the requirement for ion flux in endo/lysosome function, a role for specific K^+ channels is still developing. The luminal [K^+] exhibits a 10-fold or greater predicted increase with endosomal maturation, from ~5 mM to ~60 mM, from EEs through to lysosomes (173,258). Here, using the membrane-impermeable K^+ dye AG4, vesicles containing a high [K^+] were identified within A549 cells (Figure 3.14 A). Furthermore, vesicles with a high [K^+] did not colocalise with Magic Red positive lysosomes, indicating that the [K^+] increases with maturation into LEs, and decreases upon lysosome formation (Figure 3.14 B-D). Inhibiting K^+ channel function however with the known K^+ channel blocker TEA, correlated with a change in K^+ distribution and shifted the high [K^+] to the highly acidic lysosomes (Figure 3.16 and Figure 3.17). This alteration in endosomal K^+ distribution upon channel inhibition implicates a role of K^+ channels in the regulation of endosomal [K^+], and thus endosome functioning. Interestingly TMEM175 was shown to regulate endo/lysosomes K^+ flux in glial, neuronal (mouse) and HEK293T kidney (human) cells. The pharmacological profile of TMEM175 however (insensitive to TEA and Qd) (278) indicates an alternative channel is involved in regulating the endosomal [K^+] required for BUNV infection in A549 cells.

An important finding was that K^+ channel inhibition did not impede SYTO82/DiD-BUNV internalisation (Figure 3.18), however BUNV virions appeared to accumulate within lysosomes, suggesting that normal BUNV trafficking was impaired (Figure 3.19 and Figure 3.20). In addition, SYTO82/DiD-BUNV was trafficked into vesicles containing high [K^+] (Figure 3.15), which further indicates passage into LEs with high K^+ in agreement with *Stauffer et al* (2014) at similar timepoints (258). In this regard, it is interesting that a K^+ channel from the K_{2P} channel family is required for BUNV infection, as some are known to localise to endocytic compartments and are regulated by a multitude of signals which would be important for endosomal integrity, including pH and membrane stretch (244,253). It is interesting to speculate that the identified effects of K^+ channel modulation on BUNV may indicate a requirement for BUNV trafficking through these K^+-rich vesicles, regulated by K_{2P} functionality.

This allows a model to be predicted (Figure 3.21 A), whereby BUNV is internalised and trafficked through EEs into LEs, and endosome-resident K^+ channels facilitate [K^+] increase alongside the decreasing pH. BUNV reaches this favourable environment of low pH and high [K^+] (green box), which elicits essential structural changes in the virus required for fusion and uncoating events. Virions pre-treated with pH/K^+ therefore have already encountered this environment and may not need to reach the same compartment in order to initiate fusion (Figure 3.4). When K^+ channels are inhibited however, using TEA for example (Figure 3.21 B), endosomal K^+ influx is disrupted and does not reach similar concentrations until the more acidic lysosomal compartments (red K^+ bar). K^+ may therefore not reach the required concentration at the required pH, within this window of opportunity, and BUNV cannot therefore establish biochemical changes for uncoating, becoming trapped within the endocytic network. If this were the case, K^+ channel modulation would be expected to cause an accumulation of SYTO82/DiD-BUNV virions in endosomal compartments, through inhibiting BUNV fusion/endosome escape, at which point virions could be trafficked to the highly acidic lysosomes for degradation (as observed in the presence of TEA; Figure 3.19 and Figure 3.20). In addition K^+ channel modulation would be expected to alter endosomal [K^+], such as the lysosomal K^+ shift observed in the presence of TEA (Figure 3.16).

Identifying an endosomal role for K_{2P} channels would provide further understanding into the role of ionic concentrations in endocytic trafficking pathways and their importance during BUNV infection.

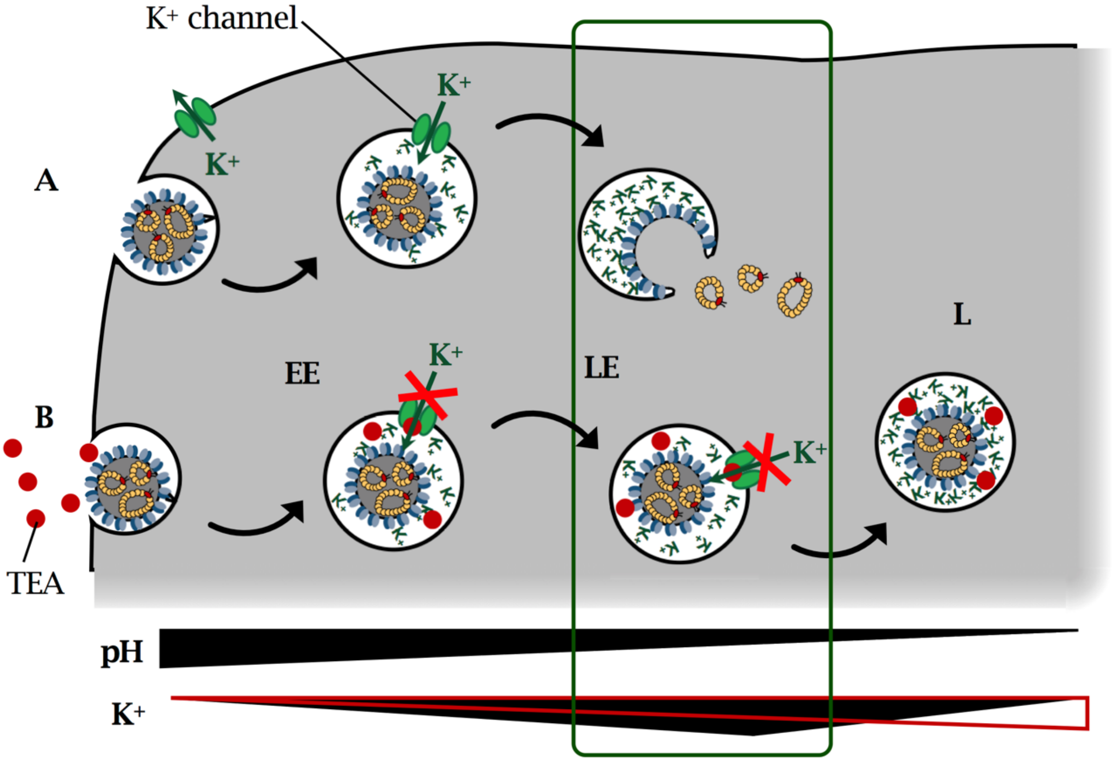

Figure 3.21 Schematic of BUNV entry facilitated by K⁺ channels

(A) Unt: During BUNV entry of mammalian cells, virions are taken up into EEs. Decreasing pH with passage through into LE compartments is accompanied with [K⁺] increase, facilitated by endosome-resident K⁺ channels. BUNV reaches a favourable pH/[K⁺], which act as biochemical cues eliciting structural changes in the virus required for fusion and vRNP release. **(B) TEA:** TEA treatment blocks endosomal K⁺ channels, slowing the [K⁺] build-up which naturally occurs within endosomes. K⁺ therefore does not build-up fast enough within this pH window for BUNV to infect and instead peaks in lysosomal compartments (red K⁺ bar), trapping BUNV within the endocytic network. From *Hover et al* (2018) (247).

Chapter 4 | Using cryo-electron tomography to elucidate K^+-induced structural changes in the BUNV glycoproteins

4.1 Introduction

It is established that for enveloped viruses which enter cells via the endosomal network, structural changes are required to trigger fusion of the viral and host membranes. Multiple biochemical fusion triggers have been identified, including endosomal acidification, lipid-composition, receptor interactions and protease activity (78,279,280). The endosomal fusion of IAV is the most well characterised of the negative sense RNA viruses and is mediated by the type 1 transmembrane protein HA GP. It is established that HA is primed by a reducing pH, which initiates multiple structural rearrangements that lead to stepwise interactions with the endosomal membrane, forming contacts between the viral and host membranes, and the formation of a fusion pore to release the vRNPs into the cytosol (see Chapter 1, Figure 1.5 for a schematic of the predicted steps) (281,282). This mechanism is thought to be similar for most virus-host membrane fusion events and similarly facilitated by viral fusion proteins (283). These proteins contain a membrane-anchored C-terminal region to maintain attachment to the viral membrane and a shielded hydrophobic region, which upon priming is exposed and facilitates the interaction with target membranes (284). Fusion proteins which have been primed for fusion can be termed a 'pre-hairpin intermediate', which is an extended conformation revealing the previously shielded fusion domain that is capable of interacting with target membranes (284). In Figure 1.5 (2) this was termed the extended intermediate conformation, after which the GP folds back on itself to pull the membranes into close contact, the 'hairpin' conformation. Alternatively for other fusion proteins, such as the GP of Filoviruses, priming involves initial cleavage of the precursor GP by cellular furins and a subsequent cleavage cascade involving multiple uncharacterised proteins, ultimately leading to a fusion-ready conformation (283,285). The role of K^+ and Ca^{2+} in EBOV priming was recently investigated, however these ions coupled with low pH and receptor binding alone were insufficient to induce fusion, indicating that neither K^+ or Ca^{2+} are involved in virus priming (286). In contrast, K^+ and H^+ ions are required for IAV entry stages, however rather than causing a conformational change in the GPs, they promote capsid destabilisation that is necessary for vRNP release into the cytoplasm post-fusion (258). Similarly an ionic cocktail mimicking endosomal K^+, Na^+, Mg^{2+} and Ca^{2+} concentrations stimulates the formation of altered capsid structures of echovirus 1 (Enterovirus), thought to facilitate vRNA release (287). The mechanisms utilised by different viruses for priming and fusion demonstrates the plethora of triggers that can be utilised to permit fusion at the appropriate stage of virus entry.

For bunyaviruses, the GPs Gn and Gc mediate virus-fusion, where the larger Gc is a class II fusion protein. However, the priming triggers that lead to fusogenic conformations are largely uncharacterised. Many bunyaviruses require a low pH to induce a fusogenic state and for some, such as the Hantavirus ANDV, this appears to be sufficient to establish post-fusion conformations (79,288). It was assumed for other bunyaviruses that low pH was sufficient to trigger fusion, however more recent studies suggest this is only part of the story. UUKV and SFTSV Phenuiviruses also require specific lipid compositions in addition to low pH for fusion (78,289). Only recently have researches begun to investigate the role of endosomal ionic balance in virus entry and fusion events, for ions other than H^+.

A requirement of cellular K^+ channels during the infection of the Peribunyaviruses BUNV and SBV and the Nairovirus HAZV was identified (244). It was subsequently shown that for BUNV, the K^+ requirement was due to the regulation of endosomal K^+ balance, where K^+ ions and low pH facilitate the release of virions from endosomal compartments (see Chapter 3) (247). HAZV was also shown to utilise endosomal K^+ as a trigger for virus entry, where elevated K^+ alone was sufficient to induce conformational changes in the GP spikes and in some cases induced interactions with co-purified vesicles (77). BUNV is an enveloped virus with no known viroporin in its envelope and the only proteins present on the virion surface are the Gn/Gc GPs. It therefore seems logical that K^+ is acting as a priming trigger, similar to HAZV, causing conformational changes in the GP spikes. A low resolution cryo-electron microscopy (cryo-EM) structure (30 Å) of the BUNV Gn-Gc trimeric arrangement has previously been published and a structural change upon pH 5.0 was identified (74), however the effect of K^+ has not been investigated.

In this chapter, cryo-electron tomography (cryo-ET) was performed to generate 3D-tomographic reconstructions of BUNV virions under different pH and $[K^+]$ conditions, to identify changes in virion architecture. Subsequently, subtomogram averaging (STA) was performed to determine the structure of the unprimed (pH 7.3) versus primed (pH 6.3 + K^+) GPs, identifying an uncoupling of the Gn-Gc trimer upon low pH/K^+ treatment, revealing a potential mechanism for BUNV priming and exposure of the fusion loop domain.

4.2 BUNV release is optimal at 48 hpi in BHK-21 cells infected at an MOI of 0.1

BHK-21 cells are typically used for BUNV propagation and purification (MOI of 0.01) (74). However, as high titres of virus are required for cryo-ET propagation, these protocols were optimised across a range of cell lines permissive to BUNV infection. Growth curves were generated for the mammalian cell lines SW13 and BHK-21 cells, previously used to propagate HAZV (77), by infection with BUNV at an MOI of 0.5 in low-serum media as previously described for the A549 cell line growth curve determined in Figure 3.2 A. Virus-containing supernatants were collected every 24 hrs until a significant proportion of cells showed cytopathic effects (Figure 4.1 A, indicated by ◆). Supernatants were serially diluted from 10^{-2} to 10^{-7} and infected onto SW13 cells. Plaque assays were performed to determine virus titres as described in Figure 3.9 A. Upon BUNV infection of both A549 (black line) and SW13 (blue line) cells, a rapid increase in virus release was observed between 24 and 48 hpi (2-log increase, Figure 4.1 A). At later time-points, viral release plateaued until cell death at ~96 hpi for SW13 cells and ~120 hpi for A549 cells. In contrast, the infection of BHK-21 cells (purple line) led to virus release at 10^{6} PFU/ml at 24 hpi and increased to $2.2\text{x}10^{7}$ PFU/ml at 48 hpi, after which viral titres decreased until cell death (~72 hpi). From these data, BHK-21 cells were taken forward for BUNV propagation for cryo-ET as, despite releasing similar quantities of BUNV to A549 cells ($1.8\text{x}10^{7}$ PFU/ml versus $2.2\text{x}10^{7}$ PFU/ml), high-titre virus was produced 48 hrs earlier (Figure 4.1 A, compare black and purple lines).

Using BHK-21 cells, the effects of MOI on the quantity of virus released was assessed. BHK-21 cells were infected with an MOI range from 1 to 0.0001 for three hours and input virus was subsequently removed through washing, as with Figure 4.1 A. Viral supernatants were collected at 48 hpi and titres were determined by plaque assay (Figure 4.1 B-C). Virus release proportionally increased with MOI peaking at 0.1 which yielded $4.9\text{x}10^{7}$ PFU/ml, after which virus release dramatically declined. An MOI of 0.1 was therefore used in subsequent viral propagation infections and representative plaques of 10^{-4} to 10^{-6} dilutions are shown in Figure 4.1 C.

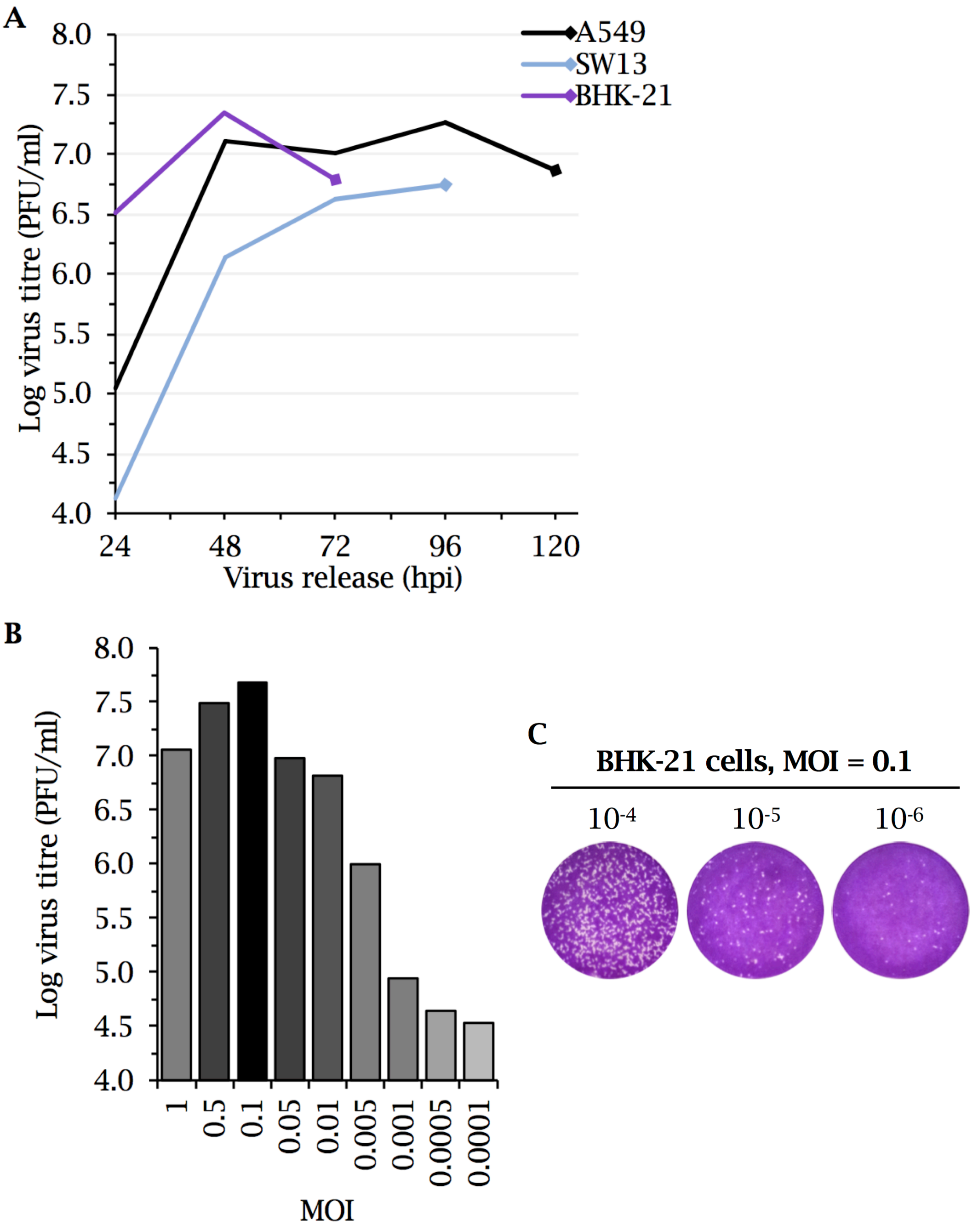

Figure 4.1 BUNV propagation is optimal in BHK-21 cells at an MOI of 0.1

(A) A549, SW13 and BHK-21 cells were infected with BUNV (MOI = 0.5) for 3 hrs, as in *Figure 3.3 (A)*. Virus-containing supernatants were collected at 24, 48, 72, 96 and 120 hpi; until the cells died (indicated by ◆). Virus titres in the supernatants were determined by plaque assay, where SW13 cells were re-infected with each sample at dilutions of 10^{-2} to 10^{-7} and plaques were allowed to develop over 6 days, at which point cells were fixed and stained using crystal violet. Plaque numbers were quantified, titres were determined (PFU/ml) and plotted as a log scale of viral titre. **(B)** BHK-21 cells were infected as in *(A)* with an MOI range of 0.0001 to 1. Viral supernatants were collected at 48 hpi and BUNV titres were determined via plaque assay as in *(A)*. **(C)** Representative images of plaque assay dilutions 10^{-4} to 10^{-6} of BHK-21 cells infected with an MOI = 0.1 for 48 hrs from *(B)*.

4.3 Producing BUNV for cryo-ET

For electron microscopy, virus samples must be of high titre, relatively pure and free from protein contaminants. BUNV was propagated in BHK-21 cells for 48 hrs, as described in Figure 4.1. Virus-containing supernatants were clarified by two centrifugation steps and filtered through a 0.22 µm filter to remove further contaminants from the media. Virus was then purified by ultracentrifugation through a 30 % sucrose cushion. Samples were collected from pre-ultracentrifugation viral supernatants (pre-spin snt), post-ultracentrifugation supernatants, the supernatant-sucrose interface and the sucrose cushion. BUNV was re-suspended from the bottom of the ultracentrifuge tube in 0.1x PBS through gentle rocking overnight at 4°C. Viruses were resuspended in 0.1x PBS to minimise salt concentrations as undiluted PBS contains 137 mM NaCl. Serial dilutions were performed from each collected sample and titres were determined by plaque assay (Figure 4.2 A-B). By comparing pre-spin supernatant titres ($4.2\text{x}10^{6}$ PFU/ml) to purified BUNV, the purification process increased viral titre by 10^{3}-fold, yielding a BUNV stock of $3.4\text{x}10^{9}$ PFU/ml. The plaques produced from purified BUNV were similar to those of WT BUNV (Figure 4.2 B), but plaques could be observed at lower dilutions (10^{-8}) confirming that infectious BUNV has been concentrated.

To confirm purity, 10 µl of each sample was resolved by SDS-PAGE gel alongside 0.5 µl of purified BUNV. Viral proteins were identified through silver staining (Figure 4.2 C). Pre-spin supernatants (lane 2) were obtained after clarification and filtering, and the absence of multiple bands indicated that a significant proportion of contaminants were removed at this stage. The sucrose cushion sample (lane 5) is additionally clear of the majority of contaminants which remained after clarification and were unable to enter the cushion. In the purified BUNV sample (lane 6), bands were identified of the predicted sizes of viral proteins, which were not present in other samples; Gc (120 kDa), Gn (35 kDa) and N (26 kDa) are clearly identifiable. The large L protein (250 kDa) may be present at the top of the SDS-PAGE gel, but was difficult to confirm. Interestingly, a band of ~17 kDa was observed, which may represent the NSm protein (~18 kDa), which has not previously been shown to be incorporated into mature virions (73). The NSs protein is thought to be non-structural and its presence was not detected by SDS-PAGE. The small number of contaminating bands present in the purified BUNV sample indicated its purity for cryo-ET.

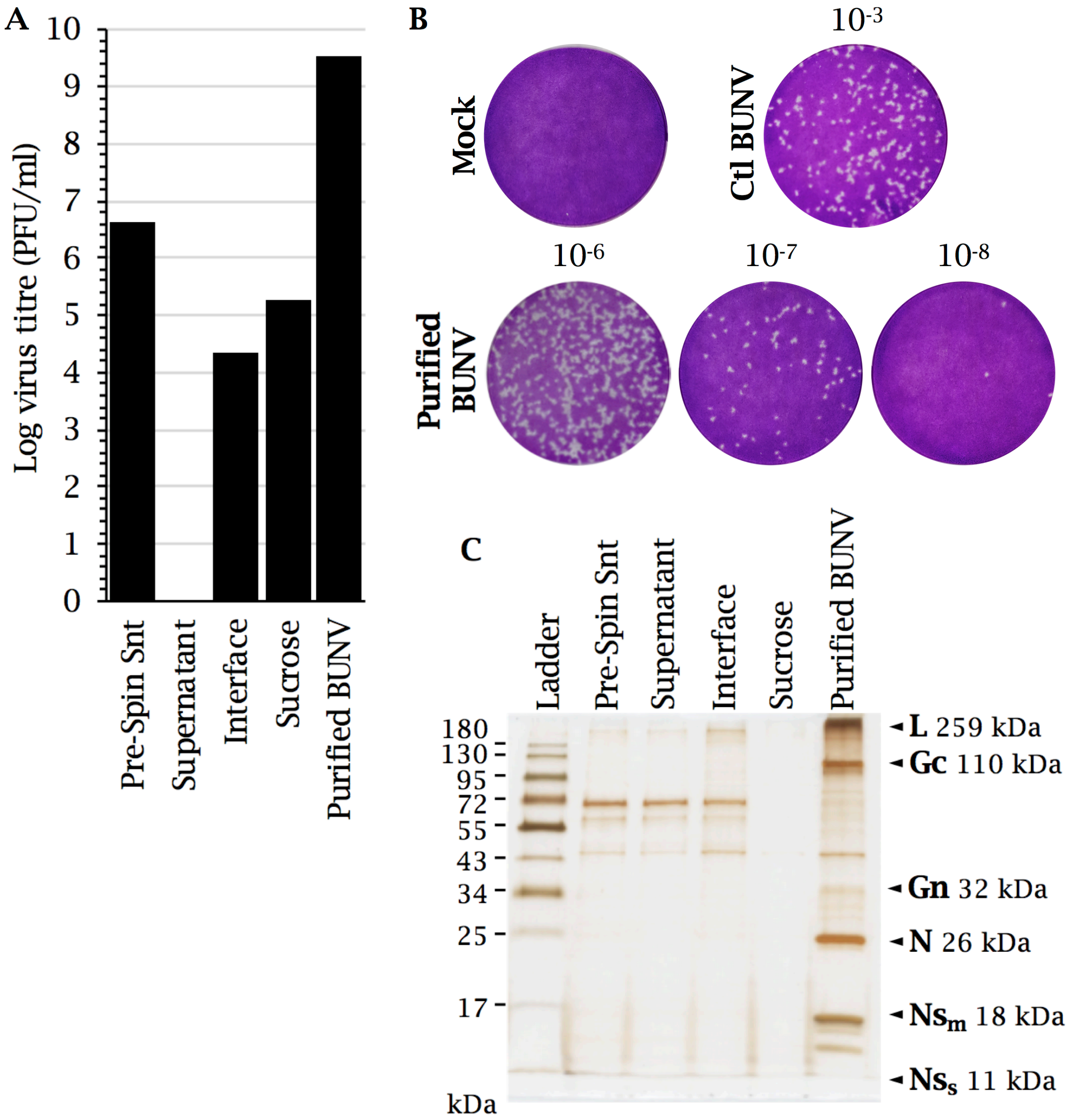

Figure 4.2 BUNV purification produces high titre virus sufficiently pure for cryo-ET

(A) BHK-21 cells were infected with BUNV (MOI = 0.1) as in *Figure 4.1 (A)* for 48 hrs. Viral supernatants were collected, clarified (pre-spin supernatant (snt) sample collected) and concentrated through 30 % sucrose. Samples of post-spin supernatants, the supernatant-sucrose interface and from the sucrose were collected; prior to virus resuspension in 0.1x PBS (purified BUNV). Each sample was serially diluted from 10^{-2} to 10^{-8} and SW13 cells were infected alongside uninfected (Mock) and 10^{-3} infected controls (Ctl BUNV). Plaque assays were performed to determine virus titres, as in *Figure 4.1 (A)*. **(B)** Representative images of uninfected mock, control BUNV and purified BUNV plaque assays in *(A)*. **(C)** SDS-PAGE was performed using 10 µl of each sample collected from *(A)*, alongside 0.5 µl purified BUNV and silver stained. Arrowheads indicate the approximate size of each viral protein and their predicted location on the gel.

To confirm purity and virion morphology, purified BUNV was loaded onto carbon-coated grids and stained with a heavy metal solution of 1 % uranyl acetate. EM micrographs obtained (Figure 4.3) from widefield images showed the presence of virions across the entire field of view, further confirming high virus titres. Virions appeared whole and unbroken by the ultracentrifugation process, as evidenced by lack of uranyl acetate (black) inside the majority of virions, see 'Zoom' images. BUNV virions were near-spherical and of ~100 nm in diameter (74) when compared to the 500 nm scale bar. Small background particles were present, but importantly these were too small to be BUNV virions and were in a significantly low quantity to interfere with cryo-ET. Purified BUNV samples were therefore taken forward for grid preparation and cryo-ET.

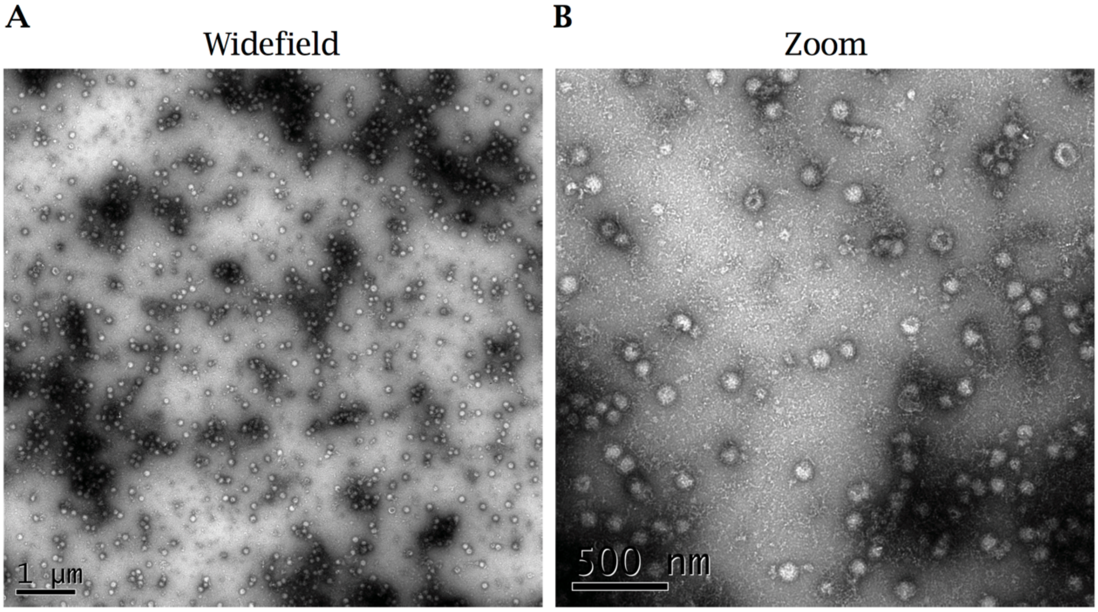

Figure 4.3 Negative stain of purified BUNV confirms sample purity for cryo-ET

Purified BUNV (from *Figure 4.2*) was loaded onto carbon-coated grids and negatively-stained with 1 % uranyl acetate. Images were taken at 120 kV on a Tecnai T12 electron microscope, using a defocus of -1 µm to -5 µm. **(A)** Representative images are shown (scale bar = 1 µm). **(B)** 'Zoom' view, scale bar = 500 nm.

4.4 pH 6.3 and K$^+$ cause changes in the BUNV architecture

The effects of pH and K$^+$ on the GP structure were next investigated. Virions were treated with buffers at pH 7.3 or 6.3 and -/+ 140 mM KCl for 2 hrs at 37ºC, as for the K$^+$ priming experiments described in Chapter 3. Protein A conjugated with 10 nm colloidal gold was added to each sample (1:1:1 dilution, BUNV:buffer:gold) to act as fiducial markers for micrograph alignment, and virus was immediately vitrified onto lacey grids (irregular holes) backed with a 3 nm-thick layer of carbon. Grids were maintained at liquid nitrogen temperatures throughout storage and imaging processes. The use of lacey carbon grids was optimised prior to this stage; comparing 200 mesh Quantifoil (regularly spaced, circular holes) and 300 mesh lacey carbon-backed grids, which also possessed a thinner carbon layer (mesh size indicates the number of holes per grid). It was determined that a similar number of virions bound to each grid under the same vitrification conditions, however on the Quantifoil grids, many virions were found around the edges of the grid holes and on the carbon backbone itself; which would reduce the number of virions that could be selected in cryo-ET, as the carbon would interfere with 3D tomographic reconstructions of virions adjacent to or on this backbone (290). The BUNV distribution was significantly improved when using the (thinner-carbon) lacey grids however, where the virions were distributed more evenly across the grids holes.

The vitrification process provides a support for virions within the grid holes and in the high vacuum conditions of the microscope, allowing virions to be imaged in a near-native state (290). Briefly, virions are adsorbed onto the grid, excess sample is blotted away leaving a thin film of liquid and the grid is rapidly frozen by plunged into liquid ethane. This method produced grids with virions frozen in a layer of thin vitreous ice (no ice crystals) and the use of an automated plunger allowed for a higher consistency between grids. This process was similarly optimised prior to final grid preparation, including blotting times and sample volume.

Prior to cryo-ET, the vitrified grids were screened by cryo-EM to determine quality and the presence of sufficient virions within the grid holes. Images were collected of each condition; pH 7.3, pH 7.3 + K$^+$, pH 6.3, and pH 6.3 + K$^+$. In micrographs of pH 7.3 treated virions, particles appeared near-spherical and were spread across the carbon holes (Figure 4.4 A). Virions were also similar to the estimated size of BUNV virions identified previously, ~108 nm (74); compare to 100 nm scale bar. The uneven ‘spikey’ exterior also indicated that the entire virion surface was covered with GP spikes, as previously described (74). The presence of dark spots in the background of the grid indicated that some contaminants had been vitrified onto the grid alongside the virions, however this did not influence cryo-ET or data processing. Upon the comparison of pH 7.3 treated and pH 7.3 + K^+ treated virions (compare Figure 4.4 A to B), a larger number of virions appeared pleomorphic (white arrowheads) with altered shapes or extensions outwards from the central sphere. This indicated that the virions had a more fluid structure upon K^+ treatment, however at this resolution, it was unclear as to whether K^+ affected the GPs or the lipid bilayer.

Interestingly, dramatic changes were observed for virions treated with pH 6.3 buffer (Figure 4.5 A). The virions aggregated into large clusters, either in contact with one another or fused, which was difficult to ascertain due to background within the clusters (Figure 4.5 A, white arrowhead). This suggested that the GPs adopted a fusogenic conformation, or a conformation that led to the clustering of GP spikes to facilitate fusion. More interestingly, pH 6.3 + K^+ treated virions did not form large clusters (Figure 4.5 B) and were largely individual virions, with less-spherical structures (white arrowhead). K^+ in the presence of low pH thus appeared to prevent virion aggregation, which could be through selective changes in GP structures that prime viruses in the absence of a fusogenic state. The effects of pH and K^+ on GP structure could not be determined at this resolution, however the grid quality allowed the samples to be taken forward for cryo-ET.

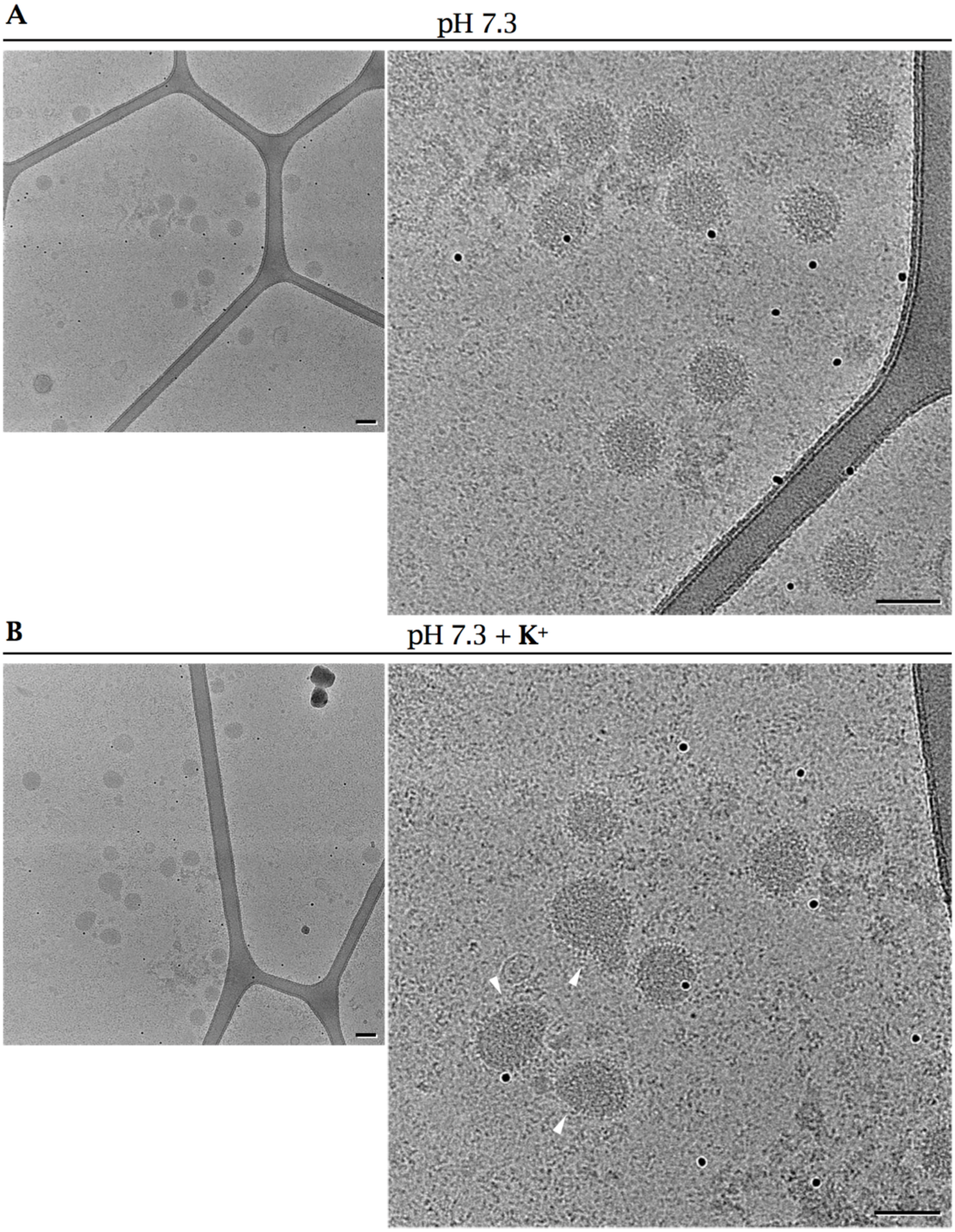

Figure 4.4 Cryo-EM reveals changes in the BUNV structure upon K+ treatment Purified BUNV was treated for 2 hrs at 37ºC at pH 7.3, without **(A)** or with **(B)** 140 mM KCl, as described in *Chapter 3 Figure 3.3 (A)*. Colloidal gold reagent (black dots) was added to the samples which were vitrified on carbon-backed grids for cryo-EM grid screening on a Titan Krios electron microscope; to identify grids appropriate for cryo-ET. White arrowheads in **(B)** indicate irregular virion shapes. Vitrification was performed with Dr Juan Fontana and images were obtained with the help of Dr Rebecca Thompson and Dr Emma Hesketh, from the Astbury Biostructure Laboratory. Scale bars = 100 nm.

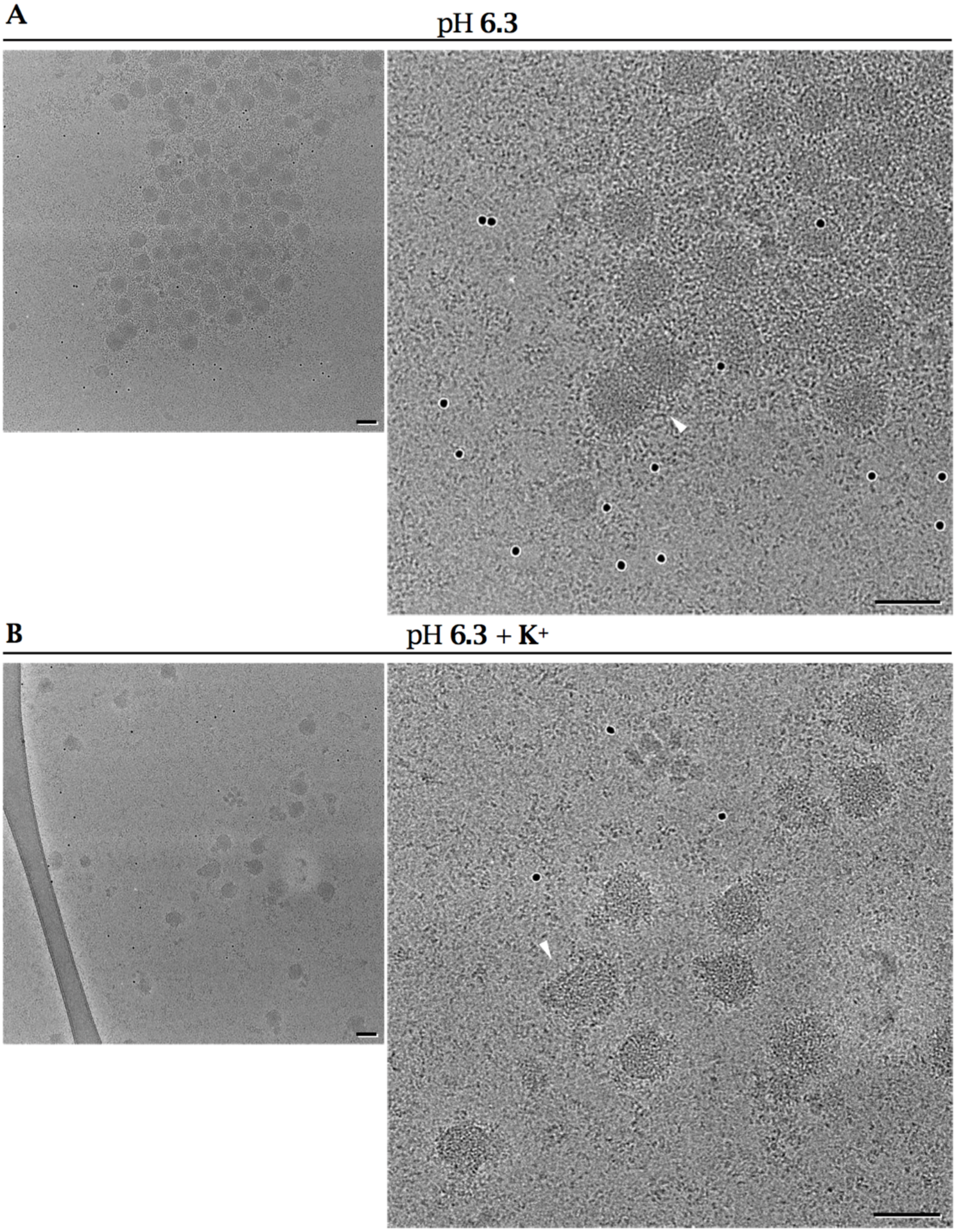

Figure 4.5 Cryo-EM of pH 6.3 treated virions reveal that K$^+$ prevents virion aggregation at lower pH

Purified BUNV was treated for 2 hrs at 37ºC with buffers at pH 6.3, without **(A)** or with **(B)** 140 mM KCl, alongside those shown in *Figure 4.4*. Vitrification and imaging were performed as in *Figure 4.4*. White arrowheads in **(A)** indicate virions attached to or fused to one another. Those in **(B)** indicate the irregular virion structures. Scale bars = 100 nm.

4.5 Cryo-ET confirms that pH 6.3 and K^+ alter virion morphology and GP arrangements

To determine any changes in the GP spikes upon virus priming, 3D reconstructions needed to be generated for each condition. BUNV virions are pleomorphic and therefore do not possess an even, regular arrangement of GPs across the surface of a single virion (such as that observed in icosahedral symmetry), nor is the arrangement identical across different virions. Cryo-ET can be utilised to generate 3D reconstructions of non-identical virions (or other samples), unlike cryo-EM which utilises homogeneous 2D particles in different orientations to create 3D reconstructions. Uniquely to ET, a set of micrographs are obtained from multiple projection angles of a single region of interest (i.e. a tilt series). In this instance the grid was physically tilted from -60° to +60° and images were obtained at 2° increments (i.e a total of 61 images per location on the grid), which can then be computationally processed into 3D-tomographic volumes (tomograms) (Figure 4.6). From these tomograms, STA can be performed to select GP spikes on the virion surface and align these identical particles to one another to generate a 3D model. A problem with cryo-ET is achieving a significant contrast to visualise structures, as low electron doses are applied for each projection obtained in order to keep a low overall electron dose and limit damage to the sample across the tilt series (i.e. across the 61 images collected). To overcome this limitation, a defocus is applied as the conventional method used to generate contrast. In the data collection here however, a Volta phase plate was utilised. This plate generates phase contrast by introducing a phase shift between the scattered and unscattered electrons, significantly improving the contrast of objects and allows imaging closer to focus (291).

To determine more detailed GP structures, cryo-ET was performed at pH 7.3 (no K^+, control (ctl)) reminiscent of the extracellular environment and pH 6.3 + K^+, reminiscent of LEs (173); from which BUNV is thought to escape. Using a Titan Krios electron microscope and Tomography 4 software for automated data collection, 20 single-axis tilt-series were collected for each condition. Using eTOMO software from the IMOD package, the tilt-series were aligned using gold particles as fiducial markers, which act as a constant feature present in all images that need be aligned in order to generate the 3D volume (292). For each condition 6 tilt series were discarded owing to poor contrast in the projections or an inability to align the tilt series (often owing to a lack of sufficient gold particles to align), therefore 14 tomographic volumes were generated per condition, with a final pixel size of 5.44 Å (after a binning factor of 2).

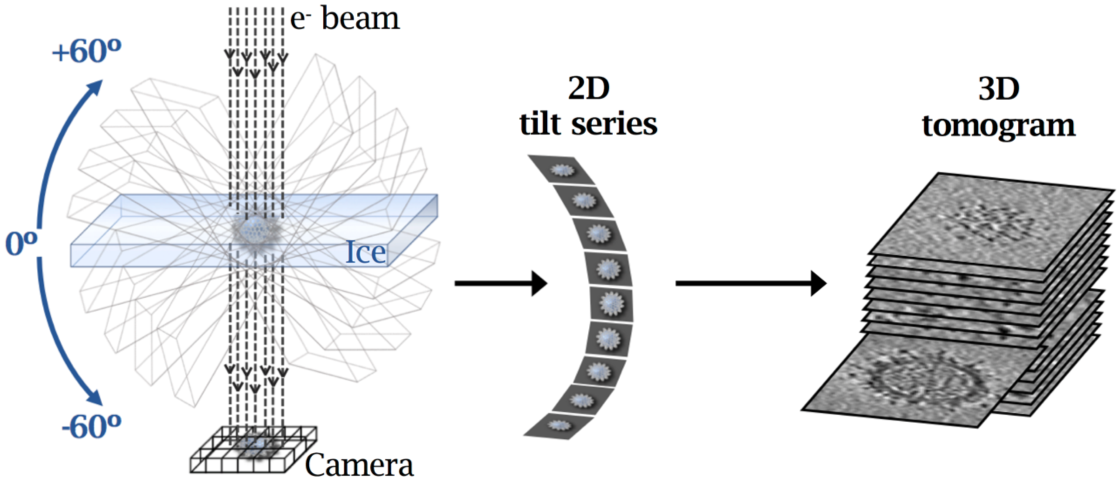

Figure 4.6 Schematic of cryo-ET workflow
Projections were collected at multiple different tilt angles. In the example case, the electron (é) beam is directed at a grid tilted from -60º to +60º with images taken at 2º increments. The 2D tilt series was aligned and a 3D tomographic reconstruction was produced. Adapted from *Kremer et al* (1996) (292).

Tomographic reconstructions allowed BUNV virions to be imaged at a higher resolution, where the lipid bilayer was clearly visualised and the virion surface was covered in GPs (Figure 4.7). Some GPs also clearly possessed the tripod-like arrangement previously described by *Bowden et al* (74) (Figure 4.7, white arrowheads). The disordered electron density within the virus interior additionally showed dense packing with vRNPs. Sagittal sections through the Z-plane of ctl BUNV virions confirmed the tripod-like arrangement of the spikes is also identifiable on the top and bottom of the virions, where a locally ordered structure of trimers was observed (Figure 4.9 A, sections 1 & 7, white arrowheads).

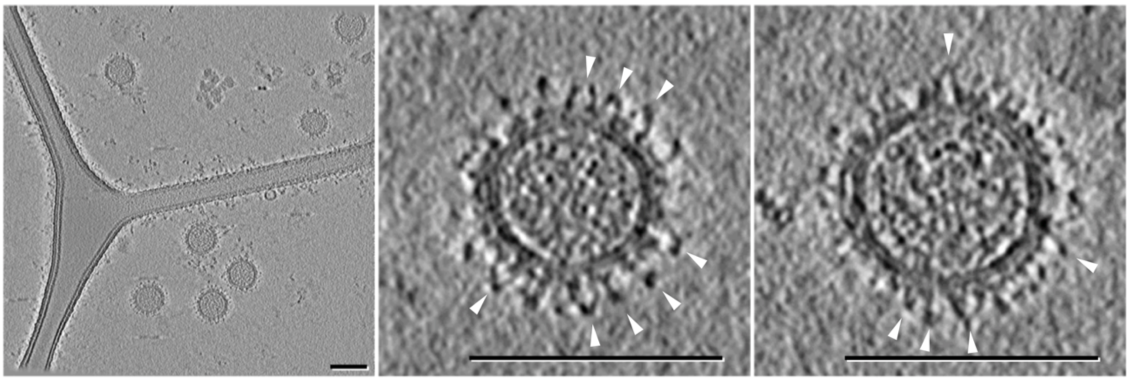

Figure 4.7 Cryo-ET of pH 7.3 (ctl) virions shows an arrangement of GP spikes present across the entire virion surface

Cryo-ET tilt series data were collected using cryo-grids prepared as previously described, see *Figure 4.4*, on a Titan Krios electron microscope at projection angles every 2° from -60° to +60° (microscope setup was performed by the Astbury Biostructure Laboratory staff and imaging areas determined by S Hover). IMOD software was used to generate 3D tomographic reconstructions of 14 tilt series (performed by S Hover). Central tomographic reconstructions of widefield and two individual virions, white arrowheads indicate tripod-like spike arrangements. Images filtered in Fiji using Gaussian Blur 3D. Scale bars = 100 nm.

When virions were treated with pH 6.3 + K^+, the tomograms showed altered GP arrangements and a larger number of pleomorphic virions (Figure 4.8). The vast majority showed regions of the membrane completely devoid of spikes (Figure 4.8, white arrowheads), which differed from the complete spike coverage observed for pH 7.3 ctl virions. Strikingly, the GP spikes showed no tripod-like arrangements on any of the virions, instead appearing disordered.

Sagittal sections also recapitulated this finding, directly comparing between ctl and primed virions (Figure 4.9 A (ctl) and B (primed)) a clear difference can be seen in virion morphology and GP architecture. With no evidence of a tripodal arrangement observed on the exterior of primed virions (Figure 4.9 B, sections 1 & 7) indicating structural rearrangements in the primed conformation. To confirm these findings and define the primed GP structure STA was required to generate an average structure of the spikes under unprimed and primed conditions.

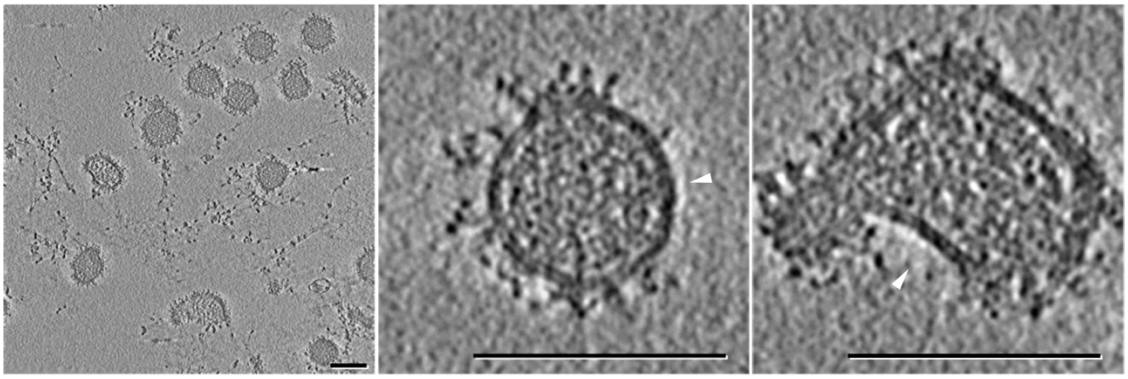

Figure 4.8 Cryo-ET of pH 6.3 + K$^+$ (primed) virions identifies clear changes in virion morphology and GP arrangements

Tilt series data and tomographic reconstructions of 14 tomograms were generated as in *Figure 4.7* for pH 6.3 + K$^+$ treated (primed) BUNV virions. Central tomographic reconstructions of widefield and two individual virions, white arrowheads indicate viral membrane areas devoid of spikes. Images filtered in Fiji using Gaussian Blur 3D. Scale bars = 100 nm.

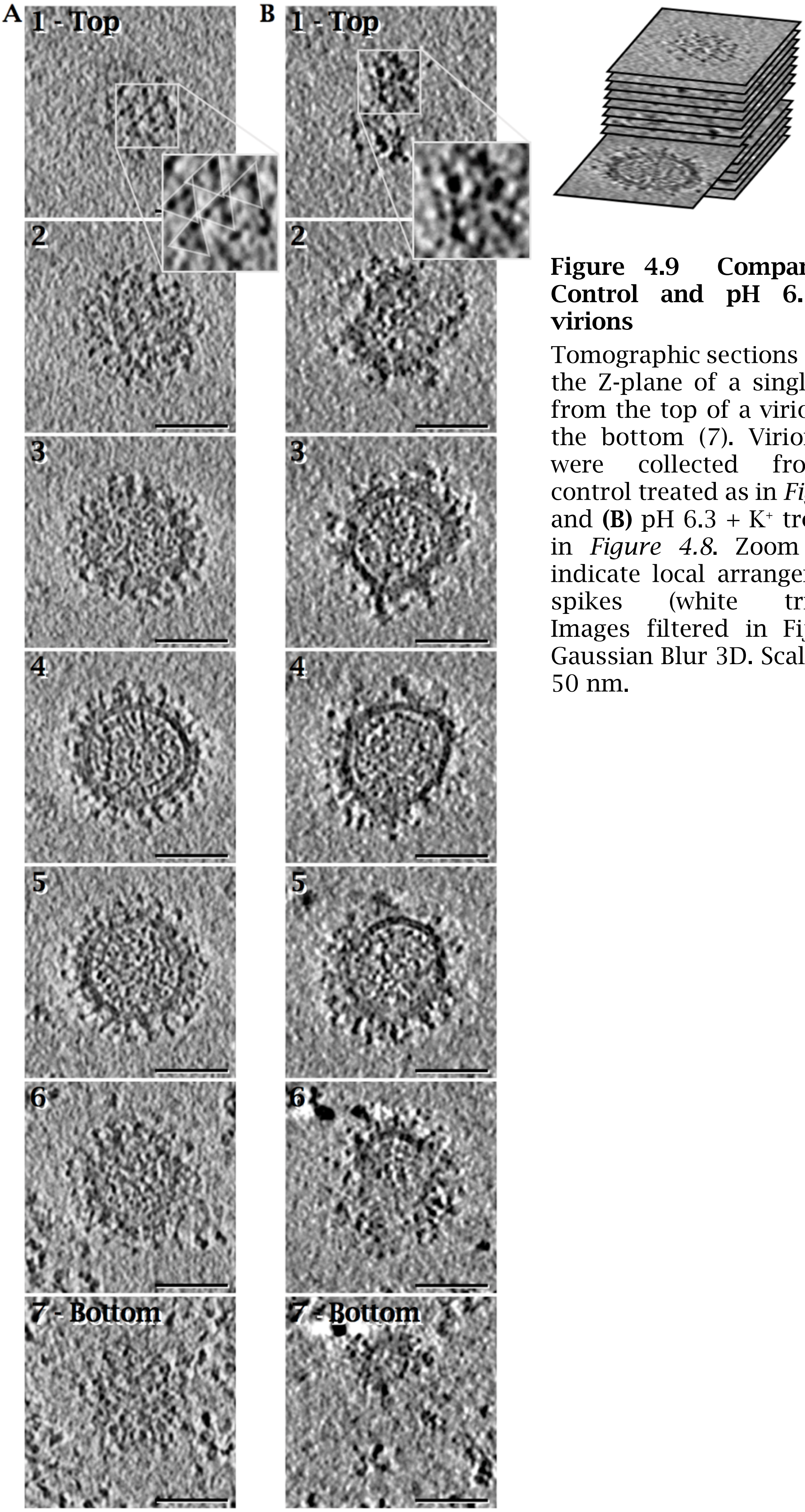

Figure 4.9 Comparison of Control and pH 6.3 + K⁺ virions

Tomographic sections through the Z-plane of a single virion from the top of a virion (1) to the bottom (7). Virion slices were collected from **(A)** control treated as in *Figure 4.7* and **(B)** pH 6.3 + K⁺ treated as in *Figure 4.8*. Zoom images indicate local arrangement of spikes (white triangles). Images filtered in Fiji using Gaussian Blur 3D. Scale bars = 50 nm.

4.6 STA of pH 7.3 GPs at 14 Å reveals newly identified structures within the trimer

STA of ctl GP spikes required multiple iterative stages of alignment and refinement, performed using PEET (Particle Estimation for Electron Tomography, IMOD) software (77,254,255). Initially, a template (or reference spike) was generated by manually selecting >200 spikes on the surface of a number of virions (across multiple tomograms). A model was generated to define the initial orientations, by approximating the viral membrane as a sphere, and assuming that the spikes are oriented perpendicular to the viral membrane. Spikes were extracted from tomograms (sub-tomograms), averaged and initially refined by allowing PEET to marginally alter the spike position on the membrane (position) and rotation of the spike (orientation) to find the best alignment of spikes with one another.

The template generated was used to aid the alignment of spikes following automated particle picking, used to save time and bias of manually selecting all individual spikes. To achieve this, the viral membrane of all virions across all tomograms was defined, then pseudo-spikes were generated with even distribution across the viral membrane (~8.2 nm apart). The number of pseudo-spikes selected was higher than the actual number of spikes, to be sure that all spikes had been selected. The pseudo-spikes were extracted as above and initially aligned to one another and, using the generated template as a reference spike. The positions and orientations of the spikes were then iteratively refined in a number of stages to achieve a final structure. In the first stage of refinement, as the positions of spikes corresponded to regions containing a spike or membrane-alone, the locations of the spikes lateral to the membrane were allowed to change to define the best positions in relation to one another. The template spike was used (and allowed to improve after the first iteration) throughout to provide a reference for the refinements. Similarly, at each stage PEET was allowed to identify and remove particles determined to be duplicates (those within 8.2 nm of one another). In the second stage, the orientations of the spikes were refined by rotating them to find the orientations which best match one another, at increasingly restricted angles (at each subsequent iteration). In the final stages it was clear that the spikes possessed three-fold (C3) symmetry, therefore C3 symmetry was applied, and all angles were allowed to change to further refine the orientations of these particles. A spherical mask was applied to restrict the refinement to a smaller area of interest (the spike), focusing on the high resolution information.

Across the 14 tomograms, 20,278 sub-tomograms were collected from 71 virions and 15 iterations of alignment and refinement were performed. In the final aligned average of the pH 7.3-treated (ctl) GP sub-tomograms, the electron density confirmed a tripodal arrangement resolved at ~14 Å (Figure 4.10). In Figure 4.10 A, black indicates the regions of high electron density, where a lipid bilayer is clearly defined at the base of the average, with a GP spike sitting on top. Images 1 and 2 show sagittal sections and slices through the centre of the spike at two angles, where the connection of each Gn/Gc monomer with one another can be identified at the top of the spike. Through imaging a slice through the centre of the spike the three ‘legs’ of the trimer are clearly visible (Figure 4.10 A (3) the dashed line ‘3’ in image ‘1’ identifies where image ‘3’ intersects the spike in ‘1’). From this average, isosurface rendering was used to generate a 3D model of the electron density, where the previously termed head, stalk and floor domains (74) of the GP can be easily identified (Figure 4.10 B). Previous STA of BUNV GP by *Bowden et al* (2013) (74) identified this tripodal arrangement, however to only ~30 Å resolution. The resolution for the BUNV ctl average here was determined by Fourier shell correlation (FSC, using a cut-off of 0.5, purple line) to be ~14 Å (Figure 4.10 C). The graph in Figure 4.10 C indicates FSC plotted against the resolution (nm = Å/10) using the maximum number of subtomograms (black line), which was used to determine resolution (~14 Å). FSC plots for decreasing numbers of subtomograms (grey lines) were also generated for comparison to the full data set and determined that increasing the number of particles further to what has been used here is unlikely to significantly increase the resolution. With this higher resolution structure, the three head domains (*), one from each Gn/Gc monomer, can be clearly visualised and are more defined. When the model is rotated, the points of contact made between the floor region of the GP and the lipid bilayer can also be identified (black arrowheads). Interestingly, the floor region revealed an extended area of density at the base of the stalk, separate from the remaining floor region mass (white arrowheads), which appears to point in an anti-clockwise direction around the C3 symmetry axes (i.e. the spike centre). In Figure 4.10 A image ‘3’ the direction of each ‘bulge’ anti-clockwise can be clearly identified here also. It is currently unclear whether this region represents part of Gn or Gc, however work is in progress to improve the resolution of this structure including un-binning the reconstructions and applying a smaller mask to limit the area of interest.

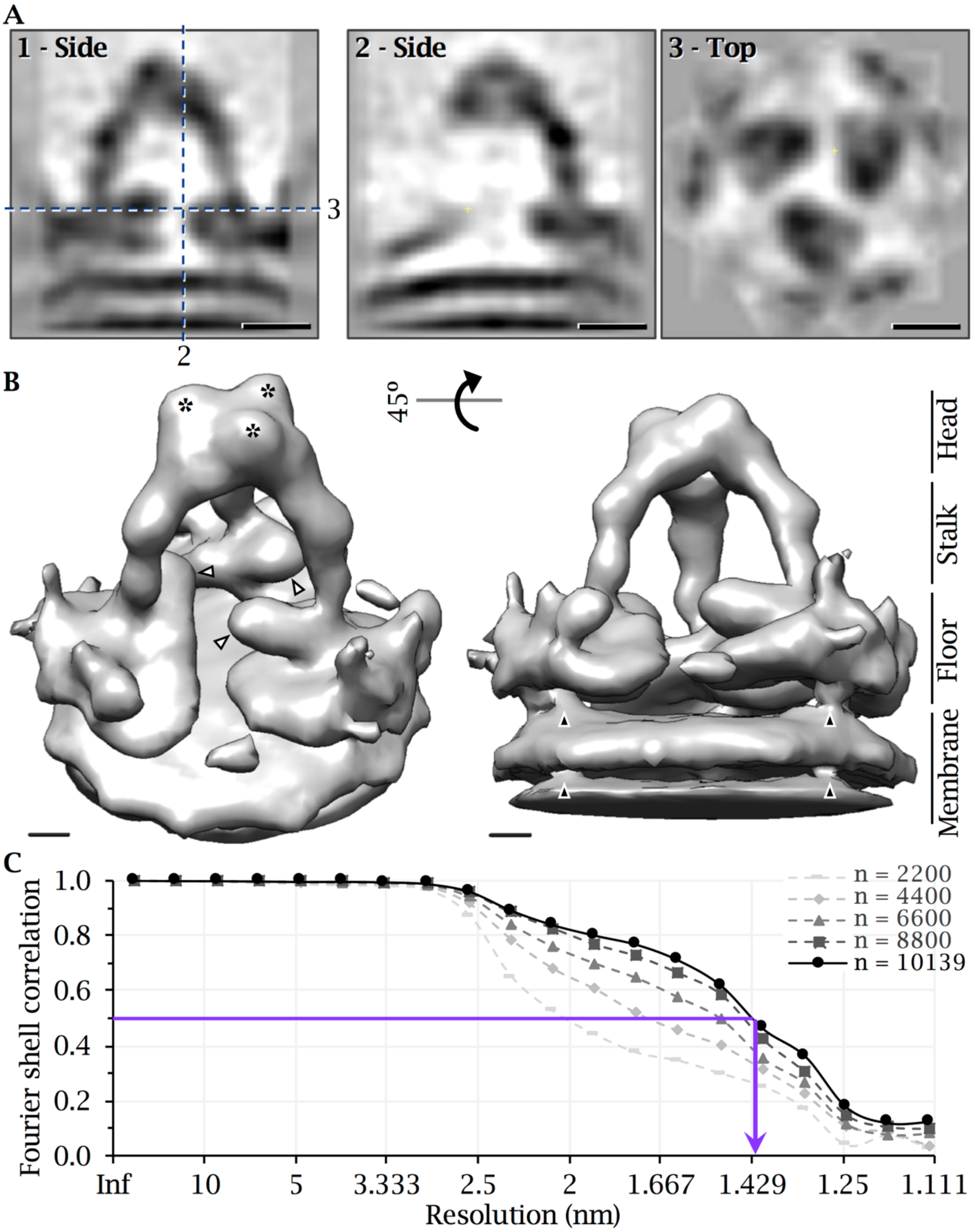

Figure 4.10 STA confirms the tripodal arrangement of BUNV GPs

STA was performed (by S Hover) on BUNV GP spikes, aligning 20,278 subtomograms through several iterations of refinement using IMOD PEET software (with help from Dr Juan Fontana). **(A)** Sagittal (1 & 2) and transverse (3) sections through the electron density averages, the dashed line indicates position of images 2 & 3 in relation to 1. Scale bar = 50 Å. **(B)** Isosurface rendering of the GP trimer, identifying the three regions; head, stalk and floor on the viral membrane. * indicates the head domains, white-filled arrowheads indicate a bulge at the base of the tripod and black-filled arrowheads indicate contacts made within the viral membrane. Scale bar = 20 Å. **(C)** FSC plot used to determine resolution of ~14 Å at a cut-off of 0.5 (purple line). 'N' indicates number of particles used, where 10,139 (black line) indicates the maximum number of particles used.

An inherent problem of cryo-EM is in ascertaining the correct direction of the handedness of the averages, which needs to be found. This is because EM is a projection-based approach, however the left and right hand projections are identical which means you lose the hand in the initial step. Additionally, in ET this is further complicated as the handedness can be altered during several different steps (293). Although for ET and STA there is not a single defined methodology for determining this, a common method is by mapping the crystal structure of the averaged molecule into the electron density and determining which hand results in the best fit. Recently, the crystal structure of the BUNV head domain trimer was solved by *Hellert et al* (2019) and was inserted into the model in Figure 4.10 (using chimera) to identify its handedness. In Figure 4.11 A the structure is in a 'Left-handed' (L hand) orientation, as identified by the 'bulge' which points anti-clockwise forming a 'L' shape; see black dotted line. In Figure 4.11 B, the handedness is inverted and the bulge now points clockwise (inverted L, previously shown in Figure 4.10). By comparing the two, small differences can be observed in the fit where the crystal structure fit is improved in the inverted L structure (B). Importantly, the location of glutamine 717 (Q717, yellow ring) was identified for each hand, as this is the residue where the 'stalk domain' of Gc will begin. It is clear that in the inverted L, Q717 is closer to the electron density forming the stalk domain, therefore the stalk region could reasonably begin at this residue and the inverted L likely represents the true handedness of the structure.

In addition to the BUNV head domain, *Hellert et al* (2019) also solved the SBV stalk domain (a related *Orthobunyavirus* (genus)) (90), which together make up the variable region of Gc. Using rigid-body-fitting (chimera) the crystal structure of both domains were mapped into the electron density as above. A tight fit was observed between electron dense regions and the Gc head domain trimer, see the blue, red and white head domains (each monomer) from Figure 4.12. The SBV stalk domain also fits within the electron density, particularly when looking at key areas of density such as the small nodules out from the stalk where regions of the crystal structure can be attributed. The regions of poor fit however likely represent differences in the BUNV and SBV stalk domains. The remaining Gc region is unsolved for Orthobunyaviruses, however based on how the head and stalk regions fit within the electron density, this forms part of the floor domain. At this resolution, Gn and Gc cannot be distinguished, but Gn is likely to be found with the core domain of Gc in the floor domain.

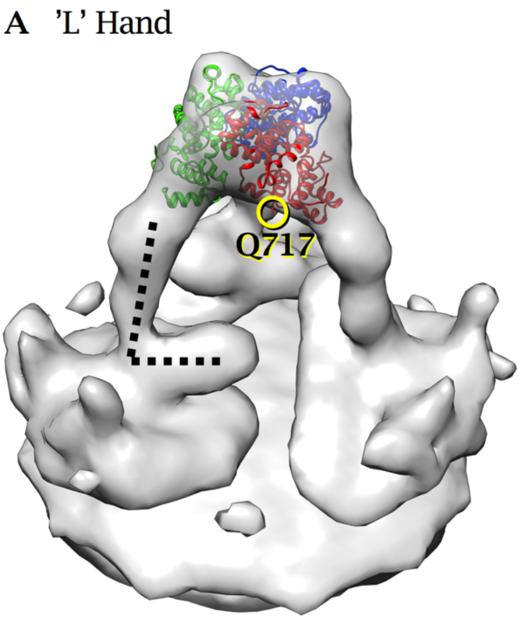

Figure 4.11 Determining the 'handedness' of the virtual GP particles

The crystal structure of the BUNV head domain solved by *Hellert et al* (2019) (90). Using chimera software and rigid-body-fitting, the crystal structure was fitted inside the electron density generated of the virtual particles by STA in *Figure 4.10*. **(A)** Shows a 'Left-handed' (L) orientation, where the protruding domain in the base points in an 'L' direction, see dotted line. **(B)** The 'Inverted Left-Hand' structure was generated to reverse the direction of symmetry, see dotted line. Green, red and blue crystal structures indicate the three BUNV Gc head domain monomers. Yellow/black circle indicates position of glutamine-717 (Q717), where the stalk domain (structure unsolved) meets the head domain.

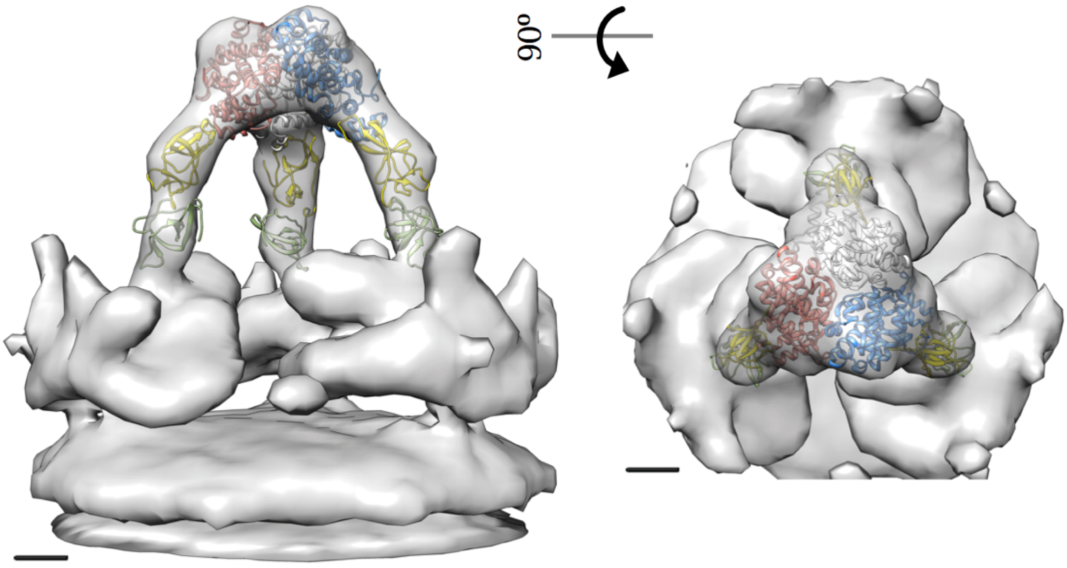

Figure 4.12 The crystal structure of *Orthobunyavirus* head and stalk domains fit within the electron density STA reconstruction

The crystal structure of the BUNV head domain and SBV stalk domain by *Hellert et al* (2019) (90). Using chimera software, the crystal structure was fitted inside the electron density as in *Figure 4.11*. White, red and blue crystal structures indicate the three BUNV Gc head domain monomers, and yellow/green indicates the Gc stalk regions of SBV (BUNV stalk region unsolved).

4.7 STA confirms that pH 6.3 + K$^+$ priming leads to uncoupling of the GP trimers

Following a similar procedure to that outlined in 4.6, STA was performed on primed-BUNV GPs, where a reference spike was generated using the manual selection of spikes and used to automatically select spikes for averaging. At the time of writing this thesis, 14,268 sub-tomograms (89 virions) had been refined through 9 iterations to produce a final aligned average. To achieve this, automatic particle picking and stages 1 and 2 of refinement were performed as previous. No obvious C3 symmetry was observed however, and therefore symmetry was not applied. However, a square mask was applied around the spike to aid alignment. A problem was encountered that thus far has limited the alignment and resolution; the ctl GP spikes are arranged relatively evenly across the virion surface (Figure 4.7), however on the primed virions (Figure 4.8) there was a disruption of this arrangement and large areas of spike-free membrane were identified. This led to a significant number of sub-tomograms which comprised spike-free regions of the viral membrane and interfered with averaging. Work is in progress however to classify these particles into two classes, spike and spike-free, to remove these particles.

An average has been generated at this stage nevertheless, and from the electron density in the average (Figure 4.13 A) it is evident that no tripodal-like arrangements of the GP spikes are present. The trimer appears to have undergone uncoupling of the three head domains and the Gn/Gc GPs have been averaged as monomers. This uncoupling was additionally confirmed in the 3D reconstruction (chimera) shown in Figure 4.13 B, where a lipid bilayer is clearly identifiable at the base of the spike and contacts can be seen where the spike intersects the membrane (black filled arrowheads). Although an uncoupling of the trimer can be defined, the spike has not aligned well at this stage. In the black electron density for the ctl spikes (Figure 4.10 A), the trimer is surrounded by white regions indicating a limited 'background' density surrounding the spike. For the primed spikes however, in Figure 4.13 A (1) grey/dark regions around the top of the defined spike region (black) are clear, indicating unresolved regions of electron density. This indicates that either the structure needs further refinement or that this represents a dynamic, unstructured region that is not identical between particles. This heterogeneity is likely as when comparing back to the primed BUNV tomograms (Figure 4.8 and Figure 4.9 B), the GPs on the virion surface did not appear to be identical.

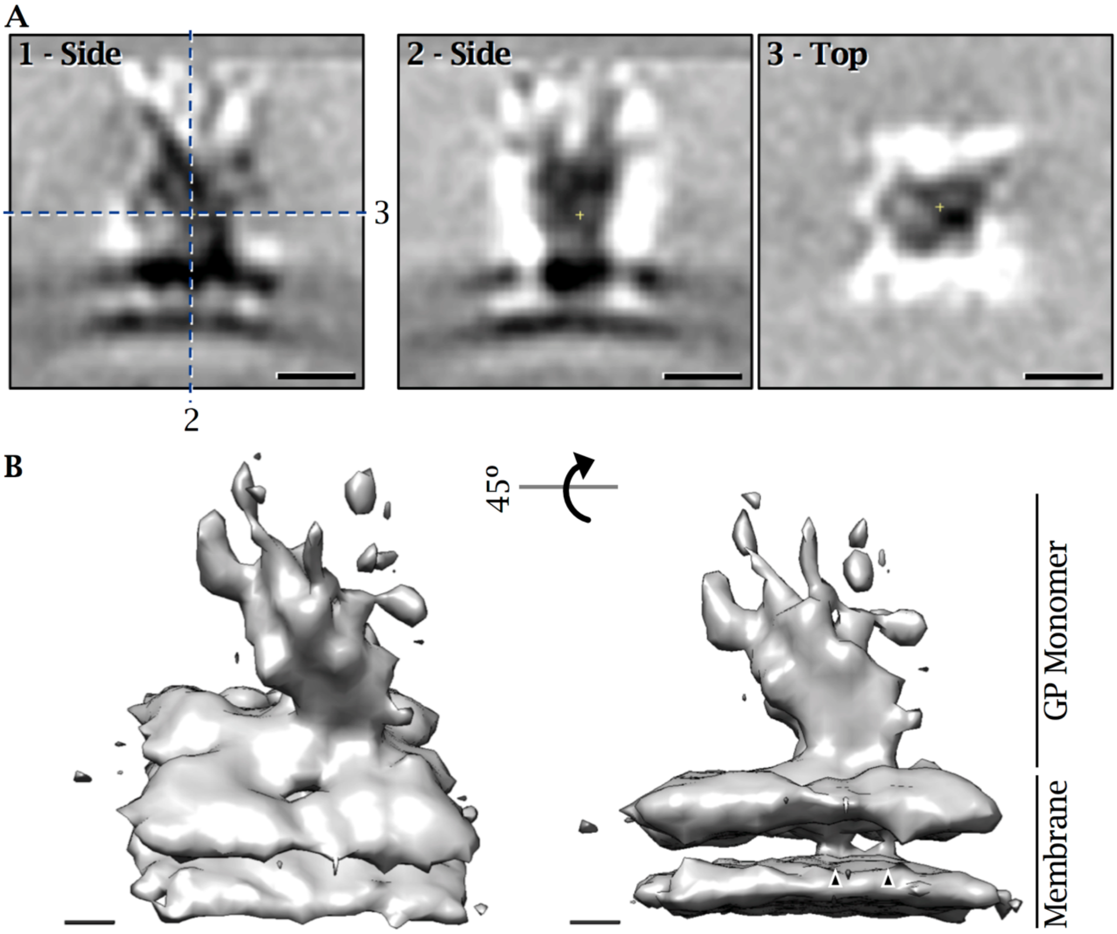

Figure 4.13 STA of pH 6.3 + K⁺ primed BUNV GPs identifies an altered spike arrangement

STA was performed on pH 6.3 + K⁺-treated BUNV GP spikes, aligning and refining 14,268 sub-tomograms as in *Figure 4.10*. **(A)** Sagittal (1 & 2) and transverse (3) sections through the electron density averages, the dashed line indicates the position of images 2 & 3 in relation to 1. **(B)** Isosurface rendering of aligned average in A, black arrowheads indicate contacts with the viral membrane. Scale bar = 20 Å.

Direct comparison by normalising the size of ctl and primed GP averages revealed more information regarding what the primed spike entails (Figure 4.14). The resolved region of the primed BUNV spike compared to the (fully resolved) ctl spike is clearly shorter (~5 nm), further indicating the electron density above this region contributes to the un-aligned electron density seen above. Interestingly the uniform floor domain of Gc (and Gn), which covers the virion surface in the ctl, has been completely disrupted in the primed spike (Figure 4.14), indicating a significant structural rearrangement of these proteins and not simply an uncoupling of the head domains. Efforts are underway to attempt to further refine the primed BUNV spike, in particular focusing on this lower region of the GP spike (and the membrane on which it sits) to provide more details regarding this structural rearrangement induced by pH 6.3 + K^+.

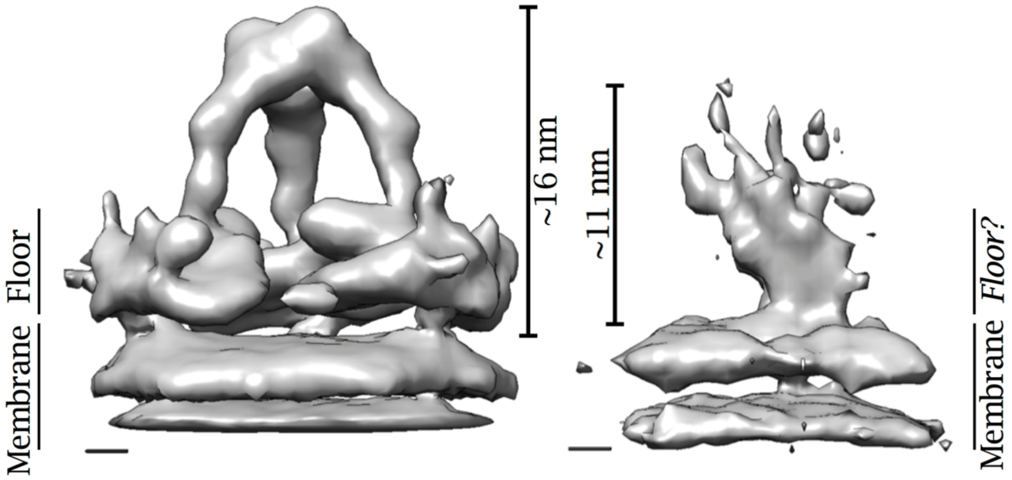

Figure 4.14 Comparison of control versus primed BUNV GP reconstructions BUNV GP reconstructions generated in *Figure 4.10* and *Figure 4.13* were scaled to one another and the distance of the highest point of electron density above the viral membrane estimated in nm.

To confirm that pH 6.3 + K^+ priming does not completely abolish GP structures, neutralisation assays were performed using anti-Gc monoclonal antibodies (anti-Gc M742 Mab (88)). In an initial experiment to determine the neutralising effect of anti-Gc on BUNV, virions were treated pre-infection with anti-Gc antibodies (1:10,000) or H_2O controls and rocked at room temperature for 1 hr. Gc-BUNV was diluted into 2 ml of DMEM and A549 cells were infected for 24 hrs prior to fixing. Infected cells were detected by immunofluorescent staining with anti-BUNV-N, followed by imaging using an IncuCyte Zoom (Figure 4.15 A). Gc antibodies were able to strongly neutralise BUNV and prevent infection, as evidenced by the lack of BUNV infected cells in Gc-antibody treated compared to H_2O control-treated samples.

The effects of Gc-neutralisation on primed BUNV was next assessed, by comparing Gc treatment of pH 7.3, pH 6.3 and pH 6.3 + K^+ treated virions. Virions were primed as previously described (see Chapter 3) and then treated with anti-Gc or H_2O controls for 1 hr. Alongside, hRSV was also treated with anti-Gc or H_2O to confirm that any inhibitory effects were BUNV specific. A549 cells were infected with treated BUNV or hRSV for 18 hrs and lysed. BUNV or hRSV infection were assessed by western blot using anti-BUNV-N and anti-hRSV-G antibodies (Figure 4.15 B). BUNV infection of the H_2O treated virions was as expected, where a reduction in BUNV-N was observed upon pH 6.3 treatment and a dramatic increase upon pH 6.3 + K^+ treatment; confirming the K^+ primed virus conditions. Interestingly, Gc was able to neutralise BUNV at pH 7.3, pH 6.3 and pH 6.3 + K^+. Whilst the region of anti-Gc binding is unknown, it is likely able to bind a region of the Gc monomer (not part dependent upon the trimer) as continued neutralisation is observed after virion priming and disassociation of the head domains (88). This anti-Gc binding and neutralisation does however confirm that the GP structure is not abolished by pH 6.3 + K^+ priming, as indicated by the STA (Figure 4.13). The specific effects of anti-Gc on BUNV were also confirmed by the lack of neutralisation of hRSV (Figure 4.15 B).

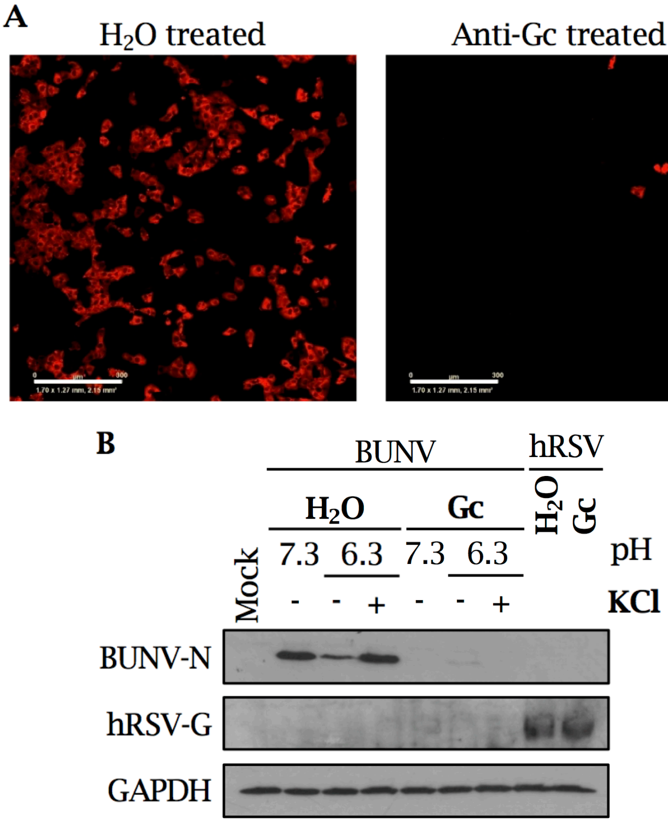

Figure 4.15 Neutralisation of BUNV by BUNV-Gc antibodies indicates that the core monomeric GP structure has not been completely disrupted by priming

(A) BUNV virions were treated with anti-BUNV Gc antibodies (1:10,000) or H_2O controls for 1 hr. Antibody/virus mixtures were diluted in DMEM and A549 cells were infected with treated virions (MOI = 0.1) for 24 hrs. Cells were labelled with anti-BUNV-N antibodies and stained with Alexa-fluor-594 secondary antibodies to identify infected cells. Widefield images were taken with the IncuCyte Zoom imaging system, scale bar = 300 µm (n=3). **(B)** BUNV virions (MOI = 0.1) were treated pre-infection with buffers at pH 7.3, or pH 6.3 -/+ KCl (140 mM), as with Figure 3.4 *(B)*, for 2 hrs at 37°C. Buffers were diluted and virions were treated alongside hRSV controls (MOI = 0.1), with H_2O (control) or anti-BUNV Gc antibodies as in *(A)*. Cells were infected with treated virions, lysed and infection was assessed by western blot analysis, using anti-BUNV-N or anti-hRSV antibodies. GAPDH was probed as a loading control (n=2).

4.8 Discussion

In this chapter the role of endosomal pH and $[K^+]$ on BUNV GP structures were assessed. Cryo-EM revealed that upon reduced pH (6.3) BUNV virions aggregate, however the presence of a high $[K^+]$ present within low pH endosomes prevents this aggregation by an unknown pro-viral mechanism; likely due to the conformational changes in the GPs. Subsequent cryo-ET and STA on the pH 6.3

+ K^+ GP spikes identified an uncoupling of the BUNV GP trimers and potential polarisation of the GPs covering the viral membrane.

The generation of an improved ~14 Å resolution structure of the BUNV Gn/Gc trimer, compared to the previous 30 Å structure (74), allows for a greater mechanistic understanding of the roles of BUNV-Gc. As shown in Figure 4.12, the recently solved BUNV-Gc head-domain and SBV stalk domain X-ray structure, fit well within the generated model from STA. When these regions were mapped back to the structure (Figure 4.16) it is clear that the head domain falls farthest from the predicted Gc-TMD (C-terminus, see polyprotein schematic in Figure 4.16) and is likely to be the furthest point from the viral membrane, as predicted by *Hellert et al 2019* (90). Additionally the stalk region of SBV, although not identical to BUNV, forms an elongated structure that fills the thin electron dense region below the head domain. It therefore follows that the floor domain contains the remainder of the extracellular Gc (grey) and the entire extracellular Gn domains (white in Figure 4.16). The head and stalk regions form a variable domain, whereby sequence complementarity between the *Peribunyaviridae* family is low (<40 %) (90), and mutations in this N-terminal region reveal its involvement in Golgi trafficking, with the function of the C-terminal region thought to facilitate fusion (91). For BUNV, the Class II fusion loop (FL) is found within this Gc C-terminal half (orange striped bar), also termed the core region, that possesses a somewhat increased sequence similarity (~50 %) between Peribunyaviruses (90,91). This is interesting as the predicted location of the FL is in the floor domain of the tripod (see Figure 4.16). Without higher resolution or crystal structures of this domain, the specific localisation of the FL cannot be determined. It is however interesting to postulate that it may be present in the extended electron-dense region (white filled arrowhead, Figure 4.16) at the base of the tripod, previously shown in Figure 4.11. The trimer itself could be acting as a shield, protecting the FL from facilitating fusion at an inappropriate stage of BUNV entry.

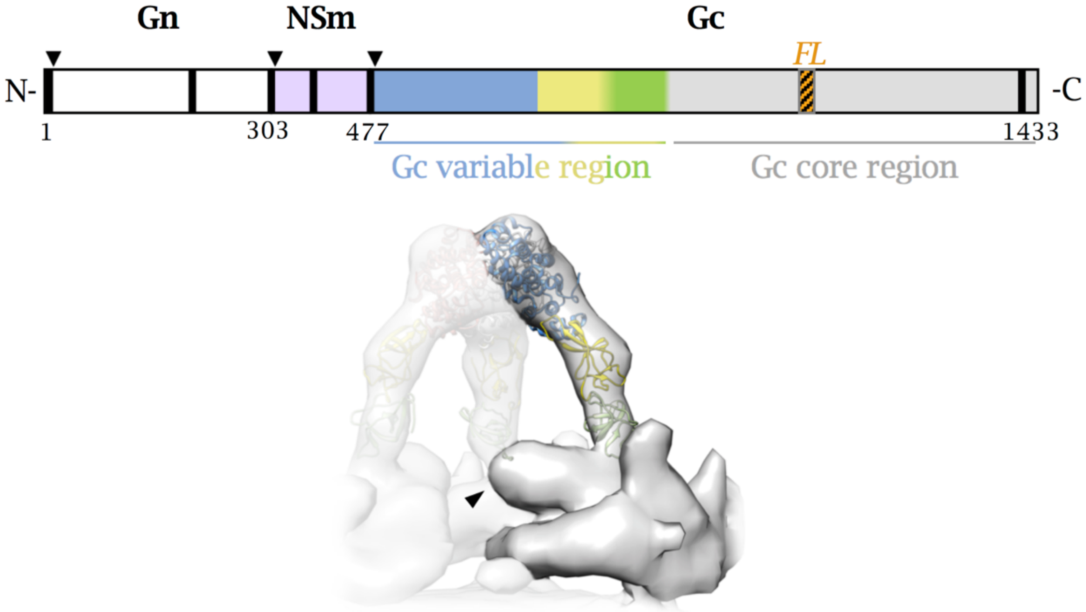

Figure 4.16 Comparison of BUNV GP structures with the protein organisation reveals mechanistic insight into Gc function

Schematic representation of the BUNV M-segment polyprotein organisation. Gn-NSm-Gc are expressed as a precursor, which is post-translationally cleaved (▼) into the two structural proteins, Gn (white) and Gc, and one non-structural, NSm (violet) protein. Amino acid residue counts indicate the protein boundaries. Gc is made up of a variable region, constituting the head (blue) and stalk (yellow/green) domains, and a core region (assumed floor domain, grey) which contains the fusion loop (*FL*, orange striped) (adapted from (90,91)). Black bars indicate transmembrane domains (TMDs). The STA model highlights one monomer of Gc and Gn, with the crystal structures fitted within (90); the head domain of BUNV is shown in blue and the stalk domain of SBV in yellow/green. Black arrowhead indicates newly identified electron-dense regions that could contain the *FL*.

It is common for viruses to shield their FLs in the native conformation, exposing them only when cued by an intracellular stimulus, often low pH, which triggers a conformational change. For the *Bunyavirales* order in particular, exposure to low pH reveals the FL for the *Phlebovirus* (genus, *Phenuiviridae* family) RVFV. *Phlebovirus* GPs exhibit icosahedral symmetry and are comprised of pentamers and hexamers, where Gn acts as the Gc-FL shield and upon low pH is repositioned to allow the fusogenic activity of Gc (129). *Hantaviridae* (family) GPs however form a tetrameric square-like arrangement, but similarly transition between closed and open conformations, where the later exposes the previously shielded FL (294). Unlike *Phenuiviridae* and *Hantaviridae* family members, the Peribunyavirus BUNV displays an elongated tripodal arrangement extending

~18 nm from the virion surface (74). This structure may also be required to act as a shield protecting the FL until the appropriate stage of entry is encountered.

If the tripod is acting to shield the FL, a biochemical priming cue would trigger structural changes in the GPs to expose the FL, permitting its interaction with endosomal membranes. This may result in the changes observed upon pH 6.3 + K^+ treatment, where the organised trimeric arrangement is disrupted by uncoupling of the head domains, allowing this floor domain containing the FL to flip up to expose the FL (Figure 4.13 and Figure 4.14). Indeed, a structural change in the BUNV GP trimer was previously reported at pH 5.0, that indicated an uncoupling of the trimer at this highly acidic pH (74). When considering virions as a whole, a large structural rearrangement to prime virions is not uncommon to the *Bunyavirales*, indeed cryo-EM of the Hantavirus TULV revealed a disruption to the ordered tetrameric arrangement of the Gn/Gc. At pH 7.0 this locally ordered lattice is clearly identifiable (76), however upon pH 5.0 treatment, TULV spike arrangements are disrupted and ordered patches cannot be identified (295). This is interesting when considering that the trimeric arrangement of BUNV is disrupted by low pH and K^+ (see Figure 4.8 and Figure 4.13), indicating that a similar process likely occurs across multiple virus families to prime virions for fusion. Consistent with these observations, K^+ was previously shown to prime HAZV virions for entry, and similarly a large structural change was observed in the virion GPs. K^+ was able to prime HAZV at neutral pH, unlike BUNV (pH 6.3), causing elongation of the GP spikes and their association with co-purified membranes (77). This was reminiscent of UUKV (*Phenuiviridae* family) where pH 5.0 causes a similar elongation of GP spikes which were shown to interact with anionic-lipid-containing liposome membranes (78).

It is clear that during the endosomal entry of many bunyaviruses, the priming of virions is essential for fusion and uncoating, that manifests in a manner dependent on both the virus family and associated GP structure. For many bunyaviruses, and other virus families, H^+ is a key facilitator of this process. However, from studies with HAZV (77) and BUNV ((247) and Chapters 3 & 4) it is becoming increasingly evident that other endosomal ions, such as K^+, are also important. It is predicted that key histidine residues are linked to the changes induced by H^+, where the altered protonation states of histidine can alter polar interactions causing electrostatic repulsion between positively charged side chains (296). It is predicted that this repulsion facilitates the structural changes required for fusion. Some histidine residues in RVFV Gc for example, have been shown to stabilise the pre-fusion conformation of GP spikes and could therefore lead to altered GP structures upon protonation at low pH (114,297). For puumala Hantavirus, the GP structure is altered by a different mechanism, whereby the post-fusion low pH structure of Gc domain II is stabilised by an aspartate-glutamate (D108-E106) hydrogen bond. In the pre-fusion, neutral pH state however, the Gc domain II is highly disordered, which could result from the deprotonation of these residues preventing formation of this stabilising hydrogen bond (298,299).

Ion coordination by non-H^+ ions could also aid structural changes and virion priming. The structure of ANDV (*Hantaviridae* family) Gc was solved at pH 6.5 with a K^+ ion coordinated within domain II, causing the glutamate residue (E106) thought to stabilise the region to deprotonate and create hydrogen bonds with different residues (299). This was not performed at physiological K^+ concentrations however (600 mM KCl used) and the functional relevance of this K^+ coordination was not investigated. Outside of the *Bunyavirales* order, rubella virus (*Togaviridae*) E1 fusion protein also coordinates ions other than H^+. The post-fusion structure of E1 was solved with a Ca^{2+} ion coordinated between the two fusion loops that is essential for fusion, highlighting a potential role for endosomal Ca^{2+} in rubella virus entry (300,301). Despite the mechanistic function of both ion coordination sites remaining unsolved, these studies highlight a role of ions other than H^+ to permit changes in GP structure and fusion events. Future experiments investigating the BUNV-K^+ requirement would seek to determine the specific residues facilitating this interaction, whereby virus is passaged through increasing concentrations of TEA, as previously described for inhibitors of hRSV entry (302). If a TEA-resistant virus is produced, it is likely mutations have developed which circumvent the K^+ requirement. Sequencing and mutagenesis of residues can then be performed to confirm this. It would also be useful to prime the recombinant GFP-tagged BUNV generated by *Shi et al* (2010), which contains an N-terminal GFP within a truncated form of Gc; in the place of residues 501 to 826 (amino acids) (303). This truncated Gc essentially lacks the entire head domain and majority of the stalk domain. Priming of this GFP-BUNV could reveal whether K^+ is acting upon the head/stalk domains or the floor domain; as the GFP-BUNV lacks the head/stalk domains and hence would not form the tripod arrangement.

When *Hellert et al* (2019) resolved the crystal structure of the BUNV head domain, they also mapped the electrostatic surface potential of the trimer interface at neutral (pH 7.0) and pH 5.5 ((90) supplementary data). An increased positive charge within the interface region was identified at pH 5.5 and led to repulsion with the opposing protomer. This predicted repulsion was thought to be coordinated by the protonation of H590, a histidine located at the centre of the trimer interface (90). Additionally, size exclusion chromatography with multi-angle static light scattering analysis (SEC-MALS) was used to theorise the molecular weight of recombinant BUNV-Gc head domain monomers under different conditions. Comparing pH 8.0 and pH 5.5 both containing 150 mM KCl showed an equivalent molecular mass of the Gc head domains upon reducing pH. Although it would have been interesting to compare both pH values with and without KCl and of the entire GP, the study confirms that at pH 5.5, the Gc head domains are still complete monomers (90). This was similarly confirmed by successful neutralisation of both WT and primed BUNV by anti-Gc (Figure 4.15). Combining information of the Gc-head domain with the structural analysis of the GPs under pH 7.3 and pH 6.3 + K^+ conditions, it is possible to predict a model of virus priming (Figure 4.17). At the trimer level, the addition of H^+ and K^+ causes altered electrostatic potentials and repulsion between the Gc trimer interfaces (head domains), leading to the dissociation of the three monomers. At the virion level, this can be seen as a virion-wide disruption of the locally ordered lattice, as seen with TULV (295). This allows free movement of the GPs on the BUNV membrane and polarisation of the virus, causes clustering of the GPs that may aid fusion, at which point areas of the membrane become devoid of spikes (Figure 4.17). Whilst the contribution of each ion cannot be determined from the data gathered here, the prevention of virus aggregation at pH 6.3 by the presence of K^+ indicates a pro-viral mechanism. It is predicted that at neutral pH the FL is protected by the Gc tripodal arrangement and K^+ at reduced pH allows more stringent structural changes that lead to virion priming whilst still protecting the FL. This indicates a stepwise mechanism (similar to the stepwise nature of IAV fusion (258)), where H^+/K^+ priming facilitates the interaction with other co-factors required for fusion at the required endosomal stage. The virion aggregation at pH 6.3 in the absence of K^+ may be caused by neighbouring GP-membrane interactions due to the exposure of the FL without the controlling influence of K^+.

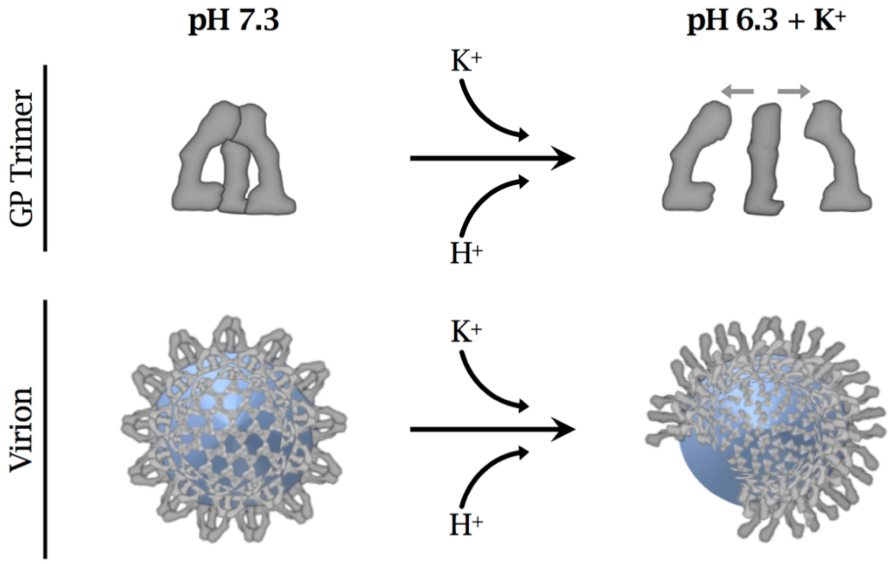

Figure 4.17 Predicted mechanism of pH 6.3/K$^+$ induced changes in BUNV GP spikes

pH 6.3 + K$^+$ induces structural changes in the GPs that disrupt the tripod-like arrangement of the GP, likely through the dissociation of the head-domains (grey arrows). At the virion level, this appears to polarise the virion, clustering the GP spikes and leaving area(s) of the virion membrane devoid of spikes.

In summary, this chapter describes a protocol for the efficient propagation of high-titre WT-BUNV. This was used to purify virus for cryo-EM which revealed an altered virion morphology upon low pH and K$^+$ conditions, mimicking the ionic changes observed through endosomal compartments. Interestingly the aggregation of virions observed at pH 6.3 was prevented by the addition of K$^+$, indicating a protective mechanism. Cryo-ET and STA of pH 7.3 GP spikes revealed potential sites for the BUNV FL which was protected by a tripod-like shield. STA of pH 6.3 + K$^+$ treated virions revealed dissociation of the GP trimer head domains under late-endosome-like conditions, which may function to allow selective structural changes that prime the virus without the full exposure of the FL. Taken together, a potential mechanism for the priming of BUNV virions is proposed, with the essential involvement of K$^+$ ions.

Chapter 5 | BUNV is dependent upon TWIK2 channels for infection of mammalian cells

5.1 Introduction

Using a panel of pharmacological inhibitors, members of the K_{2P} channel family were previously identified to be essential for BUNV infection, whilst treatment with K_V, K_{Ca} or K_{IR} channel inhibitors were ineffective against BUNV infection (244). Inhibitors of K_{2P} channels (albeit non-selective blockers), significantly inhibited BUNV infection, including curcumin and genistein, both of which are anti-cancer therapeutics (174,304). Although the inhibitors were are not entirely specific, the ability of multiple K_{2P} blockers to prevent BUNV infection implicated them as the potential K^+ channel family required for BUNV infection (244).

The K_{2P} channels are a small family of only 15 channel subunits, divided amongst six subfamilies according to sequence similarity; TWIK, TREK, TASK, TALK, TRESK and THIK (Figure 5.1 A). They are distinguished from other K^+ channels by the presence of four TMDs and two pore domains within a single subunit, with functional channels formed through subunit dimerisation (Figure 5.1 B). It has been reported for some K_{2P} channels that two different subunits heterodimerise with one another, producing channels with properties of both subunits which further increases the complexities of channel function and drug sensitivities (174).

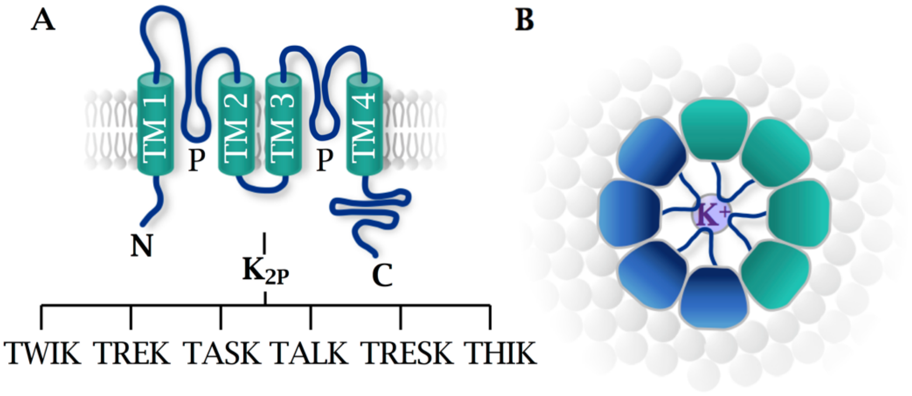

Figure 5.1 K_{2P} channel structure

(A) K_{2P} channel subunits are made up of four TMDs (TM 1-4) and additionally contain two pore domains (P), which form the selectivity filter for K^+ ions. K_{2P} channels are divided into six subfamilies based on sequence similarity and channel properties; TWIK, TREK, TASK, TALK, TRESK and THIK. **(B)** Two subunits homo- or heterodimerise to form a functional channel with 8 TMDs. Adapted from *Lesage et al (2000)* (305).

It was previously shown that K^+ channels are required during early stages of BUNV infection and this was subsequently determined to be due to the regulation of endosomal $[K^+]$ required for BUNV endosomal escape (244,247). The only K^+ channel to date identified with activity in endosomes is TMEM175, a transmembrane protein identified on endo/lysosomal membrane of glial (mouse) and HEK293 (human) cells (278). This is unlikely to be the sole K^+ channel with endosomal activity and the channel(s) regulating endosomal K^+ flux have never been defined. TMEM175 is also insensitive to TEA and Qd (278), the key inhibitors shown to inhibit BUNV. This work therefore sought to investigate if K_{2P} channels are required for BUNV entry. In this regard, K_{2P} channels present a likely target for the regulation of endosomal $[K^+]$ as channel gating is controlled by membrane stretch and pH (154), factors known to change during endosome maturation throughout the endocytic network. In particular TREK and TASK channels show sensitivity to acidification (154,306) and have been shown to form functional heterodimers (154). Owing to the lack of specific K_{2P} channel inhibitors available, their cellular functions remain largely uncharacterised.

In this chapter, the requirement of K_{2P} channels during BUNV infection were assessed using a range of BUNV-permissive cell lines, siRNA knockdown of specific K_{2P} channel subunits and site-directed mutagenesis (SDM) to knock-out channel function. This identified TWIK2 as a K_{2P} channel family member required for BUNV infection, which interestingly showed endo/lysosomal localisation in A549 cells.

5.2 BUNV infection-competent cell lines reveal four candidate K_{2P} channels required for infection

This study aimed to identify the specific K_{2P} channel family members required for BUNV infection. Owing to the lack of pharmacological modulators targeting specific family members, different mechanisms were employed to narrow down the list of candidate channels. A human (KBM-7-derived) near haploid cell line, HAP-1, was used owing to its known expression of only 4/15 K_{2P} channels (gene name KCNK). It was reasoned that if BUNV infected these cells, one of these channels would be a likely candidate required for BUNV entry (Figure 5.2 A) (307). The ability of BUNV to infect HAP-1 cells was assessed by BUNV infection (MOI = 0.1) and cell lysis at 18 hpi. Western blot analysis for BUNV-N revealed that BUNV could infect HAP-1 cells, as identified by BUNV-N detection in infected as opposed to uninfected cell lysates (Figure 5.2 B). This was confirmed by immunofluorescence for BUNV-N of infected (BUNV) versus uninfected (mock) cells, similarly identifying BUNV-N expression (Figure 5.2 C). This indicated that one of the four expressed channels may be required for BUNV infection.

The expression of KCNK1 (TWIK1), KCNK2 (TREK1), KCNK5 (TASK2) and KCNK6 (TWIK2), in other BUNV-permissive human cell lines was then assessed. BUNV infection of A549 cells, previously shown to permit BUNV infection, and MDA-MB-231 (MDA; epithelial breast cancer) cells were confirmed by western blot, identifying BUNV-N at 24 hpi (Figure 5.2 D). K_{2P} expression was then determined by PCR amplification of cDNA generated from RNA lysates of A549 and MDA cells. Primers against each K_{2P} channel were assessed. In A549 cells 10/14 K_{2P} channels were expressed, including the four channels also expressed in HAP-1 cells (Figure 5.2 E, top panel). Interestingly in MDA cells however, only 4/14 channels were expressed, which were identical to those observed in HAP-1 cells; namely KCNK1, 2, 5 and 6 (Figure 5.2 E, bottom panel), further implicating these K_{2P} channels as candidates for BUNV infection.

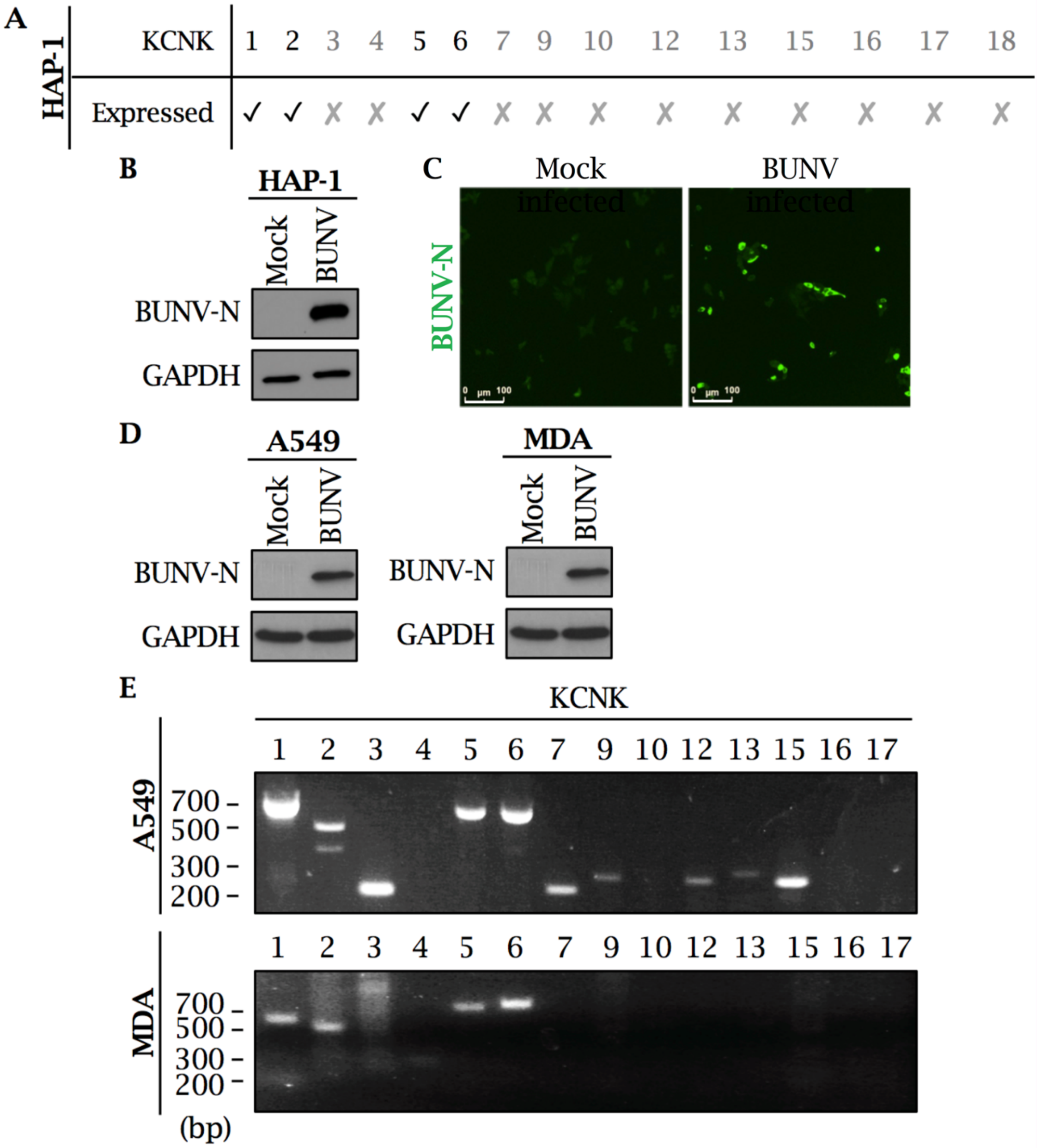

HAP-1 KCNK	1	2	3	4	5	6	7	9	10	12	13	15	16	17	18
Expressed	✓	✓	✗	✗	✓	✓	✗	✗	✗	✗	✗	✗	✗	✗	✗

Figure 5.2 BUNV infects cell lines that express 4 of the 15 K_{2P} channels

(A) Table identifying the K_{2P} channels expressed in HAP-1 cells (307). **(B)** HAP-1 cells were infected with BUNV (MOI = 0.1), or uninfected (mock). At 18 hpi cells were lysed and infection assessed by western blot using anti-BUNV-N and anti-GAPDH (loading control) antibodies (n=3). **(C)** BUNV-infected HAP-1 cells were fixed at 18 hpi and BUNV-N was fluorescently stained using Alexa Fluor-488 secondary antibodies. Images were taken using an IncuCyte Zoom (scale bar = 100 μm) (n=3). **(D)** A549 and MDA-MB-231 (MDA) cells were infected with BUNV and assessed by western blot as in *(A)*. **(E)** RT-PCR to determine K_{2P} channels expressed in A549 and MDA cells. RNA was extracted from cells and cDNA produced by first-strand synthesis using oligo-d(T) as a primer. PCRs were performed to amplify cDNA of 14 K_{2P} channels using specific primers. Amplicons were resolved on 2 % agarose gels and visualised using SYBRSafe (n=2).

5.3 siRNA silencing identified a specific K_{2P} channel required for BUNV infection

Candidate K_{2P} channel expression was silenced by siRNA-mediated knockdown of each channel subunit in A549 cells, alongside scrambled siRNA controls (Scr). Cells were transfected with siRNA 48 hrs prior to BUNV infection, to facilitate target depletion. Western blot analysis of lysates harvested 24 hpi (72 hrs post-transfection) identified that TREK1 (KCNK2), TWIK1 (KCNK1) and TASK2 (KCNK5) silencing did not significantly affect BUNV infection (Figure 5.3 A). TWIK2 (KCNK6) silencing however was highly detrimental to BUNV infection and analysis by densitometry of n=3 repeats revealed a 74.5 % reduction in BUNV-N compared to the Scr control (Figure 5.3 A & B). RT-PCR was performed to confirm successful siRNA knockdown of each channel at the time of infection (48 hrs post-transfection). Knockdown was clearly identified for each channel subunit with significantly reduced band intensity in siRNA samples compared to each Scr control (Figure 5.3 C). GAPDH expression was tested alongside for each siRNA to confirm that the knockdown of mRNAs were specific to each channel.

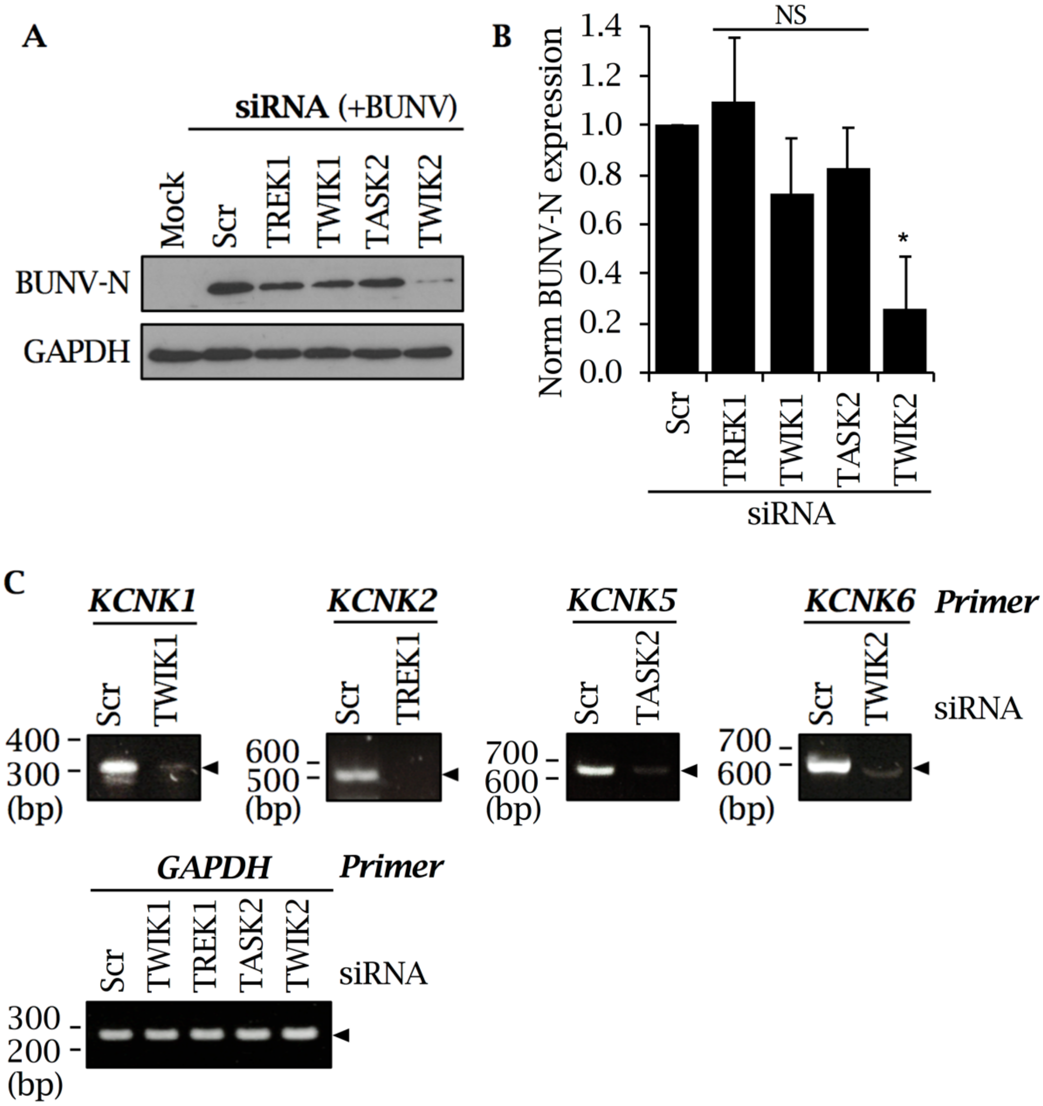

Figure 5.3 TWIK2 knockdown is detrimental to BUNV infection

(A) A549 cells were transfected with siRNA (60 nM) to knockdown TREK1 (KCNK2), TWIK1 (KCNK1), TASK2 (KCNK5) or TWIK2 (KCNK6) expression, alongside a scrambled (Scr) siRNA control. At 48 hrs post-transfection cells were infected with BUNV (MOI = 0.1) for 24 hrs, prior to lysis and assessment by western blot (n=3). **(B)** Densitometry was performed on n=3 BUNV-N western blots from *(A)*, normalised to each GAPDH (loading control) and then to the Scr siRNA control (mean of n = 3 ± SD; NS = non-significant, * = $p<0.05$). **(C)** siRNA knockdown of mRNA transcripts, from *(A)*, was confirmed at 48 hrs post-transfection (time of BUNV infection). mRNA was extracted prior to first-strand cDNA synthesis and RT-PCR using primers targeting each channel; alongside GAPDH as a control (n=2).

To further validate this finding, cells were transfected with 2-fold increasing concentrations of TWIK2 siRNA (10-80 nM) alongside 80 nM of Scr siRNA (Max. Scr). BUNV infection of these cells revealed a concentration dependent decrease in BUNV-N with increasing TWIK2 siRNA (Figure 5.4 A). Of note, at the comparable concentration of 80 nM TWIK2 siRNA to Max. Scr, there was complete ablation of BUNV-N detection. In addition, densitometry of n=3 western blots confirmed a concentration dependent decrease in BUNV-N by TWIK2 siRNA (Figure 5.4 B). These data confirm that TWIK2 is essential for BUNV infection of A549 cells.

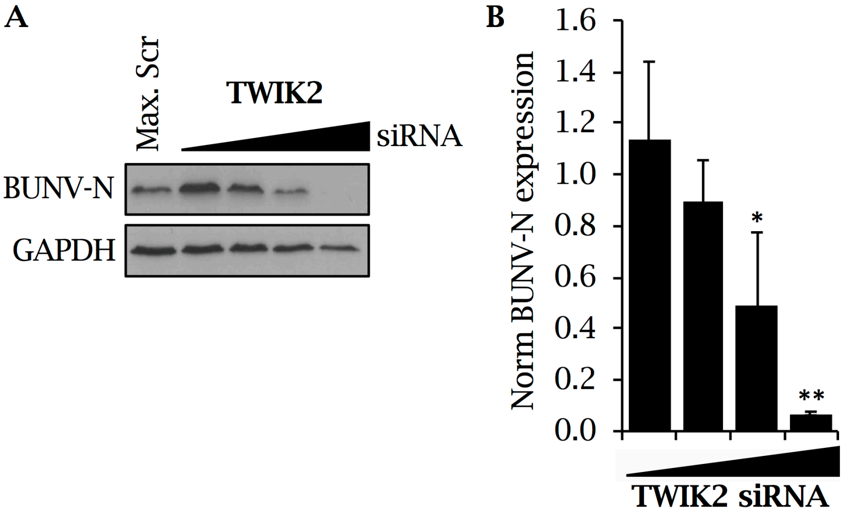

Figure 5.4 TWIK2 silencing leads to a concentration dependent decrease in BUNV infection

(A) A549 cells were transfected with a range of TWIK2 siRNAs (10, 20, 40 or 80 nM), alongside 80 nM Scr control (Max. Scr) 48 hrs prior to infection with BUNV (MOI = 0.1). At 24 hpi cells were lysed and infection assessed by western blot as in *Figure 5.3 (A)*. **(B)** Densitometry was performed on n=3 repeats of *(A)*, normalised to each GAPDH and then to the Max. Scr control (mean of n = 3 ± SD; NS = non-significant, * = $p<0.05$, ** = $p<0.005$).

5.4 Defining the role of TWIK2 in BUNV infection

5.4.1 BUNV traffics through TWIK2-containing endosomes

The expression of TWIK2 in A549 cells was found to be essential for BUNV infection, however the mechanisms of this dependence were unknown. The cellular roles of TWIK2 are similarly poorly understood. Patch clamping of specific channels generally measures currents at the plasma membrane, as opposed to intracellular organelles; therefore a reduced current may not be due to reduced expression, rather an intracellular localisation (253,308). Indeed, overexpression of recombinant TWIK2, which localised to endo/lysosomes and produced currents within human, rat and mouse cell endosomes, led to alterations in lysosome morphology (253).

To confirm endo/lysosome localisation of TWIK2 in A549 cells, recombinant TWIK2-GFP was transfected into cells. At 24 hrs post-transfection the lysosomal marker Magic Red (cathepsin B dye) was added to cells, which we previously used to study endosomal [K^+] localisation (see Chapter 3, Figure 3.14). TWIK2-GFP clearly localised to the membranes of intracellular vesicles and not the plasma membrane, as indicated by localisation to spherical, vesicle-like structures that were dispersed throughout cells (Figure 5.5). In addition, many of these structures co-localised with the lysosomal marker, Magic Red (yellow arrows), indicating that TWIK2 partially localised to lysosomes. Importantly however, not all TWIK2-GFP-containing vesicles colocalised with Magic Red (green arrows), suggesting that TWIK2 also likely localised to other endo/lysosomal compartments. It was interesting that TWIK2-GFP-containing endo/lysosomes appeared larger than expected, which may be a result of the increased TWIK2 localisation and function within these compartments.

The localisation of TWIK2 to endo/lysosomal compartments implicates a role for TWIK2 in BUNV endocytic trafficking, which was previously shown to require K^+ channel function (see Chapter 3). To investigate this, the dual-fluorescently labelled BUNV (developed in Chapter 3 (247)) was used to identify whether BUNV encounters these TWIK2-containing vesicles. Cells were transfected with TWIK2-GFP 24 hrs prior to infection with labelled-BUNV and live images were taken at 1 and 6 hpi. As early as 1 hpi, virions could be visualised within cells (white arrows) with limited visualisation within TWIK2-containing endo/lysosomes (Figure 5.6, top panel). This was more pronounced at 6 hpi, where the majority of virions colocalised within TWIK2 positive endo/lysosomes (Figure 5.6, bottom panels & zoom). The localisation of TWIK2 to endo/lysosomes and the passage of virions through these vesicles strongly implicates TWIK2 function is potentially required for BUNV endosomal trafficking and/or release.

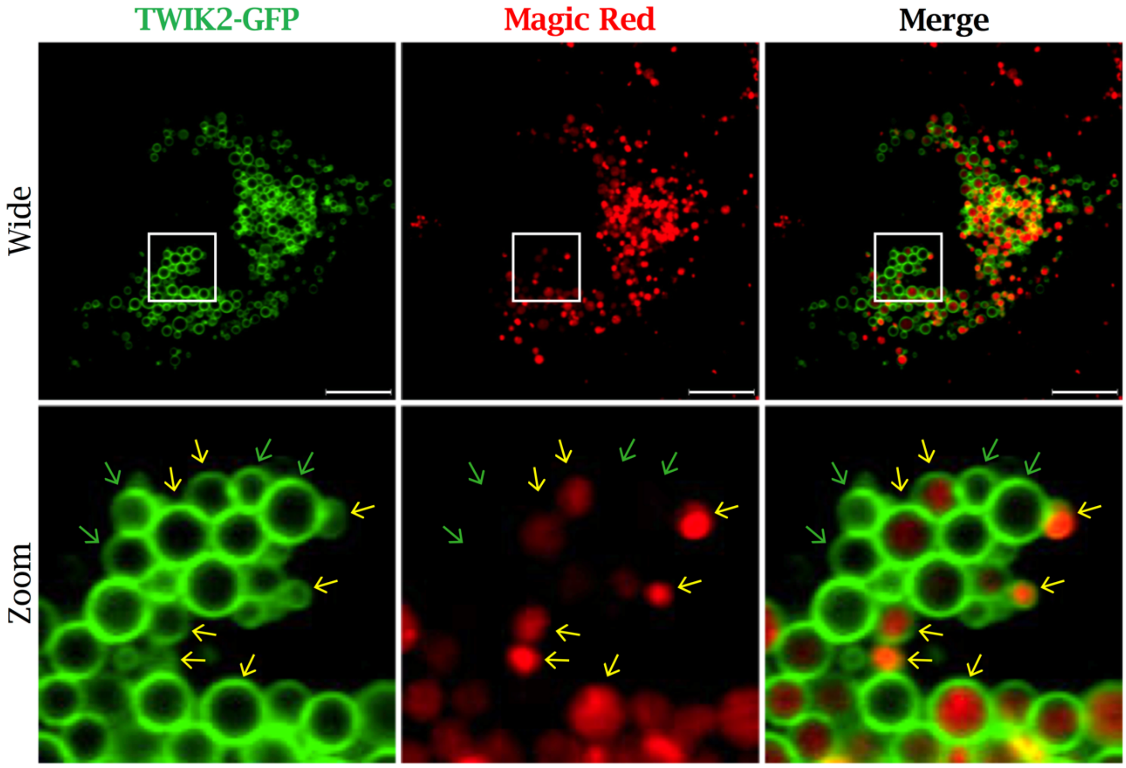

Figure 5.5 TWIK2 localises to lysosomes

TWIK2-GFP was transfected into A549 cells. After 24 hrs, Magic Red (cathepsin B dye) was added to cells for 40 mins to allow uptake prior to live cell imaging. Images (>20 cells) are representative (scale bar = 10 µm). Yellow arrows indicate TWIK2-GFP and Magic Red colocalisation, green arrows indicate no colocalisation.

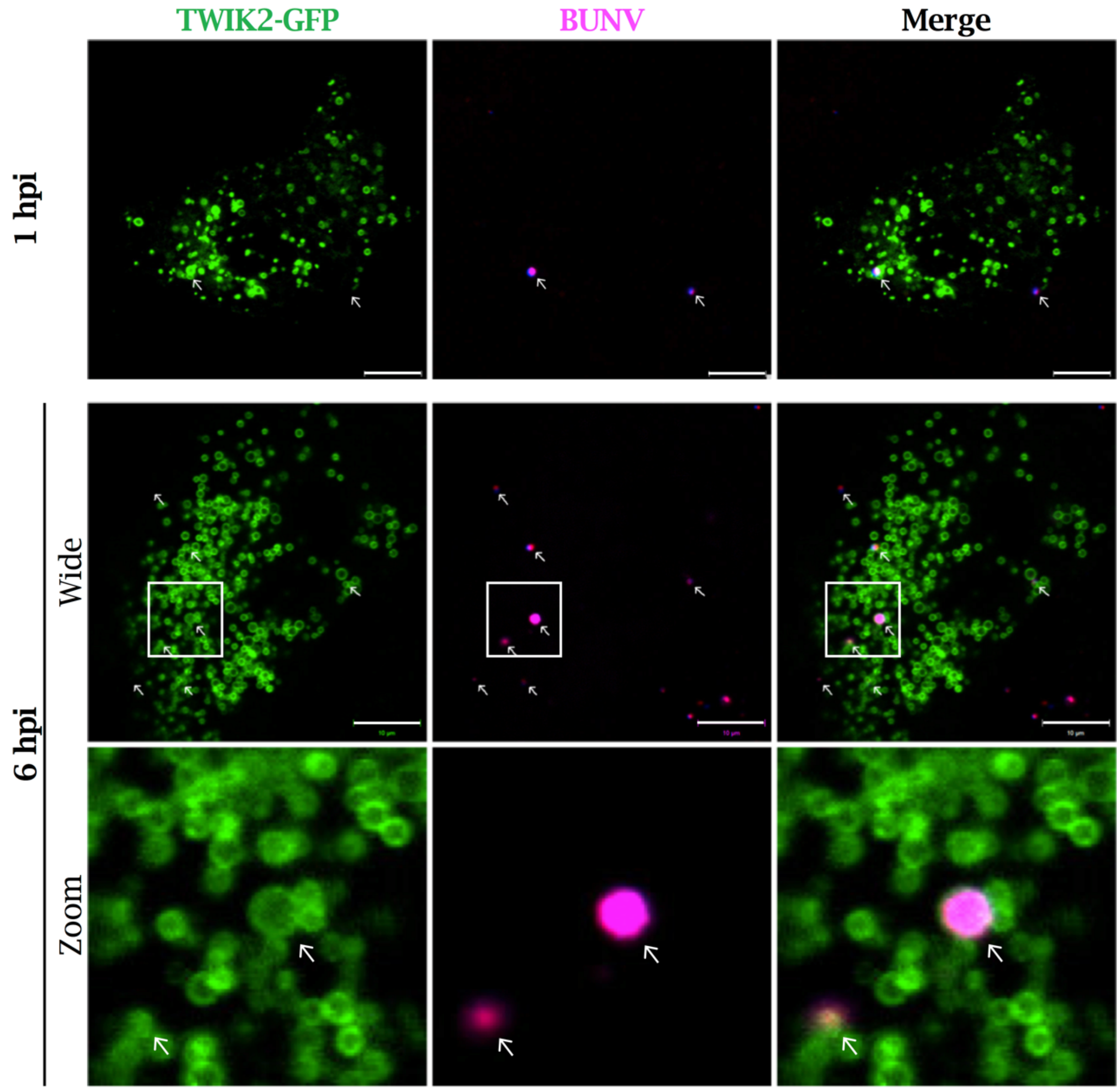

Figure 5.6 BUNV localises to TWIK2-containing endosomes
A549 cells were transfected with TWIK2-GFP 24 hrs prior to infection with SYTO82/DiD-BUNV (MOI = 0.2) and live cell images taken at 1 (>10 cells) and 6 hpi (>15 cells) (scale bar = 10 µm). White arrows indicate labelled virions.

5.4.2 SDM to abolish endosomal trafficking motifs leads to TWIK2 re-localisation

To further investigate the importance of TWIK2 localisation during BUNV endosomal events, it was reasoned that preventing TWIK2 localisation to endo/lysosomes would similarly prevent BUNV infection. *Bobak et al* (2017) recently used SDM to abolish three predicted endosomal trafficking motifs in the C-terminal cytoplasmic tail of TWIK2 (253). Various combinations of mutations were performed to alter TWIK2-GFP expression on rat and human endo/lysosomal membranes (253). Mutation of trafficking motifs led to increased plasma membrane expression and reduced internal vesicular localisation. A similar method was employed herein, in which the mutations outlined in Figure 5.7 A abolished the three endosomal trafficking motifs (Figure 5.7 A, orange spheres indicate location in C-terminus) and additionally mutated the conserved K^+-pore motif (purple sphere). A rational combination of mutated motifs were combined to generate recombinant channels where TWIK2 function was abolished (Y109A), re-localised to the plasma membrane (IL289/290AA, Y308A) or re-localised to the plasma membrane with reduced channel function (LL270/271AA, IL289/290AA, Y308A). Figure 5.7 B outlines the mutants generated alongside their predicted localisation, as determined by *Bobak et al* (2017), and the effect on channel function, which were predicted from the current amplitudes recorded (253).

The mutants were transfected into A549 cells, alongside wild type (WT) TWIK2-GFP. EGF-Texas Red was added to growth medium for 40 mins to label endosomal compartments 48 hrs post-transfection. Images showed that WT TWIK2-GFP was expressed in intracellular vesicles, some of which co-localised (yellow arrows) with EGF owing to its localisation within LEs (Figure 5.8 A). This importantly confirms that TWIK2 localises to LE, the compartments from which BUNV is thought to undergo fusion/endosomal escape. Similarly to the WT channels, the Y109A mutant (panel 1; loss of function) retained its endosomal localisation. However, the other mutants showed altered distribution (panels 2 & 3; re-localisation & reduced function/re-localisation, Figure 5.8 B) leading to reduced expression within intracellular vesicles, more diffuse plasma membrane-like expression and a loss of EGF co-localisation. This indicated that the endocytic mutants led to re-localisation of TWIK2 from endocytic compartments, likely to the plasma membrane.

To determine whether the re-localisation of TWIK2 to the plasma membrane or the prevention of its K^+ channel pore function impeded BUNV infection, cell lines stably expressing each construct were generated. This was necessary due to the low transfection efficiencies typically observed in A549 cells. However, despite efforts, cells stably expressing TWIK2-GFP (WT or mutant cells) were consistently unviable for sustained time periods. This may be explained by the prolonged expression of the WT and mutant forms of this channel perturbing normal endosomal processes that are ultimately required for cell survival. Examples include EGFR trafficking and signalling to maintain cell growth and proliferation (309).

Given the ability of TWIK2 to form heterodimeric channels with other K_{2P} family members, the identification of these specific heterodimers may reveal a more focussed drug target/silencing strategy. Of note, TWIK2 silencing in transient assays did not impede cell viability suggesting the short-term targeting remains a viable strategy.

A

	Motif	Mutation
Y109A	GYG conserved pore region	Y => A
LL270/ 271AA	ELILL predicted endosomal trafficking motif	LL => AA
IL289/ 290AA	DEDDRVDIL predicted endosomal trafficking motif	IL => AA
Y308A	YASIP predicted endosomal trafficking motif	Y => A

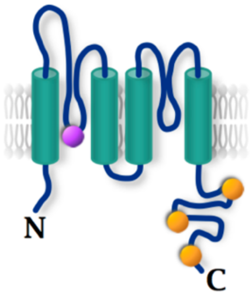

B

	WT	Y109A	IL289/290AA, Y308A	LL270/271AA, IL289/290AA, Y308A
Endosomal localisation	/ (~95%)	/ (~95%)	- - (~6%)	- - (~1%)
Channel function	/	- -	+	- -

Figure 5.7 Generating TWIK2 localisation mutants

(A) Table depicting the mutations of the conserved pore motif and the predicted localisation motifs. The diagram of a K_{2P} channel indicates the location of each motif in the pore region (GYG, purple) and cytosolic C-terminus (three trafficking motifs, orange). **(B)** Table indicating the three mutants generated and the combination of mutations used. The endosomal localisation, as predicted by *Bobak et al* (2017), is indicated for each channel alongside the % endosomal localisation in rat oocytes. The predicted effects on channel function are also indicated, as determined by patch clamping (/ = no change, -- = significant reduction, + = increased) (253).

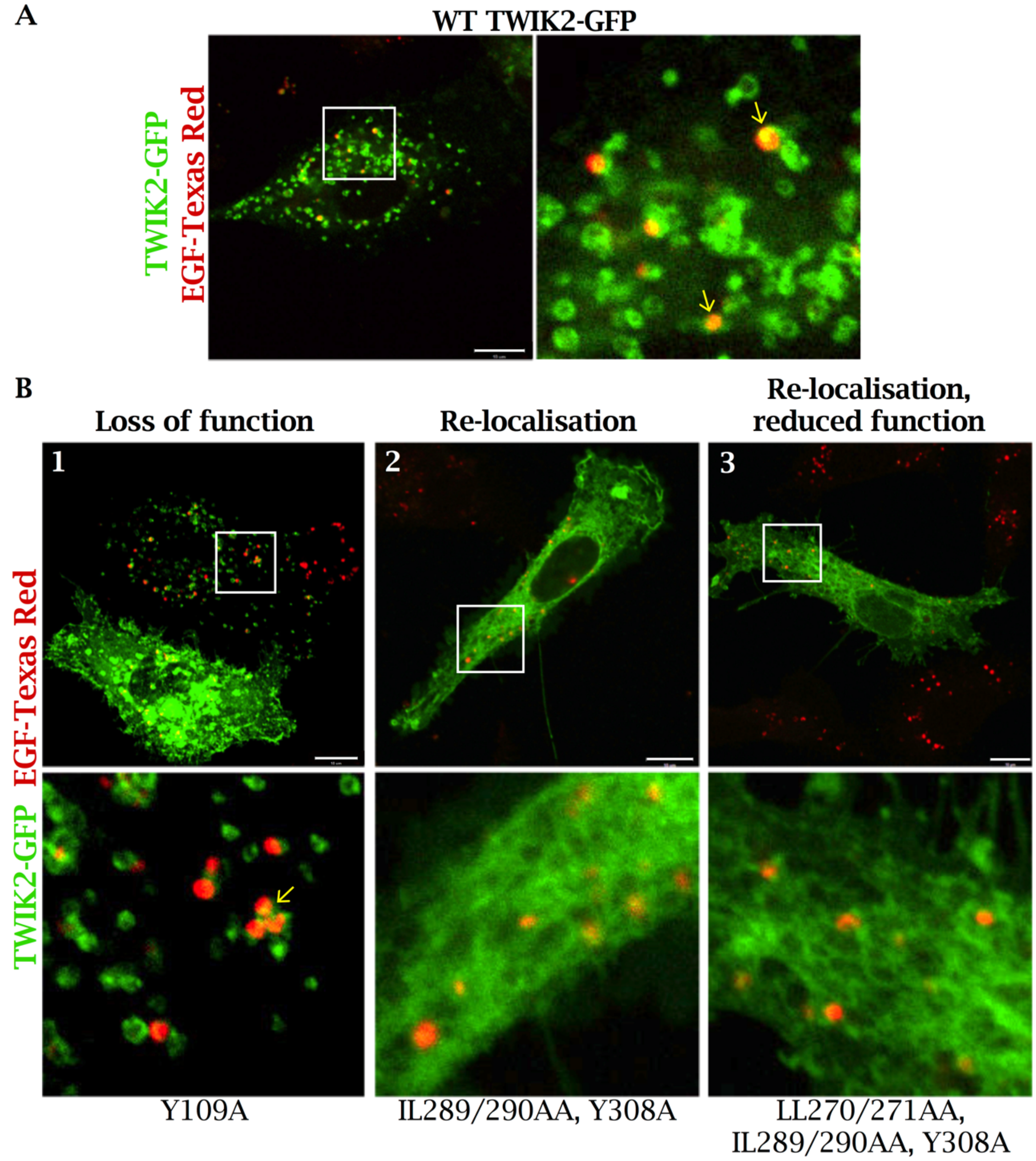

Figure 5.8 Mutations in TWIK2 endosomal localisation signals reduce TWIK2 endosomal sorting

SDM was used to generate three TWIK2-GFP mutants with a loss of function (Y109A), re-localisation to the plasma membrane (IL289/290AA, Y308A), or reduced function and re-localisation (LL270/271AA, IL289/290AA, Y308A). A549 cells were transfected with **(A)** ‘wild-type’ TWIK2-GFP (WT) and **(B)** each mutant and incubated for 48 hrs. Texas Red-conjugated EGF (EGF-Texas Red) was added to cells for 40 mins to allow endosomal uptake. Non-internalised EGF was removed and transfected cells were imaged (scale bar = 10 µm).

5.5 Discussion

In this investigation K_{2P} channels important in the lifecycle of BUNV were identified through infection of HAP-1 cells, which express only 4 of the 14 known K_{2P} channels (Figure 5.2 B) (307). As these cells were permissive to BUNV infection, it was likely that one or a number of these K_{2P} channels, were of importance to the virus fulfilling its lifecycle (244). Limited information is available regarding the cellular functions of specific K_{2P} channels, however it is established that they produce a 'leak-like' conductance on the plasma membrane which maintains the resting membrane potential of cells (174,310). The identification of individual channel functions and localisation is however convoluted, owing to discrepancies between the cell line, species and expression systems used (253,310).

Interestingly the K_{2P} channels TWIK1, TWIK2 and TREK1 have been reported to localise within intracellular vesicular membranes, and although the function of these K_{2P} channels are not fully elucidated, channel internalisation is thought to be a mechanism for controlling surface expression (311). *Bobak et al* (2017), however, identified that TWIK2 predominantly localises to lysosomal membranes in human HEK293 cells and that TWIK2 affects lysosome size, indicating a functional role within these compartments (253). Consistent with this finding, TWIK2 localised to lysosomes in A549 cells (Figure 5.5), but additionally colocalised with EGF-containing LEs and labelled endosomal compartments devoid of Magic Red fluorescence, suggesting a role beyond that predicted solely in lysosomes. It would therefore be interesting to investigate the other endosomal compartments containing TWIK2 channels, such as using markers for EEs and REs (as was performed in Chapter 3). In addition, it was intriguing that siRNA knockdown of TWIK2 in A549 cells prevented BUNV infection (Figure 5.3 & Figure 5.4), as TWIK2 could be facilitating the requirement for endosomal K^+ channels identified in Chapter 3.

Although the specific function of TWIK2 within lysosomes is unknown, in macrophages TWIK2 mediates NLRP3 and subsequent inflammasome activation, demonstrating that TWIK2 has intracellular functions (312). Lysosomes influence cell growth and autophagy, alongside canonical degradation of internalised components (313). A link has not been established between K^+ flux and lysosome-induced processes however it is interesting to speculate a role for TWIK2 in endosomal K^+ accumulation, particularly considering TWIK2 currents are regulated by factors that change through endo/lysosomal compartments;

including pH, stretch and bioactive lipids (253,310). Limited studies are available regarding the functional role of different endo/lysosomal ion channels, where cation transport is primarily thought to regulate the internal H^+ concentration and its associated organelle functions. K^+ currents have been identified across endo/lysosomal membranes and appear to contribute to organelle membrane potential (253,314). TMEM175 and TWIK2 are to-date the only K^+ channels shown to be functional within lysosomes (278), however the co-localisation of BUNV with TWIK2-containing endo/lysosomes and the requirement for TWIK2 during infection suggests a functional endosomal link. These data, alongside the requirement for the high endosomal $[K^+]$ previously established for BUNV endosomal escape (Chapter 3, Figure 3.19 and Figure 3.20), implicates a role for TWIK2 in regulating the endosomal K^+ balance. Pharmacological inhibition or knockdown of TWIK2 may alter the endosomal K^+ distribution and prevent BUNV infection. This however requires further investigation using the endosomal K^+ dye AG4 previously described (Chapter 3, Figure 3.14) alongside other endosomal markers. The effect on endosomal $[K^+]$ by TWIK2 silencing (siRNA), or mutating TWIK2 endo/lysosomal localisation signals to re-localise TWIK2 to the plasma membrane (as performed in Figure 5.7 and Figure 5.8), can also be used to confirm this link. If TWIK2 is facilitating this K^+ requirement of BUNV, pH/K^+ pre-infection priming of the virus (previously shown, Chapter 3 Figure 3.4) should allow a partial recovery in the block of BUNV infection by TWIK2 knockdown; as was found by primed-virus infection with pharmacological channel inhibition (Chapter 3, Figure 3.7 A (247)).

Although this work has not exclusively determined TWIK2 as the sole K_{2P} channel required for BUNV entry, significant progress has been made towards this goal. Further confirmation of the requirement of TWIK2 during BUNV infection requires validation with alternative silencing approaches, including TWIK2-GFP trafficking mutants and CRISPR/Cas9 TWIK2 knockouts. Identification of the K_{2P} channels to which TWIK2 heterodimerises and indeed the cellular interacting partners that regulate TWIK2 function may further reveal new cellular requirements for BUNV infection. To this effect, experiments have begun to assess a Human Silencer Select Library of 337 siRNAs targeting over 100 different ion channels (Ambion #A30084). This will be used as a high throughput technique to elucidate essential ion channels required for BUNV infection and may reveal the full complement of K^+ channels required during virus infection. It will also be interesting to investigate the identified channels, including TWIK2, for other bunyaviruses including those previously shown to require K^+ channel function (HAZV and SBV (244)). It is hoped that this will reveal new pharmacological targets to prevent virus infection across the *Bunyavirales* order.

Chapter 6 | Final Discussion

6.1 What is the cellular role for endosomal [K^+] regulation?

The data presented in Chapter 3 identified a [K^+] gradient which increases through endosomal compartments that is high within LEs, but is reduced within acidic lysosomes, suggesting specific control of endosomal [K^+] (Figure 3.14). Importantly, the inhibition of K^+ channel function altered this K^+ distribution providing a key link between K^+ channels and endosomal [K^+] (247). Limited research is available regarding the function of endosomal K^+ flux, and similarly the identity and function of endosomal K^+ channels is limited. It is established that H^+ flux is essential for endosome acidification, cargo sorting and intraluminal vesicle formation, mediated through the activity of the ATP-dependent proton pumps present in the endosomal membranes (173,315,316). Counter-ion flux in endosomes is required for complete acidification and normal endosome function. For example, endosomal ion channels and exchangers permit H^+ influx in exchange for Cl^- or K^+/Na^+ (173). The disruption of ion exchange in endosomes often leads to secondary effects on H^+, hindering the identification of specific functional roles of each of these channels or exchangers in the endosomal system (173). Investigations into endosomal ClC channel function were however amongst the first to successfully uncouple Cl^- flux from the maintenance of H^+. Endo/lysosomal defects in mice have previously been linked to altered endocytic pH, which persists after ClC channel knockout, with endocytic H^+ intact, implicating a role for Cl^- flux in endocytic function (317). It is therefore likely that endo/lysosomal K^+ channels (and others) have roles other than the maintenance of endosomal pH. Consistent with this, investigation into endosomal [K^+] in Chapter 3 demonstrated that K^+ channel inhibition altered [K^+] distribution without inhibiting lysosomal function or pH, demonstrated using pHRodo (H^+ dye) and Magic Red (lysosomal cathepsin B-cleaved dye), respectively (Figure 3.16 and Figure 3.17). Thus, similarly to ClC, endocytic K^+ accumulation is independent from H^+ maintenance.

During BUNV infection, the data presented here demonstrates an essential requirement for endosomal K^+ ions and the physical changes associated with GP architecture, as demonstrated by *in vitro* priming assays (Chapter 3 (247)) and EM (Chapter 4). This demonstrates that K^+ ions can cause structural changes in proteins. This was also shown by *Stauffer et al* (2014), where priming IAV virions for entry using K^+ ions induced structural changes in viral proteins (258). The post-fusion crystal structure of the GP from a different bunyavirus, ANDV, was solved with a K^+ ion coordinated between two residues, which stabilised the complex and was similarly essential for GP function (298). These functional roles for K^+ on viral structural rearrangements during endocytic transit demonstrates their ability to perform endosomal roles.

Viruses are known to hijack cellular components, and it is unlikely that this is a viral-specific function, as opposed to a cellular function co-opted by viruses for cell penetration. There is growing evidence that the microenvironment of endosomal membranes plays a significant role in cargo trafficking and sorting to correct endocytic destinations (173,318). Ion channels, including K^+ channels resident on endosomal membranes generate the local ionic microenvironments necessary for protein function during cargo sorting. There is evidence linking mutations in the Na^+-H^+ exchanger (NHE) 6 protein with altered expression of an E3 ubiquitin ligase (UBE3A) in which no changes in endosomal pH were observed. However, NHE6 conducts both K^+ or Na^+ into endosomes and contributes to the local ionic microenvironment within endosomes, affecting UBE3A function (173,319). Interestingly, cullin-3 is a scaffold protein which forms part of a complex with UBE3A and RNAi-mediated silencing led to altered trafficking within LE and lysosomal compartments. This was determined by IAV infection of cullin-3 silenced cells, in which trafficking to LE/lysosomes occurred, but viruses were unable to uncoat, remaining trapped within endo/lysosomes. Additionally, EGFR trafficking into lysosomes for degradation is similarly disrupted by cullin-3 knockdown, and EGF accumulated in LEs, suggesting a link between NHE6-associated ion flux and protein trafficking (263). In keeping with this, knockdown of NHE8 impaired EGFR lysosomal trafficking and its associated degradation, indicating a direct role between K^+/Na^+ influx and EGFR sorting to lysosomes (309).

The ionic environment established by endosomal ion channels contributes to receptor-ligand interactions, some of which are affected by ionic alterations (173). The low-density lipoprotein (LDL) ligand for example, binds its receptor (LDLR) and the LDL-LDLR complex is internalised into endosomes where the ligand and receptor dissociate within acidic compartments. The LDL ligand is then trafficked to lysosomes for degradation, whilst LDLR is recycled back to the plasma membrane (320). *Zhao et al* (2010) showed that LDL dissociation is facilitated by both acidic pH and Ca^{2+} concentration, where Ca^{2+}- and H^+-dependent mechanisms cooperate for efficient ligand dissociation (321). Similarly, the mannose receptor binds to high-mannose proteins and its dissociation within endosomes requires an acidic environment and Ca^{2+} efflux, whereby disruption of the Ca^{2+} gradient across endosome membranes prevents dissociation (322). This plays a role in mannose-modified hydrolase trafficking from the Golgi, through endosomes and into lysosomes, facilitated by mannose phosphate receptors (323,324). This demonstrates a direct link between ions and receptor-dissociation, but links to the control of ionic concentrations by specific endosome-resident ion channels has not been established.

There is growing evidence linking endosomal ion flux and local ionic microenvironments with endosome-resident protein function during cargo trafficking and receptor binding. Despite these links, the specific actions of endosomal K^+ accumulation on cellular proteins and its associated roles in endosome function remains unknown. The action of K^+ ions on virus structure and entry identified here does however provide a useful tool to begin to investigate this cellular role.

6.2 K^+-priming for improving therapeutic delivery

Gene therapy is increasingly investigated for treatment of multiple disorders; including CF, cancer and autoimmune diseases (325–328). The delivery of therapeutic transgenes into host cells is a key barrier for effective treatment and the employment of non-viral and viral based vectors have been investigated. Viral vectors represent improved methods for gene delivery as they are perfectly adapted for cell penetration and provide efficient modes of delivery (325). A formidable barrier for both viral and non-viral vectors however is cell penetration, where entry via receptor-mediated endocytosis improves the efficiency of gene delivery, however often leads to sequestration within endocytic compartments (329). Non-viral vectors typically include liposomes, micelles and polymers which encapsulate miRNAs, however these non-viral vectors are often associated with toxicity, poor transfection and the non-specific biodistribution shown in clinical trials (326). *Orellana et al* (2017) utilised a folate-ligand to deliver miRNAs into cancer cells which overexpress folate receptors, however their efficiency was limited due to endosomal sequestration (330). It was interesting that in their subsequent work they utilised the changing ionic environment within endosomes to improve delivery, where K^+ influx is favoured and importantly balanced by efflux of Na^+ down its electrochemical gradient into the cytosol. Nigericin, a K^+ ionophore which causes K^+ influx in exchange for H^+, led to endosome swelling and bursting (329,331). This allowed more efficient delivery of miRNAs into the cell and demonstrates how research towards the endocytic ionic environment can improve delivery for gene therapy.

Despite advances in non-viral vectors, viral-vectors remain the first choice for gene and drug delivery. Only a single virus is required to infect a cell to produce numerous virus copies. Gene therapy viral-vectors deliver exogenous nucleic acids into cells, though new copies of the viruses are not produced. The number of cells receiving the target gene are therefore relatively low and each stage of vector production and delivery requires optimisation to improve efficiency (327). In CF, it has been shown *in vitro* that 60 % of cells must receive and express a functioning copy of the CFTR channel for normal Cl^- secretion and Na^+ transport. In clinical trials however, the efficiency remains low, only reaching 20 %, meaning improved gene transfer is required (327,332). This limited transfer is due to multiple factors including cell-specific targeting of vectors, mucociliary clearance and slow endocytosis rates in the airway epithelium (327,333).

It was established in Chapter 3 that pH/K^+ priming of BUNV virions prior to infection increases virus efficiency, allowing virions to rapidly escape endosomes and more rapidly establish an infection. It would be interesting to identify the effects of pH/K^+ priming on viral-vectors for gene therapy, as endocytosis is a common barrier. For CF, slow rates of endocytosis in the airway epithelium contribute to a reduced efficacy of gene transfer (333). This in part can be caused by the dysregulated CFTR and its effects on endosomal pH in CF cells (334,335). In CF gene therapy, viral-vector priming can be used to overcome this barrier to cell entry by providing a biochemical cue, limiting the time required within endosomes to improve viral entry and gene transfer. Interestingly, alterations of pH homeostasis also occur in multiple cancers and can limit the endosomal escape of viral vectors that require an acidic pH (336). Viral priming in cancer therapy could similarly improve the efficiency of vector entry and associated gene transfer.

The priming effects on BUNV (in Chapter 3) were shared by HAZV and other viruses, such as IAV, and have been shown to similarly depend on endosomal ions for efficient entry (77,247,258). It is likely that other viruses that have not yet been identified rely on endosomal [K^+] for entry and endosomal escape, which is accelerated by priming. It would therefore be interesting to assess the effects of virion priming for those viruses currently used for gene therapies.

6.3 Ion channel drug repurposing for anti-viral therapeutics

Drug repurposing as a means to treat viral infections is emerging as a rapid method for the identification of existing licensed drugs, which expedite the approval of effective therapeutics against viral infections. Licensed drugs may act on cellular targets in diseases or anti-viral targets in virus infections, and have been assessed for their therapeutic activity against different virus infections. The repurposing potential of many drugs is determined through large scale small-molecule inhibitor screens and the specific mechanism of action against that virus is then identified (337). This method of therapeutic discovery is aimed at improving the low success rates and high costs of newly discovered drugs, exploiting their established efficacy in clinical trials.

Ion channels account for 19 % of human protein targets and 18 % of licensed small-molecule drugs target them for therapeutic activity (in the USA; FDA approved 2017) (338). This accounts for a considerable proportion of licensed drugs and demonstrates the efficacy of ion channel targeting and repurposing for therapeutic treatments. The focus of ion channel drug repurposing is currently their use as anticancer drugs (339) as many cancers are known to alter ion channel expression and function (185,197). Ion channel drugs are currently licensed as antiepileptics, anaesthetics and antiarrhythmics, however their action against specific ion channels tends to be identified after drug discovery, rather than as an initial target. This hinders their use for drug repurposing and limits information regarding the cellular function of specific ion channels as few tools are available to study them. Significant advances have however been made, which permit the identification of the mode of action of different drugs against specific ion channels (186). Well-known examples include lidocaine, a local anaesthetic that inhibits Na_V channels, and benzodiazepine Diazepam, used to treat anxiety and insomnia through inhibiting K^+ $GABA_A$ channels (202).

Despite the number of licensed inhibitors available, the wide tissue distribution and plethora of physiological roles of ion channels remain largely unexplored as anti-viral therapeutics. Verapamil, amiodarone and dronedarone are clinically available anti-hypertension drugs that inhibit L-type Ca_V channels, used by *Gehring et al* (2014) to successfully inhibit EBOV and Marburg virus (Filoviruses) entry in cell culture (235). Similarly HSV-1 entry could be inhibited by the Cl^- channel modulator and licensed anti-breast cancer drug tamoxifen (233). Although these drugs do not specifically target ion channels, their clinical availability highlights their promise for anti-viral repurposing, although to-date, this has not been pursued. It was shown previously ((244) and in Chapters 3 & 5) that multiple bunyaviruses require K^+ channel function for virus infection. This was determined to be during virus entry (247) and a specific K_{2P} channel TWIK2 was identified as required for BUNV infection. Similarly to EBOV and HSV-1, BUNV could also be inhibited by a number of FDA (US) approved drugs including bupivacaine (local anaesthetic), haloperidol (antipsychotic), fluoxetine (antidepressant) and the anti-prostate cancer drugs curcumin and genistein (244). Although these drugs possess activity against multiple ion channels, they commonly inhibit a number of K_{2P} channels, select members of which are required for BUNV infection (174,340–343). In particular, haloperidol and fluoxetine possess good oral bioavailability shown in clinical trials, tend to be well-tolerated by patients and are able to cross the blood-brain barrier (BUNV shown to infect CNS in horses) (344–346). These therefore represent candidates for anti-bunyavirus repurposing. Future investigations should aim to identify the efficacy of these drugs against BSL 3 and 4 bunyaviruses; such as CCHFV. As a mechanism of action for K^+ channel modulators against bunyaviruses has been defined, including the identification of a specific channel (TWIK2), repurposing these drugs for anti-bunyavirus therapy would expedite pre-clinical (animal) trials. This could allow assessment of the human clinical trial phase (337), where current prophylactic options are limited, providing a considerable economic advantage over new drug development.

6.4 Conclusions

The *Bunyavirales* are the largest order of negative sense ssRNA viruses with over 500 named species, members of which are capable of infecting humans, animals or plants. Over 20 bunyaviruses can lead to severe haemorrhagic fever, encephalitis and/or death in humans and new viruses are continually emerging due to the segmented nature of their genome. In addition, increasing geographic spread of the vectors also contributes to an increased pandemic potential of these viruses. It is therefore surprising that there are no effective licensed treatments or vaccines for human infections and animal experiments are limited, highlighting the need for effective anti-virals.

In an attempt to identify the anti-viral targets required to prevent infection, previous work identified cellular proteins and mechanisms required for bunyavirus infection using the prototype bunyavirus, BUNV. To this effect, K^+ channels were identified as a host-cell factor required for bunyavirus infection (244). Importantly, K^+ channels were not only necessary for BUNV infection (*Peribunyaviridae* family), but also for the model virus of the *Nairoviridae* family, HAZV, and a pathogenic animal Peribunyavirus SBV; suggesting this K^+ channel requirement could be pan-bunyaviral. Subsequent work identified K^+ channel function is vital during early stages in the BUNV lifecycle, prior to viral translation and replication however after virus internalisation into endosomes.

The work outlined in this thesis sought to identify the molecular mechanisms by which K^+ channels are required for bunyavirus infection and identify the specific K^+ channels mediating this process. Chapter 3 began by investigating the lifecycle stage that requires channel function, where the timeline of BUNV infection indicated virion trafficking through endosomes or fusion and genome release. Owing to the recent finding by *Stauffer et al* (2014) (258) that endosomal K^+ ions are required for IAV entry, it was reasoned that endosomal K^+ ions may be important during bunyavirus entry. By mimicking the endosomal pH and $[K^+]$ *in vitro*, treating virions pre-infection with pH 6.3 and high $[K^+]$ increased BUNV infection. In fact pH/K^+-priming increased the efficiency of BUNV endosomal release, expediting trafficking and fusion events. Importantly priming also reduced BUNV sensitivity to K^+ channel inhibition, where priming provides a biochemical cue for genome release established by K^+ channels in endosomes; a previously undescribed role for K^+ channels. Use of the membrane-impermeable dye AG4 which labels high-$[K^+]$ containing vesicles revealed that $[K^+]$ is high within LEs as previously shown, however is low within the highly acidic lysosomes. Endosomal [K^+] is therefore tightly regulated and increase is more than simple accumulation down the endosomal system. To investigate endosomal K^+ in BUNV fusion events, a dual-fluorescently labelled BUNV was generated to allow the live tracking of virions in endosomes. Virions could be tracked entering EEs and on into LEs, where virions localised to high-[K^+] containing endosomes (AG4) further suggesting a role for K^+ ions in endosomes. As BUNV enters sites of high-[K^+] and K^+ channels are required for infection, it was reasoned that this K^+ distribution within endosomes is important for infection and could be controlled by endosomal K^+ channel function. This was confirmed as pharmacological inhibition of K^+ channels shifted the high-[K^+] distribution from LEs, which then peaked within lysosomes. Similarly, K^+ channel inhibition shifted the localisation of BUNV into lysosomes and virions were shown to accumulate over time, indicating they were "trapped" within endocytic compartments. It was concluded that pH and K^+ are biochemical cues for BUNV fusion and entry events within endosomes and K^+ channels control this endosomal K^+ balance. Inhibition of K^+ channels therefore prevents BUNV infection by shifting this high-[K^+] into lysosomes where BUNV is not able to establish the essential biochemical changes for fusion, remaining trapped within endocytic compartments (247).

As the priming experiments outlined in Chapter 3 showed that K^+ ions are having a direct effect on the virus, Chapter 4 sought to identify the specific structural changes elicited on the virus during priming. Cryo-EM of low pH and/or K^+ treated BUNV revealed clear changes in virion architecture and when virions were treated at a reduced pH of 6.3, mass aggregation of virions occurred. Virions treated at pH 6.3/K^+ appeared more pleomorphic than controls, however did not form these large aggregates suggesting that K^+ is acting in a pro-viral mechanism preventing virion aggregation in endosomes. It was predicted that K^+ is acting on the virion exterior and likely on the GPs which cover the virion surface. Cryo-ET and STA of virion spikes were performed on pH 7.3 treated (control) and pH 6.3/K^+ treated (primed) virions, being the most physiological conditions. This revealed that BUNV virions are indeed covered by GPs, which form tripod-like structures protruding from the virion envelope. At this higher resolution than previously obtained, the three monomers were identified which neatly fit the recently solved crystal structure of the BUNV Gc head domain and SBV stalk domain. A previously unidentified region of density was also identified protruding from the base of the stalk domain which was predicted to contain the fusion loop, which facilitates viral-endosome membrane interactions and fusion. In contrast cryo-ET of the pH 6.3/K^+ primed virions revealed a disordered arrangement of GPs and regions of the membrane devoid of spikes. STA also revealed that the spike trimer had dissociated upon pH 6.3/K^+ treatment, which could indicate a pre-fusion intermediate where the virus is 'primed' for fusion and ready to interact with the endosome surface. This meant that, in comparison to the pH 6.3 (no K^+) treated virus, K^+ elicits controlled changes in GP spikes where the fusion loop is still protected to some extent and prevents virion interactions with one another. This confirmed that endosomal pH and K^+ are biochemical cues for virus entry and elicit specific structural changes essential for this process. Importantly, this established a previously unknown process for K^+ ions in endosomes and the tight control of this distribution by K^+ channels suggests K^+ plays a key role in endosomal function, which is co-opted by viruses during entry. This also suggests that the endosomal K^+ requirement may not be bunyavirus specific and could be shared with other viruses, identifying potential anti-viral targets.

To allow the development of anti-virals against BUNV and its requirement for K^+ channels, the specific K^+ channels need to be identified. Chapter 5 therefore followed previous data indicating the K_{2P} channel family contains members required for infection. Using alternative cell lines expressing specific K_{2P} channels and siRNA knockdowns, TWIK2 was identified as a K^+ channel family member required for infection. TWIK2 was shown to localise within endo/lysosomal compartments and using the labelled-BUNV colocalised with virions during entry. This indicates TWIK2 as a likely candidate that facilitates the endosomal K^+ requirement of BUNV during entry. A number of licensed pharmacological inhibitors of K_{2P} channels were previously shown to inhibit BUNV, demonstrating the efficacy of this target in preventing bunyavirus infection in the clinic. The repurposing of existing drugs would lead to a fast and economic prophylactic treatment for bunyavirus infections, where effective options are currently limited for patients.

References

1. Maes P, Alkhovsky S V., Bào Y, Beer M, Birkhead M, Briese T, et al. Taxonomy of the family Arenaviridae and the order Bunyavirales: update 2018. Arch Virol. 2018 Aug 21;163(8):2295–310.
2. Maes P, Adkins S, Alkhovsky S V., Avšič-Županc T, Ballinger MJ, Bente DA, et al. Taxonomy of the order Bunyavirales: second update 2018. Archives of Virology. 2019;
3. Abudurexiti A, Adkins S, Alioto D, Alkhovsky S V., Avšič-Županc T, Ballinger MJ, et al. Taxonomy of the order Bunyavirales: update 2019. Arch Virol. 2019 May 7;1–17.
4. Li C-X, Shi M, Tian J-H, Lin X-D, Kang Y-J, Chen L-J, et al. Unprecedented genomic diversity of RNA viruses in arthropods reveals the ancestry of negative-sense RNA viruses. Elife. 2015 Jan 29;4.
5. Wolf YI, Kazlauskas D, Iranzo J, Lucía-Sanz A, Kuhn JH, Krupovic M, et al. Origins and Evolution of the Global RNA Virome. MBio. 2018 Dec 27;9(6):e02329-18.
6. Shi M, Lin X-D, Chen X, Tian J-H, Chen L-J, Li K, et al. The evolutionary history of vertebrate RNA viruses. Nature. 2018 Apr 4;556(7700):197–202.
7. Walter CT, Barr JN. Recent advances in the molecular and cellular biology of bunyaviruses. J Gen Virol. 2011;92(Pt 11):2467–84.
8. Hallam SJ, Koma T, Maruyama J, Paessler S. Review of Mammarenavirus Biology and Replication. Front Microbiol. 2018;9:1751.
9. Mielke-Ehret N, Mühlbach H-P. Emaravirus: a novel genus of multipartite, negative strand RNA plant viruses. Viruses. 2012;4(9):1515–36.
10. Toriyama S, Kimishima T, Shimizu T, Takahashi M, Minaka N, Akutsu K. The complete nucleotide sequence of the rice grassy stunt virus genome and genomic comparisons with viruses of the genus Tenuivirus. J Gen Virol. 1998 Aug 1;79(8):2051–8.
11. Mahaffy AF, Haddow AJ, Smithburn KC. A Neurotropic Virus Isolated from Aedes Mosquitoes Caught in the Semliki Forest. Am J Trop Med Hyg. 1946 Mar 1;s1-26(2):189–208.

12. Elliott RM. Emerging viruses: the Bunyaviridae. Mol Med. 1997;3(9):572.

13. Garrison AR, Smith DR, Golden JW. Animal Models for Crimean-Congo Hemorrhagic Fever Human Disease. Viruses. 2019 Jun 28;11(7):590.

14. Mazelier M, Rouxel RN, Zumstein M, Mancini R, Bell-Sakyi L, Lozach P-Y. Uukuniemi Virus as a Tick-Borne Virus Model. J Virol. 2016;90(15):6784–98.

15. Jiang W, Wang P, Yu H, Zhang Y, Zhao K, Du H, et al. Development of a SYBR Green I based one-step real-time PCR assay for the detection of Hantaan virus. J Virol Methods. 2014 Feb 1;196:145–51.

16. McElroy Horne K, Vanlandingham DL. Bunyavirus-Vector Interactions. Viruses. 2014;6(11):4373–97.

17. Mardani M, Keshtkar-Jahromi M, Adibi P, Ataie B. Crimean-Congo Hemorrhagic Fever Virus as a Nosocomial Pathogen in Iran. Am J Trop Med Hyg. 2009 Oct 1;81(4):675–8.

18. Padula PJ, Edelstein A, Miguel SDL, López NM, Rossi CM, Rabinovich RD. Hantavirus Pulmonary Syndrome Outbreak in Argentina: Molecular Evidence for Person-to-Person Transmission of Andes Virus. Virology. 1998 Feb 15;241(2):323–30.

19. Weber F, Elliott RM. Antigenic drift, antigenic shift and interferon antagonists: how bunyaviruses counteract the immune system. Virus Res. 2002 Sep;88(1–2):129–36.

20. Briese T, Calisher CH, Higgs S. Viruses of the family Bunyaviridae: are all available isolates reassortants? Virology. 2013 Nov;446(1–2):207–16.

21. Briese T, Bird B, Kapoor V, Nichol ST, Lipkin WI. Batai and Ngari viruses: M segment reassortment and association with severe febrile disease outbreaks in East Africa. J Virol. 2006 Jun;80(11):5627–30.

22. European Centre for Disease Prevention & Control. Aedes albopictus [Internet]. Available from: http://ecdc.europa.eu/en/healthtopics/vectors/mosquitoes/Pages/aedes-albopictus.aspx

23. Elliott RM. Bunyaviruses and climate change. Clin Microbiol Infect. 2009 Jun;15(6):510–7.

24. Pepin M, Bouloy M, Bird BH, Kemp A, Paweska J. Rift Valley fever virus

(Bunyaviridae: Phlebovirus): An update on pathogenesis, molecular epidemiology, vectors, diagnostics and prevention. Vet Res. 2010;41(6):61.

25. Zeller H, Bouloy M. Infections by viruses of the families Bunyaviridae and Filoviridae. Rev Sci Tech. 2000;19(1):79–91.

26. CHUMAKOV MP. Studies of virus haemorrhagic fevers. J Hyg Epidemiol Microbiol Immunol. 1963;7:125–35.

27. Bente DA, Forrester NL, Watts DM, McAuley AJ, Whitehouse CA, Bray M. Crimean-Congo hemorrhagic fever: History, epidemiology, pathogenesis, clinical syndrome and genetic diversity. Antiviral Res. 2013 Oct 1;100(1):159–89.

28. Spengler JR, Bergeron É, Spiropoulou CF. Crimean-Congo hemorrhagic fever and expansion from endemic regions. Curr Opin Virol. 2019 Feb;34:70–8.

29. World Health Organization. Annual review of diseases prioritized under the Research and Development Blueprint. Geneva, Switzerland: World Health Organization 2018. WHO. Geneva, Switzerland: World Health Organization 2018: World Health Organization; 2018.

30. Jiang H, Du H, Wang LM, Wang PZ, Bai XF. Hemorrhagic Fever with Renal Syndrome: Pathogenesis and Clinical Picture. Front Cell Infect Microbiol. 2016;6.

31. Xu B, Liu L, Huang X, Ma H, Zhang Y, Du Y, et al. Metagenomic analysis of fever, thrombocytopenia and leukopenia syndrome (FTLS) in Henan Province, China: discovery of a new bunyavirus. PLoS Pathog. 2011 Nov;7(11):e1002369.

32. Daubney R, Hudson JR, Garnham PC. Enzootic hepatitis or rift valley fever. An undescribed virus disease of sheep cattle and man from east africa. J Pathol Bacteriol. 1931 Jan 1;34(4):545–79.

33. Rolin AI, Berrang-Ford L, Kulkarni MA. The risk of Rift Valley fever virus introduction and establishment in the United States and European Union. Emerg Microbes Infect. 2013 Dec;2(12):e81.

34. Shi J, Hu Z, Deng F, Shen S. Tick-Borne Viruses. Virol Sin. 2018;33(1):21.

35. Doceul V, Lara E, Sailleau C, Belbis G, Richardson J, Bréard E, et al. Epidemiology, molecular virology and diagnostics of Schmallenberg virus, an emerging orthobunyavirus in Europe. Vol. 44, Veterinary Research.

2013.

36. Steukers L, Bertels G, Cay AB, Nauwynck H. Schmallenberg virus: emergence of an Orthobunyavirus among ruminants in Western Europe. Vol. 81, Vlaams Diergeneeskundig Tijdschrift. 2012. p. 119–27.

37. Goller K V, Höper D, Schirrmeier H, Mettenleiter TC, Beer M. Schmallenberg virus as possible ancestor of Shamonda virus. Emerg Infect Dis. 2012 Oct;18(10):1644–6.

38. Losson B, Mignon B, Paternostre J, Madder M, Deken R De, Deken G De, et al. Biting midges overwintering in Belgium. Vet Rec. 2007 Mar 31;160(13):451–2.

39. Whitfield AE, Ullman DE, German TL. Tospovirus-Thrips Interactions. Annu Rev Phytopathol. 2005 Sep 3;43(1):459–89.

40. Prins M, Goldbach R. The emerging problem of tospovirus infection and nonconventional methods of control. Trends Microbiol. 1998 Jan 1;6(1):31–5.

41. Pappu HR, Jones RAC, Jain RK. Global status of tospovirus epidemics in diverse cropping systems: Successes achieved and challenges ahead. Virus Res. 2009 May 1;141(2):219–36.

42. Ikegami T. Rift Valley fever vaccines: an overview of the safety and efficacy of the live-attenuated MP-12 vaccine candidate. Expert Rev Vaccines. 2017;16(6):601–11.

43. Ikegami T. Candidate vaccines for human Rift Valley fever. Expert Opin Biol Ther. 2019 Sep 6;1–10.

44. Wernike K, Nikolin VM, Hechinger S, Hoffmann B, Beer M. Inactivated Schmallenberg virus prototype vaccines. Vaccine. 2013 Aug 2;31(35):3558–63.

45. Kim Y-H, Kweon C-H, Tark D-S, Lim SI, Yang D-K, Hyun B-H, et al. Development of inactivated trivalent vaccine for the teratogenic Aino, Akabane and Chuzan viruses. Biologicals. 2011 May;39(3):152–7.

46. Keshtkar-Jahromi M, Kuhn JH, Christova I, Bradfute SB, Jahrling PB, Bavari S. Crimean-Congo hemorrhagic fever: current and future prospects of vaccines and therapies. Antiviral Res. 2011 May;90(2):85–92.

47. Achee NL, Grieco JP, Vatandoost H, Seixas G, Pinto J, Ching-NG L, et al.

Alternative strategies for mosquito-borne arbovirus control. Kittayapong P, editor. PLoS Negl Trop Dis. 2019 Jan 3;13(1):e0006822.

48. Bereczky S, Lindegren G, Karlberg H, Akerstrom S, Klingstrom J, Mirazimi A. Crimean-Congo hemorrhagic fever virus infection is lethal for adult type I interferon receptor-knockout mice. J Gen Virol. 2010 Jun 1;91(6):1473–7.

49. Lindquist ME, Zeng X, Altamura LA, Daye SP, Delp KL, Blancett C, et al. Exploring Crimean-Congo Hemorrhagic Fever Virus-Induced Hepatic Injury Using Antibody-Mediated Type I Interferon Blockade in Mice. J Virol. 2018;92(21).

50. Haddock E, Feldmann F, Hawman DW, Zivcec M, Hanley PW, Saturday G, et al. A cynomolgus macaque model for Crimean–Congo haemorrhagic fever. Nat Microbiol. 2018 May 9;3(5):556–62.

51. Garrison AR, Shoemaker CJ, Golden JW, Fitzpatrick CJ, Suschak JJ, Richards MJ, et al. A DNA vaccine for Crimean-Congo hemorrhagic fever protects against disease and death in two lethal mouse models. Papa A, editor. PLoS Negl Trop Dis. 2017 Sep 18;11(9):e0005908.

52. Rodriguez SE, Cross RW, Fenton KA, Bente DA, Mire CE, Geisbert TW. Vesicular Stomatitis Virus-Based Vaccine Protects Mice against Crimean-Congo Hemorrhagic Fever. Sci Rep. 2019 Dec 23;9(1):7755.

53. Aligholipour Farzani T, Földes K, Hanifehnezhad A, Yener Ilce B, Bilge Dagalp S, Amirzadeh Khiabani N, et al. Bovine Herpesvirus Type 4 (BoHV-4) Vector Delivering Nucleocapsid Protein of Crimean-Congo Hemorrhagic Fever Virus Induces Comparable Protective Immunity against Lethal Challenge in IFNα/β/γR-/- Mice Models. Viruses. 2019;11(3).

54. Mousavi-Jazi M, Karlberg H, Papa A, Christova I, Mirazimi A. Healthy individuals' immune response to the Bulgarian Crimean-Congo hemorrhagic fever virus vaccine. Vaccine. 2012 Sep 28;30(44):6225–9.

55. Papa A, Papadimitriou E, Christova I. The Bulgarian vaccine Crimean-Congo haemorrhagic fever virus strain. Scand J Infect Dis. 2011 Mar 9;43(3):225–9.

56. Crotty S, Cameron CE, Andino R. RNA virus error catastrophe: Direct molecular test by using ribavirin. Proc Natl Acad Sci. 2001 Jun 5;98(12):6895–900.

57. Sidwell RW, Huffman JH, Khare GP, Allen LB, Witkowski JT, Robins RK. Broad-spectrum antiviral activity of Virazole: 1-beta-D-ribofuranosyl-1,2,4-triazole-3-carboxamide. Science. 1972 Aug 25;177(4050):705–6.

58. Huggins JW. Prospects for Treatment of Viral Hemorrhagic Fevers with Ribavirin, a Broad-Spectrum Antiviral Drug. Clin Infect Dis. 1989 May 1;11(Supplement_4):S750–61.

59. Ozkurt Z, Kiki I, Erol S, Erdem F, Yilmaz N, Parlak M, et al. Crimean-Congo hemorrhagic fever in Eastern Turkey: clinical features, risk factors and efficacy of ribavirin therapy. J Infect. 2006 Mar;52(3):207–15.

60. Ceylan B, Turhan V. The efficacy of ribavirin in Crimean-Congo hemorrhagic fever--randomized trials are urgently needed. Int J Infect Dis. 2014 Dec 1;29:297–8.

61. Atkins C, Freiberg AN. Recent advances in the development of antiviral therapeutics for Rift Valley fever virus infection. Future Virol. 2017 Nov;12(11):651–65.

62. Furuta Y, Komeno T, Nakamura T. Favipiravir (T-705), a broad spectrum inhibitor of viral RNA polymerase. Proc Jpn Acad Ser B Phys Biol Sci. 2017;93(7):449–63.

63. Clercq E De. Highlights in antiviral drug research: Antivirals at the horizon. Med Res Rev. 2013;33(6):1215–48.

64. Gowen BB, Wong MH, Jung KH, Sanders AB, Mendenhall M, Bailey KW, et al. In vitro and in vivo activities of T-705 against arenavirus and bunyavirus infections. Antimicrob Agents Chemother. 2007;51(9):3168–76.

65. Gowen BB, Smee DF, Wong M-H, Hall JO, Jung K-H, Bailey KW, et al. Treatment of late stage disease in a model of arenaviral hemorrhagic fever: T-705 efficacy and reduced toxicity suggests an alternative to ribavirin. PLoS One. 2008;3(11):e3725.

66. VASSILENKO S. Specific intravenous immunoglobulin for Crimean-Congo haemorrhagic fever. Lancet. 1990 Mar;335(8692):791–2.

67. Broce S, Hensley L, Sato T, Lehrer-Graiwer J, Essrich C, Edwards KJ, et al. Biochemical and biophysical characterization of cell-free synthesized Rift Valley fever virus nucleoprotein capsids enables in vitro screening to identify novel antivirals. Biol Direct. 2016 Dec 14;11(1):25.

68. Benedict A, Bansal N, Senina S, Hooper I, Lundberg L, de la Fuente C, et al. Repurposing FDA-approved drugs as therapeutics to treat Rift Valley fever virus infection. Front Microbiol. 2015;6:676.

69. Golden JW, Shoemaker CJ, Lindquist ME, Zeng X, Daye SP, Williams JA, et al. GP38-targeting monoclonal antibodies protect adult mice against lethal Crimean-Congo hemorrhagic fever virus infection. Sci Adv. 2019 Jul 10;5(7):eaaw9535.

70. Kim KH, Kim J, Ko M, Chun JY, Kim H, Kim S, et al. An anti-Gn glycoprotein antibody from a convalescent patient potently inhibits the infection of severe fever with thrombocytopenia syndrome virus. Krammer F, editor. PLOS Pathog. 2019 Feb 1;15(2):e1007375.

71. Elliott RM. Orthobunyaviruses: Recent genetic and structural insights. Nat Rev Microbiol. 2014;12(10):673–85.

72. Leonard VHJ, Kohl A, Osborne JC, McLees A, Elliott RM. Homotypic interaction of Bunyamwera virus nucleocapsid protein. J Virol. 2005;79(20):13166–72.

73. Fontana J, López-Montero N, Elliott RM, Fernández JJ, Risco C. The unique architecture of Bunyamwera virus factories around the Golgi complex. Cell Microbiol. 2008;10(10):2012–28.

74. Bowden TA, Bitto D, McLees A, Yeromonahos C, Elliott RM, Huiskonen JT. Orthobunyavirus ultrastructure and the curious tripodal glycoprotein spike. PLoS Pathog. 2013;9(5):e1003374.

75. Strandin T, Hepojoki J, Vaheri A. Cytoplasmic tails of bunyavirus Gn glycoproteins—Could they act as matrix protein surrogates? Virology. 2013;437(2):73–80.

76. Huiskonen JT, Hepojoki J, Laurinmaki P, Vaheri A, Lankinen H, Butcher SJ, et al. Electron Cryotomography of Tula Hantavirus Suggests a Unique Assembly Paradigm for Enveloped Viruses. J Virol. 2010 May 15;84(10):4889–97.

77. Punch EK, Hover S, Blest HT, Fuller J, Hewson R, Fontana J, et al. Potassium is a trigger for conformational change in the fusion spike of an enveloped RNA virus. J Biol Chem. 2018 Apr 20;jbc.RA118.002494.

78. Bitto D, Halldorsson S, Caputo A, Huiskonen JT. Low pH and Anionic Lipid-dependent Fusion of Uukuniemi Phlebovirus to Liposomes. J Biol Chem.

2016 Mar 18;291(12):6412–22.

79. Halldorsson S, Behrens A-J, Harlos K, Huiskonen JT, Elliott RM, Crispin M, et al. Structure of a phleboviral envelope glycoprotein reveals a consolidated model of membrane fusion. Proc Natl Acad Sci U S A. 2016 Jun 28;113(26):7154–9.

80. Barr JN, Elliott RM, Dunn EF, Wertz GW. Segment-specific terminal sequences of Bunyamwera bunyavirus regulate genome replication. Virology. 2003 Jul;311(2):326–38.

81. Kohl A, Lowen AC, Léonard VHJ, Elliott RM. Genetic elements regulating packaging of the Bunyamwera orthobunyavirus genome. J Gen Virol. 2006 Jan;87(Pt 1):177–87.

82. Barr JN, Rodgers JW, Wertz GW. Identification of the Bunyamwera bunyavirus transcription termination signal. J Gen Virol. 2006;87(Pt 1):189–98.

83. Pettersson RF, von Bonsdorff CH. Ribonucleoproteins of Uukuniemi virus are circular. J Virol. 1975 Feb;15(2):386–92.

84. Lowen AC, Boyd A, Fazakerley JK, Elliott RM. Attenuation of bunyavirus replication by rearrangement of viral coding and noncoding sequences. J Virol. 2005;79(11):6940–6.

85. Reguera J, Weber F, Cusack S. Bunyaviridae RNA polymerases (L-protein) have an N-terminal, influenza-like endonuclease domain, essential for viral cap-dependent transcription. PLoS Pathog. 2010 Jan;6(9):e1001101.

86. Jácome R, Becerra A, Ponce de León S, Lazcano A. Structural Analysis of Monomeric RNA-Dependent Polymerases: Evolutionary and Therapeutic Implications. Kuhn JH, editor. PLoS One. 2015 Sep 23;10(9):e0139001.

87. Gerlach P, Malet H, Cusack S, Reguera J. Structural insights into bunyavirus replication and its regulation by the vRNA promoter. Cell. 2015;161(6).

88. Lappin DF, Nakitare GW, Palfreyman JW, Elliott RM. Localization of Bunyamwera bunyavirus G1 glycoprotein to the Golgi requires association with G2 but not with NSm. J Gen Virol. 1994;75(Pt 12):3441–51.

89. Shi X, Brauburger K, Elliott RM. Role of N-linked glycans on bunyamwera virus glycoproteins in intracellular trafficking, protein folding, and virus infectivity. J Virol. 2005;79(21):13725–34.

90. Hellert J, Aebischer A, Wernike K, Haouz A, Brocchi E, Reiche S, et al. Orthobunyavirus spike architecture and recognition by neutralizing antibodies. Nat Commun. 2019 Dec 20;10(1):879.

91. Shi X, Goli J, Clark G, Brauburger K, Elliott RM. Functional analysis of the Bunyamwera orthobunyavirus Gc glycoprotein. J Gen Virol. 2009 Oct;90(Pt 10):2483–92.

92. Shi X, Lappin DF, Elliott RM. Mapping the Golgi targeting and retention signal of Bunyamwera virus glycoproteins. J Virol. 2004;78(19):10793–802.

93. Shi X, Botting CH, Li P, Niglas M, Brennan B, Shirran SL, et al. Bunyamwera orthobunyavirus glycoprotein precursor is processed by cellular signal peptidase and signal peptide peptidase. Proc Natl Acad Sci U S A. 2016 Aug 2;113(31):8825–30.

94. Salanueva IJ, Novoa RR, Cabezas P, López-Iglesias C, Carrascosa JL, Elliott RM, et al. Polymorphism and structural maturation of bunyamwera virus in Golgi and post-Golgi compartments. J Virol. 2003;77(2):1368–81.

95. Fuller F, Bhown AS, Bishop DH. Bunyavirus nucleoprotein, N, and a non-structural protein, NSS, are coded by overlapping reading frames in the S RNA. J Gen Virol. 1983 Aug;64 (Pt 8):1705–14.

96. Ruigrok RWH, Crépin T. Nucleoproteins of negative strand RNA viruses; RNA binding, oligomerisation and binding to polymerase co-factor. Viruses. 2010 Jan;2(1):27–32.

97. Wang X, Li B, Guo Y, Shen S, Zhao L, Zhang P, et al. Molecular basis for the formation of ribonucleoprotein complex of Crimean-Congo hemorrhagic fever virus. J Struct Biol. 2016 Dec 1;196(3):455–65.

98. Ferron F, Li Z, Danek EI, Luo D, Wong Y, Coutard B, et al. The Hexamer Structure of the Rift Valley Fever Virus Nucleoprotein Suggests a Mechanism for its Assembly into Ribonucleoprotein Complexes. Rey FA, editor. PLoS Pathog. 2011 May 12;7(5):e1002030.

99. Ariza A, Tanner SJ, Walter CT, Dent KC, Shepherd DA, Wu W, et al. Nucleocapsid protein structures from orthobunyaviruses reveal insight into ribonucleoprotein architecture and RNA polymerization. Nucleic Acids Res. 2013;41(11):5912–26.

100. Schoen A, Weber F. Orthobunyaviruses and innate immunity induction: alieNSs vs. PredatoRRs. Eur J Cell Biol. 2015 Jun 2;

101. Thomas D, Blakqori G, Wagner V, Banholzer M, Kessler N, Elliott RM, et al. Inhibition of RNA polymerase II phosphorylation by a viral interferon antagonist. J Biol Chem. 2004;279(30):31471–7.

102. Hart TJ, Kohl a., Elliott RM. Role of the NSs protein in the zoonotic capacity of orthobunyaviruses. Zoonoses Public Health. 2009 Aug;56(6–7):285–96.

103. van Knippenberg I, Fragkoudis R, Elliott RM. The Transient Nature of Bunyamwera Orthobunyavirus NSs Protein Expression: Effects of Increased Stability of NSs Protein on Virus Replication. PLoS One. 2013;8(5):e64137.

104. Léonard VHJ, Kohl A, Hart TJ, Elliott RM. Interaction of Bunyamwera Orthobunyavirus NSs protein with mediator protein MED8: a mechanism for inhibiting the interferon response. J Virol. 2006;80(19):9667–75.

105. ter Horst S, Conceição-Neto N, Neyts J, Rocha-Pereira J. Structural and functional similarities in bunyaviruses: Perspectives for pan-bunya antivirals. Rev Med Virol. 2019 May 1;29(3):e2039.

106. Albornoz A, Hoffmann AB, Lozach P-Y, Tischler ND. Early Bunyavirus-Host Cell Interactions. Viruses. 2016;8(5).

107. Gavrilovskaya IN, Brown EJ, Ginsberg MH, Mackow ER. Cellular entry of hantaviruses which cause hemorrhagic fever with renal syndrome is mediated by beta3 integrins. J Virol. 1999 May;73(5):3951–9.

108. Hofmann H, Li X, Zhang X, Liu W, Kuhl A, Kaup F, et al. Severe Fever with Thrombocytopenia Virus Glycoproteins Are Targeted by Neutralizing Antibodies and Can Use DC-SIGN as a Receptor for pH-Dependent Entry into Human and Animal Cell Lines. J Virol. 2013 Apr 15;87(8):4384–94.

109. Léger P, Tetard M, Youness B, Cordes N, Rouxel RN, Flamand M, et al. Differential Use of the C-Type Lectins L-SIGN and DC-SIGN for Phlebovirus Endocytosis. Traffic. 2016 Jun;17(6):639–56.

110. Suda Y, Fukushi S, Tani H, Murakami S, Saijo M, Horimoto T, et al. Analysis of the entry mechanism of Crimean-Congo hemorrhagic fever virus, using a vesicular stomatitis virus pseudotyping system. Arch Virol. 2016 Jun 3;161(6):1447–54.

111. Murakami S, Takenaka-Uema A, Kobayashi T, Kato K, Shimojima M, Palmarini M, et al. Heparan Sulfate Proteoglycan Is an Important Attachment Factor for Cell Entry of Akabane and Schmallenberg Viruses.

J Virol. 2017;91(15).

112. Salvador B, Sexton NR, Carrion R, Nunneley J, Patterson JL, Steffen I, et al. Filoviruses utilize glycosaminoglycans for their attachment to target cells. J Virol. 2013 Mar;87(6):3295–304.

113. Bourgeois C, Bour JB, Lidholt K, Gauthray C, Pothier P. Heparin-like structures on respiratory syncytial virus are involved in its infectivity in vitro. J Virol. 1998 Sep 1;72(9):7221–7.

114. de Boer SM, Kortekaas J, de Haan CAM, Rottier PJM, Moormann RJM, Bosch BJ. Heparan sulfate facilitates Rift Valley fever virus entry into the cell. J Virol. 2012 Dec 15;86(24):13767–71.

115. Plassmeyer ML, Soldan SS, Stachelek KM, Roth SM, Martín-García J, González-Scarano F. Mutagenesis of the La Crosse Virus glycoprotein supports a role for Gc (1066-1087) as the fusion peptide. Virology. 2007 Feb 20;358(2):273–82.

116. Sundin D, Beaty B, Nathanson N, Gonzalez-Scarano F. A G1 glycoprotein epitope of La Crosse virus: a determinant of infection of Aedes triseriatus. Science (80-). 1987 Jan 30;235(4788):591–3.

117. Keegan K, Collett MS. Use of bacterial expression cloning to define the amino acid sequences of antigenic determinants on the G2 glycoprotein of Rift Valley fever virus. J Virol. 1986 May;58(2):263–70.

118. Hollidge BS, Nedelsky NB, Salzano M-V, Fraser JW, González-Scarano F, Soldan SS. Orthobunyavirus entry into neurons and other mammalian cells occurs via clathrin-mediated endocytosis and requires trafficking into early endosomes. J Virol. 2012 Aug;86(15):7988–8001.

119. Shtanko O, Nikitina RA, Altuntas CZ, Chepurnov AA, Davey RA. Crimean-Congo hemorrhagic fever virus entry into host cells occurs through the multivesicular body and requires ESCRT regulators. PLoS Pathog. 2014 Oct 18;10(9):e1004390.

120. Lozach PY, Mancini R, Bitto D, Meier R, Oestereich L, Överby AK, et al. Entry of bunyaviruses into mammalian cells. Cell Host Microbe. 2010;7(6):488–99.

121. Lozach P-Y, Huotari J, Helenius A. Late-penetrating viruses. Curr Opin Virol. 2011 Jul 1;1(1):35–43.

122. Pekosz A, González-Scarano F. The extracellular domain of La Crosse virus

G1 forms oligomers and undergoes pH-dependent conformational changes. Virology. 1996 Nov 1;225(1):243–7.

123. Shi X, Kohl A, Li P, Elliott RM. Role of the cytoplasmic tail domains of Bunyamwera orthobunyavirus glycoproteins Gn and Gc in virus assembly and morphogenesis. J Virol. 2007 Sep;81(18):10151–60.

124. Santos RIM, Rodrigues AH, Silva ML, Mortara RA, Rossi MA, Jamur MC, et al. Oropouche virus entry into HeLa cells involves clathrin and requires endosomal acidification. Virus Res. 2008 Dec;138(1–2):139–43.

125. Jacoby DR, Cooke C, Prabakaran I, Boland J, Nathanson N, Gonzalez-Scarano F. Expression of the La Crosse M Segment Proteins in a Recombinant Vaccinia Expression System Mediates pH-Dependent Cellular Fusion. Virology. 1993 Apr;193(2):993–6.

126. Garry CE, Garry RF. Proteomics computational analyses suggest that the carboxyl terminal glycoproteins of Bunyaviruses are class II viral fusion protein (beta-penetrenes). Theor Biol Med Model. 2004 Jan;1:10.

127. Kleinfelter LM, Jangra RK, Jae LT, Herbert AS, Mittler E, Stiles KM, et al. Haploid Genetic Screen Reveals a Profound and Direct Dependence on Cholesterol for Hantavirus Membrane Fusion. MBio. 2015 Sep 1;6(4):e00801-15.

128. Charlton FW, Hover S, Fuller J, Hewson R, Fontana J, Barr JN, et al. Cellular cholesterol abundance regulates potassium accumulation within endosomes and is an important determinant in bunyavirus entry. J Biol Chem. 2019 May 3;294(18):7335–47.

129. Halldorsson S, Li S, Li M, Harlos K, Bowden TA, Huiskonen JT. Shielding and activation of a viral membrane fusion protein. Nat Commun. 2018 Dec 24;9(1):349.

130. Novoa RR, Calderita G, Arranz R, Fontana J, Granzow H, Risco C. Virus factories: associations of cell organelles for viral replication and morphogenesis. Biol Cell. 2005 Feb;97(2):147–72.

131. Barr JN, Rodgers JW, Wertz GW. The Bunyamwera virus mRNA transcription signal resides within both the 3’ and the 5’ terminal regions and allows ambisense transcription from a model RNA segment. J Virol. 2005 Oct;79(19):12602–7.

132. Reguera J, Gerlach P, Rosenthal M, Gaudon S, Coscia F, Günther S, et al.

Comparative Structural and Functional Analysis of Bunyavirus and Arenavirus Cap-Snatching Endonucleases. Rey FA, editor. PLOS Pathog. 2016 Jun 15;12(6):e1005636.

133. Mir MA, Panganiban AT. The bunyavirus nucleocapsid protein is an RNA chaperone: possible roles in viral RNA panhandle formation and genome replication. RNA. 2006 Feb 1;12(2):272–82.

134. Eifan SA, Elliott RM. Mutational analysis of the Bunyamwera orthobunyavirus nucleocapsid protein gene. J Virol. 2009 Nov 1;83(21):11307–17.

135. Bellocq C, Kolakofsky D. Translational requirement for La Crosse virus S-mRNA synthesis: a possible mechanism. J Virol. 1987 Dec;61(12):3960–7.

136. Kohl A, Hart TJ, Noonan C, Royall E, Roberts LO, Elliott RM. A bunyamwera virus minireplicon system in mosquito cells. J Virol. 2004;78(11):5679–85.

137. Dunn EF, Pritlove DC, Jin H, Elliott RM. Transcription of a recombinant bunyavirus RNA template by transiently expressed bunyavirus proteins. Virology. 1995 Aug 1;211(1):133–43.

138. Lee B-H, Yoshimatsu K, Maeda A, Ochiai K, Morimatsu M, Araki K, et al. Association of the nucleocapsid protein of the Seoul and Hantaan hantaviruses with small ubiquitin-like modifier-1-related molecules. Virus Res. 2003 Dec 1;98(1):83–91.

139. Novoa RR, Calderita G, Cabezas P, Elliott RM, Risco C. Key Golgi factors for structural and functional maturation of bunyamwera virus. J Virol. 2005 Sep;79(17):10852–63.

140. Kawai T, Akira S. Innate immune recognition of viral infection. Nat Immunol. 2006 Feb;7(2):131–7.

141. Weber M, Gawanbacht A, Habjan M, Rang A, Borner C, Schmidt AM, et al. Incoming RNA virus nucleocapsids containing a 5′-triphosphorylated genome activate RIG-I and antiviral signaling. Cell Host Microbe. 2013;13(3):336–46.

142. Kochs G, Janzen C, Hohenberg H, Haller O. Antivirally active MxA protein sequesters La Crosse virus nucleocapsid protein into perinuclear complexes. Proc Natl Acad Sci U S A. 2002 Mar 5;99(5):3153–8.

143. Andersson I, Bladh L, Mousavi-Jazi M, Magnusson K-E, Lundkvist A, Haller O, et al. Human MxA protein inhibits the replication of Crimean-Congo

hemorrhagic fever virus. J Virol. 2004 Apr 15;78(8):4323–9.

144. Khaiboullina SF, Rizvanov AA, Deyde VM, St. Jeor SC. Andes virus stimulates interferon-inducible MxA protein expression in endothelial cells. J Med Virol. 2005 Feb 1;75(2):267–75.

145. Bridgen A, Weber F, Fazakerley JK, Elliott RM. Bunyamwera bunyavirus nonstructural protein NSs is a nonessential gene product that contributes to viral pathogenesis. Proc Natl Acad Sci U S A. 2001 Jan 16;98(2):664–9.

146. Weber F, Bridgen A, Fazakerley JK, Streitenfeld H, Kessler N, Randall RE, et al. Bunyamwera bunyavirus nonstructural protein NSs counteracts the induction of alpha/beta interferon. J Virol. 2002;76(16):7949–55.

147. Van Knippenberg I, Carlton-Smith C, Elliott RM. The N-terminus of Bunyamwera orthobunyavirus NSs protein is essential for interferon antagonism. J Gen Virol. 2010;91(Pt 8):2002–6.

148. Pennington TH, Pringle CR, McCrae MA. Bunyamwera virus-induced polypeptide synthesis. J Virol. 1977 Oct;24(1):397–400.

149. López-Montero N, Risco C. Self-protection and survival of arbovirus-infected mosquito cells. Cell Microbiol. 2011 Feb;13(2):300–15.

150. Carvalho MG, Frugulhetti IC, Rebello MA. Marituba (Bunyaviridae) virus replication in cultured Aedes albopictus cells and in L-A9 cells. Arch Virol. 1986;90(3–4):325–35.

151. Newton SE, Short NJ, Dalgarno L. Bunyamwera virus replication in cultured Aedes albopictus (mosquito) cells: establishment of a persistent viral infection. J Virol. 1981;38(2):1015–24.

152. Rossier C, Raju R, Kolakofsky D. LaCrosse virus gene expression in mammalian and mosquito cells. Virology. 1988 Aug;165(2):539–48.

153. Alberts, Bruce; Johnson, Alexander; Lewis, Julian; Raff, Martin; Roberts, Keith; Walter P. Molecular Biology of the Cell. Fourth Edi. New York: Garland Science; 2002. 631–656 p.

154. O'Connell AD, Morton MJ, Hunter M. Two-pore domain K+ channels—molecular sensors. Biochim Biophys Acta - Biomembr. 2002 Nov;1566(1–2):152–61.

155. MacKinnon R. Pore loops: An emerging theme in ion channel structure. Neuron. 1995 May;14(5):889–92.

156. Jentsch TJ, Stein V, Weinreich F, Zdebik AA. Molecular Structure and Physiological Function of Chloride Channels. Physiol Rev. 2002 Apr 1;82(2):503–68.

157. Doyle DA, Morais Cabral J, Pfuetzner RA, Kuo A, Gulbis JM, Cohen SL, et al. The Structure of the Potassium Channel: Molecular Basis of K+ Conduction and Selectivity. Science (80-). 1998 Apr 3;280(5360):69–77.

158. Perozo E, Cortes DM, Cuello LG. Structural Rearrangements Underlying K+-Channel Activation Gating. Science (80-). 1999 Jul 2;285(5424):73–8.

159. O'Grady SM, Lee SY. Chloride and potassium channel function in alveolar epithelial cells. Am J Physiol Lung Cell Mol Physiol. 2003;284(5):L689-700.

160. Yu FH, Yarov-Yarovoy V, Gutman GA, Catterall WA. Overview of molecular relationships in the voltage-gated ion channel superfamily. Pharmacol Rev. 2005 Dec 1;57(4):387–95.

161. Catterall WA. From ionic currents to molecular mechanisms: the structure and function of voltage-gated sodium channels. Neuron. 2000 Apr;26(1):13–25.

162. Bardou O, Trinh NTN, Brochiero E. Molecular diversity and function of K+ channels in airway and alveolar epithelial cells. Am J Physiol Lung Cell Mol Physiol. 2009;296(2):L145-55.

163. Zhong Y-S, Wang J, Liu W-M, Zhu Y-H. Potassium ion channels in retinal ganglion cells. Mol Med Rep. 2013 Aug 1;8(2):311–9.

164. Ridge FP, Duszyk M, French AS. A large conductance, Ca2+-activated K+ channel in a human lung epithelial cell line (A549). Biochim Biophys Acta. 1997;1327(2):249–58.

165. Thompson-Vest N, Shimizu Y, Hunne B, Furness JB. The distribution of intermediate-conductance, calcium-activated, potassium (IK) channels in epithelial cells. J Anat. 2006;208(2):219–29.

166. Weaver AK, Bomben VC, Sontheimer H. Expression and function of calcium-activated potassium channels in human glioma cells. Glia. 2006 Aug 15;54(3):223–33.

167. Yellen G. The voltage-gated potassium channels and their relatives. Nature. 2002 Sep 5;419(6902):35–42.

168. Hibino H, Inanobe A, Furutani K, Murakami S, Findlay I, Kurachi Y.

Inwardly rectifying potassium channels: their structure, function, and physiological roles. Physiol Rev. 2010;90(1):291–366.

169. Nichols CG, Lopatin AN. Inward Rectifier Potassium Channels. Annu Rev Physiol. 1997 Oct 28;59(1):171–91.

170. Xu M, Wang Y, Ayub A, Ashraf M. Mitochondrial K(ATP) channel activation reduces anoxic injury by restoring mitochondrial membrane potential. Am J Physiol Heart Circ Physiol. 2001 Sep;281(3):H1295-303.

171. Miki T, Nagashima K, Tashiro F, Kotake K, Yoshitomi H, Tamamoto A, et al. Defective insulin secretion and enhanced insulin action in KATP channel-deficient mice. Proc Natl Acad Sci. 1998 Sep 1;95(18):10402–6.

172. Garlid KD, Paucek P. Mitochondrial potassium transport: the K+ cycle. Biochim Biophys Acta - Bioenerg. 2003 Sep;1606(1–3):23–41.

173. Scott CCC, Gruenberg J. Ion flux and the function of endosomes and lysosomes: pH is just the start. Bioessays. 2011 Feb;33(2):103–10.

174. Enyedi P, Czirják G. Molecular background of leak K+ currents: two-pore domain potassium channels. Physiol Rev. 2010 Apr 1;90(2):559–605.

175. Lesage F, Guillemare E, Fink M, Duprat F, Lazdunski M, Romey G, et al. TWIK-1, a ubiquitous human weakly inward rectifying K+ channel with a novel structure. EMBO J. 1996 Mar 1;15(5):1004–11.

176. Cadaveira-Mosquera A, Ribeiro SJ, Reboreda A, Pérez M, Lamas JA. Activation of TREK currents by the neuroprotective agent riluzole in mouse sympathetic neurons. J Neurosci. 2011 Jan 26;31(4):1375–85.

177. Czirják G, Enyedi P. Ruthenium red inhibits TASK-3 potassium channel by interconnecting glutamate 70 of the two subunits. Mol Pharmacol. 2003 Mar;63(3):646–52.

178. Bittner S, Ruck T, Schuhmann MK, Herrmann AM, Maati HM ou, Bobak N, et al. Endothelial TWIK-related potassium channel-1 (TREK1) regulates immune-cell trafficking into the CNS. Nat Med. 2013 Sep 11;19(9):1161–5.

179. Catterall WA. Structure and Regulation of Voltage-Gated Ca2+ Channels. Annu Rev Cell Dev Biol. 2000 Nov 28;16(1):521–55.

180. Dolphin AC. A short history of voltage-gated calcium channels. Br J Pharmacol. 2006 Jan;147 Suppl:S56-62.

181. Zhu MX, Ma J, Parrington J, Calcraft PJ, Galione A, Evans AM. Calcium

signaling via two-pore channels: local or global, that is the question. Am J Physiol Cell Physiol. 2010 Mar;298(3):C430-41.

182. Tyson JR, Snutch TP. Molecular nature of voltage-gated calcium channels: structure and species comparison. Wiley Interdiscip Rev Membr Transp Signal. 2013 Sep 25;2(5):181–206.

183. Berridge MJ, Bootman MD, Lipp P. Calcium--a life and death signal. Nature. 1998 Oct 15;395(6703):645–8.

184. Yu FH, Catterall WA. Overview of the voltage-gated sodium channel family. Genome Biol. 2003 Jan;4(3):207.

185. Roger S, Gillet L, Le Guennec J-Y, Besson P. Voltage-gated sodium channels and cancer: is excitability their primary role? Front Pharmacol. 2015 Jan 29;6:152.

186. Garcia ML, Kaczorowski GJ. Ion channels find a pathway for therapeutic success. Proc Natl Acad Sci. 2016 May 17;113(20):5472–4.

187. Igloi Z, Mohl B-P, Lippiat JD, Harris M, Mankouri J. Requirement for chloride channel function during the hepatitis C virus life cycle. J Virol. 2015 Apr;89(7):4023–9.

188. Kim J-B. Channelopathies. Korean J Pediatr. 2014 Jan;57(1):1–18.

189. Nieddu E, Pollarolo B, Merello L, Schenone S, Mazzei M. F508del-CFTR Rescue: A Matter of Cell Stress Response. Curr Pharm Des. 2013 Apr 1;19(19):3476–96.

190. Jentsch TJ, Hübner CA, Fuhrmann JC. Ion channels: Function unravelled by dysfunction. Nat Cell Biol. 2004 Nov;6(11):1039–47.

191. Piwon N, Günther W, Schwake M, Bösl MR, Jentsch TJ. ClC-5 Cl--channel disruption impairs endocytosis in a mouse model for Dent’s disease. Nature. 2000 Nov;408(6810):369–73.

192. Wang Q, Shen J, Splawski I, Atkinson D, Li Z, Robinson JL, et al. SCN5A mutations associated with an inherited cardiac arrhythmia, long QT syndrome. Cell. 1995 Mar 10;80(5):805–11.

193. Curran ME, Splawski I, Timothy KW, Vincen GM, Green ED, Keating MT. A molecular basis for cardiac arrhythmia: HERG mutations cause long QT syndrome. Cell. 1995 Mar 10;80(5):795–803.

194. Koch M, Steinmeyer K, Lorenz C, Ricker K, Wolf F, Otto M, et al. The skeletal

muscle chloride channel in dominant and recessive human myotonia. Science (80-). 1992 Aug 7;257(5071):797–800.

195. Neyroud N, Tesson F, Denjoy I, Leibovici M, Donger C, Barhanin J, et al. A novel mutation in the potassium channel gene KVLQT1 causes the Jervell and Lange-Nielsen cardioauditory syndrome. Nat Genet. 1997 Feb;15(2):186–9.

196. Lossin C, Wang DW, Rhodes TH, Vanoye CG, George AL. Molecular basis of an inherited epilepsy. Neuron. 2002 Jun 13;34(6):877–84.

197. Pardo LA, Stühmer W. The roles of K+ channels in cancer. Nat Rev Cancer. 2013 Dec 12;14(1):39–48.

198. Alvarez-Baron CP, Jonsson P, Thomas C, Dryer SE, Williams C. The Two-Pore Domain Potassium Channel KCNK5: Induction by Estrogen Receptor α and Role in Proliferation of Breast Cancer Cells. Mol Endocrinol. 2011 Aug 1;25(8):1326–36.

199. Moeller HB, Rittig S, Fenton RA. Nephrogenic Diabetes Insipidus: Essential Insights into the Molecular Background and Potential Therapies for Treatment. Endocr Rev. 2013 Apr 1;34(2):278–301.

200. Tomimitsu H, Arimura K, Nagado T, Watanabe O, Otsuka R, Kurono A, et al. Mechanism of action of voltage-gated K+ channel antibodies in acquired neuromyotonia. Ann Neurol. 2004 Sep;56(3):440–4.

201. Abriel H, Schläpfer J, Keller DI, Gavillet B, Buclin T, Biollaz J, et al. Molecular and clinical determinants of drug-induced long QT syndrome: an iatrogenic channelopathy. Swiss Med Wkly. 2004 Nov 27;134(47–48):685–94.

202. Bagal SK, Brown AD, Cox PJ, Omoto K, Owen RM, Pryde DC, et al. Ion Channels as Therapeutic Targets: A Drug Discovery Perspective. J Med Chem. 2013 Feb 14;56(3):593–624.

203. Royle J, Dobson S, Müller M, Macdonald A. Emerging Roles of Viroporins Encoded by DNA Viruses: Novel Targets for Antivirals? Viruses. 2015 Oct 16;7(10):5375–87.

204. Sze C, Tan Y-J. Viral Membrane Channels: Role and Function in the Virus Life Cycle. Viruses. 2015 Jun 23;7(6):3261–84.

205. Pinto LH, Holsinger LJ, Lamb RA. Influenza virus M2 protein has ion channel activity. Cell. 1992 May 1;69(3):517–28.

206. Shimbo K, Brassard DL, Lamb RA, Pinto LH. Ion selectivity and activation of the M2 ion channel of influenza virus. Biophys J. 1996 Mar;70(3):1335–46.

207. Scott C, Griffin S. Viroporins: structure, function and potential as antiviral targets. J Gen Virol. 2015 Aug;96(8):2000–27.

208. Jones CT, Murray CL, Eastman DK, Tassello J, Rice CM. Hepatitis C virus p7 and NS2 proteins are essential for production of infectious virus. J Virol. 2007 Aug;81(16):8374–83.

209. Hsu K, Han J, Shinlapawittayatorn K, Deschenes I, Marbán E. Membrane potential depolarization as a triggering mechanism for Vpu-mediated HIV-1 release. Biophys J. 2010 Sep 22;99(6):1718–25.

210. Hover S, Foster B, Barr JN, Mankouri J. Viral dependence on cellular ion channels – an emerging anti-viral target? J Gen Virol. 2017 Mar 1;98(3):345–51.

211. Redman PT, He K, Hartnett KA, Jefferson BS, Hu L, Rosenberg PA, et al. Apoptotic surge of potassium currents is mediated by p38 phosphorylation of Kv2.1. Proc Natl Acad Sci U S A. 2007 Mar 27;104(9):3568–73.

212. Mankouri J, Dallas ML, Hughes ME, Griffin SDC, Macdonald A, Peers C, et al. Suppression of a pro-apoptotic K+ channel as a mechanism for hepatitis C virus persistence. Proc Natl Acad Sci U S A. 2009;106(37):15903–8.

213. Norris CA, He K, Springer MG, Hartnett KA, Horn JP, Aizenman E. Regulation of neuronal proapoptotic potassium currents by the hepatitis C virus nonstructural protein 5A. J Neurosci. 2012 Jun 27;32(26):8865–70.

214. Kort JJ, Jalonen TO. The nef protein of the human immunodeficiency virus type 1 (HIV-1) inhibits a large-conductance potassium channel in human glial cells. Neurosci Lett. 1998 Jul;251(1):1–4.

215. Visentin S, Renzi M, Levi G. Altered outward-rectifying K(+) current reveals microglial activation induced by HIV-1 Tat protein. Glia. 2001 Mar 1;33(3):181–90.

216. Herrmann M, Ruprecht K, Sauter M, Martinez J, van Heteren P, Glas M, et al. Interaction of human immunodeficiency virus gp120 with the voltage-gated potassium channel BEC1. FEBS Lett. 2010 Aug 20;584(16):3513–8.

217. Strebel K. HIV-1 Vpu: Putting a Channel to the TASK. Mol Cell. 2004

Apr;14(2):150–2.

218. Perry SW, Norman JP, Litzburg A, Zhang D, Dewhurst S, Gelbard HA. HIV-1 Transactivator of Transcription Protein Induces Mitochondrial Hyperpolarization and Synaptic Stress Leading to Apoptosis. J Immunol. 2005 Mar 18;174(7):4333–44.

219. Kennedy PGE, Montague P, Scott F, Grinfeld E, Ashrafi GH, Breuer J, et al. Varicella-zoster viruses associated with post-herpetic neuralgia induce sodium current density increases in the ND7-23 Nav-1.8 neuroblastoma cell line. PLoS One. 2013 Jan 31;8(1):e51570.

220. Iwata M, Komori S, Unno T, Minamoto N, Ohashi H. Modification of membrane currents in mouse neuroblastoma cells following infection with rabies virus. Br J Pharmacol. 1999 Apr;126(8):1691–8.

221. Rosenblum LA, Coplan JD, Friedman S, Bassoff T. Dose-response effects of oral yohimbine in unrestrained primates. Biol Psychiatry. 1991 May 1;29(7):647–57.

222. Kunzelmann K, Sun J, Meanger J, King NJ, Cook DI. Inhibition of airway Na+ transport by respiratory syncytial virus. J Virol. 2007 Apr;81(8):3714–20.

223. Hoffmann H-H, Palese P, Shaw ML. Modulation of influenza virus replication by alteration of sodium ion transport and protein kinase C activity. Antiviral Res. 2008;80(2):124–34.

224. Lazrak A, Iles KE, Liu G, Noah DL, Noah JW, Matalon S. Influenza virus M2 protein inhibits epithelial sodium channels by increasing reactive oxygen species. FASEB J. 2009 Nov;23(11):3829–42.

225. Londino JD, Lazrak A, Jurkuvenaite A, Collawn JF, Noah JW, Matalon S. Influenza matrix protein 2 alters CFTR expression and function through its ion channel activity. Am J Physiol Lung Cell Mol Physiol. 2013 May 1;304(9):L582-92.

226. Ji H-L, Song W, Gao Z, Su X-F, Nie H-G, Jiang Y, et al. SARS-CoV proteins decrease levels and activity of human ENaC via activation of distinct PKC isoforms. Am J Physiol Lung Cell Mol Physiol. 2009 Mar;296(3):L372-83.

227. Song W, Liu G, Bosworth CA, Walker JR, Megaw GA, Lazrak A, et al. Respiratory syncytial virus inhibits lung epithelial Na+ channels by up-regulating inducible nitric-oxide synthase. J Biol Chem. 2009 Mar

13;284(11):7294–306.

228. Lingemann M, McCarty T, Liu X, Buchholz UJ, Surman S, Martin SE, et al. The alpha-1 subunit of the Na+,K+-ATPase (ATP1A1) is required for macropinocytic entry of respiratory syncytial virus (RSV) in human respiratory epithelial cells. Whelan SPJ, editor. PLOS Pathog. 2019 Aug 5;15(8):e1007963.

229. Conner SD, Schmid SL. Regulated portals of entry into the cell. Nature. 2003 Mar 6;422(6927):37–44.

230. Alkhalil A, Hammamieh R, Hardick J, Ichou MA, Jett M, Ibrahim S. Gene expression profiling of monkeypox virus-infected cells reveals novel interfaces for host-virus interactions. Virol J. 2010 Jan 28;7(1):173.

231. Dellis O, Arbabian A, Papp B, Rowe M, Joab I, Chomienne C. Epstein-Barr virus latent membrane protein 1 increases calcium influx through store-operated channels in B lymphoid cells. J Biol Chem. 2011 May 27;286(21):18583–92.

232. Biasiotto R, Aguiari P, Rizzuto R, Pinton P, D'Agostino DM, Ciminale V. The p13 protein of human T cell leukemia virus type 1 (HTLV-1) modulates mitochondrial membrane potential and calcium uptake. Biochim Biophys Acta. 2010 Jan;1797(6–7):945–51.

233. Zheng K, Chen M, Xiang Y, Ma K, Jin F, Wang X, et al. Inhibition of herpes simplex virus type 1 entry by chloride channel inhibitors tamoxifen and NPPB. Biochem Biophys Res Commun. 2014 Apr 18;446(4):990–6.

234. Müller M, Slivinski N, Todd EJAA, Khalid H, Li R, Karwatka M, et al. Chikungunya virus requires cellular chloride channels for efficient genome replication. Gromowski G, editor. PLoS Negl Trop Dis. 2019 Sep 4;13(9):e0007703.

235. Gehring G, Rohrmann K, Atenchong N, Mittler E, Becker S, Dahlmann F, et al. The clinically approved drugs amiodarone, dronedarone and verapamil inhibit filovirus cell entry. J Antimicrob Chemother. 2014 Aug;69(8):2123–31.

236. Sakurai Y, Kolokoltsov AA, Chen C-C, Tidwell MW, Bauta WE, Klugbauer N, et al. Two-pore channels control Ebola virus host cell entry and are drug targets for disease treatment. Science (80-). 2015;347(6225):995–8.

237. Chifflet S, Hernández JA. The plasma membrane potential and the

organization of the actin cytoskeleton of epithelial cells. Int J Cell Biol. 2012;2012:121424.

238. Gottlieb E, Armour SM, Harris MH, Thompson CB. Mitochondrial membrane potential regulates matrix configuration and cytochrome c release during apoptosis. Cell Death Differ. 2003 Jun 22;10(6):709–17.

239. Chavan TS, Muratcioglu S, Marszalek R, Jang H, Keskin O, Gursoy A, et al. Plasma membrane regulates Ras signaling networks. Cell Logist. 2015 Oct 2;5(4):e1136374.

240. Nakanishi S, Okazawa M. Membrane potential-regulated Ca2+ signalling in development and maturation of mammalian cerebellar granule cells. J Physiol. 2006 Sep 1;575(2):389–95.

241. Berka U, Khan A, Blaas D, Fuchs R. Human rhinovirus type 2 uncoating at the plasma membrane is not affected by a pH gradient but is affected by the membrane potential. J Virol. 2009;83(8):3778–87.

242. Markosyan RM, Kielian M, Cohen FS. Fusion induced by a class II viral fusion protein, semliki forest virus E1, is dependent on the voltage of the target cell. J Virol. 2007 Oct 15;81(20):11218–25.

243. Akeson M, Scharff J, Sharp CM, Neville DM. Evidence that plasma membrane electrical potential is required for vesicular stomatitis virus infection of MDCK cells: a study using fluorescence measurements through polycarbonate supports. J Membr Biol. 1992 Jan;125(1):81–91.

244. Hover S, King B, Hall B, Loundras E-A, Taqi H, Daly J, et al. Modulation of potassium channels inhibits bunyavirus infection. J Biol Chem. 2015 Dec 16;

245. Weber F, Dunn EF, Bridgen A, Elliott RM. The Bunyamwera Virus Nonstructural Protein NSs Inhibits Viral RNA Synthesis in a Minireplicon System. Virology. 2001 Mar 1;281(1):67–74.

246. Dubey RC, Mishra N, Gaur R. G protein-coupled and ATP-sensitive inwardly rectifying potassium ion channels are essential for HIV entry. Sci Rep. 2019 Dec 11;9(1):4113.

247. Hover S, Foster B, Fontana J, Kohl A, Goldstein SAN, Barr JN, et al. Bunyavirus requirement for endosomal K+ reveals new roles of cellular ion channels during infection. Whelan SPJ, editor. PLOS Pathog. 2018 Jan 19;14(1):e1006845.

248. Lappin DF, Nakitare GW, Palfreyman JW, Elliott RM. Localization of Bunyamwera bunyavirus G1 glycoprotein to the Golgi requires association with G2 but not with NSm. J Gen Virol. 1994 Dec 1;75(12):3441–51.

249. Bucci C, Thomsen P, Nicoziani P, McCarthy J, van Deurs B. Rab7: a key to lysosome biogenesis. Mol Biol Cell. 2000 Feb;11(2):467–80.

250. Wang Y, Chen T, Han C, He D, Liu H, An H, et al. Lysosome-associated small Rab GTPase Rab7b negatively regulates TLR4 signaling in macrophages by promoting lysosomal degradation of TLR4. Blood. 2007 Apr 19;110(3):962–71.

251. Khvotchev M V, Ren M, Takamori S, Jahn R, Südhof TC. Divergent functions of neuronal Rab11b in Ca2+-regulated versus constitutive exocytosis. J Neurosci. 2003 Nov 19;23(33):10531–9.

252. Ullrich O, Reinsch S, Urbé S, Zerial M, Parton RG. Rab11 regulates recycling through the pericentriolar recycling endosome. J Cell Biol. 1996 Nov;135(4):913–24.

253. Bobak N, Feliciangeli S, Chen C-C, Ben Soussia I, Bittner S, Pagnotta S, et al. Recombinant tandem of pore-domains in a Weakly Inward rectifying K+ channel 2 (TWIK2) forms active lysosomal channels. Sci Rep. 2017 Dec 5;7(1):649.

254. Cope J, Heumann J, Hoenger A. Cryo-electron tomography for structural characterization of macromolecular complexes. Curr Protoc protein Sci. 2011 Aug;Chapter 17:Unit17.13.

255. Li S, Sun Z, Pryce R, Parsy M-L, Fehling SK, Schlie K, et al. Acidic pH-Induced Conformations and LAMP1 Binding of the Lassa Virus Glycoprotein Spike. Pierson TC, editor. PLOS Pathog. 2016 Feb 5;12(2):e1005418.

256. Goddard TD, Huang CC, Ferrin TE. Visualizing density maps with UCSF Chimera. J Struct Biol. 2007 Jan 1;157(1):281–7.

257. Meier R, Franceschini A, Horvath P, Tetard M, Mancini R, von Mering C, et al. Genome-wide small interfering RNA screens reveal VAMP3 as a novel host factor required for Uukuniemi virus late penetration. J Virol. 2014 Aug;88(15):8565–78.

258. Stauffer S, Feng Y, Nebioglu F, Heilig R, Picotti P, Helenius A. Stepwise priming by acidic pH and a high K+ concentration is required for efficient uncoating of influenza A virus cores after penetration. J Virol. 2014

Nov;88(22):13029–46.

259. Carlton-Smith C, Elliott RM. Viperin, MTAP44, and Protein Kinase R Contribute to the Interferon-Induced Inhibition of Bunyamwera Orthobunyavirus Replication. J Virol. 2012;86(21):11548–57.

260. Shannon RD, IUCr. Revised effective ionic radii and systematic studies of interatomic distances in halides and chalcogenides. Acta Crystallogr Sect A. 1976 Sep 1;32(5):751–67.

261. Brandenburg B, Lee LY, Lakadamyali M, Rust MJ, Zhuang X, Hogle JM. Imaging poliovirus entry in live cells. PLoS Biol. 2007 Jul;5(7):e183.

262. Rowse M, Qiu S, Tsao J, Xian T, Khawaja S, Yamauchi Y, et al. Characterization of Potent Fusion Inhibitors of Influenza Virus. Pöhlmann S, editor. PLoS One. 2015 Mar 24;10(3):e0122536.

263. Huotari J, Meyer-Schaller N, Hubner M, Stauffer S, Katheder N, Horvath P, et al. Cullin-3 regulates late endosome maturation. Proc Natl Acad Sci. 2012 Jan 17;109(3):823–8.

264. Chavrier P, Parton RG, Hauri HP, Simons K, Zerial M. Localization of low molecular weight GTP binding proteins to exocytic and endocytic compartments. Cell. 1990 Jul 27;62(2):317–29.

265. Hopkins CR, Trowbridge IS. Internalization and processing of transferrin and the transferrin receptor in human carcinoma A431 cells. J Cell Biol. 1983 Aug 1;97(2):508–21.

266. Horgan CP, Hanscom SR, Jolly RS, Futter CE, McCaffrey MW. Rab11-FIP3 links the Rab11 GTPase and cytoplasmic dynein to mediate transport to the endosomal-recycling compartment. J Cell Sci. 2010 Jan 15;123(Pt 2):181–91.

267. Van Noorden CJF, Boonacker E, Bissell ER, Meijer AJ, van Marle J, Smith RE. Ala-Pro-Cresyl Violet, a Synthetic Fluorogenic Substrate for the Analysis of Kinetic Parameters of Dipeptidyl Peptidase IV (CD26) in Individual Living Rat Hepatocytes. Anal Biochem. 1997 Oct 1;252(1):71–7.

268. Leung-Toung R, Li W, Tam TF, Karimian K. Thiol-dependent enzymes and their inhibitors: a review. Curr Med Chem. 2002 May;9(9):979–1002.

269. Serfass JM, Takahashi Y, Zhou Z, Kawasawa YI, Liu Y, Tsotakos N, et al. Endophilin B2 facilitates endosome maturation in response to growth factor stimulation, autophagy induction, and influenza A virus infection.

J Biol Chem. 2017 Jun 16;292(24):10097–111.

270. Yu L, Wu WK, Gu C, Zhong D, Zhao X, Kong Y, et al. Obatoclax impairs lysosomal function to block autophagy in cisplatin-sensitive and -resistant esophageal cancer cells. Oncotarget. 2016;7(12):14693.

271. Aasen S, Pospisilova A, Eichler T, Panek J, Hruby M, Stepanek P, et al. A Novel Nanoprobe for Multimodal Imaging Is Effectively Incorporated into Human Melanoma Metastatic Cell Lines. Int J Mol Sci. 2015 Sep 8;16(9):21658–80.

272. Kornilova E, Sorkina T, Beguinot L, Sorkin A. Lysosomal targeting of epidermal growth factor receptors via a kinase-dependent pathway is mediated by the receptor carboxyl-terminal residues 1022-1123. J Biol Chem. 1996 Nov 29;271(48):30340–6.

273. Greber UF, Singh I, Helenius A. Mechanisms of virus uncoating. Trends Microbiol. 1994 Feb;2(2):52–6.

274. Yamauchi Y, Helenius A. Virus entry at a glance. J Cell Sci. 2013 Mar 15;126(6):1289–95.

275. Shrivastava IH, Tieleman DP, Biggin PC, Sansom MSP. K+ versus Na+ Ions in a K Channel Selectivity Filter: A Simulation Study. Biophys J. 2002;83(2):633–45.

276. Townsley AC, Moss B. Two distinct low-pH steps promote entry of vaccinia virus. J Virol. 2007 Aug;81(16):8613–20.

277. Sorkin A, Goh LK. Endocytosis and intracellular trafficking of ErbBs. Exp Cell Res. 2008 Oct 15;314(17):3093–106.

278. Cang C, Aranda K, Seo Y, Gasnier B, Ren D. TMEM175 Is an Organelle K + Channel Regulating Lysosomal Function. Cell. 2015 Aug 27;162(5):1101–12.

279. White JM, Whittaker GR. Fusion of Enveloped Viruses in Endosomes. Traffic. 2016 Mar 3;

280. Apellániz B, Huarte N, Largo E, Nieva JL. The three lives of viral fusion peptides. Chem Phys Lipids. 2014 Jul 1;181:40–55.

281. Fontana J, Steven AC. Influenza virus-mediated membrane fusion: Structural insights from electron microscopy. Arch Biochem Biophys. 2015 Sep 1;581:86–97.

282. Harrison SC. Viral membrane fusion. Virology. 2015 May 1;479–480:498–507.

283. White JM, Delos SE, Brecher M, Schornberg K. Structures and Mechanisms of Viral Membrane Fusion Proteins: Multiple Variations on a Common Theme. Crit Rev Biochem Mol Biol. 2008;43(3):189.

284. Harrison SC. Viral membrane fusion. Nat Struct Mol Biol. 2008 Jul;15(7):690–8.

285. Schornberg K, Matsuyama S, Kabsch K, Delos S, Bouton A, White J. Role of endosomal cathepsins in entry mediated by the Ebola virus glycoprotein. J Virol. 2006 Apr 15;80(8):4174–8.

286. Fénéant L, Szymańska-de Wijs KM, Nelson EA, White JM. An exploration of conditions proposed to trigger the Ebola virus glycoprotein for fusion. Pöhlmann S, editor. PLoS One. 2019 Jul 5;14(7):e0219312.

287. Ruokolainen V, Domanska A, Laajala M, Pelliccia M, Butcher SJ, Marjomäki V. Extracellular albumin and endosomal ions prime enterovirus particles for uncoating that can be prevented by fatty acid saturation. J Virol. 2019 Jun 12;

288. Mancini R, Bignon EA, Tischler ND, Acuña R, Lozach P-Y. Acidification triggers Andes hantavirus membrane fusion and rearrangement of Gc into a stable post-fusion homotrimer. J Gen Virol. 2015 Nov 1;96(11):3192–7.

289. Drake MJ, Brennan B, Briley Jr K, Bart SM, Sherman E, Szemiel AM, et al. A role for glycolipid biosynthesis in severe fever with thrombocytopenia syndrome virus entry. Whelan SPJ, editor. PLOS Pathog. 2017 Apr 7;13(4):e1006316.

290. Orlova E V., Saibil HR. Structural Analysis of Macromolecular Assemblies by Electron Microscopy. Chem Rev. 2011 Dec 14;111(12):7710–48.

291. Danev R, Baumeister W. Expanding the boundaries of cryo-EM with phase plates. Curr Opin Struct Biol. 2017 Oct 1;46:87–94.

292. Kremer JR, Mastronarde DN, McIntosh JR. Computer Visualization of Three-Dimensional Image Data Using IMOD. J Struct Biol. 1996 Jan 1;116(1):71–6.

293. Briegel A, Pilhofer M, Mastronarde DN, Jensen GJ. The challenge of determining handedness in electron tomography and the use of DNA origami gold nanoparticle helices as molecular standards. J Struct Biol.

2013 Jul;183(1):95–8.

294. Bignon EA, Albornoz A, Guardado-Calvo P, Rey FA, Tischler ND. Molecular organization and dynamics of the fusion protein Gc at the hantavirus surface. Elife. 2019 Jun 10;8.

295. Rissanen I, Stass R, Zeltina A, Li S, Hepojoki J, Harlos K, et al. Structural transitions of the conserved and metastable hantaviral glycoprotein envelope. J Virol. 2017;

296. Kampmann T, Mueller DS, Mark AE, Young PR, Kobe B. The Role of Histidine Residues in Low-pH-Mediated Viral Membrane Fusion. Structure. 2006 Oct 1;14(10):1481–7.

297. Guardado-Calvo P, Rey FA. The Envelope Proteins of the Bunyavirales. Adv Virus Res. 2017 Jan 1;98:83–118.

298. Willensky S, Bar-Rogovsky H, Bignon EA, Tischler ND, Modis Y, Dessau M. Crystal Structure of Glycoprotein C from a Hantavirus in the Post-fusion Conformation. Fremont DH, editor. PLOS Pathog. 2016 Oct 26;12(10):e1005948.

299. Guardado-Calvo P, Bignon EA, Stettner E, Jeffers SA, Pérez-Vargas J, Pehau-Arnaudet G, et al. Mechanistic Insight into Bunyavirus-Induced Membrane Fusion from Structure-Function Analyses of the Hantavirus Envelope Glycoprotein Gc. Kuhn RJ, editor. PLOS Pathog. 2016 Oct 26;12(10):e1005813.

300. DuBois RM, Vaney M-C, Tortorici MA, Kurdi R Al, Barba-Spaeth G, Krey T, et al. Functional and evolutionary insight from the crystal structure of rubella virus protein E1. Nature. 2013 Jan 6;493(7433):552–6.

301. Dubé M, Etienne L, Fels M, Kielian M. Calcium-Dependent Rubella Virus Fusion Occurs in Early Endosomes. J Virol. 2016;90(14):6303.

302. Yan D, Lee S, Thakkar VD, Luo M, Moore ML, Plemper RK. Cross-resistance mechanism of respiratory syncytial virus against structurally diverse entry inhibitors. Proc Natl Acad Sci U S A. 2014 Aug 19;111(33):E3441-9.

303. Shi X, van Mierlo JT, French A, Elliott RM. Visualizing the replication cycle of bunyamwera orthobunyavirus expressing fluorescent protein-tagged Gc glycoprotein. J Virol. 2010;84(17):8460–9.

304. Mukhopadhyay A, Bueso-Ramos C, Chatterjee D, Pantazis P, Aggarwal BB. Curcumin downregulates cell survival mechanisms in human prostate

cancer cell lines. Oncogene. 2001 Nov 15;20(52):7597–609.

305. Lesage F, Lazdunski M. Molecular and functional properties of two-pore-domain potassium channels. Am J Physiol Renal Physiol. 2000 Nov;279(5):F793-801.

306. Skatchkov SN, Eaton MJ, Shuba YM, Kucheryavykh Y V, Derst C, Veh RW, et al. Tandem-pore domain potassium channels are functionally expressed in retinal (Müller) glial cells. Glia. 2006 Feb;53(3):266–76.

307. Essletzbichler P, Konopka T, Santoro F, Chen D, Gapp B V, Kralovics R, et al. Megabase-scale deletion using CRISPR/Cas9 to generate a fully haploid human cell line. Genome Res. 2014 Dec;24(12):2059–65.

308. Chavez RA, Gray AT, Zhao BB, Kindler CH, Mazurek MJ, Mehta Y, et al. TWIK-2, a new weak inward rectifying member of the tandem pore domain potassium channel family. J Biol Chem. 1999 Mar 19;274(12):7887–92.

309. Lawrence SP, Bright NA, Luzio JP, Bowers K. The sodium/proton exchanger NHE8 regulates late endosomal morphology and function. Mol Biol Cell. 2010 Oct 15;21(20):3540–51.

310. Lotshaw DP. Biophysical, pharmacological, and functional characteristics of cloned and native mammalian two-pore domain K+ channels. Cell Biochem Biophys. 2007 Jun 1;47(2):209–56.

311. O'Kelly I. Endocytosis as a mode to regulate functional expression of two-pore domain potassium (K_2p) channels. Pflugers Arch. 2015 May;467(5):1133–42.

312. Di A, Xiong S, Ye Z, Malireddi RKS, Kometani S, Zhong M, et al. The TWIK2 Potassium Efflux Channel in Macrophages Mediates NLRP3 Inflammasome-Induced Inflammation. Immunity. 2018 Jul 17;49(1):56-65.e4.

313. Lawrence RE, Zoncu R. The lysosome as a cellular centre for signalling, metabolism and quality control. Nat Cell Biol. 2019 Feb 2;21(2):133–42.

314. Xu H, Ren D. Lysosomal Physiology. Annu Rev Physiol. 2015 Feb 10;77(1):57–80.

315. Clague MJ, Urbé S, Aniento F, Gruenberg J. Vacuolar ATPase activity is required for endosomal carrier vesicle formation. J Biol Chem. 1994 Jan 7;269(1):21–4.

316. Marshansky V, Futai M. The V-type H+-ATPase in vesicular trafficking: targeting, regulation and function. Curr Opin Cell Biol. 2008 Aug;20(4):415–26.

317. Weinert S, Jabs S, Supanchart C, Schweizer M, Gimber N, Richter M, et al. Lysosomal pathology and osteopetrosis upon loss of H+-driven lysosomal Cl- accumulation. Science. 2010 Jun 11;328(5984):1401–3.

318. Raiborg C, Bache KG, Gillooly DJ, Madshus IH, Stang E, Stenmark H. Hrs sorts ubiquitinated proteins into clathrin-coated microdomains of early endosomes. Nat Cell Biol. 2002 May 29;4(5):394–8.

319. Gilfillan GD, Selmer KK, Roxrud I, Smith R, Kyllerman M, Eiklid K, et al. SLC9A6 Mutations Cause X-Linked Mental Retardation, Microcephaly, Epilepsy, and Ataxia, a Phenotype Mimicking Angelman Syndrome. Am J Hum Genet. 2008 Apr;82(4):1003–10.

320. Li Y, Marzolo MP, Kerkhof P van, Strous GJ, Bu G. The YXXL Motif, but Not the Two NPXY Motifs, Serves as the Dominant Endocytosis Signal for Low Density Lipoprotein Receptor-related Protein. J Biol Chem. 2000 Jun 2;275(22):17187–94.

321. Zhao Z, Michaely P. The Role of Calcium in Lipoprotein Release by the LDL Receptor. Biochemistry. 2009;48(30):7313.

322. Diaz R, Wileman TE, Anderson SJ, Stahl P. The use of permeabilized cells to study the ion requirements of receptor-ligand dissociation in endosomes. Vol. 260, Biochem. J. 1989.

323. Staudt C, Puissant E, Boonen M. Subcellular Trafficking of Mammalian Lysosomal Proteins: An Extended View. Int J Mol Sci. 2016 Dec 28;18(1).

324. Ghosh P, Dahms NM, Kornfeld S. Mannose 6-phosphate receptors: new twists in the tale. Nat Rev Mol Cell Biol. 2003 Mar;4(3):202–13.

325. Bus T, Traeger A, Schubert US. The great escape: how cationic polyplexes overcome the endosomal barrier. J Mater Chem B. 2018 Nov 7;6(43):6904–18.

326. Wang H, Jiang Y, Peng H, Chen Y, Zhu P, Huang Y. Recent progress in microRNA delivery for cancer therapy by non-viral synthetic vectors. Adv Drug Deliv Rev. 2015 Jan;81:142–60.

327. Pickles RJ. Physical and Biological Barriers to Viral Vector-mediated Delivery of Genes to the Airway Epithelium. Proc Am Thorac Soc. 2004 Dec

1;1(4):302–8.

328. Rosman Z, Shoenfeld Y, Zandman-Goddard G. Biologic therapy for autoimmune diseases: an update. BMC Med. 2013 Dec 4;11(1):88.

329. Orellana EA, Rangasamy L, Tenneti S, Abdelaal AM, Low PS, Kasinski AL. Enhancing microRNA activity through increased endosomal release mediated by nigericin. bioRxiv. 2018 Jul 11;367672.

330. Orellana EA, Tenneti S, Rangasamy L, Lyle LT, Low PS, Kasinski AL. FolamiRs: Ligand-targeted, vehicle-free delivery of microRNAs for the treatment of cancer. Sci Transl Med. 2017 Aug 2;9(401):eaam9327.

331. Rangasamy L, Chelvam V, Kanduluru AK, Srinivasarao M, Bandara NA, You F, et al. New Mechanism for Release of Endosomal Contents: Osmotic Lysis via Nigericin-Mediated K+/H+ Exchange. Bioconjug Chem. 2018;29(4):1047–59.

332. Johnson LG, Olsen JC, Sarkadi B, Moore KL, Swanstrom R, Boucher RC. Efficiency of gene transfer for restoration of normal airway epithelial function in cystic fibrosis. Nat Genet. 1992 Sep;2(1):21–5.

333. Pickles RJ, McCarty D, Matsui H, Hart PJ, Randell SH, Boucher RC. Limited entry of adenovirus vectors into well-differentiated airway epithelium is responsible for inefficient gene transfer. J Virol. 1998 Jul;72(7):6014–23.

334. Weisz OA. Organelle Acidification and Disease. Traffic. 2003 Feb 1;4(2):57–64.

335. Lukacs GL, Chang XB, Kartner N, Rotstein OD, Riordan JR, Grinstein S. The cystic fibrosis transmembrane regulator is present and functional in endosomes. Role as a determinant of endosomal pH. J Biol Chem. 1992 Jul 25;267(21):14568–72.

336. Lucien F, Lavoie RR, Dubois CM. Targeting endosomal pH for cancer chemotherapy. Mol Cell Oncol. 2018 Mar 13;e1435184.

337. Mercorelli B, Palù G, Loregian A. Drug Repurposing for Viral Infectious Diseases: How Far Are We? Trends Microbiol. 2018 May 11;26(10):865–76.

338. Santos R, Ursu O, Gaulton A, Bento AP, Donadi RS, Bologa CG, et al. A comprehensive map of molecular drug targets. Nat Rev Drug Discov. 2017;16(1):19.

339. Kale VP, Amin SG, Pandey MK. Targeting ion channels for cancer therapy

by repurposing the approved drugs. Biochim Biophys Acta - Biomembr. 2015 Oct 1;1848(10):2747–55.

340. Mathie A, Veale EL. Therapeutic potential of neuronal two-pore domain potassium-channel modulators. Curr Opin Investig Drugs. 2007 Jul;8(7):555–62.

341. Dong YY, Pike ACW, Mackenzie A, McClenaghan C, Aryal P, Dong L, et al. K2P channel gating mechanisms revealed by structures of TREK-2 and a complex with Prozac. Science. 2015 Mar 13;347(6227):1256–9.

342. Honore E. The neuronal Background K2P Channels: Focus on TREK1. Nat Rev Neurosci. 2007;8:251–61.

343. Gierten J, Ficker E, Bloehs R, Schlömer K, Kathöfer S, Scholz E, et al. Regulation of two-pore-domain (K2P) potassium leak channels by the tyrosine kinase inhibitor genistein. Br J Pharmacol. 2008 Aug;154(8):1680–90.

344. Kudo S, Ishizaki T. Pharmacokinetics of Haloperidol. Clin Pharmacokinet. 1999 Dec;37(6):435–56.

345. Kaakkola S, Lehtosalo J, Laitinen LA. Changes in blood-brain barrier permeability to drugs in decompressed rats. Undersea Biomed Res. 1982 Sep;9(3):233–40.

346. Tauro LB, Rivarola ME, Lucca E, Mariño B, Mazzini R, Cardoso JF, et al. First isolation of Bunyamwera virus (Bunyaviridae family) from horses with neurological disease and an abortion in Argentina. Vet J. 2015 Oct;206(1):111–4.